DATA ANALYSIS FOR HIGH-SENSITIVITY COSMIC MICROWAVE BACKGROUND OBSERVATIONS

Mark Mirmelstein

Department of Physics and Astronomy
School of Mathematical and Physical Sciences

Submitted for the degree of Doctor of Philosophy
University of Sussex
September 2021

Declaration

I hereby declare that this thesis has not been and will not be submitted in whole or in part to another University for the award of any other degree.

The work in this thesis has been completed in collaboration with Antony Lewis, Julien Peloton, Julien Carron and Giulio Fabbian. Chapters 2 and 3 are comprised of the following papers:

- Mark Mirmelstein, Julien Carron, and Antony Lewis, *"Optimal filtering for CMB lensing reconstruction"*, published in Phys. Rev. D 100, 123509. DOI:10.1103/PhysRevD.100.123509. arXiv:1909.02653.
- Mark Mirmelstein, Giulio Fabbian, Antony Lewis, and Julien Peloton, *"Instrumental systematics biases in CMB lensing reconstruction: a simulation-based assessment"*, published in Phys. Rev. D 103, 123540. DOI:10.1103/PhysRevD.103.123540. arXiv:2011.13910.

I made an essential contribution to all of these papers. For Chapter 2, Julien Carron and Antony Lewis provided guidance, comments, and some of the writing and editing. For Chapter 3, Giulio Fabbian, Antony Lewis and Julien Peloton provided guidance, comments and some of the writing and editing. Giulio also provided the power spectra for the different systematics cases.
Most of the work for Chapter 4 was carried out by Julien Carron, who provided the cleaned and filtered CMB maps, quadratic estimators and likelihoods. My contribution comprised of filtering the provided quadratic estimators, and estimating the cosmological parameters.
The work in Chapter 5 was supported by Julien Peloton and Antony Lewis, who provided guidance and comments.

Signature:

Mark Mirmelstein

UNIVERSITY OF SUSSEX

MARK MIRMELSTEIN, DOCTOR OF PHILOSOPHY

DATA ANALYSIS FOR HIGH-SENSITIVITY COSMIC MICROWAVE BACKGROUND OBSERVATIONS

ABSTRACT

In recent decades, the cosmic microwave background radiation (CMB) has been one of the most important tools in cosmology. Due to its primordial origin, the CMB holds information about the early universe and how the universe evolved with time. Inferring cosmological information from the CMB is therefore essential for learning more about the universe. Our abilities to produce high-precision CMB measurements have progressed immensely over the years, which helped to constrain the standard cosmological model with remarkable accuracy. As CMB measurements improve, efforts to improve our analysis methods continue with it. The main aim of the work presented in this thesis is to continue this endeavour for improving our ability to extract information from CMB measurements.

We first explore several filtering methods for lensing reconstruction, and also devise a new filtering step. We show the benefits of using an optimal filter for upcoming ground-based CMB experiments. We adopt our lensing reconstruction method to test how instrumental systematics may affect lensing reconstruction results of an experiment similar to the Simons Observatory (SO), and show how some of the resulting lensing biases might be mitigated. We continue by using our lensing reconstruction pipeline to present new lensing results from a recent release of CMB maps from the Planck collaboration which are more accurate on large scales compared to the previous Planck analysis method. We show how the uncertainty of different cosmological parameters benefits from the improved reconstruction accuracy. We conclude by looking into a different CMB effect — the effect of Rayleigh scattering on the CMB anisotropies. We demonstrate a possible pipeline for extracting the Rayleigh signal from multi-frequency CMB measurements, and forecast the ability of detecting the Rayleigh signal from an SO-like experiment.

Acknowledgements

First and foremost, I would like to thank Antony Lewis for offering me a PhD position at the University of Sussex to begin with, and for being an incredibly patient supervisor from the beginning, all through the last 5 long years. Your continuous encouragement and support, along with invaluable brilliant and insightful comments and suggestions have taught me a lot and enabled me to reach this point in my scientific career. I could never have achieved any of the work presented in this thesis, and more, without your expertise, knowledge, dedication, and trust.

All of the research projects which led to this thesis were done in collaboration with some of the best people I could have ever worked with: Julien Peloton, Julien Carron and Giulio Fabbian. I am truly thankful for your profound contributions to these projects, and for supporting the development of my research and programming skills. You have been amazing colleagues, and I hope to continue learning from you and collaborating with you.

I would like to thank Renée Hložek for being the most wonderful, knowledgeable, supportive and creative mentor I never thought I would ever have. Your tremendous support during my PhD studies through the Simons Observatory Mentorship program has contributed immensely to my ability to finish research projects and write this thesis and provided me with many tools that strengthened my capabilities to conduct scientific work.

Some of the work presented in this thesis has benefited from the advice, help, discussions, guidelines, and more, of members of the Simons Observatory collaboration, especially Sara Simon (who also supported my research on a personal level), Neil Goeckner-Wald, Clara Vergès, Max Silva-Feaver, Kevin Crowley, Matthew Hasselfield, Michele Limon and Grant Teply. All the Simons Observatory-related work shown in this thesis has improved from your contributions.

Many more people have contributed to my life and deserve to be acknowledged here. The main ones are the following:

- Sofia Kirke Forslund for helping me with countless PhD and scholarship applications and research proposals. I would not have been where I am today without your support, kind-heartedness, extreme generosity, and brilliance. I am forever in your debt.
- Yuval Langer, my Git and Linux Guru (among other things), for always being willing to help. You have saved me countless hours of troubleshooting ridiculous problems, and I wish I could return the favour, somehow.
- Damian Hoffman, who helped me throughout my BSc and MSc studies to understand many concepts that continued to be useful throughout my PhD studies.
- My mum, for the continuous financial support that enables me to follow my dreams, and my dad, for the scientific discussions and the continuous curiosity about the universe.

Lastly, I would like to thank Kepler, for always being there for me. You will never know how much you mean to me, and how much your existence in my life has helped me survive and cope in difficult times, but I hope that the feeling is mutual.

Contents

1 Introduction **2**

1.1 The standard cosmological model . . . 2

1.1.1 Geometric spacetime . . . 2

1.1.2 The evolution of the Universe . . . 5

1.2 Large-scale structure . . . 9

1.3 The cosmic microwave background . . . 12

1.3.1 CMB physics . . . 12

1.3.2 Observing the CMB . . . 22

1.4 CMB lensing . . . 26

1.4.1 Weak gravitational lensing of the CMB . . . 26

1.4.2 CMB lensing reconstruction . . . 32

1.5 Thesis outline . . . 40

2 Optimal filtering for CMB lensing reconstruction **42**

2.1 Introduction . . . 43

2.2 Methodology . . . 44

2.2.1 Filtering methods . . . 48

2.2.2 Quadratic estimators . . . 51

2.2.3 Mean field and normalization . . . 52

2.2.4 Filtering the quadratic estimators . . . 52

2.2.5 Lensing power spectrum . . . 54

2.3 Approximate analytic model . . . 55

2.4 Results . . . 61

2.5 Conclusions . . . 65

3 Instrumental systematics biases in CMB lensing reconstruction: a simulation-based assessment **69**

3.1 Introduction . . . 69

3.2 Instrumental systematics simulations . . . 71

3.2.1 Beam ellipticity . . . 76
3.2.2 Differential pointing . . . 82
3.2.3 Boresight pointing . . . 83
3.2.4 Polarization angle . . . 85
3.2.5 Gain drifts . . . 87
3.2.6 Calibration mismatch . . . 88
3.2.7 Crosstalk . . . 90
3.3 Lensing analysis . . . 94
3.4 Systematics biases . . . 97
3.4.1 CMB power spectrum biases . . . 97
3.4.2 Lensing power biases . . . 100
3.5 Mitigation techniques . . . 106
3.6 Conclusions and future prospects . . . 113

4 Improved lensing analysis estimates using the Planck NPIPE maps 116
4.1 Introduction . . . 117
4.2 The NPIPE maps . . . 118
4.3 Lensing analysis . . . 119
4.4 Results . . . 123
4.4.1 Lensing power spectrum . . . 123
4.4.2 Cosmological parameter estimation . . . 125
4.5 Conclusions and future work . . . 129

5 A method for detecting the CMB Rayleigh scattering signal 131
5.1 Introduction . . . 132
5.2 Rayleigh scattering and the CMB . . . 133
5.3 Methodology . . . 137
5.3.1 Cleaning the CMB maps . . . 140
5.3.2 Power spectrum estimates . . . 144
5.4 Detection likelihoods and forecasts . . . 146
5.5 Conclusions and future prospects . . . 149

6 Conclusions 152

A Statistical tools and data analysis methods in CMB cosmology 155
A.1 The Fisher matrix . . . 155

A.2 Wiener filter 159
A.3 Markov Chain Monte Carlo 162

B Optimal filtering performance **164**

Bibliography **167**

“I have crossed the seas, I have left cities behind me,
and I have followed the source of rivers towards their source
or plunged into forests, always making for other cities...
I could never turn back any more than a record can spin in reverse.
And all that was leading me where?
To this very moment...”

Jean Paul Sartre

CHAPTER 1

Introduction

1.1 THE STANDARD COSMOLOGICAL MODEL

1.1.1 GEOMETRIC SPACETIME

In 1915, Albert Einstein published his geometric theory of gravitation which linked gravity to the geometric properties of space and time via field equations [1],

$$R_{\mu\nu} - \frac{1}{2}Rg_{\mu\nu} + \Lambda g_{\mu\nu} = \frac{8\pi G}{c^4}T_{\mu\nu}, \tag{1.1}$$

where $R_{\mu\nu}$ is the Ricci tensor, R is the scalar curvature, $g_{\mu\nu}$ is the metric tensor, Λ is the cosmological constant, G is the Newtonian constant of gravitation, c is the speed of light, $T_{\mu\nu}$ is the stress-energy tensor, and $\mu, \nu \in \{0, 1, 2, 3\}$ are the indices for the time (0) and space (1,2,3) components of the metric. For a given metric $g_{\mu\nu}$, one could calculate the Ricci tensor and scalar curvature, which would lead to a solution of these field equations. One such solution, which describes a homogeneous, isotropic and expanding spacetime, was developed independently between 1920-1940 by Alexander Friedmann, Georges Lemaître, Howard P. Robertson and Arthur Geoffrey Walker [2–9]. For an infinitesimal line element

$$ds^2 \equiv g_{\mu\nu}dx^\mu dx^\nu, \tag{1.2}$$

this metric is

$$ds^2 = -c^2dt^2 + a^2(t)\left[\frac{dr^2}{1-Kr^2} + r^2d\theta^2 + r^2\sin\theta d\phi^2\right], \tag{1.3}$$

where dt (dx^0) is the infinitesimal time component, dr (dx^1), $d\theta$ (dx^2) and $d\phi$ (dx^3) are the infinitesimal space components in spherical coordinates, t is time (where we define $t = t_0$ as today), a is the scale factor which describes the expansion of the Universe as a function of time, r

is the radial coordinate, and K is the spatial curvature constant. This metric, known as the FLRW metric, is used in modern cosmology to describe the physical Universe, as various cosmological observations can be described using this model with high precision.

Using this metric to calculate $R_{\mu\nu}$ and R, and using the explicit form of the stress-energy tensor, $T_{\mu\nu} = (\rho + p)\, u_\mu u_\nu - p g_{\mu\nu}$, where ρ, p and u are the density, pressure and velocity of a given material in the Universe, we can obtain the Friedmann equations,

$$\left(\frac{\dot{a}}{a}\right)^2 = \frac{8\pi G}{3}\rho - \frac{Kc^2}{a^2} + \frac{\Lambda c^2}{3}, \tag{1.4}$$

$$\frac{\ddot{a}}{a} = -\frac{4\pi G}{3}\left(\rho + \frac{3}{c^2}p\right) + \frac{\Lambda c^2}{3}, \tag{1.5}$$

which tell us how the scale factor a changes as a function of time. Because these equations depend on the properties of substances in the Universe and on the spatial curvature, the expansion of the Universe, which is often characterised using the Hubble function,

$$H(t) \equiv \frac{\dot{a}(t)}{a(t)}, \tag{1.6}$$

also depends on the substances in the Universe and their relative amounts, and on the spatial curvature. The substances that make up the Universe are typically categorised according to their different properties, which can be expressed using their equation of state,

$$p = \omega\rho, \tag{1.7}$$

where ω is usually assumed to be constant[1], and takes up different values for the different components of the Universe:

$$\omega = \begin{cases} \frac{1}{3} & \text{for radiation,} \\ 0 & \text{for pressureless matter,} \\ -1 & \text{for dark energy.} \end{cases} \tag{1.8}$$

For each component i, we can define the density parameter

$$\Omega_i(t) \equiv \frac{\rho_i(t)}{\rho_{\text{crit}}(t)}, \tag{1.9}$$

where

$$\rho_{\text{crit}}(t) \equiv \frac{3c^2 H(t)^2}{8\pi G} \tag{1.10}$$

[1] In the case of dark energy, some theories consider a time-varying ω, however there is currently no strong evidence to suggest that $\omega(t) \neq \omega$ according to observations [10].

is the density of a flat FLRW universe ($K = 0$), which is known as the *critical* density.

In an expanding universe, such as ours, it can be useful to associate cosmological times with the redshift z of the radiation in the Universe, as radiation travelling in an expanding universe is redshifted. The redshift at a given time t is related to the scale factor via

$$1 + z = \frac{1}{a(t)}, \tag{1.11}$$

such that today $a(t_0) = 1$ and $z = 0$. Using these definitions, along with the first Friedmann equation, the Hubble function can be expressed as

$$H(z) = H_0 \sqrt{\Omega_{\mathrm{m},0} \left(1+z\right)^3 + \Omega_{\gamma,0} \left(1+z\right)^4 + \Omega_{K,0} \left(1+z\right)^2 + \Omega_{\Lambda,0} + \Omega_{\nu,z}}, \tag{1.12}$$

where the subscript 0 indicates the value of the parameters today, and Ω_m, Ω_γ, Ω_K, Ω_Λ, Ω_ν are the matter, photon, curvature, cosmological constant and neutrino density parameters, such that $\Omega_\mathrm{m} + \Omega_\gamma + \Omega_K + \Omega_\Lambda + \Omega_\nu = 1$. The spatial curvature density parameter, $\Omega_K = -\frac{Kc^2}{H_0^2}$ is a fictitious energy density parameter, while the cosmological constant density parameter $\Omega_\Lambda = \frac{\Lambda}{3H_0^2}$ is related to the energy density of the cosmological constant. The matter density parameter is often defined as the sum of the baryonic and (cold) dark matter density parameters, $\Omega_\mathrm{m} \equiv \Omega_\mathrm{b} + \Omega_\mathrm{c}$. In the early Universe, when neutrinos were relativistic, the radiation energy density included the contributions of both photons and neutrinos [11]. At later times, the neutrinos became non-relativistic, and contributed to the total matter energy density. The parameters in Eq. (1.12) are some of the main cosmological parameters which are needed to describe how the Universe evolves with time.

The current standard cosmological model is often called ΛCDM, because the cosmological parameters measured from observations suggest that we live in a (flat) universe with a non-zero cosmological constant Λ, which also has a yet unknown substance named dark matter (DM) that has non-relativistic properties, hence cold dark matter (CDM). While the evidence for a non-zero Λ value rises from observations which suggest that the expansion of the Universe is accelerated (driven by a substance called dark energy), it is evident that dark matter exists because of its gravitational interaction with radiation and other matter (mainly baryons, which is what most of the non-dark structures in the Universe are made of) [12]. Dark matter is suggested to be "cold" mainly due to the way large-scale structures in the Universe are evidently formed; observations suggest that small clumps of matter collapse to form larger and more massive structures. If the temperature of the dark matter was much higher (or *relativistic*) before it decoupled from matter in

the early Universe, dark matter would have smoothed primordial matter clumps, which would have affected the scales of structures that formed as the Universe cooled down. If, on the other hand, most or all of the dark matter in the Universe had negligible velocity dispersion (*non-relativistic*) compared to other components of the Universe during the matter-radiation equality phase, the matter clumps would not have been smoothed out and would become the large-scale structure that we see in the Universe today [13, 14].

As the Universe evolves and expands, the different substances it is made of have different relative contributions toward the total density in the Universe. In the next subsection, this evolution and the various cosmological epochs are described in more detail according to our current knowledge on the Universe from cosmological observations of the last century.

1.1.2 THE EVOLUTION OF THE UNIVERSE

Cosmological observations suggest that about 13.8 billion years ago, the Universe, which initially was in a hot and dense state, underwent an inflationary period, during which it expanded very rapidly over a short time interval. Most inflationary theories suggest that during inflation quantum fluctuations occurred, such that the distribution of substances in the Universe was not entirely homogeneous [15–22]. Inflation was developed by considering a scalar field with an equation of state $p \approx -\rho$ which generates a nearly exponential expansion in the early FLWR Universe. The power spectrum of the resulting scalar perturbations as a function of scale modes k is estimated as

$$\mathcal{P}_s(k) \approx A_s \left(\frac{k}{k_0}\right)^{n_s - 1}, \tag{1.13}$$

where A_s is the amplitude of the perturbations at a pivot scale k_0, and n_s is the scalar spectral index. This power spectrum, which will be elaborated on in Sec. 1.2, is measured to be approximately scale-invariant with very small deviations from $n_s = 1$.

After inflation ended, the statistically homogeneous and isotropic Universe continued to expand, albeit less rapidly, and cool down. At this point in time, it also had small inhomogeneities in the distribution of matter which were produced during the inflationary period. These matter perturbations will be discussed in more detail in Sec. 1.2. Since inflation, the Universe underwent several phase transitions due to its content and how its components interact with each other. After inflation ended, the main component in the Universe was radiation; the density of relativistic species was considerably higher than any other substance. At that time, radiation helped to maintain a thermodynamic equilibrium between the different particles in the Universe.

Following the inflationary period, the Universe cooled down to a temperature of about 10^9 K, which was cold enough to enable the subatomic particles in it to bound and form helium-4 and small amounts of deuterium and other helium isotopes [23]. This stage in the evolution of the Universe is called "Big Bang nucleosynthesis", as it refers to the formation of nuclei shortly after the beginning of the Universe (an event which is usually referred to as the *Big Bang*). It is different than "Stellar nucleosynthesis", which is the formation of heavier nuclei in the core of stars, a process which starts at a much later stage, when stars have already formed.

Around 300 seconds after Big Bang nucleosynthesis, the temperature of the Universe was around 8×10^8 K, high enough so that the energy density is dominated by baryons and photons. At this point in time, the Universe is radiation-dominated, and the main interaction between the baryons and photons is through Thomson scattering[2], the elastic scattering of electromagnetic radiation by free-moving charged particles.

The matter perturbations from inflation still exist in the early Universe, and as the Universe expands, these perturbations evolve. The perturbations led to areas with less or more matter compared to the overall mean density. This property is usually referred to as the *inhomogeneity* of the matter. The resulting overdense regions tended to naturally become denser due to their self-gravity. Because the Universe at that time was dominated by radiation, significant amounts of photons were trapped in the resulting gravitational wells, leading to a growing outward radiation pressure in these overdense regions. This pressure grew until the overdense regions became less dense and started to expand again. As the Universe expended, the overall gravitational potentials decreased, while the radiation continued to oscillate. With time, the oscillation amplitude was damped due to dissipative diffusion between overdense and underdense regions. The radiation pressure in the overdense regions caused a spherical sound wave of both baryons and photons to start moving outwards at high velocity. The dark matter in these clumps did not follow this wave, as it only interacts gravitationally with the baryons and the photons. The wave propagation of the oscillations was effectively halted once the sound speed decreased dramatically due to decoupling of photons and baryons.

About 380,000 years after the cosmological inflation started, at redshift $z \approx 1100$, the temperature in the Universe decreased to about 3000 K, cold enough so that free electrons and protons began to form electrically-neutral hydrogen atoms. This epoch is known as the

[2]Thomson scattering is a limit of the Compton scattering in which the photon energy ($\sim$0.3 eV then) is much smaller than the rest-mass of the scattering particle ($\sim$0.5 MeV for electron).

recombination era. It led to a significant decrease of density of free electrons, which constantly scattered the photons in the plasma via Thomson scattering. With many fewer free electrons, the probability for the radiation to scatter decreased significantly, and the photons started to travel more freely. This decoupling of the photons, which resulted from the expansion of the Universe and the decreased amount of free electrons, created what is known as the *surface of last scattering*, because these photons would appear as a spherical surface of radiation around an observer in the late Universe such as ourselves. This radiation, which originated in the era of recombination, is known as the cosmic microwave background radiation (CMB). We can still observe this radiation today because the density of free electrons in the Universe never reached similar level as to those before recombination. Due to its primordial origin, the CMB is one of the main tools in cosmology that enables us to learn not only about the early Universe, but also about the late Universe due to the ways in which different structures in the Universe interact and affect this radiation. The CMB is the main topic of this thesis, and as such it is explored in more depth in Sec. 1.3 and throughout the thesis chapters.

Following recombination, as the Universe continued to expand, matter began to clump in overdense regions. This process eventually led to the formation of the large-scale structures (LSS) in the Universe [24, 25]. The matter shells that were formed from the acoustic waves of the primordial density oscillations left an imprint in these structures, which is known as the baryonic acoustic oscillations (BAO). The radius of these shells is known as the sound horizon because it is the comoving distance that a sound wave could travel from the beginning of the Universe until recombination. Due to the nature of the BAO, there is a characteristic comoving scale of the structures in the Universe. This scale can be translated into a characteristic angular size in large-scale measurements across different redshifts. We can measure this characteristic scale from observing the clustering of galaxies. Taking spectroscopic and photometric measurements of galaxies enables the 3D mapping of their clustering, such that their angular- and redshift-dependent 2-point correlation function can be estimated. The resulting correlation function then shows the characteristic galaxy separation modes which are around the sound horizon distance [26].

The LSS eventually gave rise to stars, and later on galaxies and galaxy clusters. The question of when the first stars were formed is still an open question in cosmology. CMB measurements and spectroscopic observations of quasars currently suggest that the first stars were most likely formed around $6 \lesssim z \lesssim 30$, after which the Universe is considered to be completely ionized [27,

28]. Once the first stars and quasars were formed (due to the gravitational collapse of the baryon clumps), their emitted high-energy radiation heated and ionized the hydrogen gas around them. The era in which this ionization process reionized most of the interstellar medium is known as *reionization* [29]. The ionization process created more free electrons, which could scatter the CMB radiation once again since the recombination era. The probability for the CMB photons to scatter since reionization until now depends on the reionization optical depth τ,

$$\tau(\eta) = \sigma_T \int_{\eta}^{\eta_0} a(\eta') n_e(\eta') c d\eta', \tag{1.14}$$

where σ_T is the Thomson scattering cross-section, n_e is the electron density, a is the scale factor, and

$$\eta(t) \equiv \int_0^t \frac{dt'}{a(t')} \tag{1.15}$$

is the conformal time, which is the measured time in the reference frame of the expanding Universe such that $\eta(0) = 0$. The scattering of the CMB photons since reionization are much less frequent compared to pre-recombination times, as although the Universe becomes again fully ionized, the Universe is also significantly larger at late times such that the overall electron density, and with it the scattering probability, is very small. Nonetheless, these scattering events did occur, and therefore CMB measurements can be useful for constraining reionization physics.

When the Universe was about 9.8×10^9 years old (at $z \approx 0.35$), the Universe underwent another transition, and started to accelerate faster [14, 30]. This is attributed to the dominance of the cosmological constant over matter at that time. This is the last known phase transition that occurred, and so the Universe continues to accelerate at increasing rate.

The evolution of the Universe that was described in this section was inferred from cosmological observations. These observations also enable us to estimate the various cosmological parameters that describe the Universe, and specifically the ΛCDM model. The main parameters of this model are shown in Table. 1.1. The values of these parameters are used throughout the work in this thesis to produce fiducial CMB power spectra and CMB realisations for various analysis applications. Throughout, we also assume massive neutrinos with a total mass of 0.06 eV, which is the minimal neutrino mass as measured from stellar neutrinos [11, 31].

While most of these parameters were estimated to high precision, there are still several open questions regarding their values. The most controversial parameter value is that of the Hubble parameter $H_0 \equiv 100h$ [km s^{-1} Mpc^{-1}], which has been measured from various cosmological

probes and presents a $\sim 5\sigma$ tension mainly between early Universe and late Universe probes (see, e.g., Refs. [32–36] for review on this tension). Throughout this thesis we adopt the value which is consistent with most of the early Universe probes and was obtained from CMB observations. Despite the controversy around this value, the results shown in this thesis do not depend strongly on the choice of this parameter value.

Parameter	Symbol	Value
Hubble parameter	h	0.6736 ± 0.0054
Baryon density	Ω_b	$\Omega_b h^2 = 0.02233 \pm 0.00015$
Cold dark matter density	Ω_c	$\Omega_c h^2 = 0.1198 \pm 0.0012$
Primordial power spectrum amplitude	A_s	$\ln\left(10^{10} A_s\right) = 3.043 \pm 0.014$
Spectral index	n_s	0.9652 ± 0.0042
Reionization optical depth	τ	0.0540 ± 0.0074

Table 1.1: The ΛCDM cosmological parameters. The values were obtained from the best-fit parameter estimations of the Planck collaboration [37]. They are used to construct fiducial CMB power spectra and CMB map realisations for the various analyses presented throughout this thesis. The Hubble constant is defined as $H_0 \equiv 100h$ [km s^{-1} Mpc^{-1}]. The subscript 0 is omitted for the Hubble parameter and density parameters.

1.2 LARGE-SCALE STRUCTURE

As mentioned in the previous section, without small matter perturbations in the early Universe, no structures such as planets, stars, galaxies, and galaxy clusters could have been formed in the Universe. A universe without matter perturbations would be perfectly homogeneous and isotropic, with no overdense regions which became the seeds of structure formation. To understand how the large-scale structures (LSS) that we see in the Universe formed, we therefore need to consider a perfectly homogeneous universe, add to it small perturbations, and evolve these perturbations in time. Current theories suggest that these perturbations originated from inflation. As such, an accurate description of these perturbations, along with cosmological observations, could help to constrain early Universe physics. The exact form of the matter perturbations depends on the way the background metric is defined. In this section, we will use the conventional definitions that are obtained using the synchronous gauge [38].

To quantify these perturbations, we can define the fractional deviation from the mean matter density $\bar{\rho}(t)$,

$$\Delta(\mathbf{x}, t) \equiv \frac{\rho(\mathbf{x}, t) - \bar{\rho}(t)}{\bar{\rho}(t)}, \tag{1.16}$$

where $\rho(\mathbf{x}, t)$ is the total matter density at spatial position $\mathbf{x}$ and at time t, such that at a fixed time $\langle \Delta(\mathbf{x}, t) \rangle_{\mathrm{x}} = 0$ by definition[3]. We can use an ensemble average of this measure to statistically quantify the 2-point correlation function of the matter fluctuations in Fourier space at a given time t as

$$\langle \Delta(\boldsymbol{k}, t) \Delta(\boldsymbol{k}', t) \rangle_{\Delta} = P_m(k, t) \delta(\boldsymbol{k} - \boldsymbol{k}'), \tag{1.17}$$

where $k \equiv |\boldsymbol{k}|$ is the Fourier mode of the perturbations, and our Fourier transformation convention is given by

$$\begin{aligned} f(\mathbf{x}) &= \int \frac{d^3k}{(2\pi)^{\frac{3}{2}}} f(\boldsymbol{k}) e^{-i\boldsymbol{k}\cdot\mathbf{x}}, \\ f(\boldsymbol{k}) &= \int \frac{d^3\mathrm{x}}{(2\pi)^{\frac{3}{2}}} f(\mathbf{x}) e^{i\boldsymbol{k}\cdot\mathbf{x}}. \end{aligned} \tag{1.18}$$

This can be done by using the statistical homogeneity requirement that the real-space correlation between a density at two points at fixed time is the same under a spatial translation, $\langle \Delta(\mathbf{x}) \Delta(\mathbf{x}') \rangle = \langle \Delta(\mathbf{x} + \mathbf{c}) \Delta(\mathbf{x}' + \mathbf{c}) \rangle$, for some constant spatial translation vector $\mathbf{c}$. This power spectrum is related to $\mathcal{P}(k)$ from Eq. (1.13) via

$$P_m(k) = \frac{2\pi^2}{k^3} \mathcal{P}_m(k). \tag{1.19}$$

The theoretical matter power spectrum and its measurements from different cosmological probes is shown in Fig. 1.1 [39–41]. On large scales (small k values, which describe super-horizon scales), its shape is proportional to k^{n_s}, while on small scales (sub-horizon scales) it is proportional to $k^{n_s - 4}$. For ΛCDM cosmology, the scalar spectral index is $n_s \approx 1$, and therefore the matter power spectrum has a positive inclination at low k and negative inclination at high k. At $k \approx 10^{-2}\ h\,\mathrm{Mpc}^{-1}$, the power spectrum has a maximum. The small wiggles that appear near the peak are caused by the sub-horizon baryon oscillations prior to recombination. The spacing between the peaks of the wiggles in harmonic space is inversely proportional to the size of the horizon when the baryons decoupled from the radiation.

The matter power spectrum measurements shown in Fig. 1.1 were obtained by several experiments. The Planck collaboration values were obtained by measuring the TT, EE and $\phi\phi$ CMB power spectra (defined later in Secs. 1.3-1.4) and relating them to the theoretical ΛCDM matter power spectrum of Eq. (1.17) [42].

The measurements from the Sloan Digital Sky Survey (SDSS) are from galaxy clustering

[3] Throughout the thesis we will represent vectors and matrices using bold characters. The ways in which different quantities are defined, however, may vary slightly between chapters.

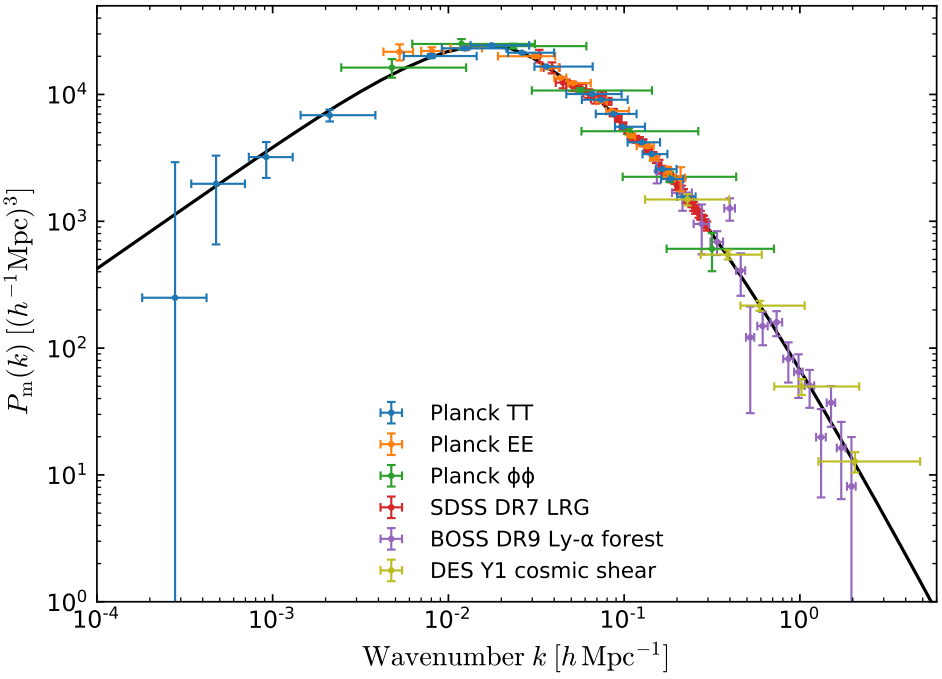

Figure 1.1: The theoretical linear theory matter power spectrum at $z = 0$ (black line) and its measurements at different k bins from several cosmological probes. Unlike the Hubble tension, which is the current disagreement in the measured value of H_0 mainly between early and late Universe probes, the power spectrum measurements, which also come from a range of different redshifts and scales are in a very good agreement with the theory. Source: [40, 41].

observations. Measurements from galaxy clustering are expected to produce a biased power spectrum amplitude, mainly because these are made by specifically observing overdense regions in the Universe. As such, they may not encompass the true matter distribution for all scales [43–47]. The resulting power spectrum is also biased due to complex mechanism of galaxy formation at low redshifts and the relation between baryonic and dark matter densities. To overcome these problems, the measurements in Fig. 1.1 were corrected for this bias using a phenomenological galaxy bias model from N-body simulations for the clustering of dark matter [48].

The Lyman-α (Ly-α) forest measurements were obtained from probing the amount of matter at different redshifts. The Ly-α forest is a series of absorption lines seen in spectroscopic measurements of far galaxies and quasars. Light from these sources can be absorbed by the neutral hydrogen in the intergalactic medium along its trajectory. This absorption then excites the electrons in the hydrogen atoms from the ground state to the first excited state. This transition is known as the Ly-α transition. The amount of absorption lines seen when observing distant galaxies and quasars is therefore sensitive to the matter density of neutral hydrogen clouds along the line of sight, which enables the measurement of the matter power spectrum [49, 50].

Lastly, the Dark Energy Survey (DES) measurements were obtained from measuring the gravitational lensing, which is caused by the LSS, of about 26 million far galaxies [51]. The

observed shapes of lensed galaxies have shear, which is correlated to the amount of the lensing mass. By measuring the correlations of these distortions, it is possible to probe both the linear and non-linear matter perturbations. Due to their dependency on the non-linear growth of structure, when using these measurements for plotting the linear theory power spectrum as in Fig. 1.1 the non-linear effects are usually deconvolved from the total measurements [42, 52].

A useful parameter to quantify the amount of linear perturbations today (at $z = 0$) is the variance of matter fluctuations in a sphere of radius $r_8 \equiv 8h^{-1}$Mpc,

$$\sigma_8^2 = \frac{\left\langle \left| \int_{r_8} d^3\mathrm{x}\Delta(\mathbf{x}) \right|^2 \right\rangle}{\left| \int_{r_8} d^3\mathrm{x} \right|^2}, \tag{1.20}$$

where $\Delta(\mathbf{x})$ are the density perturbations defined in Eq. (1.16) at $t = 0$. The specific radius was chosen as it was measured to be the characteristic scale of mass fluctuations that give rise to clusters; the fluctuation mean in a sphere of that radius is close to unity [53, 54]. This parameter measures the current amplitude of the linear matter power spectrum on a scale of r_8. It is therefore directly related to the growth of matter density perturbations in the early Universe, and to the matter power spectrum of Eq. (1.17) via

$$\sigma_8 = \sqrt{4\pi \int_0^\infty \left[\frac{3}{x^3} \left(\sin(x) - x\cos(x) \right) \right]^2 P_m(k, t_0) \frac{k^2 dk}{(2\pi)^3}}, \tag{1.21}$$

where $x \equiv kr_8$ [55][4].

1.3 THE COSMIC MICROWAVE BACKGROUND

1.3.1 CMB PHYSICS

The current cosmological model suggests that the Universe initially had very high density and temperature. At recombination, the temperature in the Universe decreased to a point where free electrons and protons coupled into neutral hydrogen atoms. This led to a significant decrease of free sub-atomic particles, which constantly scattered the photons in the Universe via Thomson scattering. Because the probability for scattering then decreased drastically, and suddenly, the radiation in the Universe was free to travel without being scattered as frequently. As mentioned

[4] See also: https://cosmologist.info/notes/CAMB.pdf.

in Subsec. 1.1.2, this radiation, known as the CMB, is the main topic of this thesis. Due to its primordial origin, and the various interactions it had along its path until reaching our telescopes, its observations are one of the key tools in modern cosmology. In this section, the formation of its anisotropies and the interactions it had throughout its trajectory across the Universe is described.

Prior to recombination, the resistance of the photon pressure to gravitational compression in the hot plasma fluid caused acoustic oscillations. At small scales during recombination, regions of compression can be represented by hot spots in a primordial CMB map, while regions of rarefaction can be represented by blue spots [56]. These are the primary CMB anisotropies which we measure today at small scales. Because some of the CMB photons escaped the gravitational wells of the overdense regions during last scattering, they underwent a gravitational redshift, which contributes to the CMB anisotropies at larger scales. Small-scale perturbations were also affected by dissipative diffusion: photons with higher energies around overdensities travel to colder regions. This effect, mostly known as *Silk damping* [57], smooths the anisotropies at scales $\ell \gtrsim 1000$ in the power spectrum [58].

During and shortly after recombination, the newly formed hydrogen atoms had the first effect on the CMB following Thomson scattering. This brief interaction, which lasted until the expansion of the Universe brought its probability to negligible levels, is known as Rayleigh scattering. This effect on the CMB photons is the main topic of Chapter 5, where it will be discussed in more detail.

The anisotropy of the gravitational wells at recombination created the primary CMB anisotropies at large scales. The CMB photons were gravitationally redshifted at different strengths due to this anisotropy, which created an uneven radiation surface with fluctuations at scales larger than $\sim 10^\circ$. This gravitational redshift is known as the Sachs-Wolfe effect [59, 60]. If the CMB anisotropies would not have been affected in various ways before they were observed today, measuring the CMB would have given us directly information on the initial perturbations at the era of recombination. Many processes, however, did affect these anisotropies as the CMB photons travelled throughout the Universe. A similar gravitational redshift process, called the integrated Sachs-Wolfe (ISW) effect [61], continued to affect the CMB also at late times due to the large-scale structures in the Universe; photons that pass through strong large-scale potential wells formed by superclusters get an increase in energy, while photons that pass through voids loose some energy. The ISW effect acts at large scales, and so its effect on the temperature power

spectrum is limited to multipoles $\ell \lesssim 100$, and can mainly be seen through cross-correlating CMB maps with galaxy density maps that are usually generated by optical sky surveys [62].

The way in which the CMB anisotropies appear today can be derived by considering photons that are moving along null geodesic lines ($ds = 0$, which is the case for massless particles). Particles free from all external non-gravitational forces move along geodesic lines which are described by the geodesic equations,

$$\frac{d^2x^\mu}{d\lambda^2} + \Gamma^\mu_{\alpha\beta}\frac{dx^\alpha}{d\lambda}\frac{dx^\beta}{d\lambda} = 0, \tag{1.22}$$

where λ is an affine parameter, and x^μ are the spacetime coordinates at point λ on the particle path. For massive particles, this equation describes the minimal path length in a general spacetime, where $\Gamma^\mu_{\alpha\beta}$ are the Christoffel symbols, that describe the properties of a given metric $g_{\mu\nu}$. The line element that is usually used to describe the early Universe from which the CMB photons emerged is a perturbed version of the FLRW metric (whose line element is defined in Eq. (1.3)),

$$ds^2 = a(\eta)^2\left[-\left(1+2\Psi\right)c^2d\eta^2 + \left(1-2\Phi\right)d\mathbf{x}^2\right], \tag{1.23}$$

where Ψ and Φ are two scalar potentials, $d\eta \equiv dt/a(t)$ is the differential conformal time (which is defined in Eq. 1.15), and $\mathbf{x}$ are the comoving Cartesian spatial coordinates, which remain constant in time in a homogeneous and isotropic expanding universe. This metric is known as the perturbed FLRW metric in the conformal Newtonian gauge [38], which is used in this context for its simplicity [63]. While the FLRW metric describes a homogeneous and isotropic universe, the perturbed line element describes a universe with some matter inhomogeneity, or matter perturbations around some average energy density.

Considering photons which propagate along null geodesics in a perturbed flat universe described by the line element of Eq. (1.23) from a sphere whose surface is the surface of last scattering around us, we can integrate Eq. (1.22) to obtain the energy of these photons today. To linear order in perturbations, this energy is given by

$$E(\eta_0) = a(\eta_{\rm re})E(\eta_{\rm re})\left[1 + \Psi(\eta_{\rm re}) - \Psi(\eta_0) + \int_{\eta_{\rm re}}^{\eta_0} d\eta\left(\Psi'(\eta) + \Phi'(\eta)\right)\right], \tag{1.24}$$

where η_0 and $\eta_{\rm re}$ are the conformal times today and at recombination, respectively, and primes denote conformal time derivatives. This result shows that at $0^{\rm th}$ order in perturbations the energy scales as $E(\eta_{\rm re}) \propto E(\eta_0)/a$, which is the expected result when the relevant metric is the

unperturbed FLRW metric of Eq. (1.3). The 1^{st} order corrections from the perturbed metric results from the difference in potentials between the point of emission and reception (photons climbing out or fall into potential wells at the two points), and from the evolving potentials along the line of sight (from which the photons also climb out or fall into). The latter is the ISW effect mentioned above. The ISW effect exists because of the late dominance of dark energy, which causes the potential wells to evolve in time from $z \gtrsim 0$. All of these effects cause the CMB to have less or more energy at different points on the sky, and these are the anisotropies we see in the CMB maps today.

Since we never observe the CMB photons from their rest frame, the energy that we measure is slightly different due to Doppler shifts, which should also be accounted or when describing the observed CMB. The velocity of the observer with respect to the CMB rest frame $\mathbf{v}_{\text{obs}}$ should therefore be considered, as well as the peculiar velocities of the CMB itself, which is essentially the velocity of the baryons that the CMB photons are coupled to then $\mathbf{v}_b$. Converting the photon energy to the photon temperature, which are related via

$$\rho_\gamma(z) = \frac{\pi^2}{15}\,(1+z)^4\,T_\gamma^4, \tag{1.25}$$

the relative observed temperature anisotropies today ΔT_{obs} in direction $\hat{\mathbf{n}}$ with respect to the mean temperature today, $T_0 = 2.72548 \pm 0.00057$ K [64], is given by

$$\frac{\Delta T_{\text{obs}}}{T_0}(\hat{\mathbf{n}}) \equiv \frac{T_{\text{obs}}(\hat{\mathbf{n}}) - T_0}{T_0} = \frac{\Delta_\gamma}{4} + \hat{\mathbf{n}}\cdot(\mathbf{v}_{\text{obs}} - \mathbf{v}_b) + \Psi(\eta_{\text{re}}) - \Psi(\eta_0) + \int_{\eta_{\text{re}}}^{\eta_0} d\eta\,\left(\Psi'(\eta) + \Phi'(\eta)\right). \tag{1.26}$$

where Δ_γ is the radiation perturbation, which represents the CMB anisotropies at recombination such that $\Delta_\gamma(\eta_0) = 0$.

Before recombination, photons were constantly interacting with the free electrons via Thomson scattering. Due to the initial CMB anisotropy, and because the Thomson scattering cross-section depends on the polarization of the radiation [65], this elastic scattering produced a net linear polarization to the scattered photons. The polarization states of the photons after their last Thomson scattering event then persevered after recombination. The polarization modes which we observe, however, are not the primordial ones, as like with the main CMB intensity, these are affected by various processes along their trajectory before reaching our telescopes.

The common method for describing radiation is via the Stokes parameters, which hold the information on the intensity (I), linear polarization (Q and U), and circular polarization (V) of the radiation. When considering the CMB specifically, V is often nullified. This is done mainly because it simplifies most of the analytical and numerical treatments which involve polarization,

but also because it is not generated via Thomson scattering. Theoretical predictions also suggest that the circular polarization of the CMB is very small compared to the other Stokes parameters [66, 67]. Throughout this thesis, we embrace this approximation, and consider only I (often referred to as T hereafter[5]), Q and U to fully describe the CMB radiation properties. The CMB temperature and polarization anisotropies are shown in Fig. 1.2. These were measured using full-sky observations of the Planck satellite over a period of about 4 years [68]. The temperature anisotropies shown in this figure have a characteristic scale of $\sim$1 degree, while the polarization anisotropies appear slightly larger due to the contribution from reionization.

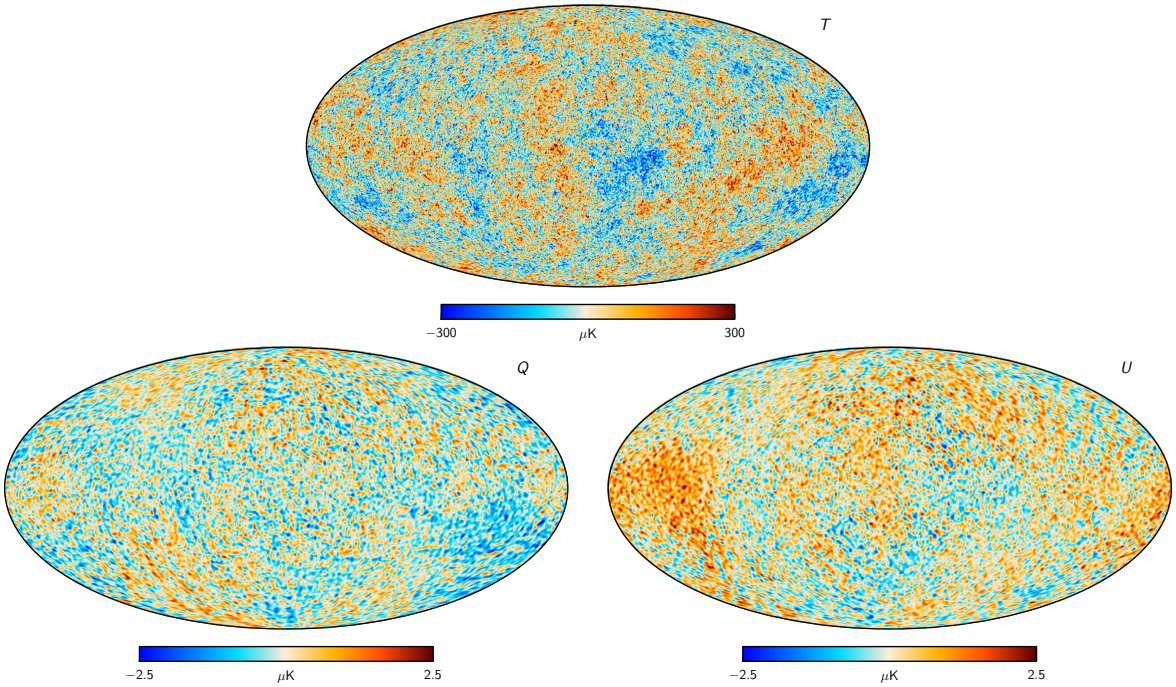

Figure 1.2: The T, Q and U anisotropies of the CMB as measured by Planck. These maps were cleaned using the 2018 SMICA foreground-cleaning algorithm. Source: Akrami [68].

It can be more useful to describe the CMB polarization using the E and B modes. They are related to the polarization Stokes parameters Q and U via [69–72]

$$E(\boldsymbol{\ell}) \pm iB(\boldsymbol{\ell}) = -\int \frac{d^2\mathrm{x}}{2\pi} \left[Q(\mathbf{x}) \pm iU(\mathbf{x})\right] e^{\mp 2i\varphi_\ell} e^{-i\boldsymbol{\ell}\cdot\mathbf{x}}, \tag{1.27}$$

where φ_ℓ is the directional angle of the 2D vector $\boldsymbol{\ell}$ with amplitude $\ell = |\boldsymbol{\ell}|$. This definition of the E and B modes is given using the flat-sky approximation, in which $\mathbf{x} = x\hat{\mathbf{x}} + y\hat{\mathbf{y}}$, $\boldsymbol{\ell} = \ell\cos\varphi_\ell\hat{x} + \ell\sin\varphi_\ell\hat{y}$, and $\ell \equiv |\boldsymbol{\ell}|$. The curved-sky definition can be found in, e.g., Ref. [70]. These polarization modes are more useful because unlike Q and U, E and B are invariant under coordinate rotations in the plane perpendicular to the polarization direction on the sphere. This

[5]For a black body, the two are related via $I(\nu) = \frac{2h\nu^3}{c^2}\frac{1}{e^{\frac{h\nu}{k_B T}}-1}$ where ν is the frequency of the radiation, h is Planck's constant and k_B is Boltzmann's constant.

means that the polarization magnitude does not depend on the specific directions in which the polarization was measured, which enables more robust treatments of CMB polarization.

Inflationary theories suggest that apart from scalar perturbations, the tensor components of the metric are also perturbed due to primordial gravitational waves [73]. As with the scalar perturbations, these would also contribute to the CMB anisotropies, especially at large angular scales. Due to the existence of the scalar perturbations, which are expected to dominate, it is currently impossible to measure the contribution of the tensor perturbations to the CMB temperature anisotropies. Another advantage of using the E and B modes is that, by construction, while E modes are sensitive to both the scalar and tensor perturbations, the B modes are only sensitive to the tensor perturbations. Measuring the CMB B modes could therefore be useful for constraining inflationary theories which predict different levels of tensor perturbations. Such measurements are one of the main targets of current and upcoming CMB experiments, as it may provide further insight on inflation [74–77].

The task of extracting this primordial information from B modes is very challenging. Not only are B modes contaminated by foregrounds [78, 79] and various instrumental systematics (as is the case also with E modes and temperature measurements), the B modes are also contaminated with E modes due to the mode mixing caused by gravitational lensing (see Sec. 1.4 for more details). It has already been shown that reconstructing the gravitational lensing potential that affects the CMB can help with removing the lensing contributions of B modes by *delensing* them [80–84]. Delensing the T and E fields will also be beneficial, as it will allow us to better constrain the cosmological parameters using the unlensed CMB likelihoods [85]. This is one of the main motivations for studying gravitational lensing, which is the main topic of this thesis, and to improve the lensing reconstruction accuracy, which would then translate into our ability to delense the B modes to uncover primordial gravitational waves signals.

To extract cosmological information from CMB measurements, it is useful to characterise the size of the observed temperature and polarization anisotropies as a function of angular scale. This relation is known as the angular power spectrum. It is defined using the expansion coefficients $a_{\ell,m}$ of a temperature or polarization CMB anisotropies map into spherical harmonics. For the temperature anisotropies,

$$\frac{\Delta T_{\text{obs}}(\mathbf{x})}{T_0} = \sum_{\ell=1}^{\infty} \sum_{m=-\ell}^{\ell} T_{\ell m} Y_{\ell m}(\mathbf{x}), \tag{1.28}$$

where $\Delta T_{\text{obs}}(\mathbf{x})$ are the temperature anisotropies at a specific direction on the sky $\mathbf{x}$, which have an order of magnitude of $10^{-5}K$, and $Y_{\ell m}$ is a spherical harmonic function of degree ℓ and order m. When using flat CMB maps, this expansion simplifies to taking the Fourier transform of the map,

such that $T_{\ell m} \to T_{\ell}$ are the Fourier coefficients. The flat-sky approach for describing measured CMB quantities will be used throughout the thesis. The only exception will be Chapters 4 and 5, where we will use curve-sky expressions. For polarization, as described earlier, we can expand the E and B modes in a similar fashion. The power spectrum of two CMB fields $x, y \in \{T, E, B\}$ is defined as the average over ensembles of these expansion coefficients,

$$\langle x_{\ell m} y^*_{\ell' m'} \rangle_{xy} = \delta_{\ell \ell'} \delta_{m m'} C_{\ell}^{xy}, \tag{1.29}$$

where δ is the Kronecker delta function. In practice, because we only observe one ensemble (we only have our Universe to observe), we instead use an average over the orders m to obtain an unbiased estimator for the power spectrum,

$$\hat{C}_{\ell}^{xy} = \frac{1}{2\ell + 1} \sum_{m=-\ell}^{\ell} x_{\ell m} y^*_{\ell m}, \tag{1.30}$$

where $2\ell + 1$ is the number of orders m in each ℓ. The variance of these power spectra is usually estimated by approximating the expansion coefficients $a_{\ell m}$ as independent random Gaussian variables of zero mean,

$$\mathrm{Var}\left(\hat{C}_{\ell}^{xy}\right) = \frac{\left(C_{\ell}^{xy}\right)^2 + C_{\ell}^{xx} C_{\ell}^{yy}}{2\ell + 1}. \tag{1.31}$$

The calculation of this variance is shown in Appendix A.1. This assumption is consistent with current CMB measurements, which also fit to simple inflationary models (e.g., where inflation is driven by one scalar field) which give rise to the CMB anisotropies [86, 87]. It is also helpful for making specific predictions for the CMB anisotropies pattern [88]. The resulting variance is usually considered as the *cosmic variance limit*, as it sets the limit of accuracy on the power spectra we can calculate.

The sky maps we observe to measure the CMB anisotropies are usually contaminated by various foregrounds, instrumental systematics, and instrumental noise. To obtain the power spectra of CMB anisotropies, these raw sky maps are first cleaned from foregrounds. It is also common practice to mask some parts of the maps to avoid contaminating the resulting power spectrum with foreground residuals which survive the cleaning process, such as the thermal emissions around the galactic plane and point sources, which will be discussed in some more detail in Subsec. 1.3.2. While applying masks can help to produce more accurate cosmological results, applying a mask reduces the observed sky area, which can increase the statistical uncertainty of the measurements. It can therefore be crucial for experiments to optimise the

amount of masked areas in CMB analyses. Unobserved sky areas in measurements of CMB experiments can also be considered as masked regions on a full-sky map. When using masked CMB fields in Eq. (1.30), the result is the pseudo-C_ℓ [89–92]. The unbiased power spectrum can be estimated from this pseudo-power spectrum by applying a mixing matrix $\mathcal{M}$ that takes into account the fact that not all modes on the sphere were fully observed due to masking. This method will be shown in more detail in Chapter 5. For a mask $M(\mathbf{x})$, one can also approximate a correction factor to the pseudo-C_ℓ,

$$f_{\rm sky} = \frac{1}{N_{\rm pix}} \sum_{i=1}^{N_{\rm pix}} M_i^2, \tag{1.32}$$

instead of calculating the mixing matrix, and obtain a fairly good approximation for the unbiased power spectrum. Although using $f_{\rm sky}$ to unbias the cut-sky CMB power spectra gives generally good results, it can be less optimal when calculating the E and B power spectra from cut-sky maps due to the mode-mixing the masks induce [93–96]. The mixing matrix, on the other hand, can be optimised to produce the pure E and B spectra [97].

The CMB power spectra that were measured by the Planck collaboration [37] are shown in Fig. 1.3. This collaboration did not produce significant measurements of the B modes due to insufficient polarization sensitivity. Most of their polarization measurements were dominated by large-scale foregrounds and instrumental noise, and even after cleaning the polarization maps the resulting BB power spectrum was compatible with zero [37]. On small scales, B modes do appear in the cleaned Planck maps, however these could only be detected by correlating the maps with other internal or external tracers [98–100].

The peaks and troughs of C_ℓ^{TT}, C_ℓ^{TE} and C_ℓ^{EE} are caused by the sound waves of the density perturbations prior to recombination. Because prior to recombination modes of different wavelengths completed different numbers of full oscillations, the characteristic length scales produce the series of minima and maxima in the power spectra [24, 25, 88, 101, 102]. At scales $\ell \lesssim 100$, the TT power spectrum is relatively flat. This large-scale plateau reflects the primordial power spectrum, which is almost scale-invariant, and does not depend on post-recombination physics. It is often called the Sachs-Wolfe plateau [59], as the Sachs-Wolfe effect dominates these scales. The slight increase of power at $\ell \lesssim 10$ is due to the integrated Sachs-Wolfe effect, which is dominant on the largest scales. The oscillations at scales $\ell \gtrsim 1000$ are smoothed due to the gravitational lensing of the CMB photons in the late Universe. Lensing also mixes modes in the CMB power spectra, which leads to an increase of power in modes with less unlensed power. While the primordial CMB anisotropies are Gaussian to good approximation [103–105], the

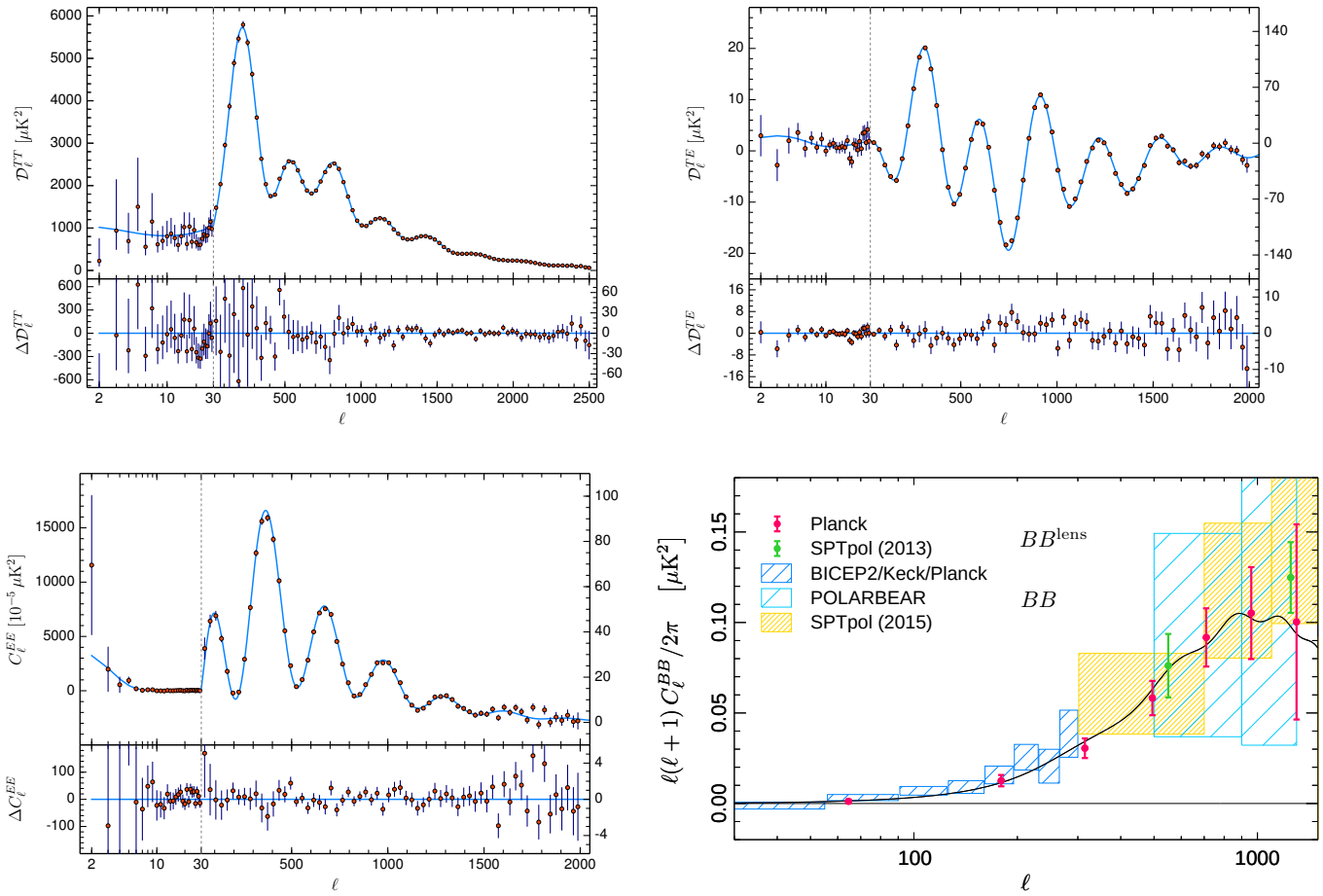

Figure 1.3: The CMB TT, TE and EE power spectra measurements and best-fit from Planck, where $\mathcal{D}_\ell \equiv \ell(\ell+1)C_\ell/(2\pi)$. The Bottom-right panel shows the current state of the CMB BB power spectrum measurements. The C_ℓ^{BB} measurements from Planck and SPTpol are from cross-correlations with a B-mode template. Sources: Aghanim [37] and Ade [99].

observed anisotropies are no longer Gaussian, mainly due to CMB lensing. The weak gravitational lensing of the CMB is described in more detail in Sec. 1.4.

In the late Universe, the CMB photons undergo further scattering during and after reionization. The resulting anisotropies come from different parts of the sky, which causes a map-level suppression of anisotropies proportional to $e^{-\tau}$ on small scales (high ℓs), where τ is the optical depth to reionization of Eq. (1.14). The resulting temperature power spectrum is therefore also suppressed by a factor of $e^{-2\tau}$. While the same factor affects the polarization power at high ℓ values as well, unlike with temperature this scattering also increases the polarization anisotropy at low multipoles [106–108]. This is due to the larger temperature quadrupole at recombination, which is the mode that generates polarization from Thomson scattering.

Another effect which induces anisotropies in the CMB in the late Universe is the Sunyaev-Zeldovich effect [24, 109]. CMB photons can collide with the much more energetic free electrons

in the intracluster medium, and as a result gain some energy on average. This additional energy changes slightly the CMB anisotropies in the direction of galaxy cluster. Measuring this energy excess can therefore be used to detect galaxy clusters [110, 111]. Masking areas with known clusters in the CMB maps can help reduce the impact of this effect when analysing CMB maps.

As discussed earlier, the relative motion between the CMB and the observer provides an additional large-scale anisotropy due to the Doppler effect. This effect manifests at the dipole level of the CMB (the monopole contribution is the mean temperature of the radiation). The measured CMB dipole, which is caused by the peculiar velocity of the solar system relative to the comoving cosmic rest frame of the CMB, indicates a relative velocity of 369.82 ± 0.11 km/sec [40, 112].

The ability to numerically compute the theoretical power spectra of the CMB temperature and polarization anisotropies is very useful in cosmology. Such computations are used extensively to relate observations with theory, and to estimate cosmological parameters. The theoretical CMB power spectra for a given model can be calculated with cosmological Boltzmann codes. These codes evolve the distribution function of the CMB photons using the Boltzmann equations, which describe the statistical interactions and forces that affect the propagation of the CMB radiation in the evolving Universe. It usually uses General Relativity to calculate the effects of gravity and spacetime curvature on the trajectory of the photons, and includes the transfer functions for baryons, neutrinos, dark matter, and dark energy. The resulting CMB statistics depends on the assumed initial conditions in the early Universe, which are used as the input parameters. The (log) primordial scalar and tensor perturbations are often parametrised as running power laws, following the slow-roll inflationary model [77],

$$\begin{aligned}
\ln\left(\mathcal{P}_s(k)\right) &= \ln\left(A_s\right) + \left(n_s - 1\right)\ln\left(\frac{k}{k_s}\right) + \frac{n_{s,\mathrm{run}_1}}{2}\left[\ln\left(\frac{k}{k_s}\right)\right]^2 + \frac{n_{s,\mathrm{run}_2}}{6}\left[\ln\left(\frac{k}{k_s}\right)\right]^3, \\
\ln\left(\mathcal{P}_t(k)\right) &= \ln\left(A_t\right) + n_t\ln\left(\frac{k}{k_t}\right) + \frac{n_{t,\mathrm{run}_1}}{2}\left[\ln\left(\frac{k}{k_t}\right)\right]^2,
\end{aligned} \tag{1.33}$$

where A_i are the perturbation amplitudes at pivot scales k_i, n_i are the spectral indices, and $n_{i,\mathrm{run}_j} \equiv d^{(j)}n_i/d\ln(k)^{(j)}$. These parameters, along with the other cosmological parameters shown in Table 1.1, are used as input to Boltzmann codes to evaluate the resulting CMB power spectra of the assumed cosmological model. The work presented in this thesis uses fiducial power

spectra that were generated by the well-known Boltzmann code CAMB [113][6]. We use these power spectra extensively for various purposes, such as generating different CMB map realisations and comparing power spectra results with the theoretical ΛCDM power spectra.

1.3.2 OBSERVING THE CMB

The CMB was originally detected in 1964 by Arno Penzias and Robert Wilson as an isotropic and homogeneous radiation with mean temperature of $T_{\rm CMB} = 3.5 \pm 1.$ K [114]. This background temperature was measured even earlier, in 1941, by Andrew McKellar from spectroscopic observations of CN absorption lines in the spectrum of a B-type start without relating it to its cosmic origin [115]. This mean temperature of the Universe today was also predicted in 1948 by Ralph Alpher and Robert Herman to be about 5 K [116].

Following the discovery of the CMB, many experiments were built to characterise this radiation with increasing accuracy. In November 1989, the COsmic Background Explorer (COBE) [117], the first satellite mission devoted mainly to CMB cosmology research, was launched. This satellite carried three distinct experiments on board: A differential microwave radiometer (DMR) that mapped the CMB anisotropies, a far-infrared absolute spectrophotometer (FIRAS) which was used to measure the spectrum of the CMB, and a diffuse infrared background experiment (DIRBE), a multi-wavelength infrared detector that mapped the galactic dust emissions. It performed measurements in 31, 53 and 90 GHz, with sensitivities in the range 15-43 mK$\sqrt{\rm sec}$. One of the main results of DMR and FIRAS experiments was that the CMB can be very well approximated as a black-body radiation with temperature of 2.728 ± 0.002 K [118, 119]. The DMR angular resolution, 7°, was not sufficiently small to measure the small-scale CMB anisotropies.

The second CMB satellite mission was the Wilkinson Microwave Anisotropy Probe (WMAP), which operated between the years 2001-2010 [120]. WMAP measured both the temperature and polarization of the CMB at five different frequency bands between 23 and 94 GHz. Its 94 GHz measurements had a resolution of 13.2 arcminutes, about 33 times higher than the COBE resolution, at a sensitivity 45 times higher than that of COBE. These significant improvements in precision enabled detailed measurements of the CMB anisotropies. As the first CMB satellite mission that was sensitive to polarization, WMAP also enabled the first detection of the TE cross-correlation [28].

Close to the end of the WMAP operation, the third and, as of writing these words, last satellite

[6] Available at https://camb.info/.

CMB mission, Planck, was launched [121]. Even almost 10 years since Planck retired, its CMB measurements are still considered as some of the most accurate ones, which help ground-based experiments to perform various calibrations for their measurements[7]. Its main improvements compared to WMAP were the much higher sensitivity in both temperature and polarization measurements, a resolution of more than 2 times greater, and a larger variety of frequency channels [122]. Planck's 5-year mission provided high-resolution maps of the CMB anisotropies, which helped to improve the estimates of the cosmological parameters, measure the E mode power spectrum, and also, for the first time, to produce the auto-power spectrum of the reconstructed CMB lensing potential due to its sensitivity to small scales [98, 100, 123].

Before Planck was launched, many ground-based CMB experiments began operating and producing cosmological results. The main advantage of such ground-based experiments is that much larger arrays can be used, which in turn provide higher resolution maps. They can also host a much larger amount of detectors to measure the sky with. Using more detectors not only increases overall sensitivity, but also improves the immunity of the resulting maps to some instrumental systematic effects, as then multiple detectors, each with its own systematic, observe the same sky area, which can lead to reduced systematics contamination due to averaging. The main disadvantage of ground-based experiments is the Earth's atmosphere. The atmosphere has many particles which absorb, reflect, or emit radiation around the same frequencies a typical CMB experiments observes in, which is usually between 30-800 GHz. Fluctuating particle densities in the atmosphere also introduce spatial and temporal correlations between measurements. These distortions can be hard to realistically simulate and remove from sky maps [124]. To minimise atmospheric noise, CMB observatories are usually constructed at high elevations where the air is relatively dry, stable, and cold. These requirements led the Atacama Desert in Chile, which is 5,200 meters above sea level, and Antarctica, which is 3,048 meters above sea level, to be the main locations for ground-based CMB experiments. Some of the CMB experiments in the Atacama Desert include the Atacama Cosmology Telescope (ACT) [125], the POLARization of the Background Radiation (POLARBEAR) experiment [126], and the Cosmology Large Angular Scale Surveyor (CLASS) [127]. The main CMB experiments that are located at the South pole are the South Pole Telescope (SPT) [128], the Background Imaging of Cosmic Extragalactic Polarization (BICEP) experiment [129], and the Keck array [130]. These experiments finished their initial observation runs and have been since then enhanced to commence observations.

[7] Unlike spaceborne CMB missions, ground-based CMB experiments have the challenge of controlling the detectors environment, which often means the measured gains are miscalibrated. To calibrate the gains, they often use the Planck measurements.

In the upcoming years, more CMB experiments are expected to be built and start observations. As recent decades showed, it is expected that these experiments will continue to become more and more sensitive to the CMB anisotropies and provide increasingly better CMB measurements. This improvement trend is illustrated in Fig. 1.4, where current experiments are considered to be between Stage-III and Stage-IV. The next CMB experiment that will start observations is the Simons Observatory [131, 132], which will provide arcminute-scale sky measurements in 6 different frequency bands between 27-280 GHz using around 60,000 detectors. Several forecasts for this experiment are done in Chapters 2, 3 and 5. The currently-proposed next-generation CMB ground-based experiment, CMB Stage-4 (CMB-S4) [133–135], is expected to produce even more sensitive CMB measurements.

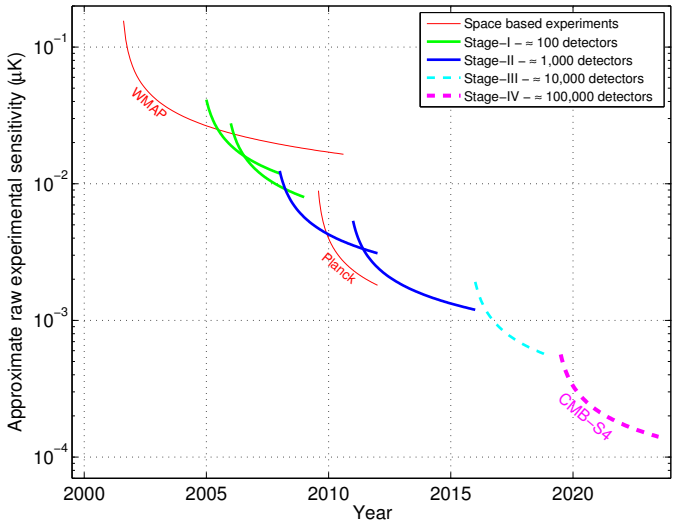

Figure 1.4: Sensitivities of past, present, and future CMB experiments in temperature measurements. Polarization sensitivities are larger by a factor of $\sqrt{2}$. ACT, SPT, POLARBEAR and BICEP are around Stage-II and Stage-III, while the Simons Observatory is planned to be between Stage-III and Stage-IV. Source: Abazajian [133].

Apart from more ground-based experiments, there have also been several approved proposals for satellite missions that will observe the CMB over a larger frequency range. One such mission, the Lite (Light) satellite for the study of B-mode polarization and Inflation from cosmic background Radiation Detection (liteBIRD) [136], which will have 15 channels (compared to Planck's 9 channels) between 34-448 GHz, is expected to be the successor of the Planck mission and provide new insights for CMB observations largely due to its expected robustness to battle foreground contamination. It is currently planned to be launched in 2028 for a 3-year mission, operating from the same location as the Planck satellite.

The main way in which today's experiments measure the CMB is through telescopes which receive signals from their environment and transfer them to bolometers. The bolometers measure the power of the incident radiation through a heating element with a temperature-dependent

electrical resistance. The input signal changes the temperature of this heating element, and this temperature is converted to an electric signal. This time-dependent signal is usually referred to as the observed time-ordered data (TOD). Using the sky location from which the TOD arrives, which is defined by the pointing matrix of the experiment, the TOD can be converted to temperature and polarization maps. The maps can then be constructed from individual detector pairs (or even individual detectors, for constructing the temperature map specifically; pair-differencing is usually required for polarization measurements), or from different combinations of detectors. If the same sky area is observed several times by the full experiment, maps can also be made by combining data from different observation runs. These different combinations are important for data analysis, as these combinations help to reduce noise, systematics, and foregrounds in the final maps. As experiments become more sensitive, the way in which CMB measurements are made can affect the uncertainty of the measurements. The measurement process and how different instrumental systematics affect the reconstructed lensing potential from future CMB observations is discussed in more detail in Chapter 3.

Producing sky observations in multiple frequencies is also very important for CMB observations. While the CMB power peaks at around 160.4 GHz (or 1.9 mm), it also has power at lower and higher frequencies. Combining different frequency maps can also help reducing contaminants in the final map. When observing the sky in these radio frequencies, we do not only see the CMB. Sky maps in different frequencies show that there are many foregrounds between the CMB and the telescope, most of which scale with the observation frequency, which contaminate the CMB anisotropies maps. The most contaminating foreground in a large range of frequencies is the thermal emissions from the intergalactic medium of the Milky Way. Another important contaminant is point sources. These are objects such as galaxies, quasars, blazars, and gamma-ray bursts that appear as point-like signals in the CMB maps but do not have a primordial origin [137]. Point sources which are detected by CMB and various radio telescopes can be used to construct point source masks that can be applied to CMB maps for cosmological analyses [138–140]. Such point source masks can then be used alongside a galactic plane mask to reduce the impact of residual foregrounds on the CMB analysis.

1.4 CMB LENSING

1.4.1 WEAK GRAVITATIONAL LENSING OF THE CMB

In the previous section, we mentioned that along its trajectory, the CMB photons were affected by the LSS in the late Universe through *gravitational lensing*. In this section, we will describe this effect in more detail, and show how the lensing potential can be inferred from CMB measurements.

To discuss the gravitational effects on the CMB, we must consider a spacetime metric which includes gravitational potentials. These potentials affect the CMB trajectory and lens the CMB photons [141]. For this, we use the perturbed FLRW metric in the conformal Newtonian gauge [141],

$$ds^2 = a^2(\eta)\left[-(1+2\Psi)\,c^2 d\eta^2 + (1-2\Phi)\left[d\chi^2 + f_K^2(\chi)d\theta^2 + f_K^2(\chi)\sin^2\theta d\phi^2\right]\right]. \quad (1.34)$$

Here, χ is the comoving radial distance,

$$\chi(t) = \int_{t_e}^{t} c\frac{dt'}{a(t')}, \quad (1.35)$$

where t_e is the time in which photons were emitted from the observed source. This distance factors out the expansion of the Universe, and so comoving distances do not increase as the Universe expands. $f_K(\chi)$ is the comoving angular diameter distance, which depends on the curvature of the Universe K, and is given by

$$f_K(\chi) = \begin{cases} K^{-1/2}\sin(K^{1/2}\chi) & \text{for } K > 0 \text{ (closed universe)}, \\ \chi & \text{for } K = 0 \text{ (flat universe)}, \\ |K|^{-1/2}\sinh(|K|^{1/2}\chi) & \text{for } K < 0 \text{ (open universe)}. \end{cases} \quad (1.36)$$

The angular diameter distance is the ratio between the physical size of the observed object and its apparent angular size as seen by an observer at comoving distance χ away from the object. The potential Ψ satisfies the relativistic Poisson equation,

$$\boldsymbol{\nabla}^2\Psi = \frac{4\pi G a^2}{c^2}\sum_i \delta\rho_i, \quad (1.37)$$

where $\delta\rho$ is the density perturbation in the total density rest-frame, and i sums over all the different components that make up the total density. For CMB lensing, the main component is dark matter. The two potentials are equal in a universe in which the anisotropic components of the stress-energy

tensor $T_{\mu\nu}$ is zero in the rest-frame of the total density [38]. As this is the case for ΛCDM during matter-domination, we set $\Psi = \Phi$ in our calculations.

The gravitational potential that is caused by a mass M at radius r away from its centre of gravity is given by

$$\Phi(r) \equiv -\frac{GM}{c^2 r}. \tag{1.38}$$

By using the geodesic equations of Eq. (1.22) and using the approximation $|\Phi| \ll 1$ along the photon's trajectory, it can be shown that a photon that is affected gravitationally by mass M will change its trajectory by an angle

$$\theta = \frac{4GM}{c^2 R_0}, \tag{1.39}$$

where R_0 is the distance of closest approach between the photon and the lensing mass. If the object that curves spacetime along the photon's trajectory is a black hole, this equation holds as long as R_0 is much larger than the black hole's Schwarzschild radius. For any other object with a relatively weak gravitational field, this equation holds when R_0 is larger than the radius of the object, as the photon could interact with the object's particles and be affected by more than just gravity. We can express the differential deflection angle as a function of the gradient of the gravitational potential which affects the CMB photons. In terms of the differential conformal distance, this deflection angle becomes

$$\delta\theta = -2\nabla_\perp \Phi(\chi)\delta\chi, \tag{1.40}$$

where $\nabla_\perp$ is the gradient in the direction of the lensing potential, which is perpendicular to the photon's trajectory, and $\delta\chi$ is a differential distance along the photon path.

For the CMB, this lensing effect is called *weak gravitational lensing*, as the deflection angles are small (typically around 1 arcminute in size [142]). This means that the observed lensed anisotropies of the CMB have small shear- and magnification-like distortions, which change the statistics of the CMB anisotropies. The effect of lensing can therefore only be measured statistically from the CMB. Such measurements provide a unique insight on the lensing potential, as unlike with some lensing probes such as background galaxies lensed by galaxy clusters, measuring the lensing potential does not require making any assumptions on the shape of the lensing mass.

In CMB lensing, we are interested to know how the deflection affects the observed CMB. We therefore want to relate the deflection angle to the observed angle shift $\delta\alpha$. For this, we use the comoving angular diameter distances between the CMB and the observer, $f_K(\chi_*)$, and between

the lensing potential and the observer, $f_K(\chi)$. The comoving distances χ and χ_*, along with the deflection angles, are shown in Fig. 1.5. Using simple trigonometry and assuming small deflection angles, the relation between the two angles is

$$\delta\alpha = \frac{f_K(\chi_* - \chi)}{f_K(\chi_*)}\delta\theta = -\frac{f_K(\chi_* - \chi)}{f_K(\chi_*)} 2\delta\chi\nabla_\perp\Phi \tag{1.41}$$

in the direction $\boldsymbol{\nabla}_\perp\Phi$. The total deflection angle from all potential gradients between us and

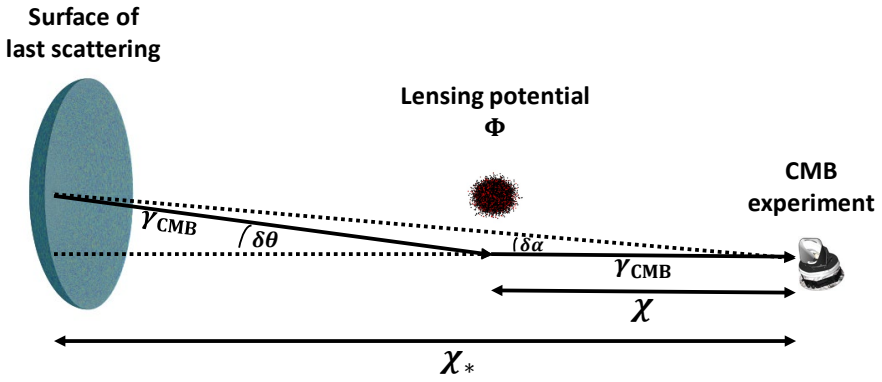

Figure 1.5: A not-to-scale illustration of the effect of gravitational lensing on a CMB photon $\gamma_{\rm CMB}$ which originates from the surface of last scattering. For CMB lensing, $\chi_* - \chi \gg \chi$, as most of the lensing potential affecting the radiation is at low redshifts. The lensing potential is illustrated as a single dark matter halo, although in practice a single photon can be deflected by many halos.

recombination is then

$$\boldsymbol{\alpha} = -2\int_0^{\chi_*} d\chi \frac{f_K(\chi_* - \chi)}{f_K(\chi_*)f_K(\chi)}\boldsymbol{\nabla}_\perp\Phi(\chi\hat{\mathbf{n}}; \eta_0 - \chi/c), \tag{1.42}$$

where $\Phi(\chi\hat{\mathbf{n}}; \eta_0 - \chi/c)$ is the gravitational potential at conformal distance χ along the direction $\hat{\mathbf{n}}$ at conformal time $\eta_0 - \chi/c$. When we observe the CMB anisotropy in direction $\hat{\mathbf{n}}$, it is in fact a 'primordial' anisotropy in the direction $\hat{\mathbf{n}} + \boldsymbol{\nabla}\phi(\hat{\mathbf{n}})$ on the sky, where $\boldsymbol{\nabla}\phi(\hat{\mathbf{n}})$ is the CMB lensing potential [142]. It is related to the observed deflection angle via $\boldsymbol{\alpha} = \boldsymbol{\nabla}\phi(\hat{\mathbf{n}})$, such that

$$\phi(\hat{\mathbf{n}}) \equiv -2\int_0^{\chi_*} d\chi \frac{f_K(\chi_* - \chi)}{f_K(\chi_*)f_K(\chi)}\Phi(\chi\hat{\mathbf{n}}; \eta_0 - \chi/c). \tag{1.43}$$

If we assume that Φ is Gaussian, we can define its power spectrum $\mathcal{P}_\Phi(\boldsymbol{k})$ as we defined the matter power spectrum. Using the Fourier transform of the lensing field,

$$\Phi(\mathbf{x}; \eta) = \int \frac{d^3k}{(2\pi)^3}\Phi(\boldsymbol{k}; \eta)e^{-i\boldsymbol{k}\cdot\mathbf{x}}, \tag{1.44}$$

such that

$$\left\langle \Phi(\boldsymbol{k};\eta)\Phi^*(\boldsymbol{k}';\eta')\right\rangle = \frac{2\pi^2}{k^3}\mathcal{P}_\Phi(\boldsymbol{k};\eta,\eta')\delta(\boldsymbol{k}-\boldsymbol{k}'). \tag{1.45}$$

Using this definition of the gravitational potential power spectrum, along with the definition of the lensing potential from Eq. (1.43) and the correlation function of the lensing potential in spherical harmonics,

$$\langle \phi_{\ell m}\phi^*_{\ell' m'}\rangle = \delta_{\ell\ell'}\delta_{mm'}C_\ell^{\phi\phi}, \tag{1.46}$$

we can express the angular power spectrum of ϕ as a function of $\mathcal{P}_\Phi(\boldsymbol{k})$ and comoving angular diameter distances,

$$C_\ell^{\phi\phi} = 16\pi\int\frac{dk}{k}\int_0^{\chi_*}d\chi\int_0^{\chi_*}d\chi'\mathcal{P}_\Phi(k;\eta_0-\chi/c,\eta_0-\chi'/c)j_\ell(k\chi)j_\ell(k\chi')\frac{f_K(\chi_*)-f_K(\chi)}{f_K(\chi_*)f_K(\chi)}\frac{f_K(\chi'_*)-f_K(\chi')}{f_K(\chi'_*)f_K(\chi')}. \tag{1.47}$$

where $j_\ell(k\chi)$ are the spherical Bessel functions.

To infer this lensing potential from CMB experiments, we can use the statistical properties it induces on the CMB anisotropies. As we will show below, lensing produces off-diagonal correlations between the modes of the CMB anisotropies across the sky in harmonic space. Studying these correlations enables the estimation of the lensing potential. A simple way to express how CMB lensing affects an observed CMB field X (either T, Q or U) is through a series expansion in small deflection angles $\boldsymbol{\nabla}\phi(\hat{\mathbf{n}})$,

$$\begin{aligned}\tilde{X}(\hat{\mathbf{n}}) =& X(\hat{\mathbf{n}}') = X(\hat{\mathbf{n}}+\boldsymbol{\nabla}\phi)\\ \approx& X(\hat{\mathbf{n}}) + \nabla^{i_1}\phi(\hat{\mathbf{n}})\nabla_{i_1}X(\hat{\mathbf{n}}) + \frac{1}{2}\nabla^{i_1}\phi(\hat{\mathbf{n}})\nabla^{i_2}\phi(\hat{\mathbf{n}})\nabla_{i_1}\nabla_{i_2}X(\hat{\mathbf{n}}) + \cdots,\end{aligned} \tag{1.48}$$

where $\tilde{X}(\hat{\mathbf{n}})$ is the observed lensed anisotropy in the direction $\hat{\mathbf{n}}$, $X(\hat{\mathbf{n}}')$ is the unlensed field in the direction $\hat{\mathbf{n}}' \equiv \hat{\mathbf{n}}+\boldsymbol{\nabla}\phi$, and i_1 and i_2 sum over the 2D coordinates in directions $\boldsymbol{e}_1, \boldsymbol{e}_2$. For polarization, since it is more convenient to use the E and B modes and not the Q and U Stokes parameters (as discussed in Subsec. 1.3.1), Eq. (1.48) can be used for $X(\hat{\mathbf{n}}) = {}_\pm X(\hat{\mathbf{n}}) \equiv Q(\hat{\mathbf{n}}) \pm iU(\hat{\mathbf{n}})$ such that ${}_\pm X(\ell) = E(\ell) \pm iB(\ell)$.

The expansion in Eq. (1.48) can be re-written in harmonic space using the Fourier transforms of the deflection angle and gradient of the CMB fields,

$$\boldsymbol{\nabla}\phi(\hat{\mathbf{n}}) = i\int\frac{d^2\ell}{2\pi}\boldsymbol{\ell}\phi(\boldsymbol{\ell})e^{i\boldsymbol{\ell}\cdot\hat{\mathbf{n}}} \tag{1.49}$$

$$\boldsymbol{\nabla}T(\hat{\mathbf{n}}) = i\int\frac{d^2\ell}{2\pi}\boldsymbol{\ell}T(\boldsymbol{\ell})e^{i\boldsymbol{\ell}\cdot\hat{\mathbf{n}}} \tag{1.50}$$

$$\boldsymbol{\nabla}Q(\hat{\mathbf{n}}) \pm i\boldsymbol{\nabla}U(\hat{\mathbf{n}}) = -i\int\frac{d^2\ell}{2\pi}\boldsymbol{\ell}\left[E(\boldsymbol{\ell}) \pm iB(\boldsymbol{\ell})\right]e^{\mp 2i\varphi_\ell}e^{i\boldsymbol{\ell}\cdot\hat{\mathbf{n}}} \tag{1.51}$$

to obtain (to first order in ϕ and using the flat-sky approximation) [143, 144]

$$\begin{aligned}
\tilde{T}(\boldsymbol{\ell}) &\approx T(\boldsymbol{\ell}) - \int \frac{d^2\ell'}{2\pi}\boldsymbol{\ell}' \cdot (\boldsymbol{\ell}-\boldsymbol{\ell}')\phi(\boldsymbol{\ell}-\boldsymbol{\ell}')T(\boldsymbol{\ell}'), \\
\tilde{E}(\boldsymbol{\ell}) &\approx E(\boldsymbol{\ell}) - \int \frac{d^2\ell'}{2\pi}\boldsymbol{\ell}' \cdot (\boldsymbol{\ell}-\boldsymbol{\ell}')\phi(\boldsymbol{\ell}-\boldsymbol{\ell}') \left[E(\boldsymbol{\ell}')\cos\left(2\left(\varphi_{\boldsymbol{\ell}}-\varphi_{\boldsymbol{\ell}'}\right)\right) - B(\boldsymbol{\ell}')\sin\left(2\left(\varphi_{\boldsymbol{\ell}}-\varphi_{\boldsymbol{\ell}'}\right)\right)\right], \\
\tilde{B}(\boldsymbol{\ell}) &\approx B(\boldsymbol{\ell}) - \int \frac{d^2\ell'}{2\pi}\boldsymbol{\ell}' \cdot (\boldsymbol{\ell}-\boldsymbol{\ell}')\phi(\boldsymbol{\ell}-\boldsymbol{\ell}') \left[E(\boldsymbol{\ell}')\sin\left(2\left(\varphi_{\boldsymbol{\ell}}-\varphi_{\boldsymbol{\ell}'}\right)\right) + B(\boldsymbol{\ell}')\cos\left(2\left(\varphi_{\boldsymbol{\ell}}-\varphi_{\boldsymbol{\ell}'}\right)\right)\right].
\end{aligned} \tag{1.52}$$

The expansions of the polarization modes can be simplified further if we assume that there are no unlensed B modes, which is the case for ΛCDM. As mentioned before, in practice the CMB temperature and polarization fields $\tilde{X}(\hat{\mathbf{n}})$ are not observed directly, as sky measurements can be contaminated by, e.g., instrumental noise and foregrounds. We neglect their contributions to the observed fields in this subsection for convenience. Some of these additional complexities will be discussed in the next subsection and in later chapters.

Eq. (1.52) shows that lensing mixes the different modes of the observed fields. We can use this to infer the lensing potential from a given sky realisation using the off-diagonal terms of the correlation of any two lensed fields $\tilde{X}$, $\tilde{Y}$ [145]. Using the definition of the power spectrum for statistically-isotropic fields,

$$\langle \tilde{X}(\boldsymbol{\ell})\tilde{Y}^*(\boldsymbol{\ell}')\rangle_{\tilde{X}\tilde{Y}} = \delta(\boldsymbol{\ell}-\boldsymbol{\ell}')C_\ell^{\tilde{X}\tilde{Y}}, \tag{1.53}$$

with the expressions of Eq. (1.52) results in

$$\langle \tilde{X}(\boldsymbol{\ell})\tilde{Y}^*(\boldsymbol{\ell}-\mathbf{L})\rangle_{\tilde{X}\tilde{Y}} = \delta(\mathbf{L})C_\ell^{XY} + \frac{1}{2\pi}f_{XY}\left(\boldsymbol{\ell}, \boldsymbol{\ell}-\mathbf{L}\right)\phi\left(\mathbf{L}\right) + \mathcal{O}(\phi^2), \tag{1.54}$$

where f_{XY} are defined in Table 1.2 for all CMB fields combinations [145]. This shows that for $\mathbf{L} = \mathbf{0}$ (which represents the diagonal elements of the covariance matrix $\boldsymbol{C}^{XY}$) we only have contributions from the unlensed XY cross-correlation power spectrum, while for $\mathbf{L} \neq \mathbf{0}$ (the off-diagonal elements) we have some dependency on the lensing potential ϕ. This means that we cannot observe the 0^{th} mode of the lensing potential, and therefore all lensing-related modes throughout the thesis will be defined only for $L \equiv |\mathbf{L}| \geq 1$ on the curved sky.

When neglecting higher-order terms in ϕ due to their smaller contribution to the overall distortions, Eq. (1.54) becomes, for all $L > 0$,

$$\langle \tilde{X}(\boldsymbol{\ell})\tilde{Y}^*(\boldsymbol{\ell}-\mathbf{L})\rangle_{\tilde{X}\tilde{Y}} = \frac{1}{2\pi}f_{XY}\left(\boldsymbol{\ell}, \boldsymbol{\ell}-\mathbf{L}\right)\phi\left(\mathbf{L}\right). \tag{1.55}$$

XY	$f_{XY}(\boldsymbol{\ell}_1, \boldsymbol{\ell}_2)$	$F_{XY}(\boldsymbol{\ell}_1, \boldsymbol{\ell}_2)$
TT	$C_{\ell_1}^{TT}\,(\mathbf{L}\cdot\boldsymbol{\ell}_1) + C_{\ell_2}^{TT}\,(\mathbf{L}\cdot\boldsymbol{\ell}_2)$	$\dfrac{f_{TT}(\boldsymbol{\ell}_1,\boldsymbol{\ell}_2)}{2C_{\ell_1}^{TT}C_{\ell_2}^{TT}}$
TE	$C_{\ell_1}^{TE}\cos\left(2\Delta\varphi_{\ell_1\ell_2}\right)(\mathbf{L}\cdot\boldsymbol{\ell}_1) + C_{\ell_2}^{TE}\,(\mathbf{L}\cdot\boldsymbol{\ell}_2)$	$\dfrac{f_{TE}(\boldsymbol{\ell}_1,\boldsymbol{\ell}_2)+f_{TE}(\boldsymbol{\ell}_2,\boldsymbol{\ell}_1)}{C_{\ell_1}^{TT}C_{\ell_2}^{EE}+C_{\ell_1}^{TE}C_{\ell_2}^{TE}+C_{\ell_1}^{EE}C_{\ell_2}^{TT}}$
TB	$C_{\ell_1}^{TB}\sin\left(2\Delta\varphi_{\ell_1\ell_2}\right)(\mathbf{L}\cdot\boldsymbol{\ell}_1)$	$\dfrac{f_{TB}(\boldsymbol{\ell}_1,\boldsymbol{\ell}_2)+f_{TB}(\boldsymbol{\ell}_2,\boldsymbol{\ell}_1)}{C_{\ell_1}^{TT}C_{\ell_2}^{EE}+C_{\ell_1}^{EE}C_{\ell_2}^{TT}}$
EE	$\left[C_{\ell_1}^{EE}\,(\mathbf{L}\cdot\boldsymbol{\ell}_1) + C_{\ell_2}^{EE}\,(\mathbf{L}\cdot\boldsymbol{\ell}_2)\right]\cos\left(2\Delta\varphi_{\ell_1\ell_2}\right)$	$\dfrac{f_{EE}(\boldsymbol{\ell}_1,\boldsymbol{\ell}_2)}{2C_{\ell_1}^{EE}C_{\ell_2}^{EE}}$
EB	$\left[C_{\ell_1}^{EE}\,(\mathbf{L}\cdot\boldsymbol{\ell}_1) - C_{\ell_2}^{BB}\,(\mathbf{L}\cdot\boldsymbol{\ell}_2)\right]\sin\left(2\Delta\varphi_{\ell_1\ell_2}\right)$	$\dfrac{f_{EB}(\boldsymbol{\ell}_1,\boldsymbol{\ell}_2)+f_{EB}(\boldsymbol{\ell}_2,\boldsymbol{\ell}_1)}{C_{\ell_1}^{EE}C_{\ell_2}^{BB}+C_{\ell_1}^{BB}C_{\ell_2}^{EE}}$
BB	$\left[C_{\ell_1}^{BB}\,(\mathbf{L}\cdot\boldsymbol{\ell}_1) + C_{\ell_2}^{BB}\,(\mathbf{L}\cdot\boldsymbol{\ell}_2)\right]\cos\left(2\Delta\varphi_{\ell_1\ell_2}\right)$	$\dfrac{f_{BB}(\boldsymbol{\ell}_1,\boldsymbol{\ell}_2)}{2C_{\ell_1}^{BB}C_{\ell_2}^{BB}}$

Table 1.2: Minimum-variance weights for reconstructing the lensing potential, with $\boldsymbol{\ell}_2 \equiv \mathbf{L} - \boldsymbol{\ell}_1$ and $\Delta\varphi_{\ell_1\ell_2} \equiv \left(\varphi_{\ell_1} - \varphi_{\ell_2}\right)$. The f_{XY} terms provide more optimal lensing estimators using power spectra which are defined by $\left\langle \tilde{\boldsymbol{\nabla}}\tilde{T}(\boldsymbol{\ell})\tilde{T}(\boldsymbol{\ell}')\right\rangle = i\boldsymbol{\ell}\delta(\boldsymbol{\ell}+\boldsymbol{\ell}')\tilde{C}_\ell^{T\nabla T}$ where $\tilde{\boldsymbol{\nabla}}T(\mathbf{x}) \equiv (\boldsymbol{\nabla}T)\,(\mathbf{x}+\boldsymbol{\nabla}\phi)$ is the lensed temperature gradient [146]. The power spectra in the denominator of the F_{XY} terms are the power spectra of the lensed CMB fields+noise.

While this equation deceivingly suggests we can easily measure ϕ directly from the off-diagonal elements of the covariance of two CMB maps, the left-hand side of the equation is an average over CMB realisations. In practice, when we want to estimate the lensing potential from CMB observations, we only have one realisation to measure ϕ from, so a more sophisticated technique is required to estimate the covariance matrix to obtain ϕ. Instead of using different realisations, we can average over all off-diagonal elements to extract statistical information on ϕ. To do this optimally, we could use a weighted mean, where the weights would minimize the variance of the lensing potential estimator $\hat{\phi}$. The estimator can then be written as

$$\hat{\phi}_{XY}(\mathbf{L}) \equiv \frac{1}{\mathcal{R}_{XY}(\mathbf{L})}\int \frac{d^2\ell}{2\pi}\tilde{X}(\boldsymbol{\ell})\tilde{Y}^*(\boldsymbol{\ell}-\mathbf{L})F_{XY}(\boldsymbol{\ell},\mathbf{L}-\boldsymbol{\ell}), \tag{1.56}$$

where F_{XY} are given in Table 1.2 for all field combinations. An unbiased estimator (such that $\left\langle\hat{\phi}(\mathbf{L})\right\rangle_{XY} = \phi(\mathbf{L})$) is obtained when the normalization is

$$\mathcal{R}_{XY}(\mathbf{L}) = \int \frac{d^2\ell}{(2\pi)^2} f_{XY}(\boldsymbol{\ell},\mathbf{L}-\boldsymbol{\ell})F_{XY}(\boldsymbol{\ell},\mathbf{L}-\boldsymbol{\ell}). \tag{1.57}$$

The optimal weights $F_{XY}(\boldsymbol{\ell}, \mathbf{L}-\boldsymbol{\ell})$ can be obtained from minimizing the estimator variance,

$$\begin{aligned}\left\langle \left(\hat{\phi}_{XY}(\mathbf{L})-\phi(\mathbf{L})\right)\left(\hat{\phi}_{ZD}(\mathbf{L}')-\phi(\mathbf{L}')\right)^{*}\right\rangle_{XYZD} &= \frac{1}{\mathcal{R}_{XY}(\mathbf{L})}\frac{1}{\mathcal{R}^{*}_{ZD}(\mathbf{L}')} \\ &\times \int\frac{d^2\ell}{2\pi}\int\frac{d^2\ell'}{2\pi}\left\langle \tilde{X}(\boldsymbol{\ell})\tilde{Y}^{*}(\boldsymbol{\ell}-\mathbf{L})\tilde{Z}^{*}(\boldsymbol{\ell}')\tilde{D}(\boldsymbol{\ell}'-\mathbf{L}')\right\rangle_{XYZD} F_{XY}(\boldsymbol{\ell},\mathbf{L})F^{*}_{ZD}(\boldsymbol{\ell}',\mathbf{L}') \\ &+\left\langle\phi(\mathbf{L})\phi^{*}(\mathbf{L}')\right\rangle .\end{aligned} \tag{1.58}$$

The trispectrum of the lensed fields can be expanded to 0^{th} order in ϕ using Wick's theorem [147], the definition of the power spectrum in Eq. (1.53), and the fact that $X(\boldsymbol{\ell}) = X^{*}(-\boldsymbol{\ell})$, such that

$$\begin{aligned}\left\langle X(\boldsymbol{\ell})Y^{*}(\boldsymbol{\ell}-\mathbf{L})Z^{*}(\boldsymbol{\ell}')D(\boldsymbol{\ell}'-\mathbf{L}')\right\rangle =& \left\langle X(\boldsymbol{\ell})Y^{*}(\boldsymbol{\ell}-\mathbf{L})\right\rangle\left\langle Z^{*}(\boldsymbol{\ell}')D(\boldsymbol{\ell}'-\mathbf{L}')\right\rangle \\ &+\left\langle X(\boldsymbol{\ell})Z^{*}(\boldsymbol{\ell}')\right\rangle\left\langle Y^{*}(\boldsymbol{\ell}-\mathbf{L})D(\boldsymbol{\ell}'-\mathbf{L}')\right\rangle \\ &+\left\langle X(\boldsymbol{\ell})D(\boldsymbol{\ell}'-\mathbf{L}')\right\rangle\left\langle Z^{*}(\boldsymbol{\ell}-\mathbf{L})Y^{*}(\boldsymbol{\ell}')\right\rangle \\ =&\delta(\mathbf{L})\delta(\mathbf{L}')C^{XY}_{\ell}C^{ZD}_{\ell'} \\ &+\delta(\boldsymbol{\ell}-\boldsymbol{\ell}')\delta(\boldsymbol{\ell}-\mathbf{L}-(\boldsymbol{\ell}'-\mathbf{L}'))C^{XZ}_{\ell}C^{YD}_{|\boldsymbol{\ell}-L|} \\ &+\delta(\boldsymbol{\ell}-(\mathbf{L}'-\boldsymbol{\ell}'))C^{XD}_{\ell}\delta(\mathbf{L}-\boldsymbol{\ell}-\boldsymbol{\ell}')C^{YZ}_{|L-\boldsymbol{\ell}|}.\end{aligned} \tag{1.59}$$

Plugging this result into Eq. (1.58), and equating the derivative of the variance with respect to ϕ to zero, leads to the weights shown in Table 1.2. This method for reconstructing the lensing potential from CMB fields assumes a linear dependency of the lensed CMB fields on the lensing potential. In the following subsection, we show a more accurate way of reconstructing the lensing potential and present the main method which is used in the lensing analyses of Chapters 2-4.

1.4.2 CMB LENSING RECONSTRUCTION

The first lensing reconstruction was done using the CMB measurements of WMAP, which enabled the first detection of the lensing field through cross-correlations with large-scale traces [148, 149]. The ACT collaboration was the first to produce lensing power estimates through CMB measurements alone [150]. Their 4σ detection for modes between $75 < L < 2050$, used CMB temperature measurements. They were followed by the SPT collaboration, which produced similar measurements [151]. The POLARBEAR collaboration was then the first to produce lensing estimates from polarization-only measurements [152], after which SPTpol produced both polarization-only and temperature+polarization lensing estimates [153]. Around the same time, the Planck collaboration produced its first lensing estimates for a larger multipole

range $40 < L < 2048$ (due to the larger sky-area Planck observed) [123], which was improved even further in their 2018 analysis to $8 < L < 2048$, and later also released estimates from combining temperature and polarization measurements [98, 100]. The BICEP2 & Keck Array collaboration also produced results which are consistent with the others using polarization-only maps [154]. The most recent lensing deflection map from Planck and lensing potential power spectrum estimates are shown in Fig. 1.6. The power spectrum estimates from all experiments are consistent with the theory spectrum, and the estimates from Planck are overall more accurate.

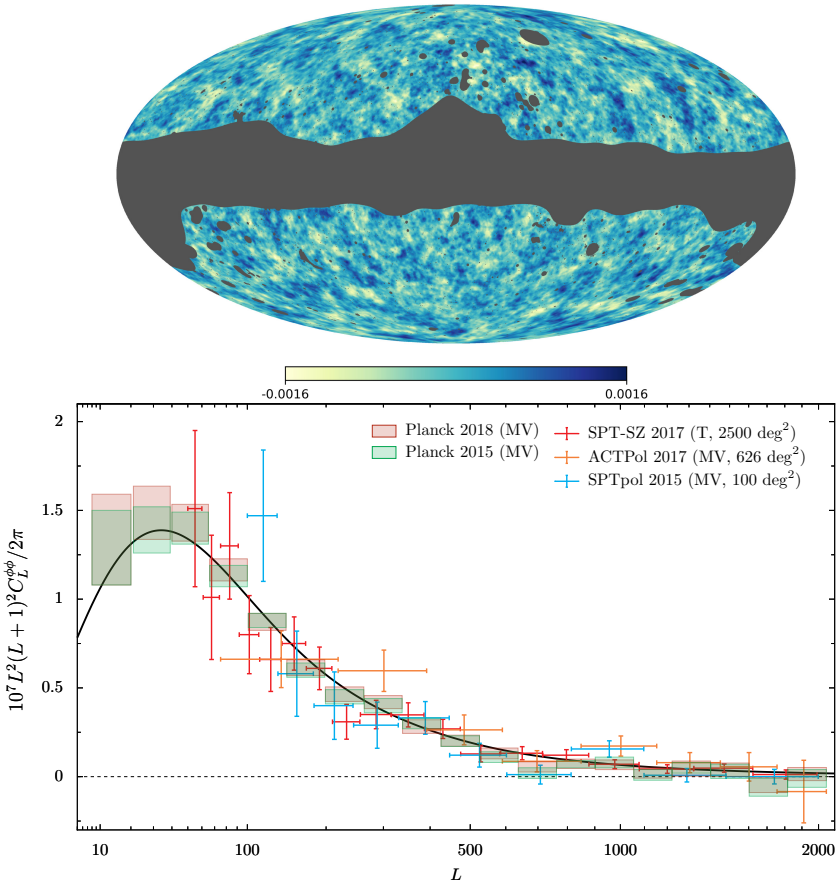

Figure 1.6: The Planck reconstructed $\alpha \equiv \nabla\phi$ map (top panel) and lensing power spectrum (bottom panels). The power spectrum plot shows that the estimates from Planck, SPT and ACT are all consistent with the theory spectrum shown (black line), and that the reconstruction uncertainties of the Planck estimates are smaller compared to the others. Source: Aghanim [100].

In the previous subsection, we saw that the lensing field can be approximately extracted from the CMB fields while neglecting their higher order dependencies on the lensing potential ϕ. Due to this approximation, it is not the most optimal method that can be used to extract the maximal amount of information about the lensing potential from CMB observations. In this subsection, a more optimal method, the maximum-likelihood estimator (MLE), is described. This method is sufficient for lensing reconstructions when the noise in the measurements is dominant, but suboptimal for signal-dominated experiments. Nonetheless, this method was improved over the years to provide better and more accurate lensing measurements, while measurements of the CMB became more

sensitive.

Although the MLE is an iterative method for reconstructing ϕ, currently all real-data implementations of this method use the first iteration for the lensing estimate. Apart from MLE, a possibly more optimal method which uses Bayes' theorem [155] was recently demonstrated by the SPT collaboration using SPTpol measurements [156]. Their Bayesian procedure produced a marginal improvement in lensing reconstruction compared to their results from the first iterative solution of the MLE. These improvements are expected to be more significant with future CMB measurements which will have much lower noise levels, especially in polarization measurements. Both reconstruction methods are based on the relatively good approximation that the lensing field, the CMB fields and the noise in the CMB maps are Gaussian. This assumption is useful, because it allows us to express various probabilities and analytical likelihoods analytically to extract information on the lensing potential from CMB fields.

The basis of the MLE method is using a given data set D, plus a model with parameter vector $\boldsymbol{\theta}$ to calculate how likely is the data given specific parameter values. This likelihood is essentially the conditional probability, $P(D|\boldsymbol{\theta})$. We can incorporate any other pieces of information into this likelihood from different data sets or estimations of other experiments to obtain more constrained parameters from this likelihood.

To apply this method for CMB lensing, let us consider a vector $\tilde{\boldsymbol{X}}$ ($\boldsymbol{X}$) of the lensed (unlensed) CMB temperature and polarization fields, such that the observed vector is $\boldsymbol{X}_{\rm tot} = \tilde{\boldsymbol{X}} + \mathbf{n}$ where $\mathbf{n}$ is the (Gaussian) noise vector. Given a theoretical covariance of the lensed fields, $\boldsymbol{S} = \left\langle \tilde{\boldsymbol{X}} \tilde{\boldsymbol{X}}^\top \right\rangle_{\boldsymbol{X},\mathbf{n}}$, which is determined by the CMB power spectra, the likelihood for measuring the specific CMB fields given a fixed lensing field ϕ is

$$P(\boldsymbol{X}_{\rm tot}|\phi, \boldsymbol{S}, \boldsymbol{N}) = \frac{1}{(2\pi)^{\frac{3N_{\rm pix}}{2}}\sqrt{|\boldsymbol{\mathcal{C}}|}} e^{-\frac{1}{2}(\boldsymbol{X}_{\rm tot})^\top \boldsymbol{\mathcal{C}}^{-1}\boldsymbol{X}_{\rm tot}}. \tag{1.60}$$

where $\boldsymbol{\mathcal{C}} \equiv \boldsymbol{C}^{\boldsymbol{X}_{\rm tot}\boldsymbol{X}_{\rm tot}} = \boldsymbol{S} + \boldsymbol{N}$ is the full covariance of $\boldsymbol{X}_{\rm tot}$ and $N_{\rm pix}$ is the number of pixels in each CMB map. Defining $\mathcal{L}[\phi] \equiv -\ln(P(\boldsymbol{X}_{\rm tot}|\phi, \boldsymbol{S}, \boldsymbol{N}))$, such that

$$\mathcal{L}[\phi] = \frac{1}{2}\left[\ln\left(|\boldsymbol{\mathcal{C}}|\right) + \left(\boldsymbol{X}_{\rm tot}\right)^\top \boldsymbol{\mathcal{C}}^{-1}\boldsymbol{X}_{\rm tot} + 3N_{\rm pix}\ln\left(2\pi\right)\right], \tag{1.61}$$

we obtain a more convenient function for finding the value of ϕ for which the likelihood is maximal. This value is found by taking the functional derivative [157] of $\mathcal{L}$ with respect to ϕ, and

setting the result to zero:

$$\frac{\delta\mathcal{L}\left[\phi\right]}{\delta\phi(\mathbf{x})} = \frac{1}{2}\left[\mathrm{Tr}\left(\boldsymbol{\mathcal{C}}^{-1}\frac{\delta\boldsymbol{\mathcal{C}}}{\delta\phi(\mathbf{x})}\right) - \left(\boldsymbol{X}_{\mathrm{tot}}\right)^{\top}\boldsymbol{\mathcal{C}}^{-1}\frac{\delta\boldsymbol{\mathcal{C}}}{\delta\phi(\mathbf{x})}\boldsymbol{\mathcal{C}}^{-1}\boldsymbol{X}_{\mathrm{tot}}\right] = 0, \tag{1.62}$$

where we used the identity $\ln\left(|\boldsymbol{X}|\right) = \mathrm{Tr}\left(\ln\boldsymbol{X}\right)$. The lensing potential estimate that solves this equation is $\hat{\phi}$.

The equation we want to solve can be rewritten as

$$g_{\phi} - \langle g_{\phi}\rangle_{\tilde{\boldsymbol{X}},\mathbf{n}} = 0, \tag{1.63}$$

where

$$g_{\phi}(\mathbf{x}) \equiv \frac{1}{2}\left[\boldsymbol{\mathcal{C}}^{-1}\boldsymbol{X}_{\mathrm{tot}}\right]^{\top}(\mathbf{x})\frac{\delta\boldsymbol{\mathcal{C}}}{\delta\phi(\mathbf{x})}\left[\boldsymbol{\mathcal{C}}^{-1}\boldsymbol{X}_{\mathrm{tot}}\right](\mathbf{x}). \tag{1.64}$$

Here, we used the identity $\mathrm{Tr}\left(\boldsymbol{A}\right) = \left\langle \mathbf{x}^{\top}\boldsymbol{A}\boldsymbol{C}^{-1}\mathbf{x}\right\rangle_{\mathbf{x}}$ for matrix $\boldsymbol{A}$ and vector of Gaussian random variables $\mathbf{x}$ with covariance $\boldsymbol{C}$. The average term $\langle g_{\phi}\rangle_{\tilde{\boldsymbol{X}},\mathbf{n}}$, known as the *mean field* (MF) term, vanishes if $\boldsymbol{X}_{\mathrm{tot}} = \tilde{\boldsymbol{X}}$ and if these fields have no masked regions, as in this case g_{ϕ} is isotropic and its ensemble average goes to zero. This term is therefore sensitive to the noise and to the masking artefacts in the CMB maps, and is considered to be a bias term that is needed to be evaluated and subtracted from the reconstructed QE $\hat{g}_{\phi}$ that maximise the likelihood.

In practice, Eq. (1.63) is usually solved numerically using the Newton-Raphson method [158], which finds the roots of a function $f(x)$ relatively efficiently [159]. It does so by iteratively finding values x_i such that $\lim_{i\to\infty} f(x_i) = 0$, starting from an initial value x_0. The next value, x_1, is obtained from the intersect of the tangent $t(x)$ to the function $f(x)$ from the point corresponding to the previous value, $(x_0, f(x_0))$, with the x-axis, which is given by $t(x) = f'(x_0)x + f(x_0) - f'(x_0)x_0$. This leads to the next guess, $x_1 = x_0 - f(x_0)/f'(x_0)$, which can then be used as the starting point for the next iteration. For CMB lensing, the initial guess is usually taken to be $x_0 = \phi_0 = 0$, and the function $f(x) = g_{\phi}$ is defined in Eq. (1.64). The first iteration of this calculation is sufficient for an accurate lensing reconstruction from current and near-future experiments, which is the estimator most CMB experiments currently use in their lensing analysis. Setting $\phi_0 = 0$, the first iteration gives

$$\begin{aligned}\hat{\phi}_1(\mathbf{x}) &= -\left(\left[g_{\phi} - \langle g_{\phi}\rangle\right]_{\phi=0}\left[\frac{\delta}{\delta\phi(\mathbf{x})}\left(\left[g_{\phi} - \langle g_{\phi}\rangle\right]_{\phi=0}\right)\right]^{-1}_{\phi=0}\right)(\mathbf{x}) \\ &= \left(\left[g_{\phi} - \langle g_{\phi}\rangle\right]_{\phi=0}\mathcal{F}_{\phi}^{-1}\Big|_{\phi=0}\right)(\mathbf{x}),\end{aligned} \tag{1.65}$$

where we approximated the derivative as the Fisher matrix $\mathcal{F}$ (see Ref. [158] and Appendix A.1 for more details) for further simplification. For current and near-future CMB observations, it was shown that this first iteration already results in a very accurate estimator [160, 161]. We therefore use the estimate $\hat{\phi} \equiv \hat{\phi}_1$ throughout.

To further simplify g_ϕ, the functional derivative of $\boldsymbol{\mathcal{C}}$ with respect to ϕ can be calculated by defining the covariance of the observed fields as a function of the lensing operator,

$$\Lambda_\phi(\mathbf{x}, \mathbf{y}) = \delta(\mathbf{x} + \boldsymbol{\nabla}\phi(\mathbf{x}) - \mathbf{y}). \tag{1.66}$$

Approximating it as a linear operator (such that $\Lambda_\phi^\top(\mathbf{x}, \mathbf{y}) = \Lambda_\phi(\mathbf{y}, \mathbf{x})$), the covariance then becomes

$$\boldsymbol{\mathcal{C}}\left[\phi\right] = \boldsymbol{\Lambda}_\phi \boldsymbol{C}^{XX} \boldsymbol{\Lambda}_\phi^\top + \boldsymbol{N}. \tag{1.67}$$

The functional derivative of the covariance is then

$$\frac{\delta \boldsymbol{\mathcal{C}}(\mathbf{y}, \mathbf{z})}{\delta\phi(\mathbf{x})} = \int d^2z' \frac{\delta\Lambda_\phi(\mathbf{y}, \mathbf{z}')}{\delta\phi(\mathbf{x})} \left(\boldsymbol{C}^{XX} \boldsymbol{\Lambda}_\phi^\top\right)(\mathbf{z}', \mathbf{z}) + \int d^2y' \left(\boldsymbol{\Lambda}_\phi \boldsymbol{C}^{XX}\right)(\mathbf{y}, \mathbf{y}') \frac{\delta\Lambda_\phi^\top(\mathbf{z}, \mathbf{y}')}{\delta\phi(\mathbf{x})}. \tag{1.68}$$

The functional derivative of the lensing operator can be calculated using the relation of this operator with some field Ξ,

$$\Lambda_\phi \Xi(\mathbf{x}) = \Xi(\mathbf{x} + \boldsymbol{\nabla}\phi(\mathbf{x})), \tag{1.69}$$

to get

$$\frac{\delta\left(\Lambda_\phi \Xi\right)(\mathbf{y})}{\delta\phi(\mathbf{x})} = \int d^2\mathrm{x}' \frac{\delta\boldsymbol{\nabla}\phi(\mathbf{x}')}{\delta\phi(\mathbf{x})} \cdot \frac{\delta\left(\Lambda_\phi \Xi\right)(\mathbf{y})}{\delta\boldsymbol{\nabla}\phi(\mathbf{x}')} = \left(\boldsymbol{\nabla}_\mathbf{y}\delta(\mathbf{y} - \mathbf{x})\right) \cdot \left(\boldsymbol{\Lambda}_\phi \boldsymbol{\nabla}\Xi\right)(\mathbf{y}). \tag{1.70}$$

Using this result, Eq. (1.68) becomes

$$\begin{aligned}
\frac{\delta\mathcal{C}(\mathbf{y}, \mathbf{z})}{\delta\phi(\mathbf{x})} &= \int d^2z' \left(\boldsymbol{\nabla}_\mathbf{y}\delta(\mathbf{y} - \mathbf{x})\right) \cdot \left(\boldsymbol{\Lambda}_\phi \boldsymbol{\nabla}\right)(\mathbf{y}, \mathbf{z}') \left(\boldsymbol{C}^{XX} \boldsymbol{\Lambda}_\phi^\top\right)(\mathbf{z}', \mathbf{z}) \\
&\quad + \int d^2y' \left(\boldsymbol{\Lambda}_\phi \boldsymbol{C}^{XX}\right)(\mathbf{y}, \mathbf{y}') \left(\boldsymbol{\nabla}_\mathbf{z}\delta(\mathbf{z} - \mathbf{x})\right) \cdot \left(\boldsymbol{\Lambda}_\phi^\top \boldsymbol{\nabla}\right)(\mathbf{z}, \mathbf{y}') \\
&= \left(\boldsymbol{\nabla}_\mathbf{y}\delta(\mathbf{y} - \mathbf{x})\right) \cdot \left(\boldsymbol{\Lambda}_\phi \boldsymbol{\nabla} \boldsymbol{C}^{XX} \boldsymbol{\Lambda}_\phi^\top\right)(\mathbf{y}, \mathbf{z}) + \left(\boldsymbol{\nabla}_\mathbf{z}\delta(\mathbf{z} - \mathbf{x})\right) \cdot \left(\boldsymbol{\Lambda}_\phi \boldsymbol{\nabla} C^{XX} \boldsymbol{\Lambda}_\phi^\top\right)(\mathbf{z}, \mathbf{y}).
\end{aligned} \tag{1.71}$$

Plugging this into Eq. (1.64), the QE g_ϕ simplifies to be

$$\boldsymbol{g}_\phi = \boldsymbol{\nabla} \cdot \left[\left(\boldsymbol{\mathcal{C}}^{-1} \boldsymbol{X}_{\text{tot}}\right)^\top \boldsymbol{\Lambda}_\phi \boldsymbol{\nabla} \boldsymbol{C}^{XX} \boldsymbol{\Lambda}_\phi^{-1} \boldsymbol{\mathcal{C}}^{-1} \boldsymbol{X}_{\text{tot}}\right]. \tag{1.72}$$

We can then interpret this form of g_ϕ to first order in ϕ as a product of filtered CMB fields [158,

160, 162],

$$g_\phi(\mathbf{x}) = \boldsymbol{\nabla} \cdot \left[\left(\boldsymbol{X}_{\rm tot}^{\rm IVF} \right)^\top (\mathbf{x}) \left(\boldsymbol{\nabla} \boldsymbol{X}_{\rm tot}^{\rm WF} \right) (\mathbf{x}) \right], \tag{1.73}$$

where $\boldsymbol{X}_{\rm tot}^{\rm IVF}$ and $\boldsymbol{X}_{\rm tot}^{\rm WF}$ are the inverse-variance filtered (IVF) and the Wiener-filtered (WF) CMB fields, respectively (see Appendix A.2 for more details), which are given by

$$\begin{aligned} \boldsymbol{X}_{\rm tot}^{\rm IVF}(\mathbf{x}) &\equiv \left[\boldsymbol{\mathcal{C}}^{-1} \boldsymbol{X}_{\rm tot} \right] (\mathbf{x}), \\ \boldsymbol{X}_{\rm tot}^{\rm WF}(\mathbf{x}) &\equiv \left[\boldsymbol{\Lambda}_\phi^{-1} \boldsymbol{C}^{\tilde{X}\tilde{X}} \boldsymbol{\mathcal{C}}^{-1} \boldsymbol{X}_{\rm tot} \right] (\mathbf{x}). \end{aligned} \tag{1.74}$$

Plugging this into Eq. (1.65), we obtain the lensing field estimator, which is our desired quantity. This form of real-space $\hat{\phi}$ is a more general expression of the harmonic-space estimator shown in Eq. (1.56), which can be simplified to the latter when taking $X = Y$.

Gravitational lensing in general can affect the size, stretch, and angle of the observed lensed object by producing (de)magnification, shear, or rotation, respectively. Generally, rotation is not produced at leading order and is therefore much smaller [158]. It can therefore be useful to refer to the convergence parameter $\kappa(\mathbf{x}) \equiv \frac{1}{2} \boldsymbol{\nabla} \cdot \boldsymbol{\alpha}(\mathbf{x})$ instead of the lensing potential [163]. This will be elaborated on more and used in upcoming chapters.

The normalized QE in Eq. (1.65) provides an estimated map of the lensing potential. From this map, the lensing power spectrum can be obtained, which, as with the CMB fields, tells us about the lens scales. The lensing potential map from CMB observations can also be used along with potential maps from other tracers, such as galaxy surveys which observe the mass in the Universe directly, to calculate cross-power spectra. These correlations can provide further constraints on the growth of dark matter, help break degeneracies between cosmology and galaxy physics, and be used to test theories of modified gravity [164, 165].

Throughout Chapters 2-4, the main lensing product of interest is the reconstructed lensing power spectrum. Unlike with the CMB temperature and polarization maps, obtaining an unbiased lensing power spectrum is somewhat more complicated due to the bias terms that result from correlating two QEs. Such correlation not only gives the wanted lensing power spectrum estimate, but also other correlations which are usually referred to as *bias terms*. We define the (biased) lensing power spectrum from two quadratic estimators that are obtained using a general combination of CMB fields as

$$C_L^{\hat{\phi}^{XY}\hat{\phi}^{ZD}} = \frac{1}{n_L} \sum_{\boldsymbol{\ell} \text{ in } \mathbf{L} \text{ bin}} \hat{\phi}(\boldsymbol{\ell})^{XY} \left(\hat{\phi}(\boldsymbol{\ell})^{ZD} \right)^*, \tag{1.75}$$

where n_L is the number of modes in each multipole L. This is the flat-sky analogy of the power spectrum definition of Eq. (1.30). The resulting power spectrum is biased due to the different contractions of the fields creating the QEs [144, 166, 167]. We can write the bias terms explicitly through the 2-point correlation of two lensing estimates,

$$\left\langle \hat{\phi}_L^{XY} \left(\hat{\phi}_{L'}^{ZD}\right)^* \right\rangle = \delta_{L-L'} \left[C_L^{\phi\phi} + \sum_{i=0}^{\infty} N_{i,L}^{\phi\phi} \right], \tag{1.76}$$

where the index i represent the dependency of the bias terms $N_{i,L}^{\phi\phi}$ on $\left(C_L^{\phi\phi}\right)^i$. These bias terms can be evaluated analytically by calculating the left-hand side of Eq. (1.76) using the definition of $\hat{\phi}_L^{XY}$ from Eq. (1.56). The resulting trispectrum would then be of the four lensed fields, and the respective map noises n^X. The lensed fields are not Gaussian, so the trispectrum cannot be simplified using Wick's theorem as before. We can, however, use the full series expansions of the lensed fields,

$$X_{\text{tot}}(\hat{\mathbf{n}}) = \sum_{j=0}^{\infty} \delta^j X(\hat{\mathbf{n}}) + n^X(\hat{\mathbf{n}}), \tag{1.77}$$

where $\delta^j X(\hat{\mathbf{n}})$ are the expansion terms of order j from Eq. (1.48) (such that, i.e., $\delta^1 X(\hat{\mathbf{n}}) \equiv \nabla^a X(\hat{\mathbf{n}}) \nabla_a \phi(\hat{\mathbf{n}})$) with

$$\delta^0 X(\hat{\mathbf{n}}) \equiv X(\hat{\mathbf{n}}), \tag{1.78}$$

and for polarization we define

$$\begin{aligned} \delta^j E_\ell &\equiv -\cos(2\varphi_\ell)\, \delta^j Q_\ell - \sin(2\varphi_\ell)\, \delta^j U_\ell, \\ \delta^j B_\ell &\equiv \sin(2\varphi_\ell)\, \delta^j Q_\ell - \cos(2\varphi_\ell)\, \delta^j U_\ell. \end{aligned} \tag{1.79}$$

The first terms of these expansions were shown in Eq. (1.52). By using these expansions, we end up with correlations of Gaussian fields (the unlensed CMB fields and the lensing field), and their correlations can again be simplified using Wick's theorem [144, 166, 167]. The various correlations are usually split according to their order of dependency on $C_L^{\phi\phi}$, as shown in Eq. (1.76). For most current and near-future CMB experiments, the main bias terms are $N_{0,L}^{\phi\phi}$ and

$N^{\phi\phi}_{1,L}$ [144]. They can be expressed analytically using the series expansions as

$$
\begin{aligned}
N^{\phi\phi}_{0,L} =& \frac{1}{\mathcal{R}^{\phi_{XY}}_{L}\mathcal{R}^{\phi_{ZD}}_{L}} \int \frac{d^2\ell}{(2\pi)^2} \\
& \times \left[f_{XY}(\mathbf{L},\boldsymbol{\ell}) f_{ZD}(\mathbf{L},-\boldsymbol{\ell}-\mathbf{L}) C^{X_{\rm tot}D_{\rm tot}}_{|\boldsymbol{\ell}+\mathbf{L}|} C^{Y_{\rm tot}Z_{\rm tot}}_{\ell} + f_{XZ}(\mathbf{L},\boldsymbol{\ell}) f_{YD}(\mathbf{L},\boldsymbol{\ell}) C^{\mathbf{X}_{\rm tot}Z_{\rm tot}}_{|\boldsymbol{\ell}+\mathbf{L}|} C^{Y_{\rm tot}D_{\rm tot}}_{\ell} \right], \\
N^{\phi\phi}_{1,L} =& \frac{1}{\mathcal{R}^{\phi_{XY}}_{L}\mathcal{R}^{\phi_{ZD}}_{L}} \int \frac{d^2\ell_1}{(2\pi)^2} \int \frac{d^2\ell'_1}{(2\pi)^2} F_{XZ}(\boldsymbol{\ell}_1,\boldsymbol{\ell}_2) F_{YD}(\boldsymbol{\ell}_1,\boldsymbol{\ell}_2) \\
& \times \left[C^{\phi\phi}_{|\boldsymbol{\ell}_1-\boldsymbol{\ell}'_1|} f_{XZ}(-\boldsymbol{\ell}_1,\boldsymbol{\ell}'_1) f_{YD}(-\boldsymbol{\ell}_2,\boldsymbol{\ell}'_2) + C^{\phi\phi}_{|\boldsymbol{\ell}_1-\boldsymbol{\ell}'_2|} f_{XD}(-\boldsymbol{\ell}_1,\boldsymbol{\ell}'_2) f_{YZ}(-\boldsymbol{\ell}_2,\boldsymbol{\ell}'_1) \right],
\end{aligned}
\tag{1.80}
$$

where $F_{XY}(\boldsymbol{\ell},\boldsymbol{\ell}')$ are the same weights of Eq. (1.56) that minimize the quadratic estimator variance, and $\boldsymbol{\ell}_1+\boldsymbol{\ell}_2=\boldsymbol{\ell}'_1+\boldsymbol{\ell}'_2=\mathbf{L}$. The analogous curved-sky biases can be found in [168]. The $N^{\phi\phi}_{0,L}$ bias will be non-zero even without a lensing field, as it does not depend on the lensing potential. The $N^{\phi\phi}_{1,L}$ term is smaller compared to $N^{\phi\phi}_{0,L}$, and is more dominant at small-scale lensing modes (high Ls).

To obtain an unbiased lensing power spectrum, these terms are needed to be calculated and subtracted from the constructed biased lensing power spectrum. When the QEs are constructed from maps with inhomogeneous and isotropic noise due to, e.g., the scanning strategy of the telescope and the mask used, these analytic estimates are not sufficient to capture the full biases. This problem can be solved by calculating these bias terms in other ways:

- **The patch approximation**: The observed sky area can be partitioned into patches such that each patch has approximately homogeneous noise. This noise can then be used to evaluate $N^{\phi\phi}_{0,L}$ and $N^{\phi\phi}_{1,L}$ for each patch. This method works well when the main problem is the inhomogeneity of the noise on the sky, but it cannot be used to properly correct for systematic effects or correlated noise which cannot be approximated as being locally white on the map.

- **Monte Carlo estimates**: Instead of evaluating these bias terms analytically, we can use the fact that they result from the connected and disconnected contractions of the 4-point correlations of lensed CMB fields to estimate them using Monte Carlo (MC) simulations via ensemble averaging. When estimating $N^{\phi\phi}_{0,L}$ with MC simulations, incorporating the specific data fields used in the reconstruction can be useful to correct any linear covariance differences between the measured fields and the simulated MC fields [169]. The resulting bias term is usually referred to as the realisation-dependent $N^{\phi\phi}_{0,L}$.

The latter method will be used throughout the thesis, while the patch approximation method will

be used in a slightly different way in our lensing reconstruction analyses. These methods will be described in more detail in Chapters 2- 4.

1.5 THESIS OUTLINE

Throughout the introduction, the theoretical background and key concepts in cosmology and CMB lensing that the work done in this thesis is based on were described. Each of the following chapters is composed of independent works, which are somewhat related in different ways.

As most of the work in the thesis deals with CMB lensing, we start by exploring in more detail how lensing reconstruction is achieved. In Chapter 2 we explore and compare several filtering methods that are applied to the CMB maps for lensing reconstruction, and add a newly-developed filtering step which is applied to the constructed quadratic estimator. We show how the different methods compare in terms of accuracy on the reconstructed lensing map, and both auto- and cross-spectrum with the input simulated lensing map, and provide improvement forecasts for the upcoming Simons Observatory (SO) and CMB-S4 experiments.

We continue by adopting the most optimal pipeline of Chapter 2 to explore how instrumental systematics might bias the lensing reconstruction analysis of an SO-like experiment. This is done by producing CMB simulations that include the effects of several instrumental systematics, and using our lensing reconstruction pipeline to analyse them. We then compare the resulting lensing power spectra that are made from simulations with and without the effects of systematics to show how each effect manifests on the lensing power spectrum and the lensing bias terms. This work is concluded by evaluating the detection significance of each effect, given the specific parameters chosen for their simulations, and discuss several mitigation strategies for the more problematic systematics.

While both first chapters concentrate on analysing CMB simulations, the next two chapters involve analysing real CMB data, specifically from the Planck mission. In Chapter 4 we use our lensing pipeline on a new release of the Planck maps, known as the `NPIPE` maps. We show that our lensing reconstruction pipeline improves the large-scale lensing estimates from Planck compared to Planck's baseline lensing analysis, and propagate this accurate to estimating cosmological parameters using likelihoods. The uncertainties of the lensing-dependent cosmological parameters also improve by applying our QE filter, which is yet another motivation for including our filtering method in the lensing analyses of upcoming CMB experiments.

The last work we present deviates from the CMB lensing theme of the other chapters, where we look into the effect of Rayleigh scattering on the CMB. Chapter 5 shows how the Rayleigh

signal, which affected the CMB photons in the early Universe, could be detected from multi-frequency CMB measurements. We describe the pipeline that can be used for this purpose while demonstrating it using the Planck CMB temperature maps. We conclude this work by providing an updated forecast on the ability to detect the Rayleigh signal from Planck maps, and also estimate its detection levels for an SO-like experiment.

The results of these works are then summarised in Chapter 6.

CHAPTER 2

Optimal filtering for CMB lensing reconstruction

MARK MIRMELSTEIN, JULIEN CARRON, ANTONY LEWIS

Abstract

Upcoming ground-based cosmic microwave background experiments will provide CMB maps with high sensitivity and resolution that can be used for high fidelity lensing reconstruction. However, the sky coverage will be incomplete and the noise highly anisotropic, so optimized estimators are required to extract the most information from the maps. We focus on quadratic-estimator based lensing reconstruction methods that are fast to implement, and compare new more-optimally filtered estimators with various estimators that have previously been used in the literature. Input CMB maps can be optimally inverse-signal-plus-noise filtered using conjugate gradient (or other) techniques to account for the noise anisotropy. However, lensing reconstructions from these filtered input maps have an anisotropic response to the lensing signal and are difficult to interpret directly. We describe a second-stage filtering of the lensing maps and analytic response model that can be used to construct lensing power spectrum estimates that account for the anisotropic response and noise inhomogeneity in an approximately optimal way while remaining fast to compute. We compare results for simulations of upcoming Simons Observatory and CMB Stage-4 experiments to show the robustness of the more optimal lensing reconstruction pipeline and quantify the improvement compared to less optimal estimators. We find a substantial improvement in reconstructed lensing power variance between optimal anisotropic and isotropic filtering of CMB maps, and up to 30% improvement in variance by using the additional filtering step on the reconstructed potential map. Our approximate analytic response model is unbiased to within a small percent-level additional Monte Carlo correction.

2.1 INTRODUCTION

Gravitational lensing of the cosmic microwave background (CMB) can be measured from the small changes induced in the observed temperature and polarization anisotropies (see Ref. [142] for a review). Precision observations of the CMB can therefore be used to reconstruct the lensing potential, and constrain the evolution and geometry of the Universe between recombination and today. Planck has measured the lensing signal over $70\,\%$ of the sky [100], but the lensing reconstruction remains noise-dominated on most scales due to the limited resolution and sensitivity of the CMB measurements. In the upcoming years, new ground-based CMB experiments will substantially improve current measurements, with Simons Observatory (SO) [131] and then CMB-S4 [133] (hereafter S4) building on the ongoing observations by ACTPol [170], SPTpol [153] and POLARBEAR [171]. However, the instrumental noise affecting the B-mode polarization used for lensing reconstruction will remain important, and the lensing reconstruction noise from the instrumental noise and cosmic variance of the unlensed CMB will continue to dominate for small-scale lensing reconstruction modes ($L > 400$ for SO)[1]. The instrumental noise also typically varies substantially over the observed sky area due to the exact way in which the sky is repeatedly scanned. It is therefore important to consider how to account for the inhomogeneous noise properties to exploit the CMB maps in an efficient way.

Since the noise and unlensed CMB are expected to be Gaussian, and lensing simply deflects points on the sky, it is straightforward to write down a likelihood for the observed CMB given a fixed lensing deflection field. The lensing potential is also Gaussian to a good approximation on most relevant scales, so finding the lensing potential that maximizes the posterior then gives an optimal estimator for the lensing potential [160, 161]. The resulting estimator is a complicated non-linear function of observed fields that has to be evaluated iteratively, but can be approximated to good accuracy for the near future by a quadratic estimator (QE) that is easier to evaluate [158, 162, 172]. To be optimal with anisotropic noise, the QE must be written as a quadratic function of filtered observed CMB fields, where the inverse-signal-plus-noise filters act to down-weight areas of the sky with higher noise (or foreground power). In this chapter we compare this optimal filtering with various simpler filtering methods that have been used in the literature, to assess the improvement that can be obtained by using optimal filtering with upcoming experiments. We also present a new more optimal estimator that uses a second filtering step applied to the quadratic estimator reconstruction map.

Converting the lensing reconstruction map into an unbiased estimate of the lensing power spectrum (and any relevant cross-spectra) is important for parameter estimation, but is more

[1] We follow the standard convention and use L rather than ℓ for lensing multipoles.

complicated if the input maps are inhomogeneously filtered as the lensing reconstruction maps then effectively have a position-dependent normalization. This can be accounted for by applying a brute-force Monte Carlo (MC) correction, but we show that a simple analytic 'patch' approximation is sufficient to capture the dominant effect. This approximation relies on the fact that the lensing estimators are quasi-local, so the lensing reconstruction at a given point mostly depends on the surrounding area of the observed CMB. If the noise varies slowly over the sky, we can therefore model the full signal as being made up of a set of patches within which the noise is nearly constant and the response can be calculated analytically. Corrections to this approximation can be measured by MC simulations and are perturbatively small, so the dominant signal can still be related analytically to the theoretical model.

Since the instrumental noise is inhomogeneous, the lensing reconstruction noise is also inhomogeneous, and an optimal spectrum estimator should account for this. It is possible to write down an approximate full likelihood for the lensing power spectrum and maximize it [161]; however, this again has to be solved iteratively, and makes the final lensing spectrum estimate a highly non-trivial function of the theoretical model parameters. Instead, we consider a simpler approximate solution that estimates the power spectrum from filtered QE maps, and assess the improvement using an approximate model for the reconstruction noise. The resulting power spectrum depends only on the four-point function of the CMB maps, and hence can be modelled straightforwardly as a function of parameters in a similar way to other QE-based analyses.

We start in Sec. 2.2 by outlining the lensing reconstruction methodology and steps required to estimate the lensing power from the observed maps, and discuss various possible ways of filtering the CMB maps. In Sec. 2.3 we develop the analytic patch approximation and assess its accuracy by comparison with simulations. Sec. 2.4 presents our main results, where we show the improvement in signal-to-noise that can be obtained using the two optimal filtering steps. Throughout, we assume a Gaussian unlensed CMB and inhomogeneous but uncorrelated pixel instrumental noise. For illustration we show results assuming a fiducial ΛCDM model using parameters similar to those estimated by Planck [31].

2.2 METHODOLOGY

We broadly follow the methodology of the Planck lensing analysis [100]. For simplicity, we use the flat-sky approximation when showing numerical results, using lensing analysis tools and simulated lensed CMB from LENSIT[2]. Our lensing analysis is based on QEs, which can be

[2] https://github.com/carronj/LensIt

evaluated efficiently in the case of full-sky observations with isotropic noise using methods explained in Refs. [142, 158, 172]. Here, we will briefly review the motivation for using quadratic estimates and explain the need for filtered maps.

Following Ref. [158], we take the observed maps to be a vector of fields[3] $\boldsymbol{X}$ (with temperature T, and/or polarization Stokes parameters Q or U) with $\boldsymbol{X}(\mathbf{x}) = \tilde{\boldsymbol{X}}(\mathbf{x}) + \mathbf{n}(\mathbf{x})$ in pixel space at position $\mathbf{x}$, where $\mathbf{n}$ is the instrumental noise realization which is assumed to be Gaussian, anisotropic and spatially uncorrelated. Here $\tilde{\boldsymbol{X}}$ is the beamed and lensed CMB given in terms of the unlensed fields $\boldsymbol{X}$ and deflection angle $\boldsymbol{\alpha}$ by $\tilde{\boldsymbol{X}}(\mathbf{x}) = \boldsymbol{b}\boldsymbol{X}(\mathbf{x}+\boldsymbol{\alpha})$ where $\boldsymbol{b}$ accounts for the beam transfer function. For a fixed lens model, we can write down the log-likelihood $\mathscr{L}$ of the observed CMB given the lensing potential ϕ (which is related to the deflection angle, $\boldsymbol{\alpha} = \boldsymbol{\nabla}\phi$) as

$$-\mathscr{L}(\boldsymbol{X}|\phi) = \frac{1}{2}\boldsymbol{X}^\top \left(\boldsymbol{C}_\phi^{\boldsymbol{X}\boldsymbol{X}}\right)^{-1} \boldsymbol{X} + \frac{1}{2}\ln\left|\boldsymbol{C}_\phi^{\boldsymbol{X}\boldsymbol{X}}\right|, \tag{2.1}$$

where $\boldsymbol{C}_\phi^{\boldsymbol{X}\boldsymbol{X}} \equiv \boldsymbol{C}_\phi^{\boldsymbol{X}\boldsymbol{X}}(\mathbf{x},\mathbf{y}) = \boldsymbol{C}_\phi^{\tilde{\boldsymbol{X}}\tilde{\boldsymbol{X}}}(\mathbf{x},\mathbf{y}) + \boldsymbol{N}(\mathbf{x},\mathbf{y})$ is the covariance of the map for fixed lensing potential ϕ. Here the coordinates are integrated over in the contractions and $\boldsymbol{N}$ is the covariance of the noise, which we take to be diagonal in pixel space and uncorrelated between T, Q, U. We want to maximize the likelihood with respect to $\phi(\mathbf{x})$. This is done by equating the log-likelihood's derivative with respect to $\phi(\mathbf{x})$ to zero,

$$\begin{aligned}\frac{\delta\mathscr{L}}{\delta\phi(\mathbf{x})} &= \frac{1}{2}\boldsymbol{X}^\top \left(\boldsymbol{C}_\phi^{\boldsymbol{X}\boldsymbol{X}}\right)^{-1} \frac{\delta \boldsymbol{C}_\phi^{\boldsymbol{X}\boldsymbol{X}}}{\delta\phi(\mathbf{x})} \left(\boldsymbol{C}_\phi^{\boldsymbol{X}\boldsymbol{X}}\right)^{-1} \boldsymbol{X} - \frac{1}{2}\mathrm{Tr}\left[\left(\boldsymbol{C}_\phi^{\boldsymbol{X}\boldsymbol{X}}\right)^{-1} \frac{\delta \boldsymbol{C}_\phi^{\boldsymbol{X}\boldsymbol{X}}}{\delta\phi(\mathbf{x})}\right] \\ &= 0.\end{aligned} \tag{2.2}$$

The trace term can be written as a 'mean field' (MF) average of the first term ($\equiv \hat{g}^\phi(\mathbf{x})$, see Ref. [158, 162]), so that we require a solution to $\hat{g}^\phi(\mathbf{x}) - \langle \hat{g}^\phi(\mathbf{x})\rangle = 0$. The general solution for $\phi(\mathbf{x})$ has to be obtained iteratively, but the first step of Newton-Raphson from zero (denoted by a subscript of 0 below) gives the approximate QE solution

$$\hat{\boldsymbol{\phi}} = \boldsymbol{\mathcal{F}}^{-1}\left(\hat{\boldsymbol{g}}_0^\phi - \langle \hat{\boldsymbol{g}}_0^\phi\rangle\right), \tag{2.3}$$

where $\hat{\boldsymbol{g}}_0^\phi$ now depends on the CMB maps only via the inverse-variance filtered combination $\left(\boldsymbol{C}_{\phi=0}^{\boldsymbol{X}\boldsymbol{X}}\right)^{-1}\boldsymbol{X}$. Here technically the covariance is evaluated with $\phi = 0$, however the accuracy of the estimator can be improved beyond leading order by using $\left(\boldsymbol{C}^{\boldsymbol{X}\boldsymbol{X}}\right)^{-1}\boldsymbol{X}$, i.e. filtering using the covariance evaluated using lensed CMB power spectra [146, 173].

In Eq. (2.3) the Hessian matrix of second derivatives of the log-likelihood is approximated by

[3] Throughout, bold symbols are used to describe vectors or matrices.

its expectation, the Fisher matrix $\mathcal{F}$ (see Appendix A.1 for more details). This normalizes the result, and can be evaluated analytically in the case of full sky and isotropic noise where it is diagonal in harmonic space; more generally it is non-trivial to evaluate exactly. The approximate optimal maximum likelihood solution involves inverse-variance filtering, but it is also possible to make other choices: as long as $\mathcal{F}$ is adjusted appropriately, the estimator can remain unbiased (at the expense of some increase in reconstruction noise compared to the optimal case).

In the limit of a perturbatively Gaussian lensing field, the optimal maximum-likelihood estimator for the power spectrum can also be derived from the likelihood function. As shown by Appendix B of Ref. [174] this reduces to a (bias-subtracted) QE up to a Fisher-normalization, where the QE is calculated using inverse-variance filtered fields. The CMB maps only enters via their inverse-variance filtered version, as for the estimator of ϕ itself, so our first filtering step of the CMB maps should remain perturbatively optimal. The optimal power spectrum estimator also only depends on the naive power spectrum of the (unnormalized) ϕ estimator, corresponding to the inverse-noise weighted ϕ estimator (in agreement with Ref. [100] that for noise-dominated reconstructions uniform weighting of the inverse-noise filtered field is optimal). The limit of small $C_L^{\phi\phi}$ does not of course apply directly in the case of lensing reconstruction, where the signal can be measured at high signal-to-noise, but we can expect that for larger $C_L^{\phi\phi}$ the inverse-noise weighting will approximately generalize to inverse-signal-plus-noise weighting, which is consistent with the perturbatively-optimal estimator in the small-signal limit.

In general, the QE lensing power spectrum analysis consists of the following five stages:

A. Filtering the observed CMB maps. As mentioned, there are several filtering methods one could use on the CMB maps before obtaining the QE. In this work, we compare the optimal method to alternative methods that have been used in the literature.

B. Constructing the quadratic lensing estimators. The filtered fields are efficiently combined in real space to obtain the unnormalized lensing QE.

C. Subtracting the mean field. The map-level MF signal expected from mask, noise and other anisotropic features of the map in the absence of lensing is subtracted. Here we also apply an approximate analytic and isotropic normalization at the map level, though this has no impact on the resulted lensing power as long as everything is done consistently.

D. Filtering the reconstructed κ map. This optional step is new to our analysis. Approximating the unnormalized convergence (κ) reconstruction map as depending locally on the CMB maps and their filtered versions of stage A, we can apply an approximate local normalization to obtain the noisy reconstructed κ map and then inverse-variance filter it

using an approximate model for the local variance.

E. Estimating the power spectrum. The power spectrum of the filtered κ is biased, due to reconstruction noise, other lensing contractions, masking and other non-idealities, and because it is not yet normalized (the unfiltered-κ spectrum is also biased, but with different debiasing terms). We subtract an MC estimate of the $N_{0,L}$ reconstruction noise and $N_{1,L}$ signal contractions, both obtained using 500 MC simulations, and multiply the resulting spectrum by an analytic correction made using a patch approximation (the latter is needed as the normalization of the QE applied in Stage C is only a local approximation; even without filtering the κ map, any analytic response model would need to be corrected due to the inhomogeneity of the noise in the map).

These steps are shown in Fig. 2.1 and discussed in more detail below.

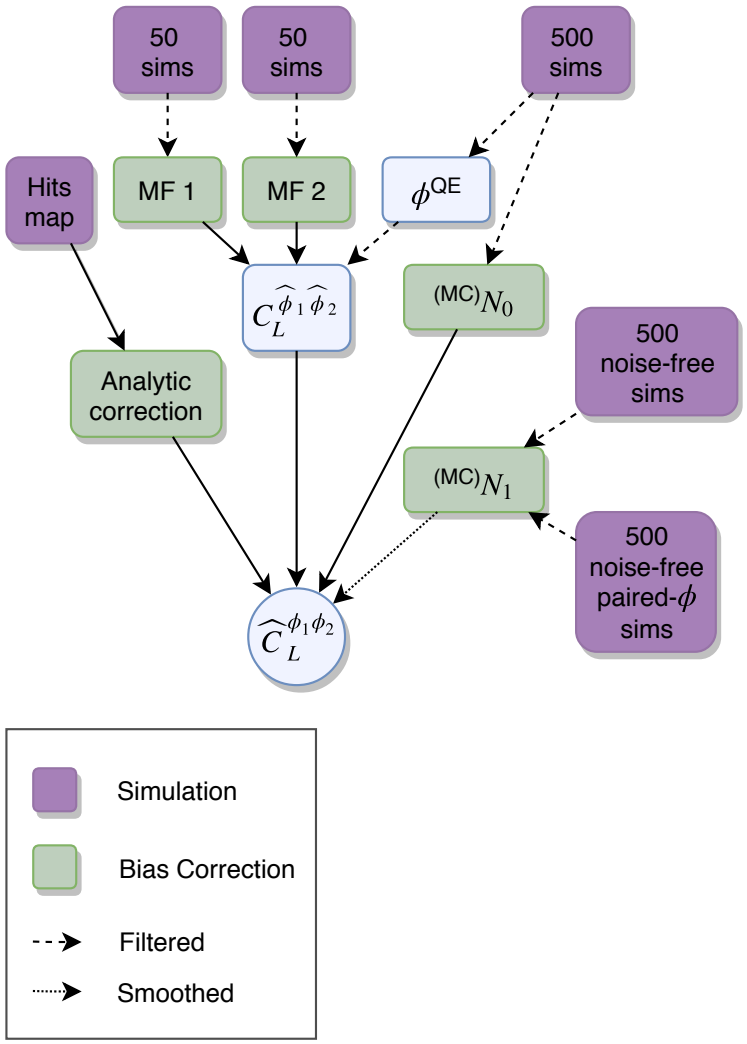

Figure 2.1: The structure of the optimized QE lensing reconstruction pipeline which was used in this work. Here we use the same CMB realizations for constructing the QEs, $^{\rm (MC)}N_{0,L}$ and $^{\rm (MC)}N_{1,L}$ terms. The analytic correction is calculated using the simulated hit count map shown in Fig. 2.2.

2.2.1 FILTERING METHODS

The first filtering step is a linear operation that is applied to the CMB maps giving a filtered CMB field

$$\bar{\boldsymbol{X}} \equiv \boldsymbol{M}\boldsymbol{X}, \tag{2.4}$$

where $\boldsymbol{M}$ is some linear filtering matrix that's designed to removed masked areas and (optionally) down-weight noisier pixels or other noisy or contaminated modes. For optimal filtering $\boldsymbol{M}$ is non-diagonal, and performs the full anisotropic inverse-variance filtering. For comparison we also consider approximate filtering methods where $\boldsymbol{M}$ is taken to be diagonal in pixel space, which is somewhat faster to implement but less optimal.

We compare three different filtering methods by using them for lensing reconstruction on simulated sky maps with inhomogeneous noise. To simulate realistic noise inhomogeneity we use a part of a suggested scanning strategy for Simons Observatory's Small Aperture Telescope (SAT), the "opportunistic" scanning strategy presented in Ref. [175] as the hit count map. Note that while the lensing analysis of SO will come mainly from its Large Aperture Telescope (LAT), we chose to work with a part of the SAT scan as this scan has a well-contained area and is therefore more convenient for our flat-sky analysis. To obtain the flat scanned area, we used the Cartesian projection from the HEALPix package[4] [176] to project the curved sky hit count map onto the flat sky. The normalized hit count map $m_{\rm hits}(\mathbf{x})$ is shown in Fig. 2.2. The white pixels are seen more frequently during the sky scan simulation and so have a higher hit count (corresponding to lower noise), while the blue and purple areas show pixels which were scanned less often. Black pixels are not scanned.

We then use the hit count map to model the white noise standard deviation map

$$m_{\rm noise}(\mathbf{x}) = \sqrt{\frac{s^2 N_{\rm hits,tot}}{t_{\rm obs} m_{\rm hits}(\mathbf{x})}}\,, \tag{2.5}$$

where s is the instrument sensitivity for temperature or polarization, $t_{\rm obs}$ is the total observation time on the patch (with 1/5 efficiency), and $N_{\rm hits,tot}$ is the total number of hits in the hit count map $m_{\rm hits}(\mathbf{x})$. Using this model, noise is taken to be infinite outside the scanned region. The specifications we consider are discussed in Sec. 2.4.

In the following, each filtering method is presented along with motivation and assumptions. We filter modes below 4096 in the input maps using each method, and cut the filtered fields to $40 \leq \ell \leq 3000$ before using them to obtain the QEs in stage B.

[4] http://healpix.sf.net/

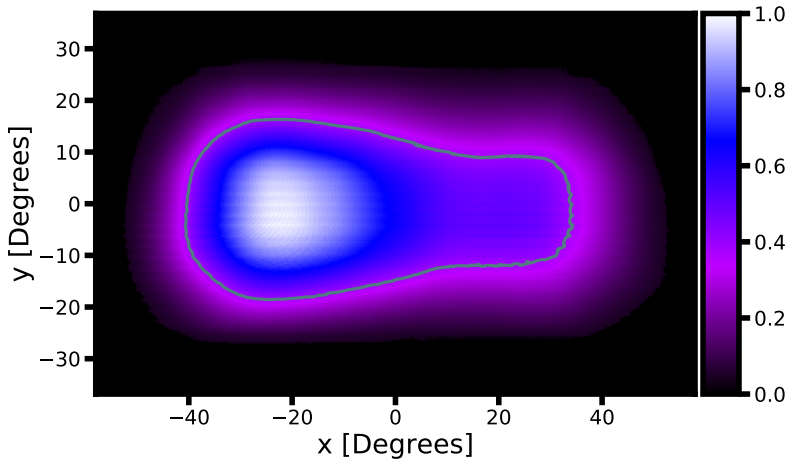

Figure 2.2: The normalized hit count map used to simulate anisotropic noise in the simulations. The white pixels are those which were scanned for longer time, while the dark blue-purple fade shows pixels which were scanned less frequently. The black pixels are those which were not scanned. The area within the green boundary shows the unmasked regions used for the comparison isotropic-filtering analysis described in Sec. 2.2.1. The normalized hit count map is also used as the weights for the comparison weighted maps analysis (Sec. 2.2.1). The area with non-zero hits corresponds to 39% of the flat-sky map we simulate, and about 13% of the full sky area 4π. The figure above is centred on the main observed area and does not show additional unobserved regions which all together form a 4096x4096 pixels map, which is 116 degrees on the side.

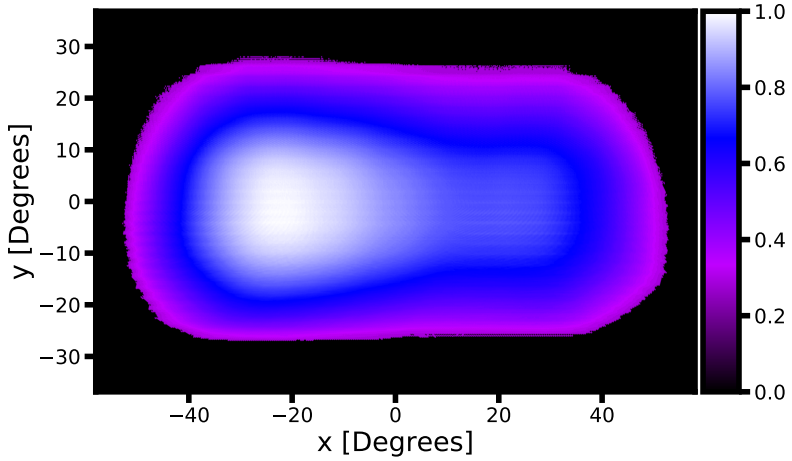

Figure 2.3: The normalized inverse approximate lensing reconstruction noise $\left(N^{\kappa}_{0,\mathrm{eff}}(\mathbf{x})\right)^{-1}$ from an analysis for an SO-like experiment using temperature and polarization. Compared to the hit count map in Fig. 2.2, the reconstruction noise varies less strongly across the patch because it depends on the (isotropic) CMB variance as well as the (anisotropic) noise. The approximate effective white reconstruction noise $N^{\kappa}_{0,\mathrm{eff}}(\mathbf{x})$ is defined as the average value of the isotropic $N^{\kappa}_{0,L}$ over the multipole range $40 \leq L \leq 90$ on local approximately constant noise patches. This figure, along with most of the figures in this thesis, were produced using the Matplotlib [177] Python library.

Optimal filtering

The inverse-variance filtered CMB maps can be written as

$$\bar{\boldsymbol{X}} \equiv \left(\boldsymbol{b}\boldsymbol{C}^{\mathrm{fid}}\boldsymbol{b}^{\top} + \boldsymbol{N}\right)^{-1}\boldsymbol{X} = \left(\boldsymbol{C}^{\mathrm{fid}}\right)^{-1}\left[\left(\boldsymbol{C}^{\mathrm{fid}}\right)^{-1} + \boldsymbol{b}^{\top}\boldsymbol{N}^{-1}\boldsymbol{b}\right]^{-1}\boldsymbol{b}^{\top}\boldsymbol{N}^{-1}\boldsymbol{X}, \tag{2.6}$$

where $\boldsymbol{b}$ is the transfer function (here we consider a simple isotropic Gaussian beam with full-width half-maximum θ_{FWHM}) and $\boldsymbol{C}^{\mathrm{fid}}$ is a set of fiducial lensed power spectra. The noise can include variance due to foreground residuals, and a mask can be accounted for simply by taking

the elements of $\boldsymbol{N}^{-1}$ to be zero in the corresponding pixels.

There are various possible ways to solve Eq. (2.6). We follow the multi-grid-preconditioned conjugate gradient method first demonstrated in the context of lensing by Ref. [148] and then by the Planck and SPTpol lensing analyses [98, 100, 123, 153]. The pixel noise is in general spatially varying, but for simplicity the main Planck lensing analyses approximate the noise as isotropic and white. Ref. [100] demonstrated that accounting for inhomogeneous noise in the filter can substantially improve Planck's noise-dominated polarization reconstruction, and in this chapter we only use 'optimal' to refer to the full anisotropic filter.

Rearranging (2.6) to the form $\left(\boldsymbol{b}C^{\rm fid}\boldsymbol{b}^\top + \boldsymbol{N}\right)\bar{\boldsymbol{X}} = \boldsymbol{X}$, we define our stopping criterion for convergence to be when the norm of the difference of the two sides of the equation is smaller than $\epsilon|\boldsymbol{X}|$. We use $\epsilon = 10^{-5}$ for reconstructions using temperature and $\epsilon = 10^{-4}$ when using only polarization. We discuss some details of the choice of preconditioner and numerical performance in Appendix B.

Isotropic filtering of masked maps

The covariance matrix $\left(\boldsymbol{b}C^{\rm fid}\boldsymbol{b}^\top + \boldsymbol{N}\right)$ in Eq. (2.6) is trivial to invert in harmonic space if the noise (and beam) is taken as isotropic, as both the theory and noise covariance matrices are then diagonal in harmonic space. We refer to this approximation as 'isotropic filtering', which is substantially faster than optimal filtering since it avoids the conjugate-gradient inversion. The isotropic filter is expected to be close to optimal over scales on which the corresponding CMB fields are signal dominated, or when the noise is close to uniform. However, since it does not account for masking, even in these cases it is expected to be suboptimal. In practice the isotropic filter is applied to maps multiplied by an apodized mask, following Ref. [178]. This maintains quasi-locality of the lensing in real space, so masking artefacts are then only expected to be significant near the mask boundaries. For this filtering method, we mask all pixels with (temperature map) noise over $\sim$9.6 μK arcmin for SO and $\sim$1.8 μK arcmin for S4. Before applying this new mask, it is apodized using a 30 arcmin-width Gaussian to avoid power spectrum errors due to a sharp cut-off in the sky maps. Both of these procedures result in an effective scanned area which is $\sim$46% smaller than the original scanned area, shown by the green outline in Fig. 2.2. The assumed isotropic noise level in the filter is taken to be that which minimizes the variance of the reconstructed lensing potential (we consider all reconstructed multipoles for this minimization as we saw no significant differences using different multipole ranges).

Isotropic filtering of weighted maps

Instead of applying isotropic filtering to apodized masked maps, one can also apply it to a more generally weighted map, for example to try to down-weight regions with higher noise. This corresponds to using the filter $\left(\boldsymbol{b}C^{\rm fid}\boldsymbol{b}^\top + \boldsymbol{N}\right)^{-1}\boldsymbol{W}\boldsymbol{X}$, where $\boldsymbol{W}$ is diagonal in pixel space and $\boldsymbol{N}$ is taken to be isotropic. We consider the specific case where $W(\mathbf{x},\mathbf{x})$ is proportional to the inverse of the instrumental pixel noise variance, similar to the weighting applied by ACTPol [170], so the diagonal of $\boldsymbol{W}$ is the normalized hit count map, having values between zero (for masked areas) and one. This is expected to be close to optimal when the CMB fields are dominated by instrumental noise, so that the $\sim\boldsymbol{N}^{-1}$ dependence of the optimal filter is mostly captured by the weights.

In the case of polarization, specific window functions can also be used for separation of E and B modes on the partial sky [92]. Several authors have applied lensing reconstruction EB estimators to the separated modes [154, 170, 179]. This has the advantage of being relatively fast to implement, but is clearly sub-optimal and previous analyses have not attempted to also accurately account for spatial variation in the noise. The optimal filter described in 2.2.1 already accounts for the cut-sky-induced B modes, since the optimal filter automatically down-weights B modes that are substantially contaminated by variance of the E modes.

2.2.2 QUADRATIC ESTIMATORS

We calculate the unnormalized QE $\hat{g}_0^\phi(\mathbf{x})$ using different field combinations: temperature-only (T), polarization-only (P), or temperature+polarization (minimum variance, MV). We cut lensing modes outside the range $40 \leq L \leq 3000$ in harmonic space where our reconstruction is considered unreliable.

Unless we use isotropic filtering (or even in this case close to the mask boundaries), the estimator normalization in Eq. (2.3) is non-diagonal and difficult to calculate exactly, effectively varying spatially over the sky. We do not attempt to correctly normalize the lensing reconstruction map here, but instead correct the normalization at the level of the power spectrum (see below). If the filter varies smoothly over the map, an approximately-normalized reconstruction map could be made by using locally-defined values of the analytic isotropic normalization (see Sec. 2.3 below).

2.2.3 MEAN FIELD AND NORMALIZATION

We calculate the mean field (MF) of the unnormalized QE $\langle \hat{g}_0^{\phi} \rangle_{\rm MC}$ twice, each calculation using 50 different MC simulations. This gives two MF estimates, MF_1 and MF_2, with independent MC noise, so the lensing power spectrum calculated from a pair of MF-subtracted QEs will not have any MC noise bias. Following the MF subtraction and response normalization we obtain the estimator for the lensing potential $\hat{\phi}$ given by

$$\hat{\phi}_{\mathbf{L}} \equiv \frac{1}{\mathcal{R}_L^{\phi,\rm fid}} \left(\hat{g}^{\phi}_{0,\mathbf{L}} - \langle \hat{g}^{\phi}_{0,\mathbf{L}} \rangle_{\rm MC} \right), \tag{2.7}$$

where $\mathcal{R}_L^{\phi,\rm fid}$ is a fiducial isotropic response for the reconstruction (see Eq. (2.15)), and $\mathbf{L}$ is the 2D flat-sky multipole vector. The definition of the isotropic response is discussed later in Sect. 2.3, along with how the power spectrum can be corrected for the anisotropy.

2.2.4 FILTERING THE QUADRATIC ESTIMATORS

The likelihood-based lensing power spectrum estimator given by Ref. [161] involves the CMB maps via the maximum a posteriori (MAP) estimate of the lensing field. Since MAP estimators give an estimate of the Wiener-filtered (i.e. $\boldsymbol{C}^{\kappa\kappa} \left(\boldsymbol{C}^{\kappa\kappa} + \boldsymbol{N}^{\kappa}_{0,\rm MAP} \right)^{-1}$-filtered, see Appendix A.2 for more details) field, this suggests that a close-to-optimal analysis should use estimated lensing maps weighted by their inverse covariance. More generally, if we approximate the lensing reconstruction as a Gaussian lensing field plus Gaussian reconstruction noise, the optimal power spectrum would also involve the inverse-covariance weighted fields.

When using isotropic filtering the reconstruction noise is considered to be isotropic, so an additional isotropic filtering step would simply be a re-definition of the diagonal normalization. With optimal anisotropic filtering things are more complicated, but we can use the same iterative filtering method presented in Sec. 2.2.1 if we approximate the lensing reconstruction noise as diagonal in pixel space. This is clearly not a good approximation in general since the lensing reconstruction noise spectrum is not white; however, if the noise is slowly varying, the large-scale effect of slowly varying reconstruction noise can be approximately modelled using a patch-uncorrelated estimate of the local noise variance $N^{\kappa}_{0,\rm eff}(\mathbf{x})$. Here we use the lensing convergence (κ) reconstruction noise, since it is the convergence reconstruction which is approximately local in real space, and hence is uncorrelated between patches on large scales and has approximately white noise. We take the effective reconstruction noise $N^{\kappa}_{0,\rm eff}(\mathbf{x}^p)$ in each

patch p to be the average value of $N^{\kappa}_{0,L}$ (the isotropic reconstruction noise $N_{0,L}$ for $\kappa_{\mathbf{L}} \equiv L(L+1)\phi_{\mathbf{L}}/2$ and the local patch noise value[5]) over the multipole range $40 \leq L \leq 90$. Each patch is composed of pixels of approximately the same instrumental noise (each patch could be taken to be a single pixel, but it is more numerically convenient to model batches of pixels with similar noise levels together).

An example for the inverse of the reconstruction noise map is shown in Fig. 2.3 for lensing reconstruction from temperature and polarization. Averaging over a different multipole range to define $N^{\kappa}_{0,\mathrm{eff}}(\mathbf{x})$ would result in a better agreement with the full $N_{0,L}$-filtered theory variances across corresponding multipoles, although we demonstrate that our chosen range is already quite optimal for the multipoles in which the improvement from this filtering stage is considered significant (see Fig. 2.7 for comparison between using $N^{\kappa}_{0,\mathrm{eff}}$ and $N_{0,L}$ in the filter).

The $\boldsymbol{C}^{\kappa\kappa}_{\mathrm{fid}}\left(\boldsymbol{C}^{\kappa\kappa}_{\mathrm{fid}}+\boldsymbol{N}^{\kappa}_{0,\mathrm{eff}}\right)^{-1}$ filtering process should be applied to the correctly normalized reconstructed convergence map, but the QE constructed from optimally-filtered CMB maps is not correctly normalized locally. However, in the patch approximation, we can approximately normalize the map locally using a local response: we take the un-normalized full QE field $\hat{g}^{\kappa}(\mathbf{x})$, and normalize locally in real space by an effective local response map $\mathcal{R}^{\kappa}_{\mathrm{eff}}(\mathbf{x})$. This gives a reconstruction which is approximately locally normalized following Eq. (2.14), where we define the approximate effective $\mathcal{R}^{\kappa}_{\mathrm{eff}}$ analogously to $N^{\kappa}_{0,\mathrm{eff}}$. The final approximately filtered estimator is then

$$\hat{\boldsymbol{\kappa}}^{\mathrm{filt}} \equiv \boldsymbol{C}^{\kappa\kappa}_{\mathrm{fid}}\left(\boldsymbol{C}^{\kappa\kappa}_{\mathrm{fid}}+\boldsymbol{N}^{\kappa}_{0,\mathrm{eff}}\right)^{-1}\left(\boldsymbol{\mathcal{R}}^{\kappa}_{\mathrm{eff}}\right)^{-1}\hat{\boldsymbol{g}}^{\kappa}, \tag{2.8}$$

where[6]

$$\hat{g}^{\kappa}_{\mathbf{L}} \equiv \left(\hat{g}^{\phi}_{\mathbf{L}} - \langle \hat{g}^{\phi}_{\mathbf{L}} \rangle_{\mathrm{MC}}\right) \times \frac{2}{L(L+1)}. \tag{2.9}$$

Here $\boldsymbol{C}^{\kappa\kappa}$ is diagonal in harmonic space and we have defined $\boldsymbol{\mathcal{R}}^{\kappa}_{\mathrm{eff}}$ and $\boldsymbol{N}_{0,\mathrm{eff}}$ to be diagonal in pixel space (with $N^{\kappa}_{0,\mathrm{eff}}(\mathbf{x})^{-1} = 0$ in masked areas). The only non-trivial filtering step involving $\left(\boldsymbol{C}^{\kappa\kappa}_{\mathrm{fid}}+\boldsymbol{N}^{\kappa}_{0,\mathrm{eff}}\right)^{-1}$ is therefore analogous to the optimal CMB map filtering discussed in Sec. 2.2.1, and can be performed using the same conjugate gradient techniques.

Although the filtering is very approximate, it does not introduce any biases in the power spectrum as long as the approximate filter is propagated self-consistently into the normalization (see Sec. 2.3 for more details). For simplicity, we call this estimator the κ-filtered estimator.

[5] We use $L(L+1)$ albeit the flat-sky analysis, as this factor is arbitrary when used consistently throughout.

[6] Notice that the $\phi_{\mathbf{L}} \to \kappa_{\mathbf{L}}$ conversion factor $L(L+1)/2$ is being divided instead of multiplied, as the conversion here is between the unnormalized QEs of ϕ and κ, so the scaling also accounts for the conversion of the response.

2.2.5 LENSING POWER SPECTRUM

For a pair of lensing map estimates $\hat{\phi}_1$ and $\hat{\phi}_2$ (from Eq. (2.7) without filtering κ; numerical indices indicate that a different MF was used), we obtain the cross-spectrum

$$C_L^{\hat{\phi}_1\hat{\phi}_2} \equiv \frac{1}{f_{A,L} n_L} \sum_{\boldsymbol{\ell} \text{ in } \mathbf{L} \text{ bin}} \hat{\phi}_{1,\boldsymbol{\ell}} \hat{\phi}^*_{2,\boldsymbol{\ell}}, \tag{2.10}$$

where n_L is the somewhat irregular number of modes on the flat sky assigned to lensing multipole L in our simulation maps and $f_{A,L}$ is a normalization defined to make the estimator approximately unbiased in a fiducial model. We give an approximate analytic formula for $f_{A,L}$ in Sec. 2.3 below; in simple cases it can just be interpreted as an effective fractional area of our flat-sky simulation map (see Fig. 2.2).

Analogous definitions apply for the κ-filtered estimator of Eq. (2.8). For brevity, in this section we only explicitly give results for ϕ; when using the filtered κ estimators, $\hat{\kappa}^{\rm filt}$, the resulting biases are related by the usual scaling. We subtract the connected Gaussian noise bias from the power spectrum estimator using the estimator [153]

$$\begin{aligned} {}^{\rm (MC)}N_{0,L}^{\hat{\phi}\hat{\phi}} = \Big\langle C_L^{\hat{\phi}\hat{\phi}} \left[\bar{\boldsymbol{X}}_{\mathrm{MC}_1^{\phi_1}}, \bar{\boldsymbol{X}}_{\mathrm{MC}_2^{\phi_2}}, \bar{\boldsymbol{X}}_{\mathrm{MC}_2^{\phi_2}}, \bar{\boldsymbol{X}}_{\mathrm{MC}_1^{\phi_1}} \right] \\ + C_L^{\hat{\phi}\hat{\phi}} \left[\bar{\boldsymbol{X}}_{\mathrm{MC}_1^{\phi_1}}, \bar{\boldsymbol{X}}_{\mathrm{MC}_2^{\phi_2}}, \bar{\boldsymbol{X}}_{\mathrm{MC}_1^{\phi_1}}, \bar{\boldsymbol{X}}_{\mathrm{MC}_2^{\phi_2}} \right] \Big\rangle_{\mathrm{MC}_1,\mathrm{MC}_2}. \end{aligned}$$

Likewise, we subtract the signal-dependent ${}^{\rm (MC)}N_{1,L}^{\hat{\phi}\hat{\phi}}$ bias estimated using [144, 153]

$$\begin{aligned} {}^{\rm (MC)}N_{1,L}^{\hat{\phi}\hat{\phi}} = \Big\langle C_L^{\hat{\phi}\hat{\phi}} \left[\bar{\boldsymbol{X}}_{\mathrm{MC}_1^{\phi_1}}, \bar{\boldsymbol{X}}_{\mathrm{MC}_2^{\phi_1}}, \bar{\boldsymbol{X}}_{\mathrm{MC}_1^{\phi_1}}, \bar{\boldsymbol{X}}_{\mathrm{MC}_2^{\phi_1}} \right] \\ + C_L^{\hat{\phi}\hat{\phi}} \left[\bar{\boldsymbol{X}}_{\mathrm{MC}_1^{\phi_1}}, \bar{\boldsymbol{X}}_{\mathrm{MC}_2^{\phi_1}}, \bar{\boldsymbol{X}}_{\mathrm{MC}_2^{\phi_1}}, \bar{\boldsymbol{X}}_{\mathrm{MC}_1^{\phi_1}} \right] \\ - C_L^{\hat{\phi}\hat{\phi}} \left[\bar{\boldsymbol{X}}_{\mathrm{MC}_1^{\phi_1}}, \bar{\boldsymbol{X}}_{\mathrm{MC}_2^{\phi_2}}, \bar{\boldsymbol{X}}_{\mathrm{MC}_2^{\phi_2}}, \bar{\boldsymbol{X}}_{\mathrm{MC}_1^{\phi_1}} \right] \\ - C_L^{\hat{\phi}\hat{\phi}} \left[\bar{\boldsymbol{X}}_{\mathrm{MC}_1^{\phi_1}}, \bar{\boldsymbol{X}}_{\mathrm{MC}_2^{\phi_2}}, \bar{\boldsymbol{X}}_{\mathrm{MC}_1^{\phi_1}}, \bar{\boldsymbol{X}}_{\mathrm{MC}_2^{\phi_2}} \right] \Big\rangle_{\mathrm{MC}_1,\mathrm{MC}_2}, \end{aligned} \tag{2.11}$$

where we use noise-free (beamed) CMB simulations, and in the first two terms each pair of MC simulations in the average have the same lensing field ϕ_1, while the last two terms constitute a (negative) instrumental noise-free ${}^{\rm (MC)}N_{0,L}$. When analysing data maps (instead of simulations), using the realization-dependent (RD) $N_{0,L}$ will account for fluctuations in realization power and correct for small errors in the assumed fiducial spectrum [98, 153, 173]. We do not use ${}^{\rm (RD)}N_{0,L}$ here since it is numerically expensive to calculate for 500 "data" simulations, but we do not expect that this would change our main results, which are based on comparisons between variances of

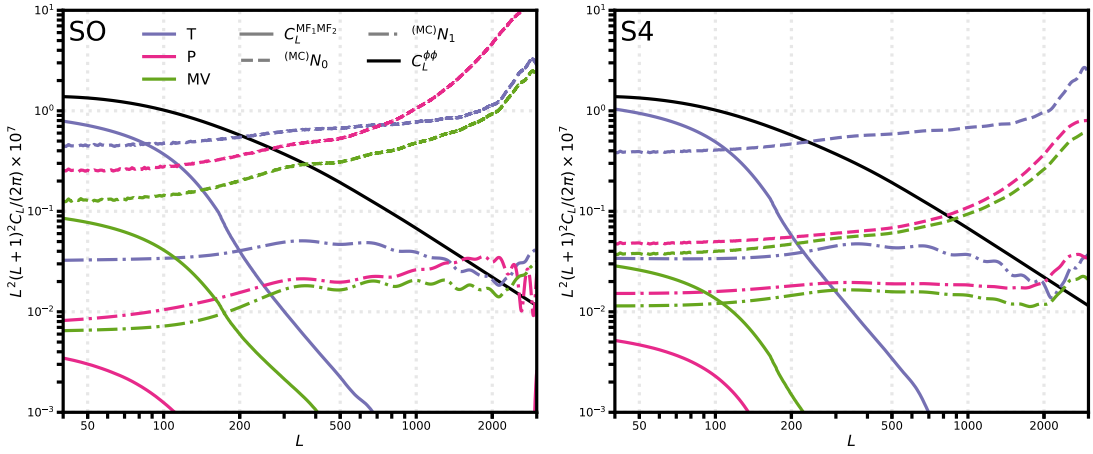

Figure 2.4: Mean field power spectrum $C_L^{\mathrm{MF_1MF_2}}$ (solid lines), reconstruction noise $^{(\mathrm{MC})}N_{0,L}$ (dashed lines) and $^{(\mathrm{MC})}N_{1,L}$ bias (dot-dashed lines) for anisotropic-filtering analyses of temperature (green), polarization (pink) and temperature+polarization (purple) for SO (left) and S4 (right). The theory $C_L^{\phi\phi}$ curve (black) is shown to indicate which biases dominate the reconstruction and over which L range. The MF power is the cross-correlation of the two MF values (each was obtained using 50 different simulations). The MF curves were smoothed for aesthetics, while the smoothed $^{(\mathrm{MC})}N_{1,L}$ shown is used in the pipeline for debiasing the reconstructed spectrum. The $N_{0,L}$ and $N_{1,L}$ curves shown for S4 are analytic using the effective noise level shown in Table 2.1.

different reconstruction methods.

The resulting power spectrum estimate is then

$$\hat{C}_L^{\phi\phi} \equiv C_L^{\hat{\phi}_1\hat{\phi}_2} - {}^{(\mathrm{MC})}N_{0,L}^{\hat{\phi}\hat{\phi}} - {}^{(\mathrm{MC})}N_{1,L}^{\hat{\phi}\hat{\phi}}. \tag{2.12}$$

The de-biasing components are shown in Fig. 2.4 for SO- and S4-like experiments using $(\ell_{\mathrm{min}}, \ell_{\mathrm{max}}) = (40, 3000)$ of the filtered CMB maps. We see that the temperature noise $N_{0,L}$ is similar for both SO and S4 (though this may change if a larger ℓ-range is considered for S4). However, the S4 lensing reconstruction benefits much more from using polarization where the reconstruction is signal-dominated for a larger L-range. We also see the importance of MF subtraction on large scales in the presence of anisotropic noise, especially for lensing reconstructions using temperature.

2.3 APPROXIMATE ANALYTIC MODEL

In the case of full sky and isotropic noise, the QE of Eq. (2.3) simplifies considerably and we can obtain analytic results. For harmonic-space field combinations

$$\boldsymbol{X} \in \begin{cases} T & \mathrm{T} \\ (E,B) & \mathrm{P} \\ (T,E,B) & \mathrm{MV} \end{cases} \tag{2.13}$$

the estimator can be written as [145]

$$\hat{\phi}(\mathbf{L}) \equiv \left(\mathcal{R}_L^{\phi}\right)^{-1} \int \frac{d^2\boldsymbol{\ell}}{(2\pi)^2} \boldsymbol{X}(\boldsymbol{\ell}-\mathbf{L})^{\dagger} \boldsymbol{F}_X(\boldsymbol{\ell}, \boldsymbol{\ell}-\mathbf{L}) \boldsymbol{X}(\boldsymbol{\ell}), \tag{2.14}$$

where $\boldsymbol{F}_X(\boldsymbol{\ell}, \boldsymbol{\ell}-\mathbf{L})$ collects the optimized filter and QE weights [145]. The normalization (response) $\mathcal{R}_L^{\phi}$ is diagonal in harmonic space, and to obtain an unbiased estimator for cross-correlation with the true field the normalization is given by

$$\mathcal{R}_L^{\phi} = \int \frac{d^2\boldsymbol{\ell}}{(2\pi)^2} \mathrm{Tr}\left[\boldsymbol{F}_X(\boldsymbol{\ell}, \boldsymbol{\ell}-\mathbf{L}) \boldsymbol{f}_X(\boldsymbol{\ell}, \boldsymbol{\ell}-\mathbf{L})\right], \tag{2.15}$$

where the mode response functions $\boldsymbol{f}_X$ are defined by

$$\left\langle \frac{\delta}{\delta\phi(\mathbf{L})} \left(\boldsymbol{X}(\boldsymbol{\ell}_1)\boldsymbol{X}(\boldsymbol{\ell}_2)^{\dagger}\right) \right\rangle = \delta(\boldsymbol{\ell}_1 - \boldsymbol{\ell}_2 - \mathbf{L}) \boldsymbol{f}_X(\boldsymbol{\ell}_1, -\boldsymbol{\ell}_2). \tag{2.16}$$

We use gradient spectra to calculate the components of the mode response functions $\boldsymbol{f}_X(\boldsymbol{\ell}_1, \boldsymbol{\ell}_2)$ following Refs. [146] and [164], and all theory power spectra were obtained from CAMB[7] [113]. Note that the response is related to the reconstruction noise by $\mathcal{R}_L \sim N_{0,L}^{-1}$ [145], but without exact equality here because of the use of gradient rather than lensed spectra in the mode response functions $\boldsymbol{f}_X$.

In the presence of anisotropic noise and optimal filtering, the above results no longer hold, but we can still predict the lensing spectrum's normalization fairly accurately using the simple independent-patch approximation. The lensing convergence QEs are all quasi-local, in that the lensing field estimated at $\mathbf{x}$ depends mostly on nearby pixels of the CMB fields where the noise level is similar if the noise is slowly varying.

Dividing the sky into patches p with different approximately constant noise levels, we can define a local (correctly-normalized) isotropic estimator $\hat{\phi}^p_{\mathbf{L}}$ in each patch using the appropriate local noise level. The full filtered estimators all locally provide estimators of the same lensing field, but have different local normalizations. We can therefore write the estimators approximately as

$$\hat{\phi}_{\mathbf{L}} \simeq \sum_p w_L^p \hat{\phi}^p_{\mathbf{L}}, \tag{2.17}$$

where w_L^p is a local normalization for patch p and $\hat{\phi}^p_{\mathbf{L}}$ is taken to vanish outside patch p. Hence,

[7] https://camb.info

approximating the patches as uncorrelated, the power spectrum estimator of Eq. (2.10) becomes

$$\begin{aligned} C_L^{\hat{\phi}\hat{\phi}} &\simeq \frac{1}{f_{A,L} n_L} \sum_p \sum_{\boldsymbol{\ell} \text{ in } \mathbf{L} \text{ bin}} (w_L^p)^2 \hat{\phi}_{\boldsymbol{\ell}}^p \hat{\phi}_{\boldsymbol{\ell}}^{p*} \\ &\simeq \frac{1}{f_{A,L}} \sum_p (w_L^p)^2 f_p \hat{C}_L^{\phi^p \phi^p}, \end{aligned} \tag{2.18}$$

where $\hat{C}_L^{\phi^p\phi^p}$ is the normalized power spectrum estimator over patch p and f_p is the fraction of the map area in patch p. To be correctly normalized after bias subtraction, this implies

$$f_{A,L} \simeq \sum_p f_p (w_L^p)^2, \tag{2.19}$$

which gives our analytic patch approximation for the estimator normalization. In the case of isotropic filtering with a simple binary mask, $f_{A,L}$ reduces to the fraction of the map area that is unmasked. The estimator is quadratic in the CMB fields, so when the filtering is an apodized mask or local weighting $W(\mathbf{x})$, the local estimator normalization is just the square of the corresponding CMB map weight function, $w_L^p = [W(\mathbf{x}^p)]^2$. The normalization $f_{A,L}$ then defines an L-independent effective map area fraction [178].[8] In the case of the cross-correlation power spectrum $C_L^{\hat{\phi}\phi}$, the corresponding normalization to be unbiased is instead

$$f_{A,L}^{\text{cross}} \simeq \sum_p f_p w_L^p. \tag{2.20}$$

For the case of optimal anisotropic filtering, each patch is effectively locally isotropically filtered using the appropriate local noise level. Since in Eq. (2.7) we applied a single fiducial response $\mathcal{R}_L^{\phi,\text{fid}}$ (with a different, somewhat arbitrary, fiducial noise level), the local estimate in a patch centred on $\mathbf{x}^p$ is biased by an L-dependent factor

$$w_L^p = \frac{\mathcal{R}_L^{\phi,p}}{\mathcal{R}_L^{\phi,\text{fid}}}, \tag{2.21}$$

where $\mathcal{R}_L^{\phi,p}$ is the true response according to the local noise levels in patch p [100]. Since $\mathcal{R}_L^{\phi,p}$ is easily calculated analytically for each patch using Eq. (2.15), this provides an approximate analytical normalization for the optimally-filtered estimator.

[8] In our case, this effective area fraction equals to 0.13 and 0.03 when we mask and weight the maps respectively (corresponding to effective full-sky fractions $f_{\text{sky}} \approx 0.04$ and 0.01); for the cross-correlation cases $f_{A,L}$ becomes 0.14 and 0.06 respectively.

Fully optimal κ-filtering would give

$$w_L^p = \frac{C^{\kappa\kappa}_{L,\rm fid}}{C^{\kappa\kappa}_{L,\rm fid} + N^{\kappa,p}_{0,L}}, \tag{2.22}$$

so that each correctly normalized patch is appropriately Wiener-filtered. Our approximate κ-filtering instead first approximately locally normalizes the optimally-filtered reconstruction map using $\mathcal{R}^{\kappa}_{\rm eff}$, and then approximately Wiener filters it with white noise $N^{\kappa}_{{\rm eff},L}$ giving

$$w_L^p = \frac{C^{\kappa\kappa}_{L,\rm fid}}{C^{\kappa\kappa}_{L,\rm fid} + N^{\kappa,p}_{0,\rm eff}} \frac{\mathcal{R}^{\kappa,p}_L}{\mathcal{R}^{\kappa,p}_{\rm eff}}. \tag{2.23}$$

The patch approximation is reminiscent of the patch lensing estimator of Ref. [180], where the authors combine lensing estimators on patches with different noise levels to optimize the signal. However, our patch approximation is only used for approximate theoretical modelling of the responses and to motivate the κ-filtering step using a locally defined effective lensing reconstruction noise. Our estimator is continuous on the observed sky, so we do not have to deal with complexities related to actually dividing the CMB maps into patches, and it should also handle filtering for mask and noise variation more accurately. Ref. [181] also combine different patches, however their motivation is different, being focussed on how to combine observations from different overlapping experiments.

In Fig. 2.5, we compare the analytic correction $f_{A,L}$ (obtained using 160 patches in our baseline analysis, but we find the same results if we use 10 times fewer patches) with the required correction as determined from 500 MC simulations. The analytic estimate agrees well with the MC result on most scales with a slight deviation at low-L (where the patch approximation is expected to break down because the real-space lensing mode size becomes comparable to the scale of variation of the noise). Similar-size MC corrections have been seen in previous analyses [100]. Improving the tolerance level for convergence of the conjugate-gradient filtering does not improve this consistency: at low-L the fractional difference of the ϕ power spectra between a tolerance of 10^{-5} and 10^{-6} for the temperature map is $\lesssim 0.1\%$. The number of patches we used to obtain the analytic correction is converged, with more patches changing the result by $\lesssim 0.1\%$.

Fig. 2.5 shows that the $f_{A,L}$ estimates are in good agreement with simulations for $100 \lesssim L \lesssim 1500$. To correct for the remaining inconsistency of the reconstructed power compared to the theory spectrum, especially at low-L, an additional small MC correction can be applied to obtain the unbiased lensing power. Fig. 2.6 shows that the additive MC correction is close to zero over the above multipole range, and is a small but important correction elsewhere. This correction is

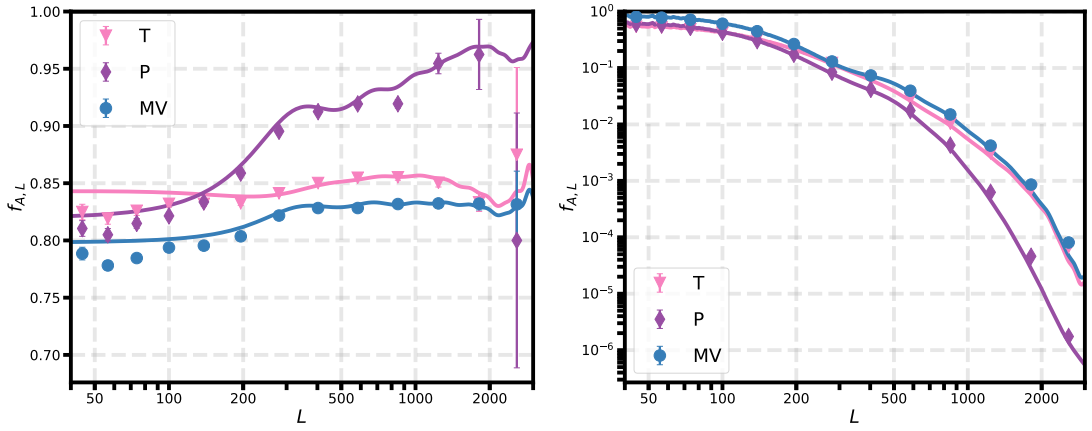

Figure 2.5: Comparison between the approximate analytic $f_{A,L}$ normalization (lines) and Monte Carlo normalization (markers) required to obtain unbiased lensing reconstruction power spectra from SO-like simulations. The left plot shows the result for just optimally filtering the input CMB maps (Eq. (2.19)+(2.21)), which is close to unity on all scales; its magnitude shows how close $\mathcal{R}_L^{\phi,\mathrm{fid}}$ is to the true response. The right plot shows the result for the estimator which is also κ-filtered (Eq. (2.19)+(2.23)), which spans many orders of magnitude due to its dependence on $C/(C+N)$ (which goes to zero on small scales but near unity on large scales). A discrepancy with the analytic result is evident on large scales for both results; the discrepancy for the κ-filtered case is shown more clearly by the additional final MC correction shown in Fig. 2.6.

obtained by adding $C^{\phi\phi}_{L,\mathrm{fid}} - \left\langle \hat{C}^{\phi\phi}_L \right\rangle$ to the reconstructed power as a final debiasing step. Since the MC correction is small, it is likely to be a good approximation to neglect its dependence on the fiducial theoretical model.

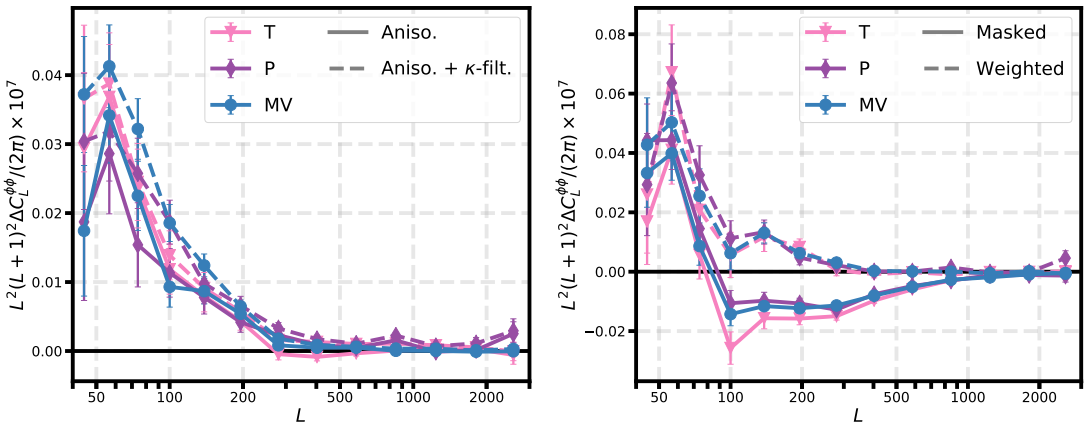

Figure 2.6: The additive MC correction required after applying analytic $f_{A,L}$ normalization for reconstruction using anisotropic filtering and combined with κ-filtering (left) and using the two isotropic filtering methods (right) from SO-like simulations. The MC correction for all methods is relatively small. We use this additional MC correction when plotting the final reconstruction variances in Fig. 2.9.

The patch approximation could also be used to obtain analytic predictions for $N_{0,L}$ and $N_{1,L}$ and then use them to debias the lensing power instead of using the MC versions. It was shown in Ref. [100] that the analytic patch $N_{1,L}$ is in good agreement with ${}^{(\mathrm{MC})}N_{1,L}$ in the case of Planck. However, an MC result is required to make a reliable assessment of accuracy. In the case of $N_{0,L}$, an accurate result is critical to obtain an unbiased power spectrum: if the approximation were wrong by a few percent that would translate to a large power spectrum bias on small scales, so an accurate MC result should be used rather than the approximation. On real data, the

realization-dependent ${}^{(\mathrm{RD})}N_{0,L}$ would also reduce the variance and correct leading-order sensitivity to inaccuracies in the simulations [173]. The analytic approximations should however be accurate enough to account for the model dependence of the spectra and hence construct a likelihood by straightforward generalization of the linear correction method developed by Ref. [98].

We can also use the patch approximation to assess the variance of the different estimators. The variance of the unbiased estimator $\hat{C}_L^{\phi^p\phi^p}$ measured only over patch p is given approximately by the Gaussian result

$$\mathrm{Var}\left(\hat{C}_L^{\phi^p\phi^p}\right) \approx \frac{2(C_L^{\phi\phi}+N_{0,L}^p)^2}{f_p n_L}, \tag{2.24}$$

where we neglect contributions to the variance from $N_{1,L}$ variance (which could become important on small scales) and a p index indicates the value in a patch with corresponding local noise value. Using Eq. (2.18) and again taking the patches to be uncorrelated we then have

$$\mathrm{Var}\left(\hat{C}_L^{\phi\phi}\right) \simeq \frac{1}{[f_{A,L}]^2}\sum_p \frac{2(C_L^{\phi\phi}+N_{0,L}^p)^2}{n_L} f_p (w_L^p)^4, \tag{2.25}$$

which is approximately reduced by a factor ΔL for bins of width ΔL centred at L.

Without κ-filtering the expected (binned) power variance from optimally filtering the CMB maps is then

$$\mathrm{Var}\left(\hat{C}_L^{\kappa\kappa}\right) = \frac{\sum_p \frac{2(C_L^{\kappa\kappa}+N_{0,L}^{\kappa,p})^2}{\Delta L n_L} f_p \left(\frac{\mathcal{R}_L^{\kappa,p}}{\mathcal{R}_L^{\kappa,\mathrm{fid}}}\right)^4}{\left[\sum_p f_p \left(\frac{\mathcal{R}_L^{\kappa,p}}{\mathcal{R}_L^{\kappa,\mathrm{fid}}}\right)^2\right]^2}. \tag{2.26}$$

The best-case expected variance after filtering κ using the ideal full L-dependency of $N_{0,L}^\kappa$ is

$$\mathrm{Var}\left(\hat{C}_{L,\mathrm{filt}}^{\kappa\kappa}\right) = \frac{\sum_p \frac{2(C_L^{\kappa\kappa}+N_{0,L}^{\kappa,p})^2}{\Delta L n_L} f_p \left(\frac{C_{L,\mathrm{fid}}^{\kappa\kappa}}{C_{L,\mathrm{fid}}^{\kappa\kappa}+N_{0,L}^{\kappa,p}}\right)^4}{\left[\sum_p f_p \left(\frac{C_{L,\mathrm{fid}}^{\kappa\kappa}}{C_{L,\mathrm{fid}}^{\kappa\kappa}+N_{0,L}^{\kappa,p}}\right)^2\right]^2}. \tag{2.27}$$

Instead, using the effective noise level (which is what we use in practice), the expected variance becomes (from Eq. (2.23))

$$\mathrm{Var}\left(\hat{C}_{L,\mathrm{filt}}^{\kappa\kappa}\right) = \frac{\sum_p \frac{2(C_L^{\kappa\kappa}+N_{0,L}^{\kappa,p})^2}{\Delta L n_L} f_p \left(\frac{\mathcal{R}_L^{\kappa,p}}{\mathcal{R}_{\mathrm{eff}}^{\kappa,p}}\right)^4 \left(\frac{C_{L,\mathrm{fid}}^{\kappa\kappa}}{C_{L,\mathrm{fid}}^{\kappa\kappa}+N_{0,\mathrm{eff}}^{\kappa,p}}\right)^4}{\left[\sum_p f_p \left(\frac{\mathcal{R}_L^{\kappa,p}}{\mathcal{R}_{\mathrm{eff}}^{\kappa,p}}\right)^2 \left(\frac{C_{L,\mathrm{fid}}^{\kappa\kappa}}{C_{L,\mathrm{fid}}^{\kappa\kappa}+N_{0,\mathrm{eff}}^{\kappa,p}}\right)^2\right]^2}. \tag{2.28}$$

The fractional differences between the unfiltered variance and the two filtered variances are shown (in percent) in Fig. 2.7. The κ-filtering step significantly reduces the variance of the large-scale power spectrum, while having little effect on small scales where just optimally-filtering the CMB maps is already nearly optimal (because the local response is effectively automatically inverse-noise weighting, and inverse-noise weighting is optimal when the noise is large).

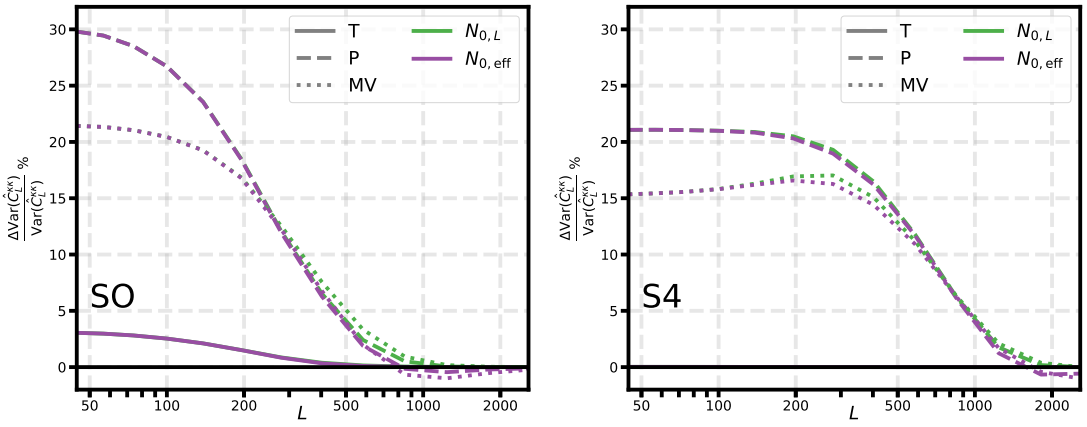

Figure 2.7: Fractional improvement in the theoretical binned variance of $\hat{C}_L^{\kappa\kappa}$ when using an additional κ-filtering step for an SO-like experiment (left) and an S4-like experiment (right), estimated using an analytic patch approximation with 64 patches. The green curves show the optimal result which would be obtained if we could locally filter with $N^p_{0,L}$ (Eq. (2.27)), while the purple curves show the very similar result from our approximate local normalization followed by filtering using an effective white reconstruction noise $N^{\kappa}_{0,\mathrm{eff}}(\mathbf{x})$ in the filter (Eq. (2.28)). The reconstruction from polarization alone benefits most from this additional filtering step since it is most affected by the noise anisotropy.

The improvement expected from κ-filtering depends on the CMB noise level relative to the signal, and is therefore different for temperature and polarization. For temperature analysis with our choice of ℓ_{max} the improvement for SO-like noise is small, and negligible for S4, since the CMB temperature is signal dominated in both cases (so the lensing responses are already nearly isotropic because the contribution from noise variance is small). For polarization the gains are significant because the polarization noise (and hence its anisotropy) is significant in both experiments, with a somewhat larger improvement for SO where the noise is relatively more important.

The impact of both filtering steps compared to other methods will depend on the specific hit count distribution and hence relative importance of noise variations. For larger areas (such as the survey areas available for lensing in SO and S4) the counts may be more or less anisotropic than in the patch we tested in detail, leading to somewhat larger or smaller overall gains respectively.

2.4 RESULTS

We now compare simulation-based lensing reconstruction results from the different filtering methods described in Sections 2.2.1 and 2.2.4. We compare power spectrum results from

applying an isotropic filter on masked or weighted CMB maps, as used by several previous experiments, to applying an optimal anisotropic filtering with or without also filtering the reconstructed κ map. The reconstructions were made from simulations with SO- and S4-like noise and beam while for simplicity considering the same scanning strategy, corresponding to a sky fraction of $f_{\rm sky} = 0.13$ and strongly anisotropic hit count map shown in Fig. 2.2. The instrument sensitivities, (effective) noise levels, beam widths and observation time considered for each experiment are given in Table 2.1. We assume an observation efficiency of $1/5$ for both experiments, and each simulation has 4096 pixels on a side with 1.7 arcminute pixel size.

Experiment	s_T [μK-$\sqrt{\rm sec}$]	Δ_T [μK-arcmin]	$\theta_{\rm FWHM}$ [arcmin]	$t_{\rm obs}$ [years]
SO	6.7	5.0	1.4	5
S4	1.5	1.0	1.5	7

Table 2.1: Experimental specifications for our SO- and S4-like simulations. The Δ_T effective map-level sensitivity is not used for the simulations, but obtained from the power spectrum of weighted noise map realizations. The value of SO's temperature sensitivity s_T is the LAT 'baseline' level for 145 GHz from [131] and the corresponding Δ_T is the result from the specific hit count map considered. For S4, on the other hand, we determined the sensitivity for 145 GHz so that Δ_T results in the forecast value from [133, 135][9]. Polarization sensitivity is taken to be $\Delta_P = \sqrt{2}\Delta_T$. We consider the same scanning time efficiency of $1/5$ and (post-filtering) CMB multiple range $(\ell_{\rm min}, \ell_{\rm max}) = (40, 3000)$ for both experiments.

We perform lensing reconstructions from different field combinations, T, P, and MV, using 500 simulations, from which we calculate the reconstruction variances and the cross-correlation coefficients with the input lensing map.

The reconstructed power before applying an additive MC correction is shown in Fig. 2.8 from SO using P and MV, and from S4 using P. These spectra were obtained using the optimal anisotropic filter followed by filtering the reconstructed κ map, and demonstrate that the analytic patch normalization described in Sec. 2.3 is accurate to the percent level. Comparing the two SO power spectra, we see that while the low-L bias is relatively similar as expected (as this results from the mask/scan area), the high-L bias is much less significant for MV, most likely due to the contribution from the signal-dominated T. To obtain the unbiased spectra, we apply small additional MC corrections. These additional corrections are shown in Fig. 2.6, and for both experiments are smaller than 3%.

The unbiased lensing reconstruction power spectra variances for the various filtering methods are shown in Fig. 2.9. As expected, lower variances are achieved when using both temperature and polarization maps for the reconstruction. For reconstructions using temperature, the optimal anisotropic filter yields an improvement in variance by a factor of 2-5 compared to isotropic filtering a masked or weighted map, though the level of improvement does depend on the mask

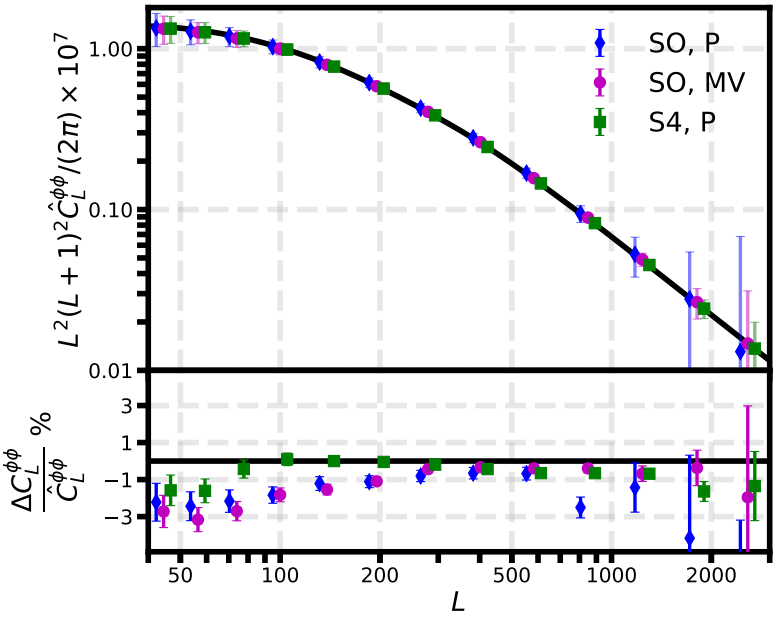

Figure 2.8: Simulated lensing potential reconstruction power spectrum and residuals from optimal anisotropic filtering of the CMB maps and approximate κ-filtering, for the SO MV estimator (magenta) and using only polarization maps for SO (blue) and S4 (green). An MC correction can be further applied to get the final unbiased power; see Fig. 2.6. The opaque error bars in the residual plot are the MC errors expected from the average of 500 simulations, while the translucent error bars in the upper panel are the latter scaled by $\sqrt{500}$ to show the uncertainty for one lensing realization (points offset for clarity, and errors slightly underestimated on small scales because we neglect the ${}^{(\mathrm{MC})}N_{1,L}$ MC error).

chosen for the isotropic-filtering analysis. The improvement is smaller for a polarization-only reconstruction where reconstruction noise rather than cosmic variance is relatively more important near the edges of the scanned area. The isotropic filtering results depend both on the noise level used in the isotropic filter, which was chosen to minimise the variance, and (in the masked case) also the masked area actually used (to reduce variance from very noisy areas near the edge). We did not optimize the mask area, but testing with several sensible masking schemes showed no large variance improvement. Compared to the isotropic filtering methods, the optimal and κ-filtering methods have fewer free parameters, and varying these only has a small effect on results, which are already close to optimal.

The difference plots in Fig. 2.9 show the further fractional improvement in variance after applying our approximate additional κ reconstruction filtering. Results agree well with the predicted theoretical curves shown in Fig. 2.7, demonstrating that the patch approximation is capturing the main effect well. The predicted $\sim$30% reduction in variance on large scales is therefore achievable in practice, at only a small additional numerical cost.

We also compare some reconstructed real-space lensing maps from the various reconstruction method. Fig. 2.10 shows the input α map (where $\alpha_{\mathbf{L}} = \sqrt{L(L+1)}\,\phi_{\mathbf{L}}$) of one simulation in comparison to the MV reconstruction maps using the same lensing realization with the various different filtering methods. Qualitatively, all maps demonstrate a good reconstruction in the low-

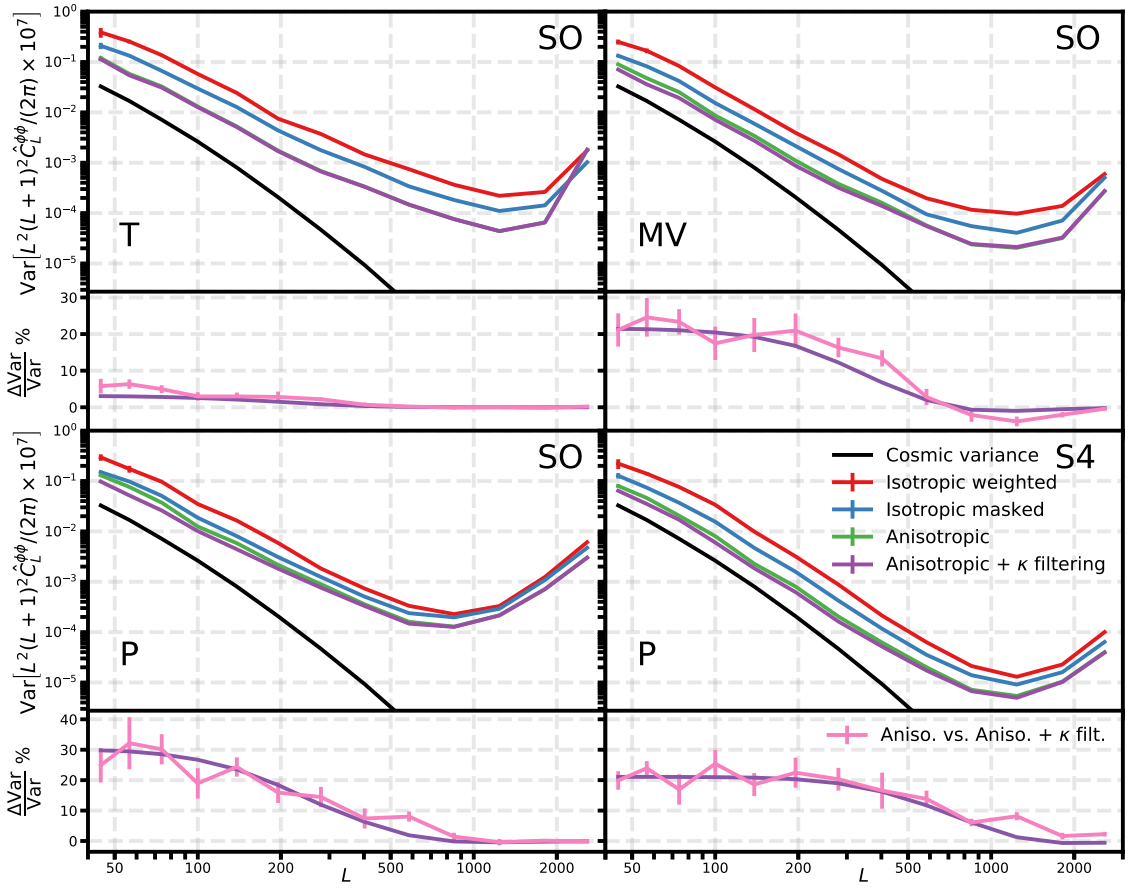

Figure 2.9: Reconstructed lensing power spectrum variances from the various filtering methods for an SO-like experiment and an S4-like experiment (bottom right). The error bars on the variance and the fractional differences were estimated using 10 sub-batches of variance estimates. The black curve is the cosmic variance for the lensing power shown as a reference for the minimal variance we could obtain with no noise over the entire scanned area. Using the optimal anisotropic filter leads to variance improvements by a factor of 2-5 for most of the considered L-range compared to considering isotropic filtering over a reduced sky area. The improvement is largest for reconstructions using polarization, which is less signal-dominated than temperature. The lower panels of each plot show the fractional difference between reconstruction variances with and without additional κ reconstruction filtering (pink), plotted against the corresponding theoretical curves from Fig. 2.7 (purple lines), demonstrating good agreement with the approximate analytic model. For S4, polarization dominates the reconstruction, so we only show the polarization results.

noise pixels near the centre of the patch that have longer observation times. Isotropic filtering on weighted maps significantly down-weights the reconstruction in the higher-noise pixels, while the reconstruction from masked maps only down-weights around the edges of the mask (however the effective area is reduced due to the mask excluding high noise pixels). When applying the optimal anisotropic filter, we reconstruct the lensing potential on most of the scanned region giving lower power spectrum variance. Applying the further κ-filtering step on the locally normalized map removes the effective down-weighting around the edges of the scanned sky area, which can explain the variance improvements we see at low-L where the reconstruction is signal-dominated.

We then calculate the cross-correlation coefficients with the input lensing map,

$$\hat{\rho}_L \equiv \frac{C_L^{\hat{\phi}\phi}}{\sqrt{C_L^{\hat{\phi}\hat{\phi}} C_L^{\phi\phi}}}. \tag{2.29}$$

The cross-correlation coefficients of the SO reconstructions are shown in Fig. 2.11. We see an improved correlation after filtering the reconstructed κ map compared to only anisotropically filtering the CMB maps. This improvement is most visible for the signal-dominated regime at $L \lesssim 300$. The lensing reconstruction from the isotropic filtering process is done over a smaller effective area, in which the signal-to-noise is already high, so the cross-correlation coefficient restricted to that area is higher (over the same area the more optimal methods would also give substantially higher cross-correlation coefficients).

2.5 CONCLUSIONS

In this chapter we demonstrated the importance of optimizing the reconstruction pipeline to minimize the lensing spectrum variance when sky maps have anisotropic noise. We showed that optimal CMB map filtering can have significant gains compared to simple isotropic filtering (a factor of 2-5 decrease in variance for our choice of masking on the configurations tested).

Lensing reconstructions using optimally filtered maps are effectively inverse-noise weighted because the normalization response is directly related to the reconstruction noise in simple cases. This weighting is nearly optimal for the power spectrum on small scales where the reconstruction is noise dominated, however it is significantly suboptimal on larger scales where lensing modes are reconstructed with high signal-to-noise. We showed that an additional approximate κ-reconstruction filtering stage can significantly improve the variance of power spectrum estimates in the signal dominated regime on large scales, while also smoothly approaching close to the original optimal result on small scales. The anisotropic filtering performs well for both SO- and S4-like noise levels, and for the specific anisotropic noise we tested the κ filtering step reduces the variance by about 30% on large scales. Our optimal filtering steps use a conjugate gradient approach, making the optimized estimators easily numerically tractable (but still somewhat numerically expensive; there is potential for further gains using other methods, e.g. filtering using a pre-trained neutral network [182]).

We used a flat-sky analysis, but do not expect our results to be significantly different when applying to a full-sky lensing reconstruction, though developing a full-sky analysis is clearly a requirement for analysis of realistic data over large sky areas. We also considered only a single frequency map and ignored the complication of foreground residual modelling. The relative improvements that we have shown should however still remain valid as they only depend on the overall broad distribution of the map hit counts. Realistic ground-based data also usually has

[9]Reference design is also available at https://cmb-s4.org/wiki/index.php/Expected_Survey_Performance_for_Science_Forecasting.

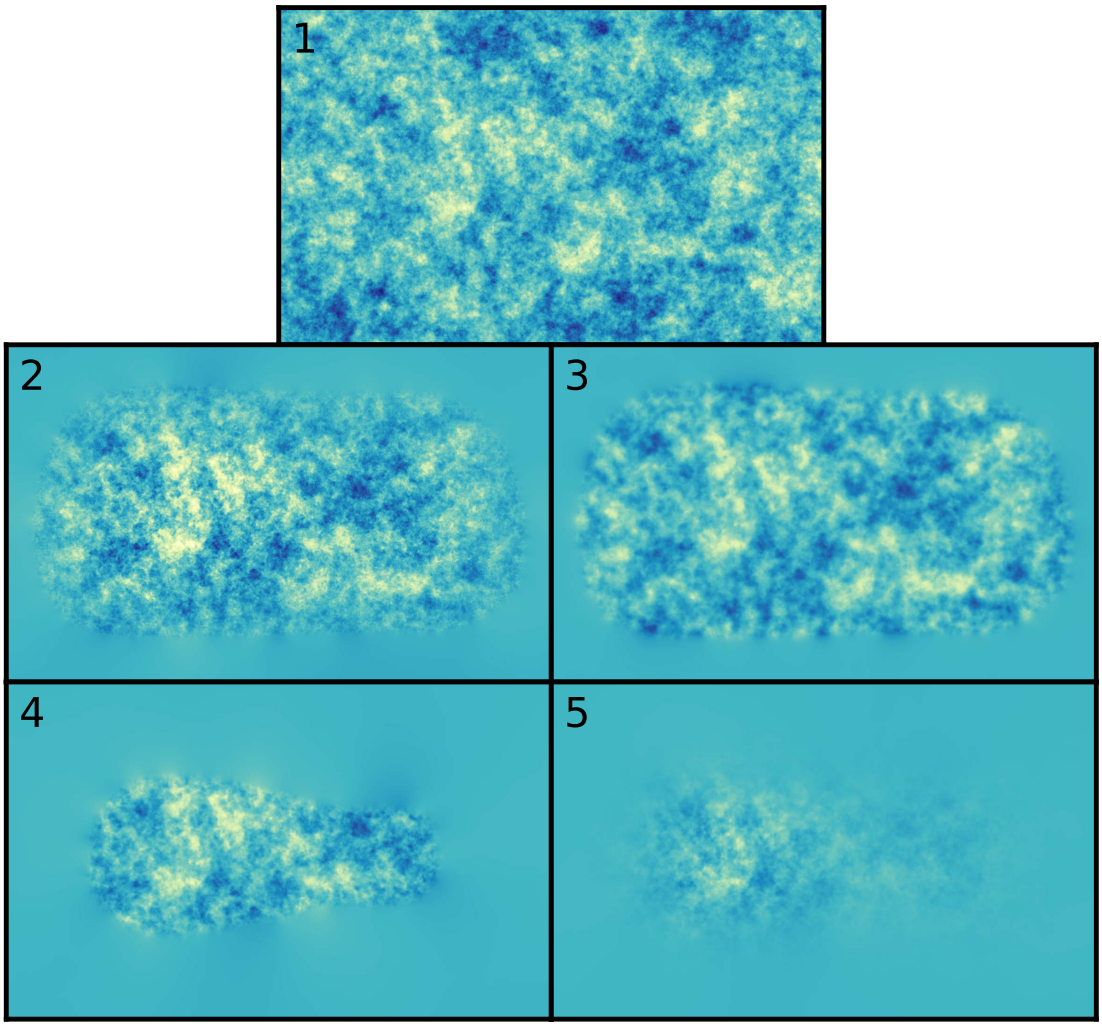

Figure 2.10: **1**: Input deflection α map of one of the realizations used (where $\alpha_{\mathbf{L}} = \sqrt{L(L+1)}\,\phi_{\mathbf{L}}$). **2**: The Wiener-filtered reconstructed α obtained when applying an optimal anisotropic filter to the temperature and polarization maps. The map is normalized using a fiducial isotropic normalization $\mathcal{R}_L^{\rm fid}$, where the specific choice of effective isotropic noise chosen has some impact on the map, and the isotropic WF applies $\frac{C^{\phi\phi}_{L,\rm fid}}{C^{\phi\phi}_{L,\rm fid}+{}^{\rm (MC)}N^{\phi}_{0,L}}$ to $\hat{\phi}_{\mathbf{L}}$. **3**: The α reconstruction map from applying a further anisotropic filter on the optimally-reconstructed κ map after approximate local normalization. The approximate white local normalization improves the match to the input near the patch boundaries, but underweights small scales compared to the true normalization ($\mathcal{R}^{\kappa}_L \sim {N^{\kappa}_{0,L}}^{-1}$ falls at high L compared to fixed value we chose that matches on large scales), so this map appears smoother. This is corrected at the power spectrum level by the analytic patch normalization correction. **4**: The Wiener-filtered reconstructed α map using an isotropic filter on a masked map. The same WF as in panel 2 is applied with the respective ${}^{\rm (MC)}N^{\phi}_{0,L}$. **5**: The Wiener-filtered reconstructed α map using an isotropic filter on a weighted map. The same WF as in panel 2 is applied with the respective ${}^{\rm (MC)}N^{\phi}_{0,L}$. All reconstructed maps are from the same lensing potential realization, and show the same colour ranges as the input map.

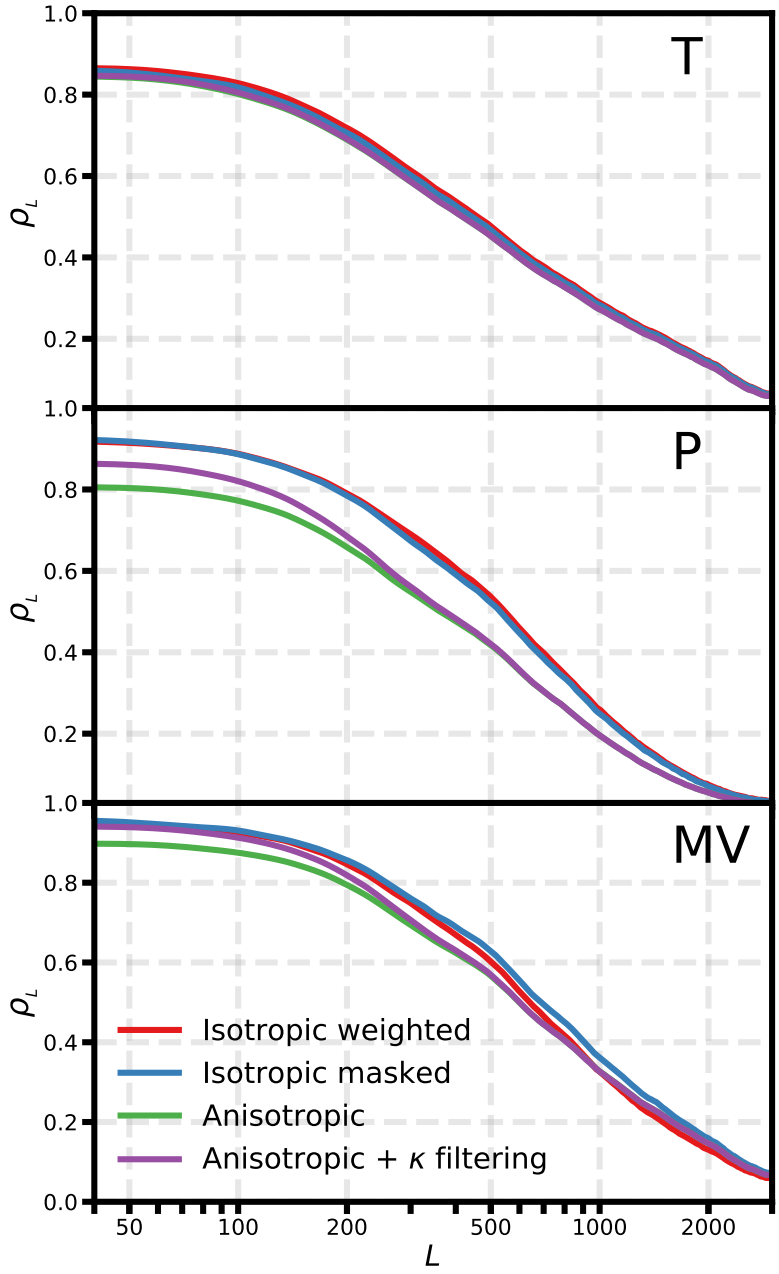

Figure 2.11: Cross-correlation coefficients (Eq. (2.29)) for the various reconstruction methods and an SO-like experiment. The curves were smoothed with a $\sigma_L = 12$ width Gaussian to reduce sampling noise. The best reconstruction is made from a combined analysis of temperature and polarization maps (MV). The improvement due to the additional κ-filtering step when using anisotropic filter on the CMB maps is mostly visible for $L \lesssim 200$. The most correlated maps are those obtained from applying an isotropic filter over a reduced sky area, but this reduced sky area loses information compared to other methods using the full observed area.

strongly correlated noise, making full signal-plus-noise filtering substantially more challenging; however, the amplitude of the noise would still follow the broad hit count distribution, so the uncorrelated noise approximation that we made may still be sufficient to obtain significant gains compared to less optimized estimators. Further work would be needed to study the best way to filter correlated noise in practice.

The fast optimized QE lensing pipeline presented in this work can easily be run on many

simulations, and so may prove valuable for quantifying the impact of systematics, foregrounds, and other effects that can be simulated on lensing reconstruction. The effect of several potentially dangerous systematics will be explored in Chapter 3. The simple but accurate analytic patch approximations results may also prove valuable for optimization of observing strategies.

Although we have demonstrated significant gains compared to simple QE estimators, our results are clearly not fully optimal both because of approximations in the κ-filtering and because the estimator is still fundamentally quadratic. A likelihood based approach using iterative estimators [160, 161] could perform substantially better in the high signal-to-noise regime where quadratic estimators become suboptimal. However, a fully optimal power spectrum estimator applicable to realistic cut-sky data with inhomogeneous noise does not currently exist, and developing such an estimator would be an interesting avenue for future research. Comparison with a fully optimal estimator would allow us to assess gains compared to the approximate estimators we have presented. However, our approximate estimators are likely to still remain useful as they are fast to calculate and straightforward to approximately model analytically using the patch approximation.

CHAPTER 3

Instrumental systematics biases in CMB lensing reconstruction: a simulation-based assessment

MARK MIRMELSTEIN, GIULIO FABBIAN, ANTONY LEWIS, JULIEN PELOTON

Abstract

Weak gravitational lensing of the cosmic microwave background (CMB) is an important cosmological tool that allows us to learn about the structure, composition and evolution of the Universe. Upcoming CMB experiments, such as the Simons Observatory (SO), will provide high-resolution and low-noise CMB measurements. We consider the impact of instrumental systematics on the corresponding high-precision lensing reconstruction power spectrum measurements. We simulate CMB temperature and polarization maps for an SO-like instrument and potential scanning strategy, and explore systematics relating to beam asymmetries and offsets, boresight pointing, polarization angle, gain drifts, gain calibration and electric crosstalk. Our analysis shows that the majority of the biases induced by the systematics we modelled are below a detection level of $\sim 0.6\sigma$. We discuss potential mitigation techniques to further reduce the impact of the more significant systematics, and pave the way for future lensing-related systematics analyses.

3.1 INTRODUCTION

One of the main scientific objectives of upcoming cosmic microwave background (CMB) experiments is to measure the gravitational lensing of the CMB photons over a substantial sky area with the highest precision to date. This will enable us to better constrain dark energy models and inflation, provide more information on neutrino masses, and learn more about the large-scale

structure of the Universe up to high redshift. To achieve this from upcoming observations, it is crucial to understand how instrumental systematics could bias the lensing potential reconstruction. This challenge will be more important for future CMB experiments such as the Simons Observatory (SO) [131] and CMB-S4 [133], as small systematics become more significant with higher resolution and lower noise levels.

The ability to effectively reconstruct the lensing potential (see [142] for a review) from upcoming ground-based CMB experiments could be limited by various instrumental systematics. For example, systematics could induce lensing-like features in the CMB maps or act to effectively increase the reconstruction noise. Previous work in the literature has characterized the influence and potential significance of several systematics on lensing reconstruction [183–185]. However, these treatments have mostly used analytic approximations and idealized scanning strategies, rather than employing realistic instrument, scans, and modelling of systematics based on levels observed in real data. Several experiments have used a simulation-based approach to characterize residual systematic uncertainties, but focused on the CMB power spectra [40, 171, 186] or to guide the design of future instruments [e.g. 187]. The POLARBEAR collaboration has recently used a simulation-based approach to propagate residual systematics uncertainties in their latest lensing reconstruction measurements [188].

In this work, we adopt a similar end-to-end simulation approach to propagate the most common instrumental effects related to beam, calibration, pointing and readout electronics through to a lensing reconstruction analysis for a next-generation SO-like instrument. We assume a realistic amplitude for the modelled systematics, as observed in the current generation of experiments, or as expected for the next generation instruments given their design specifications. Our baseline reconstruction pipeline performs a semi-optimal treatment of noise inhomogeneities induced by the scanning strategies of ground-based experiments (see Chapter 2), however it does not automatically mitigate possible residual systematic biases. Using systematics-free Monte Carlo (MC) simulations to obtain the noise-debiasing terms for the CMB lensing power spectrum could lead to biases on real data. It is therefore crucial to understand the detailed behavior of systematics-induced biases and their potential significance for a more accurate lensing reconstruction, and to design mitigation strategies when required (for example, by including an accurate model of the most important effects in the corresponding MC simulations used in the lensing analysis). In this work, we focus on the CMB lensing power spectrum reconstruction, and do not consider the impact on other important analyses such as the delensing of CMB polarization. A more detailed study may be required for the delensing analysis, as small systematics-induced map-level effects could become relatively more important.

This chapter is structured as follows. We begin in Sec. 3.2 by describing how we model the instrumental systematics that we consider, and how these systematics affect the time-stream data simulations. Sec. 3.3 gives a short overview of the lensing reconstruction pipeline that we use to analyze our simulations. The systematics-induced biases and their significance on the CMB power spectra and the reconstructed lensing power spectrum are shown in Sec. 3.4. We discuss possible mitigation strategies in Sec. 3.5, and summarize our findings and future prospects in Sec. 3.6. Throughout this chapter we assume a Gaussian unlensed CMB model corresponding to a fiducial ΛCDM model with Planck-estimated parameters [31], and inhomogeneous but pixel-uncorrelated instrumental noise (e.g. neglecting $1/f$ noise from the atmosphere or from instrument electronics). We also do not attempt to model systematics that couple to foregrounds, and consider an experiment which is insensitive to the CMB temperature monopole and dipole. For the scanning strategy considered here, the latter are largely removed by the filtering usually employed on real data to handle slowly varying correlated $(1/f)$ noise induced by the atmosphere.

3.2 INSTRUMENTAL SYSTEMATICS SIMULATIONS

Due to the time dependency of the data acquisition chain of CMB experiments, the most accurate and natural way to include the effects of instrumental systematics is to inject them at the raw time-ordered data (TOD) level. For this purpose, and to construct sky maps from the simulated TOD, we use the public Python package `s4cmb`[1] [189]. This software, which is derived from the POLARBEAR data analysis systematics pipeline, has been used to perform a preliminary systematics study for SO [187, 190, 191], and to explore the effects of systematics on B-mode measurements on real data [171, 192]. Injecting systematics directly into the simulated detector-by-detector TOD allows us to explore a wider set of systematics in a more realistic way than other possible treatments of systematics (such as effective induced map-domain systematics), and includes their variation across the focal plane of the instrument.

We start by converting noise-free and beam-free CMB temperature and polarization realization maps, $\boldsymbol{s} = \{T, Q, U\}$, to TOD based on instrument specifications. The instrument (white) noise $\boldsymbol{n}$, instrument beam b, and systematics, are then injected into the TOD, which is then converted to temperature and polarization maps following a scanning strategy's pointing model. We can write the generated data time stream d_t for a specific time sample t as

$$d_t = T_t + Q_t \cos(2\psi_t) + U_t \sin(2\psi_t) + n_t, \tag{3.1}$$

[1] Available at https://github.com/JulienPeloton/s4cmb/.

where ψ is the polarization angle of the detector with respect to the sky coordinates, T_t, Q_t and U_t are the T, Q, U Stokes parameters of the CMB observed in the sky direction where the telescope is pointing at given time t, and n is the instrument noise. At this point we define the CMB signals to already be affected by the instrument beam and systematic effects. The instrument noise, which is not affected by the beam, may also be affected by some systematic effects such as gain variations. Throughout, we hereafter drop the t subscript for convenience. The way in which the systematics we model affect the TOD is shown individually in the following subsections.

The generated TOD with systematics is then converted into three temperature and polarization flat-sky maps using a binned map-making process; rewriting Eq. (3.1) in vector notation,

$$\boldsymbol{d} = \boldsymbol{A}\boldsymbol{s} + \boldsymbol{n}, \tag{3.2}$$

where $\boldsymbol{A}$ is the pointing matrix of the scanning strategy, the reconstructed sky maps $\hat{\boldsymbol{s}}$ are the generalized least square solution of Eq. (3.2) [193, 194],

$$\hat{\boldsymbol{s}} = \left(\boldsymbol{A}^\top \boldsymbol{N}^{-1} \boldsymbol{A}\right)^{-1} \boldsymbol{A}^\top \boldsymbol{N}^{-1} \boldsymbol{d}, \tag{3.3}$$

where $\boldsymbol{N}$ is the time-domain instrument noise correlation matrix that we assume is diagonal and proportional to the noise variance of the TOD (and the same for all the detectors). In the following we will use a pair-differencing approach, where we map independently the half sum and half difference of the TOD from a pair of detectors within a focal plane pixel that observe the sky with orthogonal polarization angles [195]. This is a commonly-used strategy to isolate the polarized and unpolarized components of the signal while minimizing the mixing between the two. Mixing between intensity and polarization is particularly dangerous for polarization measurements from the ground, for which any leakage of the unpolarized signal is dominated by the strong atmospheric emission. We do not use any filtering during the map-making process to avoid the need to correct the reconstructed lensing potential power spectrum by additional MC corrections due to filter-induced biases. While some filtering procedures [194, 196] or other map-making-stage modifications [197–199] may mitigate some systematic effects, in this work we only demonstrate to leading order the potential lensing biases which may result from systematics alone.

We use the process described above to obtain three groups of simulations:

1. *MC simulations*: systematics-free simulations which are obtained using our default instrument specifications and scanning strategy. These make up different simulation sets used for calculating different debiasing terms for the lensing reconstruction analysis. In

total, we use 576 MC simulations. Their allocation to the different debiasing terms is described in Sec. 3.3.

2. *Systematics-free "data" simulations*: 10 simulations similar to the MC simulations, but using a specific set of 10 CMB + noise realizations. These simulations are used for a systematics-free lensing reconstruction analysis for comparison.

3. *"Data" simulations*: same as group 2, but with the effect of systematics. Each considered systematic has its own set of 10 "data" simulations from which we reconstruct the lensing potential. The averaged reconstructed lensing power spectra of this set are compared to the same power spectra obtained from the systematics-free "data" set.

To simulate realistic observations, we use an existing scanning strategy in `s4cmb`, the "deep patch" scan, for all simulations. This simulates observations covering $\sim$5% of the sky, which is consistent with the plan of the deepest CMB observations of SO and CMB-S4 [175, 200]. The specific scanning strategy we adopted throughout this work is composed of 12 individual constant elevation scans (CESs) having a unique scanning pattern, as shown in Fig. 3.1. Future surveys dedicated to CMB lensing science will typically cover a much larger sky area ($\sim 50\%$ of the sky). However, our specific choice of scanning strategy is a good compromise that allows us to perform rapid simulations relatively inexpensively numerically. As we will discuss later on, the amount of cross-linking of the scans is a crucial factor affecting the impact of several instrumental systematics.

The normalized hit count map of the full 12-day scan is shown in Fig. 3.2. This "weights" map is used throughout the lensing analysis as a baseline for the anisotropic noise covariance map. A hit, or *sample*, is acquired every 1/15 seconds with a telescope's constant azimuth speed of $0.4^{\circ}/sec$ at an elevation of 5,200 meters for an observatory located in the Atacama plateau (which is the SO location). Since we simulate only 12 days of observations, which is only a fraction of a CMB experiment's full multiyear run, the effects of systematics which are expected to average out with time will be larger than in reality. Our bias estimates from these systematics should therefore be closer to an upper bound for what a similar experiment might observe in reality.

While our chosen scanning strategy is commonly employed by ground-based CMB experiments, other scans may be more optimal for mitigating systematics [201]. We focus on the scan defined above to characterize any lensing biases, so we can understand in a baseline configuration which systematics may be important for upcoming CMB experiments, and hence require more detailed study. Using a simple scan also avoids underestimating biases due to the choice of a specific more-complex scanning pattern that may not actually be implemented by future experiments.

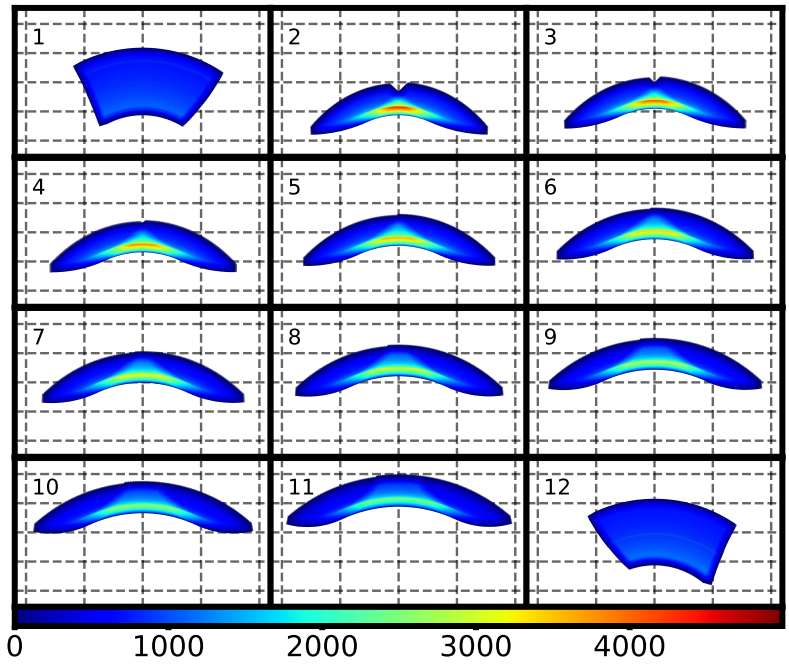

Figure 3.1: Sky coverage of each constant elevation scan (CES) of our scanning strategy. Each of scans 2-11 simulates $\sim$4 observation hours while scans 1 and 12 simulate $\sim$5 hours. In each CES, all detectors in the focal plane operate at the same time. The color map shows the number of observations per pixel in the scanned regions. Blue areas are observed less, and red areas are observed more times. The sub-panels of this figure cover the same area of Fig. 3.2, where we show the full composition of the scans.

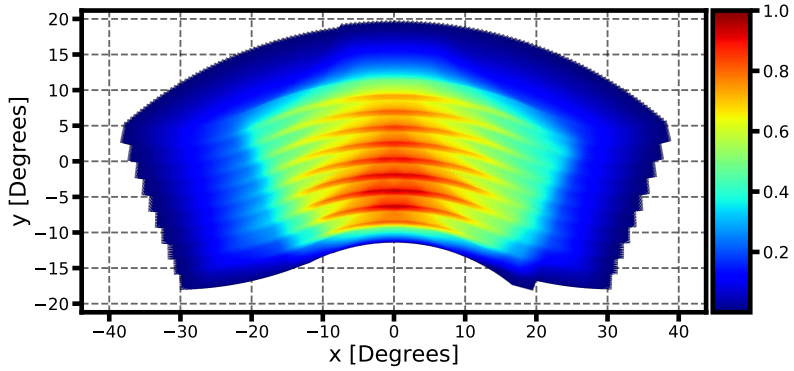

Figure 3.2: The full normalized hit count map composed of the different CESs from Fig. 3.1. This hits map is the baseline for constructing the anisotropic noise covariance map which is used in the lensing reconstruction filtering processes. Blue areas are observed less, and red areas are observed more times. The resolution of the maps is 1.7 arcminutes and the total sky area observed is $\sim$5% of the full sky.

For the instrument specifications, instead of simulating a full-sized SO-like experiment, which could be a very numerically expensive task, we consider an instrument with 6,272 bolometers (3,136 detector pairs) distributed over 4 different detector wafers. The way in which detectors are wired in the focal plane, and the specific readout technology used in experiments, affect the electronic crosstalk systematic. We consider two hardware configurations based on fMUX and μMUX technologies, which we describe in more detail in Subsec. 3.2.7. The square focal plane we consider is 60 cm on the side and has a field of view (FOV) on the sky of 3°[2]. The central

[2]This makes up a subset of the full SO focal plane, which has a field of view of $\sim$5° [202].

region of the focal plane is shown in Fig. 3.3. Although the total number of detectors and the FOV are reduced compared to the current SO design, the configuration is the ballpark expected for CMB-focused frequency channels of large-aperture telescopes targeting CMB lensing surveys in the upcoming years. In the absence of specific pointing or polarization angle systematics, which we describe further below, each bolometer pair (top and bottom detectors in the following) in the focal plane has a specific coordinate such that two detectors within a pair are on top of each other and have a 90-degree difference in their polarization angle orientation. The focal plane is cut into four quadrants which represent a wafer. Within a quadrant, pixels form rows or columns which correspond to either Q or U modes in detector coordinates (with a fixed exact 45-degree difference between them, in absence of polarization angle systematics), depending on their polarization angle (indicated by the angle of the markers in the figure). Each quadrant is rotated by 90° with respect to the next quadrant. This layout is commonly adopted in the design of bolometric focal planes to allow an efficient averaging over orientation of angles during the scans.

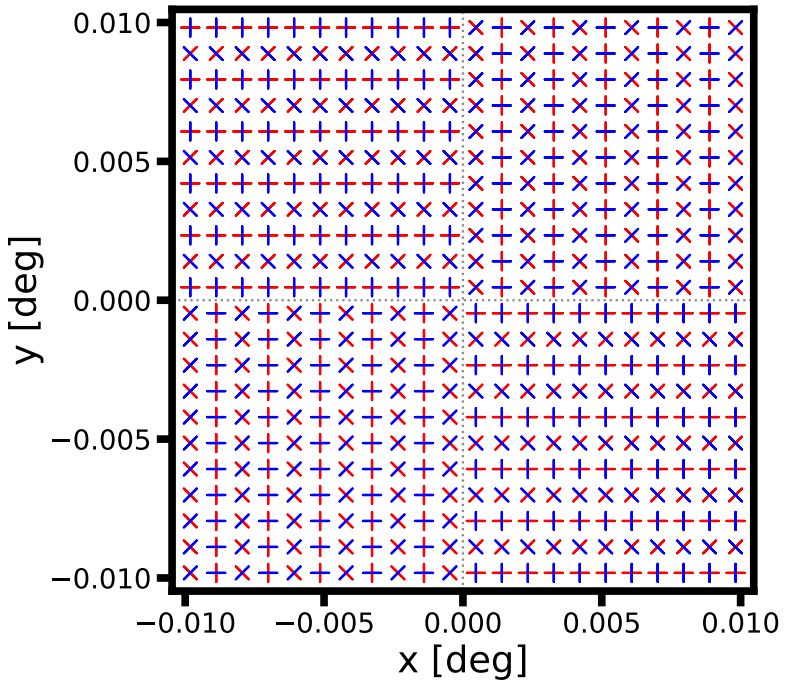

Figure 3.3: The center of the focal plane model used in the simulations, projected on the sky. The focal plane is composed of 4 wafers (illustrated by the dividing dashed gray lines) in which detectors within a pair (top and bottom, illustrated by the blue and red bars respectively) are on top of each other. The different marker-pair angles correspond to pairs belonging to the two polarization modes Q and U (forming "+" and "×"-like shapes in the figure respectively). The full focal plane extends to 60 cm on the side.

All other instrument properties we consider are based on the SO 'baseline' large aperture telescope (LAT) specifications at 145 GHz, described in Refs. [131, 203]. We use a baseline circularly-symmetric (CS) Gaussian beam with a full width at half maximum (FWHM) of 1.4 arcminutes. We rescale the SO baseline noise level to mimic the observations of an SO-like instrument scanning 5% of the sky with a 20% observation efficiency for 2.5 years. The

corresponding map-domain white noise is 5.4 (7.6) μK-arcminutes for temperature (polarization) after 12-days of simulated scanning. Since the noise in the map is inhomogeneous due to the nature of the scan, this white-noise level is estimated from the power spectrum of weighted temperature and polarization noise maps. It is between the homogeneous noise level expected for an SO-like experiment observing 5% of the sky for 5 years (3.5 μK-arcminutes), and the $10\mu K$-arcminutes on 40% of the sky expected for the baseline SO survey[3]. While using CMB maps with relatively low scaled noise may reduce noise-coupled systematic biases, the relative noise-related errors will also be smaller in our analysis, so we should still be sensitive to important effects.

Consistent with the design of SO LAT, our instrument model does not simulate the effects of a half-wave plate (HWP). Although a HWP could help to mitigate instrumental systematics for polarization [204, 205], especially if operated at cryogenic temperatures, the large-aperture telescopes typically used for lensing surveys do not normally use one as it is challenging to produce the large-sized plates required, and the HWP could also produce large unwanted systematics of its own [206].

The configurations described above are used for all of our simulations. For each "data" set (apart from the systematics-free ones) we also include one systematic effect. Below, we describe how each injected systematic effect is modelled and how it affects the TOD. The impact of these systematics on the corresponding CMB power spectra and lensing reconstruction are discussed in Sec. 3.4.

3.2.1 BEAM ELLIPTICITY

An ideal bolometer observes a patch of the sky with a known shape (or beam), usually taken to be a circularly-symmetric (CS) Gaussian. Realistically, however, a detector's beam has some deviation from this symmetric shape. A realistic beam instead has an approximately elliptical shape with unequal minor and major axes which have some tilt angle with respect to the predefined focal plane axes. This means that realistic detectors do not observe the same sky area that detectors with circular beams would. When each beam in an array of detectors has some different deviation from a CS shape, this can cause "smearing" effects in the resulting sky map. This could look similar to shearing or varying magnification expected from CMB lensing, and hence cause a lensing bias. When producing polarization maps using pair differencing, if the two beams of a detector-pair have a different shape there could be a substantial leakage between temperature and polarization

[3]These estimated values were obtained using the SO noise calculator, available at https://github.com/simonsobs/so_noise_models [131], and assume a 20% efficiency in the observing time.

measurements. This would induce biases both in the maps' power spectra and in the reconstructed lensing potential.

The effects of beam ellipticity on lensing reconstruction have been previously explored analytically [184], and several methods have been developed for mitigating beam asymmetry effects in CMB maps [207, 208]. Precise simulations of beam asymmetry in TOD simulations can be a very numerically-expensive task. The map of each simulated observation sample would need to be convolved with a specific pointing-dependent beam over a 4π solid angle [209]. Since it is too expensive to perform such convolution on a large number of samples (in our case, this would be performing a convolution over 4×10^{10} times for each simulation), we consider an approximate treatment for simulating the beam-shape systematic effects as TOD leakage terms following Ref. [210]. This approach does not account for the effect of far sidelobes, but these are expected to be more important for large-scale CMB modes that only have a minor impact on lensing reconstruction.

Given a temperature sample T in a specific (time-dependent) position on the sky $\mathbf{x}$ and its corresponding beam $b(\mathbf{x})$, which is not necessarily circular, the observed signal of this sample is

$$T_{\rm obs}(\mathbf{x}) \equiv b(\mathbf{x}) \circledast T(\mathbf{x}) = \int b(\mathbf{x}-\mathbf{y}) T(\mathbf{y}) d\mathbf{y}. \tag{3.4}$$

We can approximate the true beam $b(\mathbf{x})$ as a perturbed CS Gaussian beam $b_{\rm cs}(\mathbf{x}-\mathbf{y})$ with width $\sigma_{\rm FWHM}$,

$$b(\mathbf{x}) \approx \alpha_0 b_{\rm cs}(\mathbf{x}) + \alpha_{1,i} \frac{\partial b_{\rm cs}(\mathbf{x})}{\partial x^i} + \alpha_{2,ij} \frac{\partial^2 b_{\rm cs}(\mathbf{x})}{\partial x^i \partial x^j}, \tag{3.5}$$

where α_i are sets of expansion coefficients for the $0^{\rm th}$-, $1^{\rm st}$- and $2^{\rm nd}$-order derivatives of $b_{\rm cs}(\mathbf{x})$. Eq. (3.4) is then approximated as

$$\begin{aligned} T_{\rm obs}(\mathbf{x}) &\approx \int \left[\alpha_0 b_{\rm cs}(\mathbf{x}-\mathbf{y}) + \alpha_{1,i} \frac{\partial b_{\rm cs}(\mathbf{x}-\mathbf{y})}{\partial x^i} + \alpha_{2,ij} \frac{\partial^2 b_{\rm cs}(\mathbf{x}-\mathbf{y})}{\partial x^i \partial x^j} \right] T(\mathbf{y}) d\mathbf{y} \\ &= \alpha_0 T_{\rm b}(\mathbf{x}) + \alpha_{1,i} \frac{\partial T_{\rm b}(\mathbf{x})}{\partial x^i} + \alpha_{2,ij} \frac{\partial^2 T_{\rm b}(\mathbf{x})}{\partial x^i \partial x^j}, \end{aligned} \tag{3.6}$$

where

$$T_{\rm b}(\mathbf{x}) \equiv \int b_{\rm cs}(\mathbf{x}-\mathbf{y}) T(\mathbf{y}) d\mathbf{y} \tag{3.7}$$

is the temperature signal convolved with the CS beam. We can therefore approximate the observed samples as a map convolved with a CS beam, $T_{\rm b}$, plus leakage terms as shown in Eq. (3.6). The leakage terms depend on the derivatives of $T_{\rm b}$ and on the coefficients α_i which are derived from expanding the perturbed beam $b(\mathbf{x})$ around the CS beam $b_{\rm cs}$. Instead of repeating this convolution process for each sample, we can obtain $T_{\rm b}$ from convolving our input sky map with the CS beam

and use this map and its derivatives to get the leakage terms for each observed sample.

Using this treatment, we can analyze how these leakage terms affect the TOD and the resulting temperature and polarization signals. The time streams of top and bottom detectors within a pair (two orthogonal detectors which are in this case aimed towards the same sky area) can be written as

$$\begin{aligned} d_{\rm top} &= b_{\rm top} \circledast \left[T + Q\cos\left(2\psi\right) + U\sin\left(2\psi\right)\right], \\ d_{\rm bottom} &= b_{\rm bottom} \circledast \left[T - Q\cos\left(2\psi\right) - U\sin\left(2\psi\right)\right], \end{aligned} \tag{3.8}$$

where $b_{\rm top}$ and $b_{\rm bottom}$ are the top and bottom bolometers' beams, respectively, and ψ is the polarization angle. The temperature and polarization time streams are then given by the sum and the difference of the pair's time streams:

$$\begin{aligned} d_{+} &= b_{+} \circledast T + b_{-} \circledast \left[Q\cos\left(2\psi\right) + U\sin\left(2\psi\right)\right], \\ d_{-} &= b_{-} \circledast T + b_{+} \circledast \left[Q\cos\left(2\psi\right) + U\sin\left(2\psi\right)\right], \end{aligned} \tag{3.9}$$

where

$$b_{\pm} \equiv \frac{b_{\rm top} \pm b_{\rm bottom}}{2}. \tag{3.10}$$

Repeating the beam approximation above for the convolution terms in Eq. (3.9), we get

$$\begin{aligned} d_{+} &= \alpha_{0(+)} T_{\rm b} + \alpha_{1,i(+)} \frac{\partial T_{\rm b}(\mathbf{x})}{\partial x^i} + \alpha_{2,ij(+)} \frac{\partial^2 T_{\rm b}(\mathbf{x})}{\partial x^i \partial x^j} \\ &\quad + \alpha_{0(-)} P_{\rm b} + \alpha_{1,i(-)} \frac{\partial P_{\rm b}(\mathbf{x})}{\partial x^i} + \alpha_{2,ij(-)} \frac{\partial^2 P_{\rm b}(\mathbf{x})}{\partial x^i \partial x^j}, \\ d_{-} &= \alpha_{0(-)} T_{\rm b} + \alpha_{1,i(-)} \frac{\partial T_{\rm b}(\mathbf{x})}{\partial x^i} + \alpha_{2,ij(-)} \frac{\partial^2 T_{\rm b}(\mathbf{x})}{\partial x^i \partial x^j} \\ &\quad + \alpha_{0(+)} P_{\rm b} + \alpha_{1,i(+)} \frac{\partial P_{\rm b}(\mathbf{x})}{\partial x^i} + \alpha_{2,ij(+)} \frac{\partial^2 P_{\rm b}(\mathbf{x})}{\partial x^i \partial x^j}, \end{aligned} \tag{3.11}$$

where the coefficients $\alpha_{i(\pm)}$ correspond to $b_{\pm}$, and we define $P_{\rm b} \equiv Q_{\rm b}\cos\left(2\psi\right) + U_{\rm b}\sin\left(2\psi\right)$, the polarization field convolved with the CS beam in analogy with Eq. (3.7), for convenience. In practice, the $\alpha_{i(\pm)}$ coefficients are time-dependent. The time dependency is due to the different orientation of the expansion basis used for computing their values and the sky coordinate system at a given observation time. The difference in orientation can be easily accounted for by rotating the coefficients computed in Eq. (3.5) by a suitable angle.

Leakage which results from $\alpha_{0(+)} \neq 1$, and thus from a loss of optical power, is usually mitigated during gain calibration or polarization efficiency estimation. We therefore set $\alpha_{0(+)}$ to 1 for all detectors to focus on the less trivial leakage terms, and perform a separate analysis of gain systematics in a later subsection. When a pair's beams have the same shape, even if

elliptical, $b_- = 0$ and $b_+ = b_{\rm top} = b_{\rm bottom}$. In this case, $\boldsymbol{\alpha}_{\mathbf{1}(-)} = \boldsymbol{\alpha}_{\mathbf{2}(-)} = 0$, and all $T \to P$ and $P \to T$ leakage terms vanish. Any biases in this scenario are attributed only to $T \to T$ and $P \to P$ leakages which depend on the deviation of the elliptical beam b_+ from being CS. When a pair's beams do not have the same shape, the $T \to P$ and $P \to T$ leakage terms do not vanish. This can induce a significant bias in the polarization maps due to the large temperature signal amplitude, which can then affect the lensing reconstruction. We simulate the most general case of beam asymmetry systematics described above, in which all leakage terms (apart from the gain-related ones) are injected into the TOD. To calculate the fitting coefficients $\alpha_{i(\pm)}$, we define the CS and the parametrized elliptical beams as

$$\begin{aligned} b_{\rm cs}(\mathbf{x}) &\equiv \frac{1}{2\pi\sigma_{\rm cs}^2} e^{-\frac{\mathbf{x}^2}{2\sigma_{\rm cs}^2}}, \\ b(\mathbf{x}) &\equiv \frac{1}{2\pi\sigma_{\rm min}\sigma_{\rm maj}} e^{-\frac{1}{2}\left[\boldsymbol{\sigma}^{-1}\cdot\mathbf{R}(\varepsilon)\cdot\mathbf{x}\right]^2}, \end{aligned} \tag{3.12}$$

where

$$\begin{aligned} \sigma_{\rm cs} &\equiv \frac{\sigma_{\rm FWHM}}{\sqrt{8\ln 2}}, \\ \boldsymbol{\sigma} &\equiv \begin{pmatrix} \sigma_{\rm maj} & 0 \\ 0 & \sigma_{\rm min} \end{pmatrix}, \\ \mathbf{R}(\varepsilon) &\equiv \begin{pmatrix} \cos(2\varepsilon) & -\sin(2\varepsilon) \\ \sin(2\varepsilon) & \cos(2\varepsilon) \end{pmatrix}, \end{aligned} \tag{3.13}$$

$\sigma_{\rm maj}$ ($\sigma_{\rm min}$) is the size of the semi-major (minor) axis, and $\mathbf{R}$ is a matrix responsible for rotating the ellipse by some angle ε between the major axis of beam ellipse and the focal plane's x axis. The beam parameters are illustrated in Fig. 3.4. The minor and major ellipse axes of each beam deviate symmetrically from $\sigma_{\rm cs}$,

$$\sigma_{\substack{\rm maj \\ \rm min}} = \sigma_{\rm cs} \pm \frac{\Delta\sigma}{2}, \tag{3.14}$$

where $\Delta\sigma$ is determined using the ellipticity $e_{\rm beam}$ definition,

$$e_{\rm beam} \equiv \frac{\sigma_{\rm maj}^2 - \sigma_{\rm min}^2}{\sigma_{\rm maj}^2 + \sigma_{\rm min}^2}. \tag{3.15}$$

Each detector beam is assigned with a random ellipticity $e_{\rm beam}$ and a random ellipticity angle ε. To add a level of realism to the ellipticity models, we correlate each ellipticity and angle to the detector's distance from the boresight coordinates and polar angle, respectively, by assuming a $2^{\rm nd}$ degree polynomial that mimics the fact that detectors observing regions close to the edge of

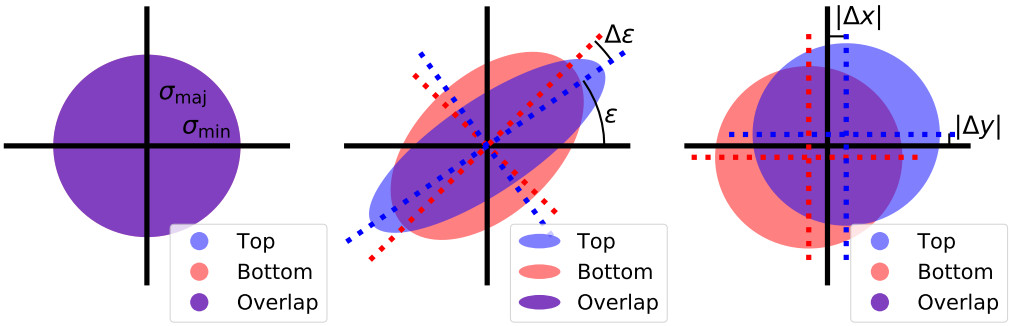

(a) CS beams. **(b)** Differential beam ellipticities. **(c)** Differential pointing.

Figure 3.4: Illustration of the beam models and parameters in Eq. (3.12). Panel (a) shows the two overlapping circularly-symmetric (CS) Gaussian beams ($\sigma_{\rm maj} = \sigma_{\rm min} = \sigma_{\rm cs}$) of a detector pair. This represents the beam shape in all simulations apart from the beam ellipticity and differential pointing "data" simulation sets. Panel (b) shows the beam ellipticity model we use. In this case, the two beams of a detector pair have a different ellipticity: $\sigma_{\rm maj} \neq \sigma_{\rm min}$ for each beam, different axes lengths for each detector, and some angle difference $\Delta\varepsilon$ also exists between their major axes (on top of the 90° orthogonality of the two detectors). Panel (c) shows the same unperturbed beam shapes as in (a), however in this case each beam's center is shifted. This is our differential pointing model, in which the beam centers of a detector pair are shifted according to Eq. (3.16).

the FOV are subject to more optical distortions[4]. The polynomial functions, along with the beam ellipticities and angles, are shown in Fig. 3.5. The ellipticities and angles are drawn from a normal distribution with mean centered on the respective polynomial function with 2% and 45° standard deviations, respectively. These dispersion values are consistent with e.g. POLARBEAR [171] and BICEP2 [211] beam measurements. On top of the ellipticity angles, which are the same for two detectors in a pair, a random differential angle $\Delta\varepsilon$ is also used to perturb the beams of all bottom detectors. These angles are drawn from a normal distribution with a zero mean and a 5° width. All beam parameters are drawn once per simulation and therefore remain constant in time throughout the simulated observation period. The relevant derivatives of the temperature and polarization maps, which are used in the leakage terms, are obtained using the `synfast` routine of the HEALPix [176] package.

In our simulations, we do not model the cross-polar beam response. This response is expected to be subdominant for an SO-like instrument based on modern optical coupling technologies for bolometric detectors and cross-Dragone telescopes [187, 190]. We also assume that all baseline beams have a perfect circular shape with a Gaussian radial profile. In practice, this is an approximation, as diffraction effects in the optics will cause the beam to decay asymptotically as $\sim 1/\theta^3$, where θ is the angle from the beam peak [171, 212]. Any characterization of the beam properties in the field through dedicated calibration observations will naturally include these effects in the main beam model, and hence include it in the transfer function used for subsequent steps of the data analysis. While we do not include diffraction effects in our baseline beams, we

[4] A good demonstration of these correlations is shown in Ref. [202], where a more comprehensive review of the SO optics can also be found.

found that when perturbing our elliptical beams around a beam which includes diffraction tails, the resulting leakage coefficients $\alpha_{i(\pm)}$ are similar to those obtained using the fully Gaussian beam. As such, although the diffraction tails affect the beam beyond its FWHM scale, we do not expect these corrections to significantly change our results for beam-related or other systematics considered in this work. In general, diffraction tails could be important, as they allow the telescope to pick up spurious emissions coming from the ground or other astronomical sources, and would have to be included in a dedicated analysis of the telescope sidelobes, which we did not consider in this work.

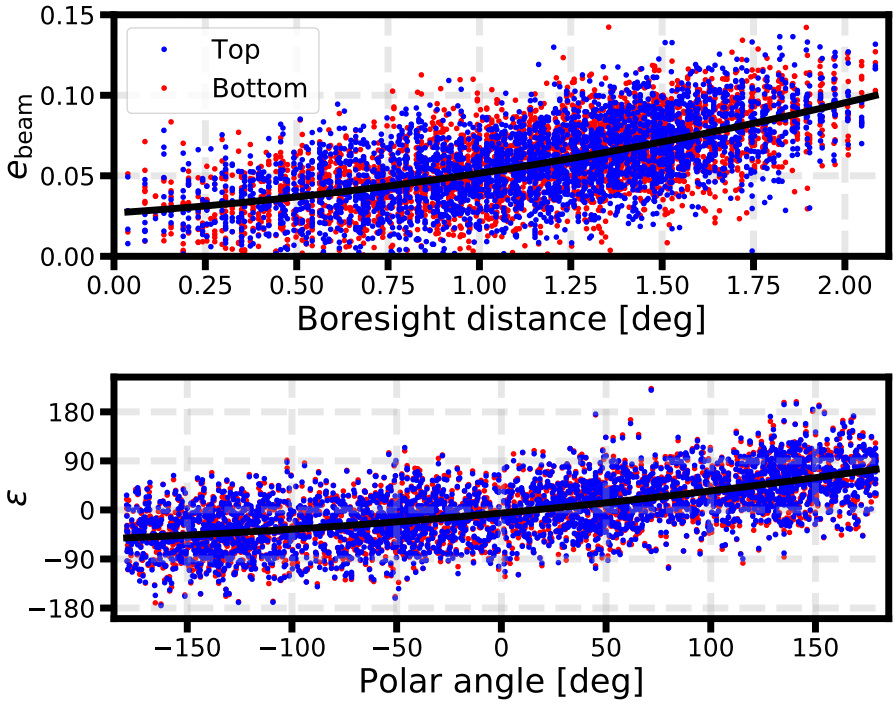

Figure 3.5: Beam ellipticities and angles of all simulated top (blue markers) and bottom (red markers) detectors. Each plot shows the function used as the normal distribution mean for generating the beam random variables (black lines). The functions were estimated using the NumPy [213] and SciPy [214] Python libraries.

The $b_{\pm}$ maps are shown in Fig. 3.6 for a detector pair from our simulations. The beam difference b_{-} map for beam ellipticity has quadrupole-like symmetry, corresponding to the main leakage terms for this systematic coming from the 2^{nd} derivative terms. The map-level effects of beam ellipticity for temperature and polarization are shown in Fig. 3.7. Compared to the simulation with CS beams, the residuals seem negligible relative to the signal amplitudes. Expectedly, the polarization residuals are larger than those of the temperature due to the $T \rightarrow P$ leakage terms.

3.2.2 DIFFERENTIAL POINTING

Another beam-related systematic that we model results from detectors in a focal plane pixel not being centered on the same sky coordinates. In other words, the beams of two detectors in a pair are not aligned in the focal plane reference frame. When this occurs, the temperature and polarization maps, which are produced from the sum and difference of the pair data streams, will be distorted. Typically, this is mitigated during map-making by considering the mid-point beam centers as the true center of each beam in a pair. The residual of this effect can, however, produce smearing features and $T \rightarrow P$ leakage in the maps, which could potentially propagate to the lensing reconstruction. Analytic approaches for characterizing the differential pointing effects on the lensing potential were previously explored in Refs. [184, 185].

In our simulations, this systematic effect is modelled by introducing an offset to the beam-center coordinates of two detectors within a pair. A different offset is drawn for each detector pair. For a given pair, the unperturbed pointing coordinates (x_0, y_0) in the focal plane reference frame is shifted by

$$(\Delta x, \Delta y)_{\substack{\text{top} \\ \text{bottom}}} = \pm \frac{\rho}{2} (\cos\theta, \sin\theta) \,, \tag{3.16}$$

where $\rho \in \boldsymbol{N}(15'', 1.5'')$ is the offset magnitude and $\theta \in \mathcal{U}(0, 2\pi)$ is the offset direction angle with respect to the horizontal focal plane axis. The magnitude of the ρ that we use is conservative, as current-generation experiments with on-chip detectors achieved differential pointing well below the mean value assumed here [192]. The differential pointing offset is illustrated in Fig. 3.4c. Following the previous sections, the perturbed beams are then used to compute the coefficients α_i for the leakage terms which are injected into the temperature and polarization time streams as in Eq. (3.11).

The $b_\pm$ maps for the differential pointing systematic are shown in Fig. 3.6 for a detector pair from our simulations. The beam difference b_- map has dipole-like features, which suggests that the main leakage terms for this systematic would stem from the 1^{st} derivative leakage terms.

The map-level effects of differential pointing for temperature and polarization are shown in Fig. 3.7. The differential pointing residuals for both temperature and polarization maps are larger compared to the beam ellipticity residuals. For both of these beam-related systematic effects, the temperature residuals appear to be nearly spatially uncorrelated. The polarization residuals in the differential pointing case do not have Q- and U-like features as with the beam ellipticity residuals.

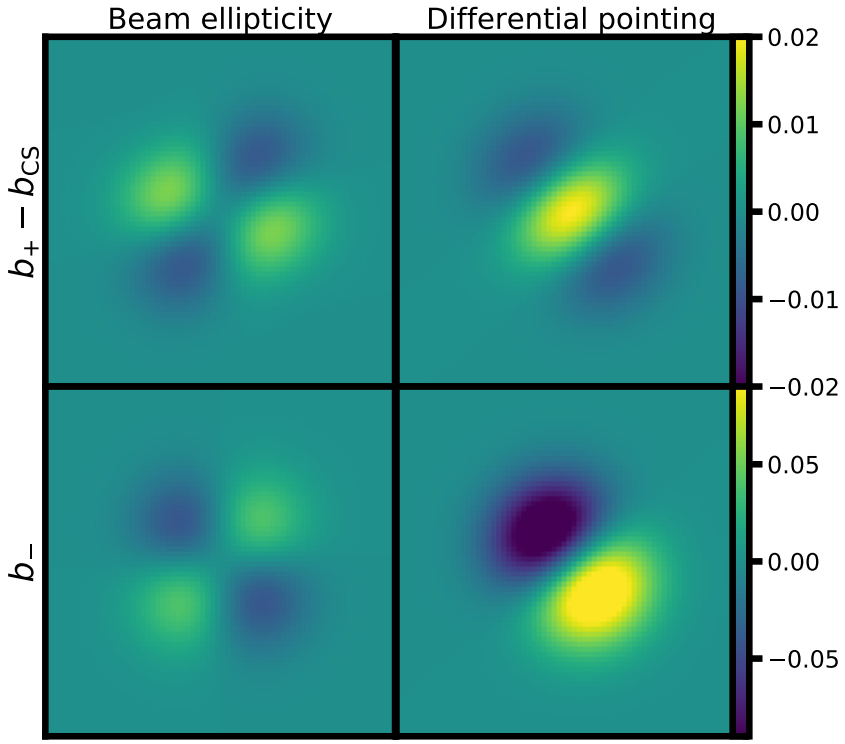

Figure 3.6: *Row 1*: Difference between b_+ maps of the perturbed and CS beams for the beam ellipticity (left panel) and differential pointing (right panel) systematics for a detector pair in our simulations. The deviation from CS is larger for the differential pointing systematic. *Row 2*: The b_- maps for the beam ellipticity (left panel) and differential pointing (right panel) systematics of a detector pair from our simulations. As with b_+, the difference between the two beams within a pair is larger for the differential pointing systematic. The shape of b_- for beam ellipticity (differential pointing) has quadrupole-(dipole-)like features.

3.2.3 BORESIGHT POINTING

The systematics discussed in the previous subsections involved perturbed models of detector beams. In this subsection, we describe a systematic effect that is produced from inaccuracies in the pointing coordinates of the entire focal plane, or *boresight pointing*, during scans. The exact pointing of the telescope needs to be reconstructed from the position of known sources. The direction in which the focal plane of a telescope is pointing during a scan might differ slightly from the pointing direction recorded by the telescope position encoders. These errors can originate from wind gusts, temperature changes, temperature gradients across the focal plane due to heating of the telescope structure, vibrations due to the motion of the telescope, deformation of the telescope's mirror due to its own weight, and more. The errors due to deformation can mostly be corrected by estimating the variations of the pointing correction (that relates the recorded telescope position to the position of known sources) as a function of time, while other effects can be assumed as random. We therefore simulate the pointing errors by perturbing the boresight's azimuth and elevation for each sampling, while using their original unperturbed values in the pointing matrix in the map-making stage. The azimuth and elevation offsets are drawn from a

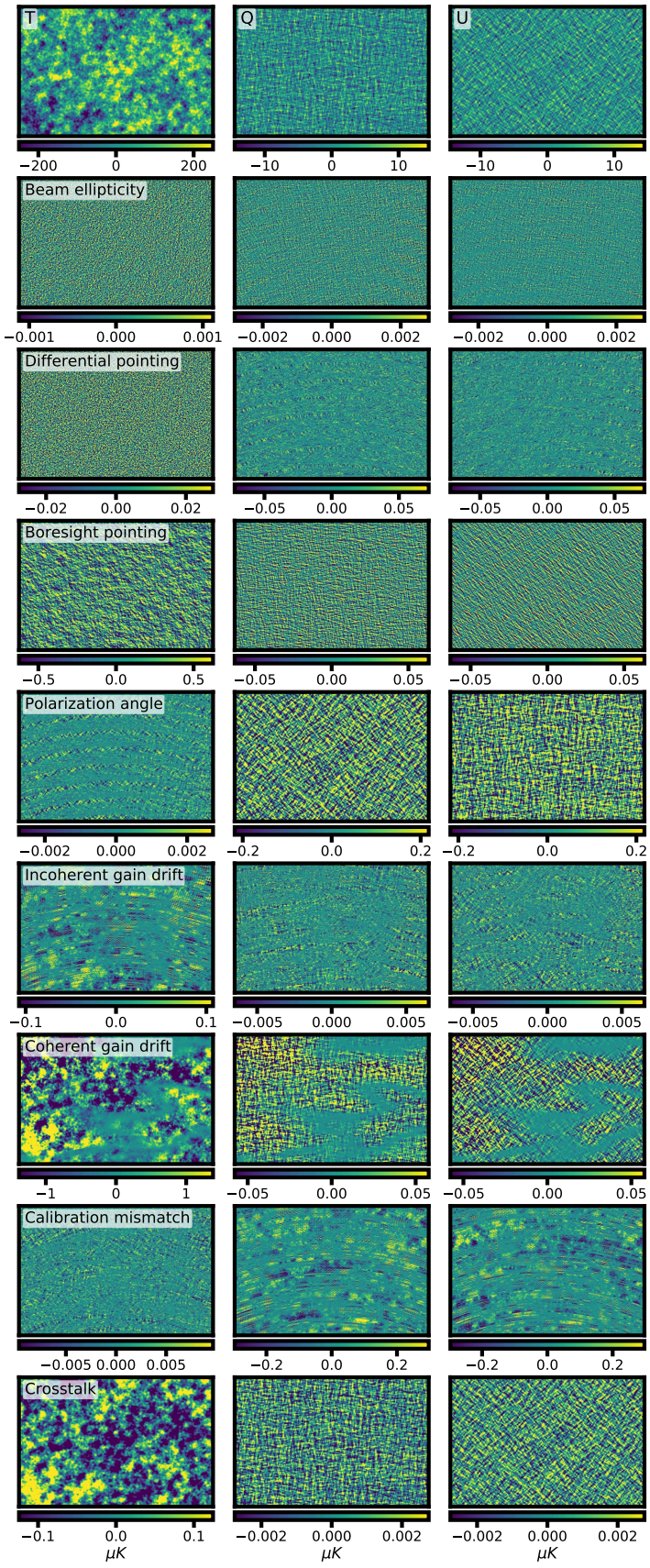

Figure 3.7: *Row 1*: White-noise-free temperature (left), Q (middle) and U (right) maps of a systematics-free "data" simulation. *Rows 2-8*: Difference maps of the same realization with and without systematics for temperature (left column), Q (middle column) and U (right column). All panels show the middle area of the full simulated box with dimensions $17 \times 25.5\,\mathrm{deg}^2$.

normal distribution with a 3 arcseconds mean (a typical precision of a telescope position encoder) and a variance such that the total pointing uncertainty is 13 arcseconds and error in azimuth and elevation are uncorrelated. This pointing error is about $\sim 10\%$ of the CS beam FWHM we considered in this work and is consistent with typical results of state-of-the-art experiments [192].

The map-level effects of the boresight pointing systematic for temperature and polarization are shown in Fig. 3.7. Unlike the previously mentioned systematics, the residuals from perturbing the boresight coordinates are as important for temperature as for polarization. The map-level residuals are small-scale changes arising from a small additional smoothing-like effect on the maps due to the randomized pointing. This systematic does not produce any $T \leftrightarrow P$ mixing.

3.2.4 POLARIZATION ANGLE

The accuracy of polarization angle measurements is important to correctly characterize the E and B modes of the CMB [215, 216]. If the true polarization angles of each detector deviate from their estimated values, which are used to make the Q and U maps, E/B mixing is introduced. This not only contaminates the resulting E and B modes, but also produces non-zero EB and TB correlations. These correlations are expected to vanish in cosmological models where parity is preserved [70, 76, 217–220]. Models that include non-standard physical mechanisms which manifest on cosmological scales (such as cosmic birefringence, parity violation) predict the existence of intrinsic EB or TB correlations that can also get contaminated by a polarization angle miscalibration [221].

In general, the polarization angles of the top and bottom detectors can each be different from the expected angle ψ by a different $\Delta\psi$, such that the time streams of a detector pair are

$$\begin{aligned} d_{\rm top} &= T + Q\cos\left[2\left(\psi + \Delta\psi_{\rm top}\right)\right] + U\sin\left[2\left(\psi + \Delta\psi_{\rm top}\right)\right], \\ d_{\rm bottom} &= T - Q\cos\left[2\left(\psi + \Delta\psi_{\rm bottom}\right)\right] - U\sin\left[2\left(\psi + \Delta\psi_{\rm bottom}\right)\right]. \end{aligned} \tag{3.17}$$

The temperature and polarization time streams are then

$$\begin{aligned} d_+ = T &+ Q\frac{\cos\left[2\left(\psi+\Delta\psi_{\rm top}\right)\right]-\cos\left[2\left(\psi+\Delta\psi_{\rm bottom}\right)\right]}{2} \\ &+ U\frac{\sin\left[2\left(\psi+\Delta\psi_{\rm top}\right)\right]-\sin\left[2\left(\psi+\Delta\psi_{\rm bottom}\right)\right]}{2}, \\ d_- = &\ Q\frac{\cos\left[2\left(\psi+\Delta\psi_{\rm top}\right)\right]+\cos\left[2\left(\psi+\Delta\psi_{\rm bottom}\right)\right]}{2} \\ &+ U\frac{\sin\left[2\left(\psi+\Delta\psi_{\rm top}\right)\right]+\sin\left[2\left(\psi+\Delta\psi_{\rm bottom}\right)\right]}{2}. \end{aligned} \tag{3.18}$$

When $\Delta\psi_{\rm top} = \Delta\psi_{\rm bottom} \equiv \Delta\psi$, there is no $P \rightarrow T$ leakage. When all detector pairs are perturbed with the same $\Delta\psi$ value, the recovered polarization maps are effectively equivalent to the true polarization sky signals rotated by a constant angle $\Delta\psi$. Under this assumption, it is straight-forward to propagate this systematic effect all the way to the E and B modes and their power spectra [215]. When the polarization angle perturbations in the top and bottom detectors are completely anti-correlated, i.e. $\Delta\psi_{\rm top} = -\Delta\psi_{\rm bottom}$, the polarization bias becomes an effective gain error of the size $\cos(2\Delta\psi_{\rm top})$. In this work, we consider the most general case, in which both $\Delta\psi_{\rm top}$ and $\Delta\psi_{\rm bottom}$ are independently drawn for each detector pair, such that both the polarization and temperature signals are affected by the perturbed angles.

We model differential polarization angle perturbations by drawing a different value for $\Delta\psi$ from $\boldsymbol{N}(-1.1^\circ, 0.5^\circ)$ for each detector in each detector pair. This perturbation level will be referred to as "setup A" throughout the chapter. The perturbation values for this setup are consistent with the polarization angle errors measured by POLARBEAR and BICEP2 prior to applying a polarization angle self-calibration procedure (see [222, 223] and discussion around Eq. (3.44) in Sec. 3.5). Other experiments, such as ACTPol and SPTpol, have reported lower mean values for the polarization angle errors consistent with $\Delta\psi \sim 0.5^\circ$ [224, 225]. Although we do not consider this case in detail for estimating lensing biases, we give a comparison between setup A and an ACTPol-like setup with $\Delta\psi$ drawn from $\boldsymbol{N}(-0.5^\circ, 2.0^\circ)$ ("setup B") in Secs. 3.4.2 and 3.5.

The map-level effects of the polarization angle systematic for temperature and polarization are shown in Fig. 3.7. The small temperature residuals are the $P \rightarrow T$ leakage induced by the differential polarization angles within a detector pair. These residuals also show the scanning strategy stripes due to its correlation with the polarization angles. Because this systematic effectively rotates the polarization maps, the Q residual map mostly consist of U features, and vice versa.

3.2.5 GAIN DRIFTS

In this and the next subsection we discuss detector-level systematics which relate to the TOD gains. During an observation run, various internal or external factors could change the measured bolometer gain that calibrates the raw data to physical units: local temperature gradients across the focal plane could induce gain drifts for each detector pair until a gain recalibration is performed; external heating of the entire focal plane or a coherent change of the detectors' optical loading could cause a coherent gain drift for all detectors. In our simulations, we model these gain drift effects as a function of time using a linear drift model,

$$g(t) = 1 + \Delta g \frac{(t \bmod t_R)}{t_R}, \tag{3.19}$$

such that after each time interval t_R the gain is recalibrated back to unity. This assumes that the gain calibration procedure restores a perfect calibration relative to the input map. As such, we assume potential effects due to bandpasses can be characterized with a sufficient level of precision. In Subsec. 3.2.6 we also consider a related effect in which the recalibration produces some gain mismatch between the detectors in a pair, producing an inter-calibration problem. We consider a retuning interval of $\sim$1.2 hours, and draw the gain perturbation variable Δg for each pair (and once for each drifting duration) from a normal distribution with a zero mean and a 0.05 width. Although the retuning interval can be optimized depending on the exact scanning strategy, we use a value similar to those employed for observations performed from the Atacama plateau with a similar scanning strategy [226].

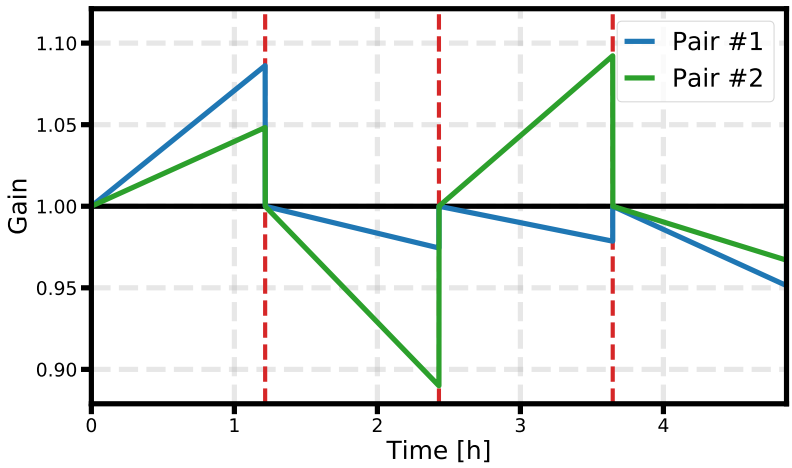

Figure 3.8: Illustration of the linear gain drift model during the course of CES 1 from Fig. 3.1 for two detector pairs (green and blue lines). Recalibration occurs 4 times during each CES, shown by the dashed red lines. For this CES, which lasts $\sim$5 hours, recalibration occurs every $\sim$1.25 hours. For the shorter CESs, recalibration occurs roughly every hour. This illustration shows the incoherent gain drift of two detector pairs. In our coherent gain drift simulations, the green gains are identical to the blue gains, and represent the drift of all detector pairs.

This gain drift model, which is illustrated in Fig. 3.8, simulates the effect of *incoherent gain drifts* between detector pairs. As mentioned before, another possibility is a *coherent gain drift* across the focal plane. We therefore produce an additional simulation set for this effect. We consider these two extreme gain drift scenarios instead of simulating a local (on the focal plane) drifting model to demonstrate how different drifting scenarios affect the lensing reconstruction. For coherent gain drift, the same random variable Δg is used for all detector pairs for each drifting duration, but is different after each recalibration. This type of drift is similar to that illustrated in Fig. 3.8, but with the gains of both pairs (and all other pairs in the focal plane) being the same in each drifting period.

Since gain is a multiplicative parameter for the time-stream signal and noise,

$$\begin{aligned} d_{\rm top} &= g\left[T + Q\cos\left(2\psi\right) + U\sin\left(2\psi\right) + n\right], \\ d_{\rm bottom} &= g\left[T - Q\cos\left(2\psi\right) - U\sin\left(2\psi\right) + n\right], \end{aligned} \tag{3.20}$$

we can estimate its average effect on the 2-point and 4-point correlation functions, which we define later in Sec. 3.3, analytically.

The map-level effects of the incoherent and coherent gain drift systematics for temperature and polarization are shown in Fig. 3.7. Expectedly, the incoherent gain drift residuals are much smaller compared to the coherent drifts. This happens because when different pairs have a different drift, the systematic effect averages out quickly for a sky area which is observed by multiple pairs over time. Coherent drift biases take a longer time to average out. As such, their residuals leave large-scale areas which are affected by an incorrect calibration. The resulting patterns depend on the scanning strategy, sampling frequency, and gain recalibration frequency. Longer observations using the same basic scan, but a more frequent recalibration strategy, would change these patterns and reduce the residual amplitude.

3.2.6 CALIBRATION MISMATCH

Another gain-related systematic effect results from an inaccurate gain inter-calibration process between two detectors in a given pair. During an observation run, gains are usually calibrated back to unity multiple times. This recalibration process could potentially produce some level of differential gain, or *calibration mismatch*, if the new gains of a detector pair are not equal. In this case, each detector gain has some deviation from unity. This gain offset can be different after each gain recalibration. We simulate this effect by symmetrically offsetting the top and bottom gains g

of each detector pair such that

$$g_{\rm top}(t) - g_{\rm bottom}(t) = 2\epsilon_g(t). \tag{3.21}$$

We model this systematic effect symmetrically so that only the leakage terms in the temperature and polarization time streams depend on the gain mismatch level, and the overall absolute calibration of the T, Q and U Stokes parameters is not affected. This is consistent with the choice made in the previous sections where we assumed absolute calibration and polarization efficiencies effects can be correctly measured or calibrated on other external data sets such as e.g. Planck. A different gain offset ϵ_g is applied after each calibration and for each detector pair. The modified gains of a detector over time are illustrated in Fig. 3.9. We use the same probability distribution as before, $\boldsymbol{N}(0, 0.05)$, to draw a different offset ϵ_g for each detector pair. This distribution is a conservative estimate of possible gain systematics as current generation of experiments have demonstrated the feasibility of minimizing differential gain effects if reliable inter-calibration sources are available. POLARBEAR, for example, estimated the upper limit of these effects to be $\lesssim 0.3\%$ [192], while SPTpol constrained them to be $\sim 1\%$ prior to any marginalization [227].

Using this calibration mismatch model in Eq. (3.20), a detector pair's TOD are

$$\begin{aligned} d_{\rm top} &= (1+\epsilon_g)\left[T + Q\cos(2\psi) + U\sin(2\psi) + n\right], \\ d_{\rm bottom} &= (1-\epsilon_g)\left[T - Q\cos(2\psi) - U\sin(2\psi) + n\right], \end{aligned} \tag{3.22}$$

and the corresponding sum and difference time streams read

$$\begin{aligned} d_+ &= T + \epsilon_g\left[Q\cos(2\psi) + U\sin(2\psi)\right], \\ d_- &= \epsilon_g T + Q\cos(2\psi) + U\sin(2\psi), \end{aligned} \tag{3.23}$$

such that $T \to P$ and $P \to T$ leakage terms depend on the gain offset parameter. We expect the former leakage term to be more significant than the latter given the lower amplitude of the polarization signal, and that cross-linking during observation runs will reduce overall leakage in both d_+ and d_-.

The map-level effects of the calibration mismatch systematic for temperature and polarization are shown in Fig. 3.7. Expectedly, the temperature residuals are smaller compared to the polarization residuals. As this effect produces T/P mixing, the temperature residual map has features similar to the spatial distribution of the polarization signal, and vice versa for the polarization maps, where the residual amplitude is $\sim 10\%$ of the input map. As with the other

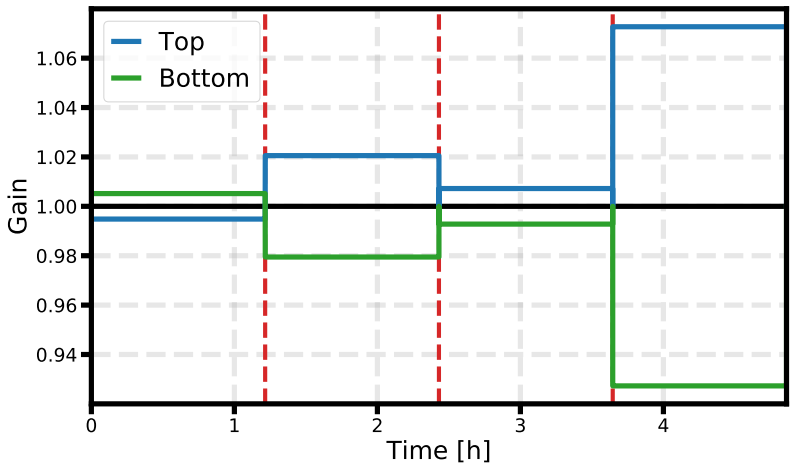

Figure 3.9: Illustration of the calibration mismatch model during the course of CES 1 from Fig. 3.1 for top (blue) and bottom (green) detectors within a pair. As with the gain drift model which is illustrated in Fig. 3.8, recalibration occurs 4 times during each CES, shown by the dashed red lines. For this CES, which lasts $\sim$5 hours, recalibration occurs every $\sim$1.25 hours. For the shorter CESs, recalibration occurs roughly every hour. Unlike the gain drift model, here each calibration process adds a symmetrically gain distortion between the two detectors in a pair.

gain-related systematics, this effect is also expected to average-out with more frequent calibrations, more detectors, and longer observation time.

3.2.7 CROSSTALK

The last systematic effect we explore in this work is due to the experiment's electronic readout systems. Modern CMB experiments typically employ bolometric detectors operating in cryogenic environments. They adopt complex multiplexing technologies to simultaneously read out signals from many bolometers on a single readout line. This capability is required to minimize thermal losses in the cryostat that hosts the focal plane. Due to the complexity of readout technologies in cryogenic environments, the readout device can introduce a mixing of the electric signals of bolometers transported on the same readout line, an effect which is called electric *crosstalk* [228]. We give baseline results for a readout electronic setup similar to the one employed in μMUX technologies, where all 1,568 bolometers in a wafer are multiplexed together in a single SQUID (superconducting quantum interference device; used to read out the signal from the transition-edge sensors). Future experiments such as SO are expected to adopt a μMUX technology and therefore have a readout scheme close to the one we simulate [229]. We also consider an alternative setup with 7 frequency-domain multiplexers (fMUX) with 4 SQUIDs per fMUX, and 28 detector pairs per SQUID. This is the reference technology for several current generation of experiment such as POLARBEAR-2/Simons Array and SPT-3G [230, 231], and has also been discussed in the context of future experiments [187]. The results we obtain with this setup are similar to those presented in the following.

The effect of crosstalk is such that the acquired raw TODs $\boldsymbol{d_t}$ at a given time are in reality a linear combination of the true sky measurements of each detector $\boldsymbol{d_t^{\rm det}}$ acquired at the same time. This can be characterized by the crosstalk leakage matrix $\boldsymbol{L}$ as

$$\boldsymbol{d_t} = (\mathbb{1} + \boldsymbol{L})\boldsymbol{d_t^{\rm det}}, \tag{3.24}$$

where $\mathbb{1}$ is the identity matrix. To identify the signal $d_i \in \boldsymbol{d_t^{\rm det}}$ from each detector i, each detector carrier is modulated to a different readout frequency f_i for detectors that are all wired together within a SQUID. A realistic representation of the element i, j of the leakage matrix is then

$$L_{ij} = \frac{k_{ij}}{(\Delta f_{ij})^2}, \tag{3.25}$$

where k_{ij} is a leakage coefficient, and the leakage depends on Δf_{ij}, the location-dependent frequency spacing between bolometers i and j in the focal plane [228]. We set $k_{ii} = 0$ to avoid additional gain miscalibration, and the resulting time-stream leakage then attenuates with a constant power of 2 with respect to Δf. While there are a large number of possible modulation schemes, we use a simple linearly-spaced modulation. The readout frequencies of all bolometers within a SQUID form an arithmetic progression between a minimal and a maximal frequency $f_{\rm min}$ and $f_{\rm max}$ based on the detector's sequential placement order in rows within the SQUID. In this case, $\Delta f_{ij} \equiv (f_{\rm max} - f_{\rm min})/n_{\rm MUX}$ for two consecutive detectors i, j where $n_{\rm MUX}$ is the number of bolometers connected together within a SQUID. While this modulation model is not optimized, as bolometers which are physically near do not have the maximal possible frequency difference within the specific frequency range, the leakage amplitude proved to be dominated by the overall hardware settings (for instance resistance and induction in the readout system) such that optimizing the modulation pattern is less important. We also use $n_{\rm MUX}$ as the leakage radius so that all the bolometers within a SQUID are affected by crosstalk to achieve realistic and conservative results.

The off-diagonal leakage coefficients k_{ij} for detectors within a SQUID are drawn once for each simulation (so that the crosstalk leakage matrix remains constant during the full observation time) from a normal distribution with a -0.03% mean and a 0.01% width [187]. These values are consistent with the current capabilities of the readout technologies considered for SO and CMB-S4 instruments [229, 232]. The modulation frequency range is set between $f_{\rm min} = 4$ GHz and $f_{\rm max} = 8$ GHz for μMUX and $f_{\rm min} = 1$ MHz and $f_{\rm max} = 5$ MHz for the fMUX setup, which are typical values for these technologies. A block of the full simulated crosstalk leakage matrix $\boldsymbol{L}$ is shown in Fig. 3.10. Leakages beyond the correlation radius represent the SQUID-to-SQUID

crosstalk. Since this effect is subdominant, and laboratory measurements usually only provide an upper limit for it, these leakage values are drawn from a Gaussian distribution with zero mean and 0.01% width [187].

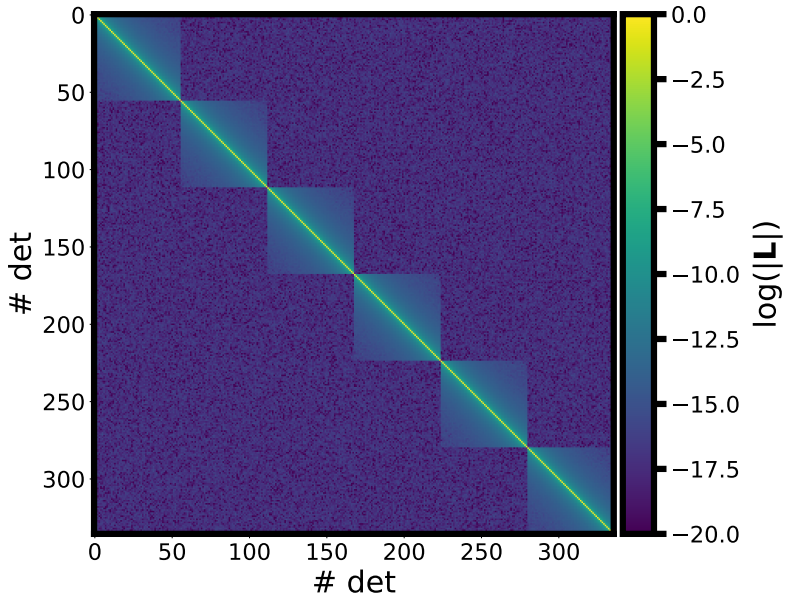

Figure 3.10: The simulated (log) crosstalk leakage matrix $\boldsymbol{L}$ for a subsection of the simulated detectors, given the fMUX setup. The axes correspond to a detector's placement order across the focal plane. The leakage coefficients for detectors which are wired together in the same SQUID are obtained using the power-law leakage term in Eq. (3.25). Leakage decreases as a function of frequency-distance between bolometers. The leakage appears as noise for bolometers that are sufficiently separated in frequency space. This intra-SQUID noise level is also the stochastic SQUID-to-SQUID crosstalk leakage. Diagonal elements are by default set to 1 to avoid inducing systematics that are corrected during the calibration of the bolometers. For this fMUX setup, the figure shows 6 SQUIDs in a wafer, for which bolometers placed at the largest separation distance in frequency space (the top-right and bottom-left corners of each SQUID block) start having crosstalk levels which resemble the overall SQUID-to-SQUID levels. For the μMUX setup, a similar plot would show more intra-SQUID correlations, as there are more detectors within a SQUID. However, due to the frequency spacing choice, most of the additional correlations would be lower than our SQUID-to-SQUID levels.

To understand the effect of crosstalk on the time streams, we follow the toy model of Ref. [187]. For an experiment with only two detector pairs, the (crosstalk- and noise-free) time stream d of each detector is

$$\begin{aligned} d_i &= T_1 + P_1 \\ d_j &= T_1 - P_1 \end{aligned} \Big\} \text{Pair 1} \qquad \begin{aligned} d_k &= T_2 + P_2 \\ d_l &= T_2 - P_2 \end{aligned} \Big\} \text{Pair 2} \quad , \tag{3.26}$$

where we assume that both in-pair bolometers point to the same direction $\hat{\mathbf{n}}_r$ so that $T_r \equiv T(\hat{\mathbf{n}}_r)$ and $P_r \equiv Q(\hat{\mathbf{n}}_r)\cos(2\psi_r) + U(\hat{\mathbf{n}}_r)\sin(2\psi_r)$ for $r \in \{1, 2\}$. The induced crosstalk leakage in

each time stream is then

$$\begin{aligned} d_i^{\rm leak} &= L_{ji} d_j + L_{ki} d_k + L_{li} d_l \\ d_j^{\rm leak} &= L_{ij} d_i + L_{kj} d_k + L_{lj} d_l \\ d_k^{\rm leak} &= L_{ik} d_i + L_{jk} d_j + L_{lk} d_l \\ d_l^{\rm leak} &= L_{il} d_i + L_{jl} d_j + L_{kl} d_k, \end{aligned} \tag{3.27}$$

with no summation, such that the resulting temperature and polarization time-stream leakages are

$$\begin{aligned} d_+^{\rm leak} =& \frac{1}{2}\left[L_{ji} + L_{ij}\right] T_1 + \frac{1}{2}\left[L_{ji} - L_{ij}\right] P_1 \\ &+ \frac{1}{2}\left[L_{ki} + L_{kj} + L_{li} + L_{lj}\right] T_2 \\ &+ \frac{1}{2}\left[L_{ki} - L_{kj} + L_{li} - L_{lj}\right] P_2, \\ d_-^{\rm leak} =& \frac{1}{2}\left[L_{ji} - L_{ij}\right] T_1 - \frac{1}{2}\left[L_{ji} + L_{ij}\right] P_1 \\ &+ \frac{1}{2}\left[L_{ki} - L_{kj} + L_{li} - L_{lj}\right] T_2 \\ &+ \frac{1}{2}\left[L_{ki} - L_{kj} - L_{li} + L_{lj}\right] P_2. \end{aligned} \tag{3.28}$$

A joint calibration of detectors within a pair should cancel the in-pair leakage terms, in which case $L_{ij} = L_{ji} = 0$ for i, j within a detector pair. The leakage terms then become

$$\begin{aligned} d_+^{\rm leak} =& \frac{1}{2}\left[L_{ki} + L_{kj} + L_{li} + L_{lj}\right] T_2 + \frac{1}{2}\left[L_{ki} - L_{kj} + L_{li} - L_{lj}\right] P_2, \\ d_-^{\rm leak} =& \frac{1}{2}\left[L_{ki} - L_{kj} + L_{li} - L_{lj}\right] T_2 + \frac{1}{2}\left[L_{ki} - L_{kj} - L_{li} + L_{lj}\right] P_2. \end{aligned} \tag{3.29}$$

Since $T \gg P$, the dominant temperature leakage term is $T_2 \to T_1$. The multiplicative factor of T_2 in this leakage term is negative, as crosstalk coefficients are mostly negative, which results in a decreased temperature power. This would also be the case if the in-pair leakage elements of Eq. (3.28) are not nullified. The polarization biases are not easily estimated given the analytic leakage terms above. They depend on the specific simulated crosstalk leakage matrix and how it is coupled to the effective cross-linking with which a given sky pixel is observed. In our simulations, we keep the in-pair leakage terms for completeness, and comment on their significance in Subsec. 3.4.2.

The map-level effects of the crosstalk systematic for temperature and polarization are shown in Fig. 3.7. Both temperature and polarization residual maps have smoothed features of the base maps, with amplitudes consistent with the induced leakage level of -0.03%. Future experiments will employ dichroic detectors sensitive to multiple CMB frequencies at the same time, where crosstalk in the electronics will in practice generate crosstalk between the sky signal (and between

its different components) at different frequencies. We did not consider this effect in this work and defer its study to future work.

Lastly, we note that other non-crosstalk-related electronic effects that are related to the readout chain may also introduce systematics that affect the low frequency part of the TOD. Detectors coupled to circuits with large time constants or data acquisition chains having a non-linear analog-to-digital (ADC) response in the electronics might distort the signal along the scan direction. It has been shown that both of these effects can be particularly complicated to deal with in the case of past experiments. Therefore, they should be given serious attention in the analysis of real data. Planck, for example, accounted for ADC non-linearities and time-constant effects in the data analysis, but showed that the major residual contamination induced by both of these effects have an important impact on the largest angular scales $\ell \lesssim 200$ [233, 234]. These scales carry a limited weight in the lensing reconstruction, and we not to investigate them in this work. Furthermore, the typical time constants of modern detectors have a lower amplitude compared to that of Planck [235] so their impact on future CMB experiments should be less severe.

3.3 LENSING ANALYSIS

We reconstruct the lensing potential of each simulation from the different "data" simulation sets. We perform a flat-sky quadratic estimator (QE) lensing reconstruction using the pipeline presented in Chapter 2. After performing the standard quadratic estimator lensing reconstruction, this analysis also includes a filtering step applied to the reconstructed lensing field, which is designed to approximately minimize the corresponding power spectrum errors. The filtering is based on a patch approximation, which considers small patches within the observed area to have homogeneous noise with an effective lensing reconstruction response. This approach was shown to deliver an approximately optimal estimate of the lensing power in the presence of smoothly-varying inhomogeneous noise. We use one set of 10 systematic-free simulations to obtain an averaged reconstructed lensing power spectrum, and then repeat this calculation with sets of 10 simulations with the same CMB and noise realizations but including the effects of one of the systematics discussed in Sec. 3.2.

The lensing reconstruction stages are as follows. First, each simulation from a given set is optimally filtered using the inhomogeneous noise maps for temperature and/or polarization $\boldsymbol{N}$ (constructed from the pixel weights shown in Fig. 3.2, with $\boldsymbol{N}^{-1}$ set to zero in unobserved pixels),

$$\begin{aligned}\bar{\boldsymbol{X}} &\equiv \left(\boldsymbol{b}\boldsymbol{C}^{\rm fid}\boldsymbol{b}^\top + \boldsymbol{N}\right)^{-1}\boldsymbol{X} \\ &= \left(\boldsymbol{C}^{\rm fid}\right)^{-1}\left[\left(\boldsymbol{C}^{\rm fid}\right)^{-1} + \boldsymbol{b}^\top\boldsymbol{N}^{-1}\boldsymbol{b}\right]^{-1}\boldsymbol{b}^\top\boldsymbol{N}^{-1}\boldsymbol{X},\end{aligned} \tag{3.30}$$

where

$$\boldsymbol{X} \in \begin{cases} T & \mathrm{T} \\ (E,B) & \mathrm{P} \\ (T,E,B) & \mathrm{MV} \end{cases} \tag{3.31}$$

is a vector of the CMB maps, $\boldsymbol{b}$ is the transfer function (a CS Gaussian beam with $\sigma_{\rm FWHM}$ width) and $\boldsymbol{C}^{\rm fid}$ is a set of fiducial lensed power spectra which were obtained from CAMB[5] [113]. Eq. (3.30) is solved using the multi-grid-preconditioned conjugate gradient method [98, 100, 123, 148, 153]. Then, the filtered simulations from each "data" set are used to estimate $\hat{\phi}(\mathbf{x})$, the unnormalized QE, using

$$\hat{\phi}(\mathbf{x}) = \frac{1}{2}\bar{\boldsymbol{X}}^\top\frac{\delta\boldsymbol{C}^{\boldsymbol{X}\boldsymbol{X}}}{\delta\phi(\mathbf{x})}\bar{\boldsymbol{X}}, \tag{3.32}$$

where $\boldsymbol{C}^{\boldsymbol{X}\boldsymbol{X}}$ is the covariance of the map $\boldsymbol{X}$ [158]. This QE is biased by non-zero average values of statistical anisotropy in the map (due to e.g. sky masking and noise anisotropy). This mean field (MF) bias, $\langle\hat{\phi}\rangle_{\rm MC}$, is subtracted from the lensing estimator $\hat{\phi}$. The unbiased, and unnormalized, QE is then converted to the convergence estimator

$$\hat{\kappa}_{\mathbf{L}} \equiv \left(\hat{\phi}_{\mathbf{L}} - \langle\hat{\phi}_{\mathbf{L}}\rangle_{\rm MC}\right) \times \frac{2}{L(L+1)}. \tag{3.33}$$

This is then filtered using the effective patch-approximated response $\boldsymbol{\mathcal{R}}^{\kappa}_{\rm eff}$, the reconstruction noise $\boldsymbol{N}^{\kappa}_{0,\rm eff}$ (see Chapter 2) and a fiducial κ spectrum $\boldsymbol{C}^{\kappa\kappa}_{\rm fid}$, to define

$$\hat{\boldsymbol{\kappa}}^{\rm filt} \equiv \boldsymbol{C}^{\kappa\kappa}_{\rm fid}\left(\boldsymbol{C}^{\kappa\kappa}_{\rm fid} + \boldsymbol{N}^{\kappa}_{0,\rm eff}\right)^{-1}(\boldsymbol{\mathcal{R}}^{\kappa}_{\rm eff})^{-1}\,\hat{\boldsymbol{\kappa}}. \tag{3.34}$$

The QE is also normalized in this step using the effective response. This additional filtering is specifically performed on the convergence (κ) map and not directly on $\hat{\phi}$ as the κ reconstruction is approximately local in real space and has approximately white noise. The (noise biased) lensing power spectrum is then obtained from the filtered κ maps,

$$C_L^{\hat{\phi}_1\hat{\phi}_2} \equiv \frac{4}{f_{A,L}n_L L^2(L+1)^2}\sum_{\boldsymbol{\ell}\,\text{in}\,\mathbf{L}\,\text{bin}}\hat{\kappa}^{\rm filt}_{1,\boldsymbol{\ell}}\left(\hat{\kappa}^{\rm filt}_{2,\boldsymbol{\ell}}\right)^*, \tag{3.35}$$

[5] https://camb.info/.

where n_L is the number of modes on the flat sky assigned to lensing multipole L in our simulation maps[6] and

$$f_{A,L} = \sum_p f_p \left(\frac{\mathcal{R}_L^{\kappa,p}}{\mathcal{R}_L^{\kappa,\mathrm{fid}}} \right)^2 \tag{3.36}$$

is the required normalization for our analytic patch approximation estimator (see Chapter 2). f_p is the fraction of the map area in patch p. The MF is calculated twice, from two sets of 48 MC simulations. The subscripts of κ and ϕ in Eq. (3.35) indicate the MF set which was used to debias each estimator. Each MF estimate has independent MC noise, so the lensing power spectrum calculated from a pair of MF-subtracted QEs has no MC noise biases. We do not include systematics in the MF simulations during the analysis, but we comment on this possibility in Sec. 3.5.

Since the lensing power spectrum estimator is a 4-point correlation function, it has a disconnected bias arising from the correlation of Gaussian fields, $N^{\phi\phi}_{0,L}$. There is an additional bias term, $N^{\phi\phi}_{1,L}$, resulting from connected contractions that are not proportional to the lensing spectrum at L. Both terms can be modelled analytically to correct the obtained lensing power spectrum [144, 166], although calculating a realization-dependent $N^{\phi\phi}_{0,L}$ and a $N^{\phi\phi}_{1,L}$ term using the patch approximation corrects the reconstruction biases more optimally. We subtract an estimate of $N^{\phi\phi}_{0,L}$ from each power spectrum estimate, with the respective realization-dependent estimate ${}^{(\mathrm{RD})}N^{\phi\phi}_{0,L}$ obtained from a set of 480 MC simulations [98, 153],

$$\begin{aligned}
{}^{(\mathrm{RD})}N^{\hat{\phi}\hat{\phi}}_{0,L} = \Big\langle & -C_L^{\hat{\phi}\hat{\phi}} \left[\bar{\boldsymbol{X}}_{\mathrm{MC}_1^{\phi_1}}, \bar{\boldsymbol{X}}_{\mathrm{MC}_2^{\phi_2}}, \bar{\boldsymbol{X}}_{\mathrm{MC}_2^{\phi_2}}, \bar{\boldsymbol{X}}_{\mathrm{MC}_1^{\phi_1}} \right] \\
& - C_L^{\hat{\phi}\hat{\phi}} \left[\bar{\boldsymbol{X}}_{\mathrm{MC}_1^{\phi_1}}, \bar{\boldsymbol{X}}_{\mathrm{MC}_2^{\phi_2}}, \bar{\boldsymbol{X}}_{\mathrm{MC}_1^{\phi_1}}, \bar{\boldsymbol{X}}_{\mathrm{MC}_2^{\phi_2}} \right] \\
& + C_L^{\hat{\phi}\hat{\phi}} \left[\bar{\boldsymbol{X}}_{\mathrm{MC}_1^{\phi_1}}, \bar{\boldsymbol{X}}_{\mathrm{dat}}, \bar{\boldsymbol{X}}_{\mathrm{dat}}, \bar{\boldsymbol{X}}_{\mathrm{MC}_1^{\phi_1}} \right] \\
& + C_L^{\hat{\phi}\hat{\phi}} \left[\bar{\boldsymbol{X}}_{\mathrm{dat}}, \bar{\boldsymbol{X}}_{\mathrm{MC}_1^{\phi_1}}, \bar{\boldsymbol{X}}_{\mathrm{MC}_1^{\phi_1}}, \bar{\boldsymbol{X}}_{\mathrm{dat}} \right] \\
& + C_L^{\hat{\phi}\hat{\phi}} \left[\bar{\boldsymbol{X}}_{\mathrm{dat}}, \bar{\boldsymbol{X}}_{\mathrm{MC}_1^{\phi_1}}, \bar{\boldsymbol{X}}_{\mathrm{dat}}, \bar{\boldsymbol{X}}_{\mathrm{MC}_1^{\phi_1}} \right] \\
& + C_L^{\hat{\phi}\hat{\phi}} \left[\bar{\boldsymbol{X}}_{\mathrm{MC}_1^{\phi_1}}, \bar{\boldsymbol{X}}_{\mathrm{dat}}, \bar{\boldsymbol{X}}_{\mathrm{MC}_1^{\phi_1}}, \bar{\boldsymbol{X}}_{\mathrm{dat}} \right] \Big\rangle_{\mathrm{MC}_1^{\phi_1}, \mathrm{MC}_2^{\phi_2}}
\end{aligned}$$

where $\bar{\boldsymbol{X}}_{\mathrm{dat}}$ is the vector of our "data" simulations and the 1 and 2 subscripts refer to the matching CMB and lensing potential realizations of a given MC simulation. Using the realization-dependent debiasing term rather than a general MC $N^{\phi\phi}_{0,L}$ is crucial, as it automatically mitigates systematic biases that arise entirely from small changes to the noise and CMB power spectra that enter the

[6] In a full-sky analysis, $n_L = 2L + 1$.

disconnected bias. We show the differences between ${}^{(\mathrm{RD})}N^{\phi\phi}_{0,L}$ from "data" simulations with and without systematics in Sec. 3.4.2.

The debiased lensing power is then

$$\hat{C}^{\phi\phi}_L \equiv C^{\hat{\phi}_1\hat{\phi}_2}_L - {}^{(\mathrm{RD})}N^{\hat{\phi}\hat{\phi}}_{0,L}. \tag{3.37}$$

We do not debias the reconstructed power using ${}^{(\mathrm{MC})}N^{\phi\phi}_{1,L}$ as this term would vanish when differencing power spectra with and without systematics (because our MC simulations are systematics-free).

Lastly, all 10 power spectra from each set are averaged and compared to the averaged systematics-free power spectrum to assess how the systematics affect the reconstructed CMB lensing power spectrum. We perform temperature-only (T), polarization-only (P) and minimum-variance (MV) temperature+polarization lensing reconstructions for each "data" set to show how the systematics bias different estimators. The resulting systematic effects on lensing reconstruction are shown and discussed in the following section.

3.4 SYSTEMATICS BIASES

3.4.1 CMB POWER SPECTRUM BIASES

We start by examining the effects of the systematics described in Sec. 3.2 on the temperature and polarization power spectra C_ℓ. Apart from providing a good consistency check, these power spectra can help us understand the nature of some of the induced lensing biases and hence suggest possible mitigation techniques.

We first calculate the pseudo power spectra $\tilde{C}_\ell$s of the flat-sky maps using the discrete 2D Fourier components of the weighted temperature or polarization maps, $a_{\boldsymbol{\ell}}$,

$$\tilde{C}_\ell \equiv \frac{1}{n_\ell b^2_\ell} \sum_{\ell \text{ in } \boldsymbol{\ell} \text{ bin}} a_{\boldsymbol{\ell}} a^*_{\boldsymbol{\ell}}, \tag{3.38}$$

where n_ℓ is the number of modes on the flat sky assigned to the multipole ℓ in our simulation maps. To obtain an unbiased estimate of C_ℓ we then deconvolve the effect of the sky mask using the MASTER approach, using a pure estimator to avoid E/B mixing [92] in the polarization field as implemented in the publicly available code `NaMaster`[7] [236, 237] (for the lensing reconstruction, our first optimal filtering step optimally suppresses E/B mixing variance as the filter includes the

[7] https://github.com/LSSTDESC/NaMaster

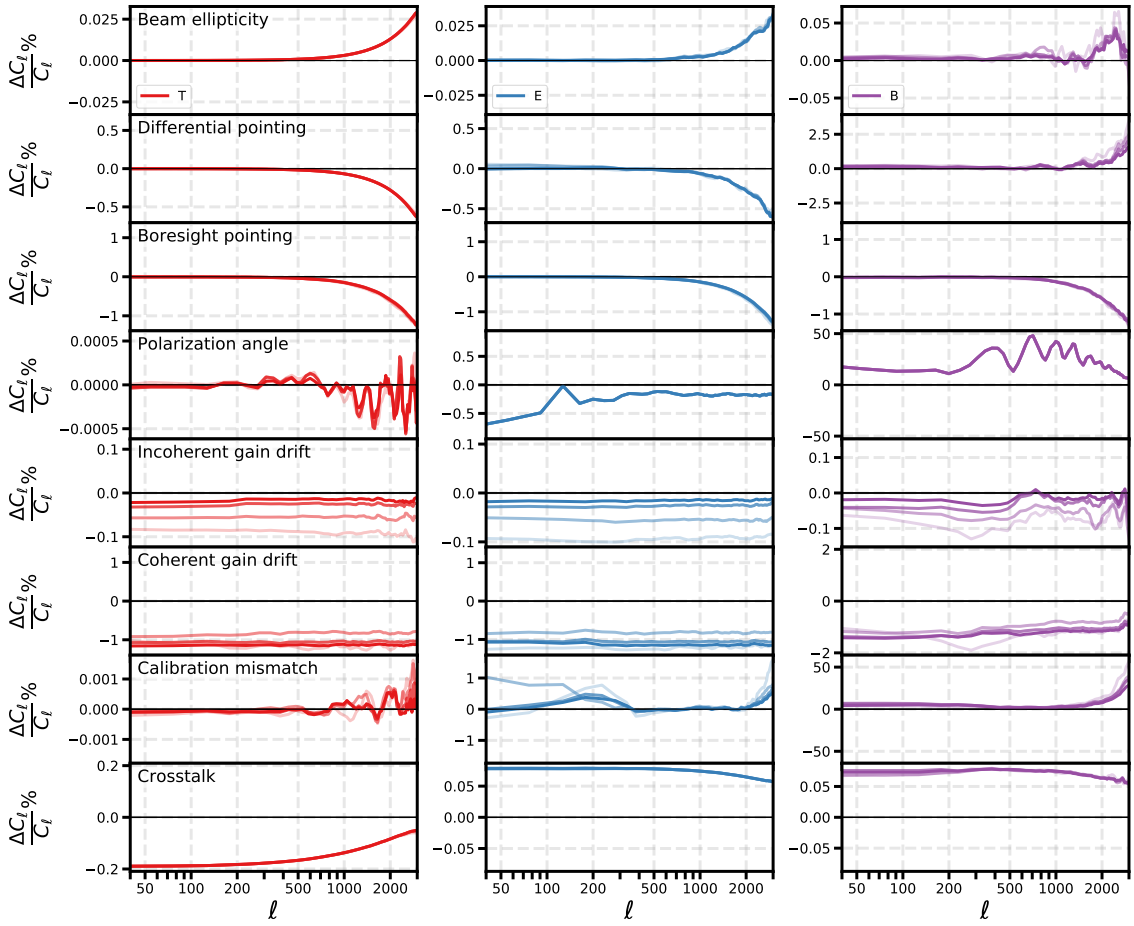

Figure 3.11: The fractional differences between the T (red lines), E (blue lines) and B (purple lines) power spectra C_ℓ with and without systematics in the multipole range $40 < \ell < 3000$. The bright to dark curve shades correspond to observation times of 3, 6, 9 and 12 days respectively. Curves were smoothed with $\sigma_\ell = 5$ to highlight the bias differences for different observation times. For temperature, C_ℓ is mostly signal-dominated, while for the B-mode it is noise-dominated. Noise becomes dominant for the E-mode spectrum at $\ell \gtrsim 2000$.

full noise and mask inhomogeneity, so no further E/B projection is required). The fractional differences between C_ℓs of maps with and without systematics are shown in Fig. 3.11. These power spectra were computed from noise-free simulations in order to highlight the impact of the systematics on the signal.

The fractional differences in the power spectra due to beam ellipticity, differential pointing, and boresight pointing systematics have a similar shape to a beam transfer function, especially for the temperature and E-mode spectra. The B-mode spectrum residual shapes for beam ellipticity and differential pointing are affected by leakage from T and E, which are large relative to the B-mode power amplitude, and causes them to have a somewhat different shape. In practice, the effects of these systematics, combined with the scanning strategy, produce a modified smoothing to the map which is not corrected by the CS beam transfer function b_ℓ used for constructing the power spectra (in our beam-related systematic analyses, the reference beam window function does not account for these beam-like effects, nor do we include any beam uncertainties in the analysis). For the

beam ellipticity and differential pointing systematics, this bias stems from the leakage terms of Eq. (3.11) which are coupled to b_+. The increase of power observed at small scales induced by the beam ellipticity systematic is consistent with the fact that an elliptical beam, whose axes are given by Eq. (3.14), has effectively a smaller average width than a circular Gaussian beam of width $\sigma_{\rm cs}$ (the average width of the elliptical beam is taken as $\sqrt{\sigma_{\rm min}\sigma_{\rm maj}}$).

The boresight pointing systematic smoothing stems from the nature of the systematic itself: jitters during an observation run induce additional smoothing in the map. Fig. 3.11 also shows the fractional differences for 3, 6, 9 and 12 days of observation. For these three systematics, the biases remain relatively constant in time and do not average out. The beam ellipticity systematic produces the smallest biases compared to the other systematics we simulate. The lensing bias induced by these effective beam mismatches is largely corrected at the lensing reconstruction step by ${}^{\rm (RD)}N_{0,L}$, as we show in Sec. 3.5. Using a beam window function with an effective width tailored to each of these systematics in the lensing reconstructing analysis should also mitigate most of their biases that originate from differences in power (see Sec. 3.5).

The polarization angle biases are quite substantial for the polarization power spectra. These biases are characterized well by the analytic approximations [215] for an effective constant angle perturbation $\Delta\psi$,

$$\begin{aligned} C_\ell^{\tilde{E}\tilde{E}} &= \cos^2(2\Delta\psi)\, C_\ell^{EE} - \sin^2(2\Delta\psi)\, C_\ell^{BB}, \\ C_\ell^{\tilde{B}\tilde{B}} &= \sin^2(2\Delta\psi)\, C_\ell^{EE} + \cos^2(2\Delta\psi)\, C_\ell^{BB}, \end{aligned} \tag{3.39}$$

where $\tilde{E}$ and $\tilde{B}$ are the perturbed polarization modes. From these equations, we see that the large C_ℓ^{BB} bias is mostly the C_ℓ^{EE} power spectrum, scaled by a constant which depends on an effective polarization angle error, while the C_ℓ^{EE} bias is an effective gain which also depends on this error, as the $B \to E$ leakage term is sub-dominant. As the analytic approximations describe these biases well for an effective $\Delta\psi$ despite each detector having a different polarization angle error, they may be used to sufficiently mitigate these biases (see Sec. 3.5 for more details on this bias mitigation).

The incoherent gain drift biases evidently decrease with increased observation time. The power spectra from the full 12 observation days have a negligible bias relative to the C_ℓ amplitudes for temperature and polarization. For the coherent gain drift, however, more frequent gain calibrations are required for the biases to average out, or a longer observation time that improves the overall cross-linking. While a long-lasting coherent gain drift induces relatively significant biases, the majority of this effect would be identified and mitigated during early stages of an experiment's data analysis prior to the lensing reconstruction. For example, it is possible to correct for this bias during the map-making stage using the signal variations of bolometers inside the cryostat that

are not coupled to the optical chain, as those are insensitive to the sky signal. Our estimates for this systematic effect are therefore pessimistic. Both of these gain systematics have a relatively constant amplitude effect on the spectra across the considered ℓ-range, as expected from the mean gain described in Subsec. 3.2.5.

For the calibration mismatch systematic biases, while these also decrease with longer observation times, they continue to be significant for the polarization spectra after 12 observation days. Expectedly, the temperature power spectrum biases are small, as they stem from $P \rightarrow T$ leakage which is small compared to the temperature power amplitude. The $T \rightarrow P$ leakage, however, is quite substantial, especially for the mid-ℓ-range B-mode power spectrum. As the B-mode spectrum is noise-dominated at $\ell > 1000$, the large bias in that multipole range is not very significant.

As seen in Fig. 3.11, crosstalk is the only systematic for which the temperature biases are higher than the polarization biases. Excluding the in-pair leakage terms of Eq. (3.28) in both temperature and polarization time streams results in a $\sim 30\%$ bias decrease. Since the overall leakage is already quite negligible, we reconstruct the lensing potential from systematics which include the in-pair leakage terms. As discussed in Subsec. 3.2.7, the temperature power spectrum bias is negative. For our specifications the resulting polarization power spectra have additional power.

3.4.2 LENSING POWER BIASES

As there are various ways in which the lensing power can be used for constraining cosmological observables, it is useful to show the significance of the systematics-induced lensing biases in several ways. We first demonstrate how significant these biases are with respect to the lensing power spectrum. The fractional differences between the averaged reconstructed lensing power from simulations with and without systematics for T, P and MV reconstructions are shown in Fig. 3.12.

All bias amplitudes are below the 5% level compared to the lensing power, with most under 0.5%. These levels are generally consistent with their expected values from the C_ℓ-level biases. The main difference between the C_ℓ and the $\hat{C}_L^{\phi\phi}$ biases is in their shapes. Beam-like C_ℓ biases appear as a bias on the ϕ power spectrum amplitude. This is expected to be roughly constant on large scales, as the $\hat{\phi}$ estimator is normalized using biased fiducial CMB power spectra, so the resulting $\hat{C}_L^{\phi\phi}$ have a different amplitude. Moreover, for beam-like systematics the MV reconstruction biases appear to be bounded by the T and P biases. The most significant bias of these cases comes from the boresight pointing systematic, which is at a 1% level for an MV

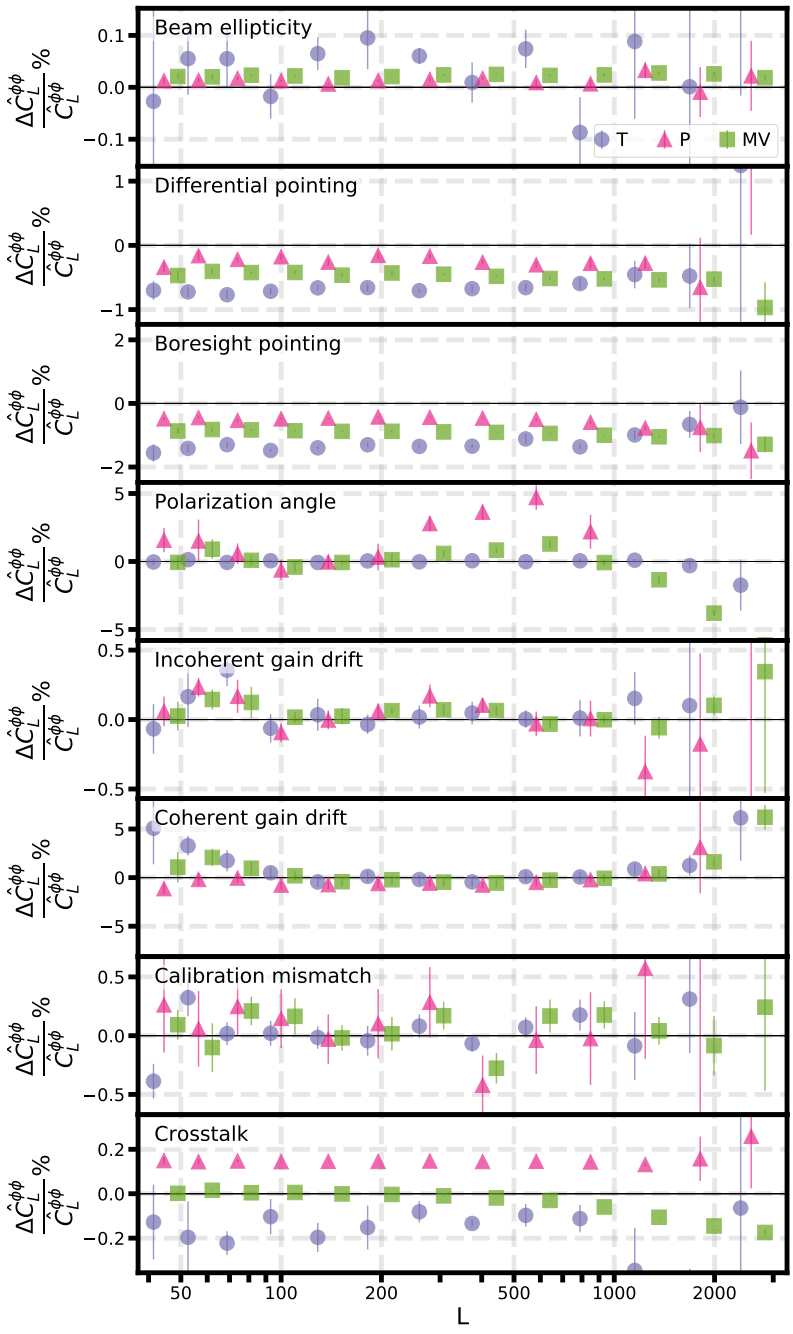

Figure 3.12: The fractional differences between $\hat{C}_L^{\phi\phi}$ with and without systematics for T (purple circles), P (pink triangles), and MV (green squares) lensing reconstructions. The reconstruction noise dominates at $L \gtrsim 200$ for T and P reconstructions, and at $L \gtrsim 300$ for MV reconstruction. The 13 bin widths are log-spaced between 10 and 1000.

reconstruction. As with the power spectra, the beam ellipticity biases on the reconstructed lensing power spectra are negligible.

The polarization-only lensing reconstruction is most problematic in the presence of unmitigated polarization angle errors. From our pessimistic probability distribution for $\Delta\psi$, the resulting amplitude of polarization-only lensing biases is up to $\sim$5% for $L < 1000$. MV reconstruction benefits from the low $P \to T$ leakage, and the bias levels remain below $\sim$1.5% for the same multipole range.

The gain-related systematics biases are randomly scattered around zero with varying levels of significance. As with the C_ℓ, the most prominent bias is that of the coherent gain drift. Its temperature-only reconstructed power is $\sim 5\%$ higher compared to the systematics-free reconstructed power in the signal-dominant multipole range, although with a large uncertainty. Its MV reconstruction bias is $\lesssim 2.5\%$.

For crosstalk, while the reconstruction biases are consistently below 0.3%, the MV reconstruction proves to be the least biased over the signal-dominated L-range. This is most likely due to the opposite signs of the biases in T and P reconstructions, which seems to cancel in the combined reconstruction.

The only systematics for which the MV biases are the smallest of the three are incoherent gain drift, calibration mismatch and crosstalk.

Another way to quantify systematic-induced lensing biases is by performing a likelihood analysis to estimate their detectability in the lensing spectrum. Although significance values estimated from our 12-day scaled-noise simulations are not expected to correspond to what an experiment with a realistic observing time would see, they provide a useful reference point. We use the simplified log-likelihood

$$\ln \mathcal{L} = -\sum_{L_{\rm bin}} \frac{A^2 \left(\hat{C}^{\phi\phi,\rm syst}_{L_{\rm bin}} - \hat{C}^{\phi\phi}_{L_{\rm bin}}\right)^2}{2\sigma^2_{\hat{C}^{\phi\phi}_{L_{\rm bin}}}}, \tag{3.40}$$

where $\hat{C}^{\phi\phi,\rm syst}_{L_{\rm bin}}$ and $\hat{C}^{\phi\phi}_{L_{\rm bin}}$ are the reconstructed lensing power spectra with and without systematic effects, respectively, in a specific multipole bin $L_{\rm bin}$. The parameter A is the amplitude parameter for the bias with uncertainty σ_A, which quantifies how significant the bias is compared to the reconstructed lensing power error bar $\sigma_{\hat{C}^{\phi\phi}_{L_{\rm bin}}}$. The second derivative of $\mathcal{L}$ with respect to A is the inverse variance of A, σ_A^{-2}, such that

$$\sigma_A = \left[\sum_{L_{\rm bin}} \frac{\left(\hat{C}^{\phi\phi,\rm syst}_{L_{\rm bin}} - \hat{C}^{\phi\phi}_{L_{\rm bin}}\right)^2}{\sigma^2_{\hat{C}^{\phi\phi}_{L_{\rm bin}}}}\right]^{-\frac{1}{2}}. \tag{3.41}$$

A constant bias for which $\sigma_A < 1$ will be detectable by more than 1σ, and vice versa. The values of σ_A^{-1} for the different systematics are shown in Table 3.1. For the study-case we considered, the only systematic that can be detected by more than 1σ is the polarization angle systematic. For this systematic, the unmitigated polarization-only bias detection level is the highest, however including the temperature map in the analysis significantly reduces the bias significance. Only the boresight pointing, coherent gain drift and polarization angle systematics produce biases with

detection levels above 0.5σ. Unlike the polarization angle systematic, for coherent gain drift the highest bias detection level occurs when using the temperature map alone to reconstruct the lensing potential, while for polarization angle this is the case for only for the polarization-only reconstruction.

For differential beam ellipticity, we found that the leakage reduced to significantly below the detection level, mainly due to the number of bolometers used. An experiment with the same beam width and only 10-100 detectors, or larger beam-width and similar number of detectors, would be more affected by this systematic.

Apart from the polarization angle systematic, the biases resulting from our coherent gain drift model also seem to be relatively problematic for SO and future CMB experiments. This is not the case for the incoherent drift, mainly because scanning the sky repeatedly with a large number of detectors, each of which has a different gain drift, helps to average out the effect. Performing gain calibrations at shorter time intervals, or observing each sky area more times, may mitigate some of the effect of coherent drifts. On the other hand, experiments using a scanning strategy with less cross-linking may find a larger effect.

Systematics	T	P	MV
Beam ellipticity	0.06	0.00	0.01
Differential pointing	0.27	0.09	0.28
Boresight pointing	0.52	0.20	0.52
Polarization angle	0.05	2.20	0.60
Incoherent gain drift	0.36	0.05	0.04
Coherent gain drift	0.56	0.28	0.64
Calibration mismatch	0.38	0.11	0.09
Crosstalk	0.11	0.06	0.03

Table 3.1: Detection significance of systematics biases with respect to the lensing power uncertainty for T, P and MV reconstructions. The values in the table are calculated using Eq. (3.41). The values are color-coded from most significant biases (darker red) to less significant (lighter red). The detection significance for the polarization-only reconstruction beam ellipticity bias is $\sim 1 \times 10^{-3}$. Assuming that all the biases are independent, the combined bias is measured with a $\sim 0.9\sigma$ significance for MV and T reconstructions.

Our chosen parameters for modelling the calibration mismatch are relatively pessimistic, as most CMB experiment have a lower gain uncertainty. While this systematic can potentially be a problem, it is evident that for our specifications, especially the number of detectors and scanning

strategy, even this pessimistic case does not affect our reconstructed lensing power spectra in an important way. Decreasing the gain uncertainties by a factor of 10 to $\approx 1\%$ compared to the baseline case shown here would lead to $C_L^{\phi\phi}$-level biases lower than $\sim 0.1\%$ for all three reconstruction setups and detection levels of 0.18 (T), 0.01 (P), and 0.03 (MV). A moderate improvement compared to the pessimistic case we assumed should thus already be sufficient to mitigate this bias to an acceptable level, although a more realistic scanning time may also be sufficient.

Our crosstalk simulations use realistic but relatively pessimistic parameters. Excluding in-pair leakage terms, which can be usually corrected when performing in-pair gain calibrations, reduces the C_ℓ bias levels by 30%. Optimizing the frequency spacing of the different bolometers can also be achieved to establish lower leakage levels. Since the overall bias levels we show are very low, we did not perform further optimization to our crosstalk modelling. Increasing the crosstalk leakage coefficient distribution's mean and width by a factor of 10, the C_ℓ bias levels also increased by a factor of 10, although the significance stays below $\sim 1\sigma$. This suggests that controlling the crosstalk leakage levels to about -0.3% is sufficient for the purpose of lensing reconstruction. This crosstalk level is higher than the expected performance of future-generation instruments based on μMUX technologies. We therefore conclude that crosstalk is not expected to become a major systematic for lensing. Moreover, since crosstalk is constant in time (as it mainly depends on the wiring of the electronics), it should be possible to account for its potential biases, at least partly, in the simulations used to evaluate the mean field of the quadratic estimator if needed (see Sec. 3.5 for more details). For the most extreme scenarios, the crosstalk leakage matrix can be estimated from dedicated calibration data and used to correct for its effect at the time-stream level prior to the map-making step, but at the cost of inducing correlated noise [238].

The last thing we consider for characterizing systematics-induced lensing biases relates to the lensing curl signal. The CMB photon deflection field $\mathbf{d}$ is a vector field defined on the sphere, and as such it can be written as a combination of a gradient and a curl-like mode, $\mathbf{d} = \boldsymbol{\nabla}\phi + \star\boldsymbol{\nabla}\Omega$, where ϕ is the lensing potential and Ω the curl potential[8]. In addition to biases in the lensing potential power spectrum, we also tested whether instrumental systematics produce a non-zero lensing curl signal. While cosmological curl signal is already expected to be non-zero from second-order lensing effects [161, 239–241], these would remain undetectable in the curl power spectrum for the foreseeable future. As for the lensing potential, the lensing curl mode can also be reconstructed using the quadratic estimators [242]. We use a pipeline analogous to the one described in Sec. 3.3 for ϕ, but using the lensing response functions relevant to Ω. We found that

[8]We recall that in two dimensions and in the flat sky approximation $\star\hat{e}_x = \hat{e}_y$ and $\star\hat{e}_y = -\hat{e}_x$.

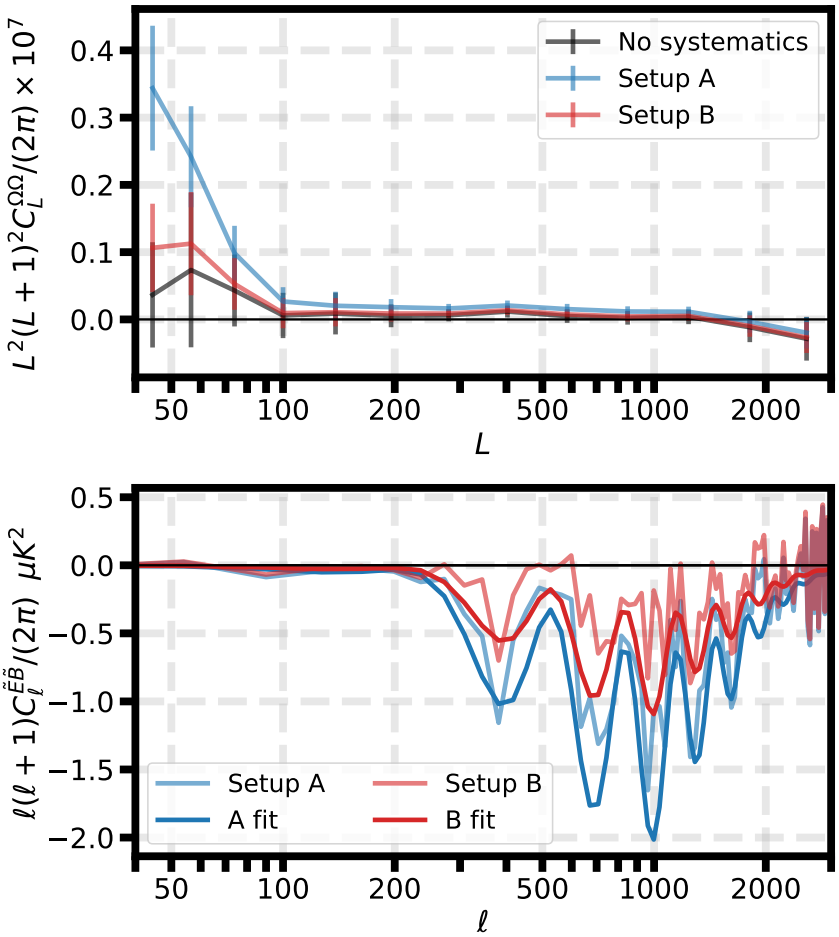

Figure 3.13: *Top*: The lensing curl signal induced by the polarization angle systematic for a polarization-only reconstruction. For setup A ($\Delta\psi \in \boldsymbol{N}(-1.1°, 0.5°)$, blue line), this signal is detectable by just over 2σ at $L \lesssim 50$. For setup B ($\Delta\psi \in \boldsymbol{N}(-0.5°, 2.0°)$, red line), this signal has $\lesssim 1\sigma$ detection level for $L > 40$. The polarization angle shift of setup A was used as a baseline in the lensing biases analysis. *Bottom*: $C_\ell^{\tilde{E}\tilde{B}}$ power spectra of one simulation induced by a miscalibration of the polarization angles of the detectors for setup A (blue) and setup B (red). The darker solid lines for each power spectrum show the power spectra corresponding to the best-fit value of $\Delta\psi$ obtained by fitting the analytic approximation of Eq. (3.44) to the simulated $C_\ell^{\tilde{E}\tilde{B}}$ and assuming the theoretical E and B power spectra expected from the underlying cosmological model. The recovered effective values of $\Delta\psi$ for each fit deviate from the mean of the input error by up to $\sim$6%.

the only systematic which produces a significant non-zero lensing curl signal is the polarization angle miscalibration. The resulting curl signal, shown in Fig. 3.13, manifests more significantly at large scales, for $L \lesssim 50$. When the polarization angle perturbations are drawn from the less pessimistic distribution of setup B, this signal is less prominent and remains below detection levels. This suggests that having a non-zero curl signal could be a useful tool for diagnosing problems with the calibration of polarization angles.

3.5 MITIGATION TECHNIQUES

Systematics mitigation can generally be performed at different levels, from instrument planning through data collection to the final analysis stage. In this section, we focus on mitigation techniques performed at the analysis stage. This is mainly motivated by the results of our work, which demonstrate that our realistic and conservative assumptions on instrument specifications already yield relatively small bias levels.

Before discussing analysis-level mitigation techniques, we first briefly discuss how an experiment's scanning strategy affects systematic biases. Some systematic biases are automatically mitigated by scanning the same region of the sky from different directions. Each time a given sky pixel is observed by a different detector pair, the final map value in the pixel is less sensitive to systematic variations between detectors (as well as a reduced instrument white-noise level). Observing the same sky area with the same detector pair also contributes toward mitigation, as a given detector pair may also have systematics that vary randomly in time. This is important when an experiment plans its scanning strategy, as there is a trade-off between repeated observation of specific areas in a given time frame, and using the same given time frame to scan more areas of the sky at the expense of reduced cross-linking.

In our simulations, we modelled observations over a relatively small sky patch, within which most CESs had some overlapping region. For the systematics that do not depend on properties of the instrument that are constant in time, we found that the process of repeated observation over the same area reduces most of the biases in the CMB maps and power spectra, which in turn also reduces the biases on the lensing reconstruction power. A scanning strategy can also be devised to mitigate specific systematic biases. For example, differential pointing and differential gain systematics can be mitigated by introducing a boresight rotation to the scanning strategy [201]. It may also be possible to mitigate differential pointing effects by knowing analytically how the scanning strategy couples to the pointing signal [243]. To avoid experiment-specific conclusions, in this work we adopted the most conservative approach and did not try to implement scans that

are optimized to mitigate systematic effects (as done for several instruments); most of the biases we find are in any case only of marginal importance. Below, we also show that the differential pointing and polarization angle biases can be mitigated also at the analysis stage. Mitigation at the analysis stage may be more generally applicable, as it does not depend strongly on a given experiment's scanning strategy or other specifications.

As for mitigating systematic biases at the analysis stage, we first discuss techniques that are potentially helpful at the map-making level. Solving Eq. (3.2) can be done more optimally by including deprojection terms in the signal vector, or by employing filters to mitigate unwanted signal contaminants. In our efforts to mitigate some of the gain drift biases, we tried using a simple deprojection technique to solve for an additional gain which contaminates the polarization maps [222], but depends only on the sky pointing. This is done by solving for an additional sky component G which enters the polarization time stream as

$$d_- = G + Q\cos(2\psi) + U\sin(2\psi)\,. \tag{3.42}$$

Our simulated gain variation is not constant in time, so this deprojection model did not mitigate any of the biases we observe. Using different deprojection methods, such as those using template fitting [244] or solving for additional degrees of freedom that mimic leakages that depend on $\cos(2\psi)$ and $\sin(2\psi)$ may help mitigating gain or beam-related biases [243], at the cost of an increased noise in the final map.

Mitigating systematic biases on the lensing power spectrum specifically can also be achieved by calculating cross-spectra. Reconstructing the lensing potential using different pairs of maps from different observation runs, frequencies, detector-pair sets, or other data splits, and using these to calculate cross-power spectra, could help in averaging out systematic effects, as each map is affected differently by random systematics and the size of the connected bias terms may be substantially reduced [245]. The resulting power spectrum might be less affected by the systematics, but its uncertainty is likely to increase due to the estimator being less optimal, as well as potentially more issues with missing pixels and other issues affecting map-making using less data.

The lensing reconstruction analysis could also adopt some mitigation techniques. Due to the strong dependency of a lensing reconstruction analysis on the experiment forward modelling through MC simulations, the most direct way of mitigating most biases is by modelling the systematics in the MC simulations used to obtain the debiasing terms, namely MF, ${}^{(\mathrm{RD})}N^{\phi\phi}_{0,L}$ and ${}^{(\mathrm{MC})}N^{\phi\phi}_{1,L}$. In our analysis, the only similarities between the MC and "data" simulation sets are the instrument specifications and scanning strategy. Investing resources into more precise modelling

of systematics in the MC simulations could reduce their impact on the lensing reconstruction if they are partly simulated. However, not all systematics can be accurately simulated, and some parameter uncertainty in the systematic modelling would not mitigate lensing reconstructions biases entirely. Since the detection level of the systematics-induced lensing biases shown in this work are already low, we do not explore this method of mitigation. We do, however, compare between the MF debiasing terms with and without systematics to understand if any systematics-induced biases may be mitigated by including systematics in the MF simulations.

Including systematics in the MC simulations will only give a non-zero contribution to the mean field in specific cases, e.g. where the amplitude of the noise mean field is affected by systematics, or where systematics-inducing parameters are known (e.g. the actual beam ellipticities or the crosstalk scheme). Systematics leading to a specific spatial pattern that depends on the specific actual realization or time variation of random variables would average to zero if only random realizations can be simulated. To test whether modelling randomized systematic effects in the MF simulations might help, we use random variables with the same parameter distributions as with the "data" sets. The fractional differences between the cross-MF power spectra $C_L^{\mathrm{MF}_1\mathrm{MF}_2}$ with and without systematics and the lensing power spectrum are shown in Fig. 3.14. The resulting biases are all consistent with zero, meaning that including a level of variance in the systematics modelling in the MF simulations may not improve the lensing reconstruction. Planck showed that for their specifications (e.g. beam size and scanning strategy) the known beam ellipticity was also negligible when calculating the MF [246] over the multipole range we consider. We have shown that systematic effects from the narrow beams that we considered are relatively negligible for lensing reconstruction, so we do not attempt to model them in the MF simulations. The polarization angle and coherent gain drift systematics are more important, but including these systematic effects in the MF simulations with parameter uncertainties similar to those used in the "data" simulations did not result in bias mitigation. We did, however, find that including the polarization angle systematic in the MF simulations when reconstructing the curl lensing signal successfully mitigated the signal to undetectable levels.

The other debiasing term, ${}^{(\mathrm{RD})}N_{0,L}^{\phi\phi}$, already responds to the "data" CMB power spectrum amplitude and shape, and mitigates (to leading order) some of the biases that affect the connected reconstruction noise. The fractional differences between ${}^{(\mathrm{RD})}N_{0,L}^{\phi\phi}$ for a given realization for "data" simulations with and without systematics are shown in Fig. 3.15. The calibration mismatch systematic bias is largely mitigated by the ${}^{(\mathrm{RD})}N_{0,L}^{\phi\phi}$ subtraction, especially for polarization-only reconstruction; its lensing power spectrum-level biases are less than 0.5% of the lensing power spectrum amplitude while its ${}^{(\mathrm{RD})}N_{0,L}^{\phi\phi}$ amplitude is about 1% higher than the

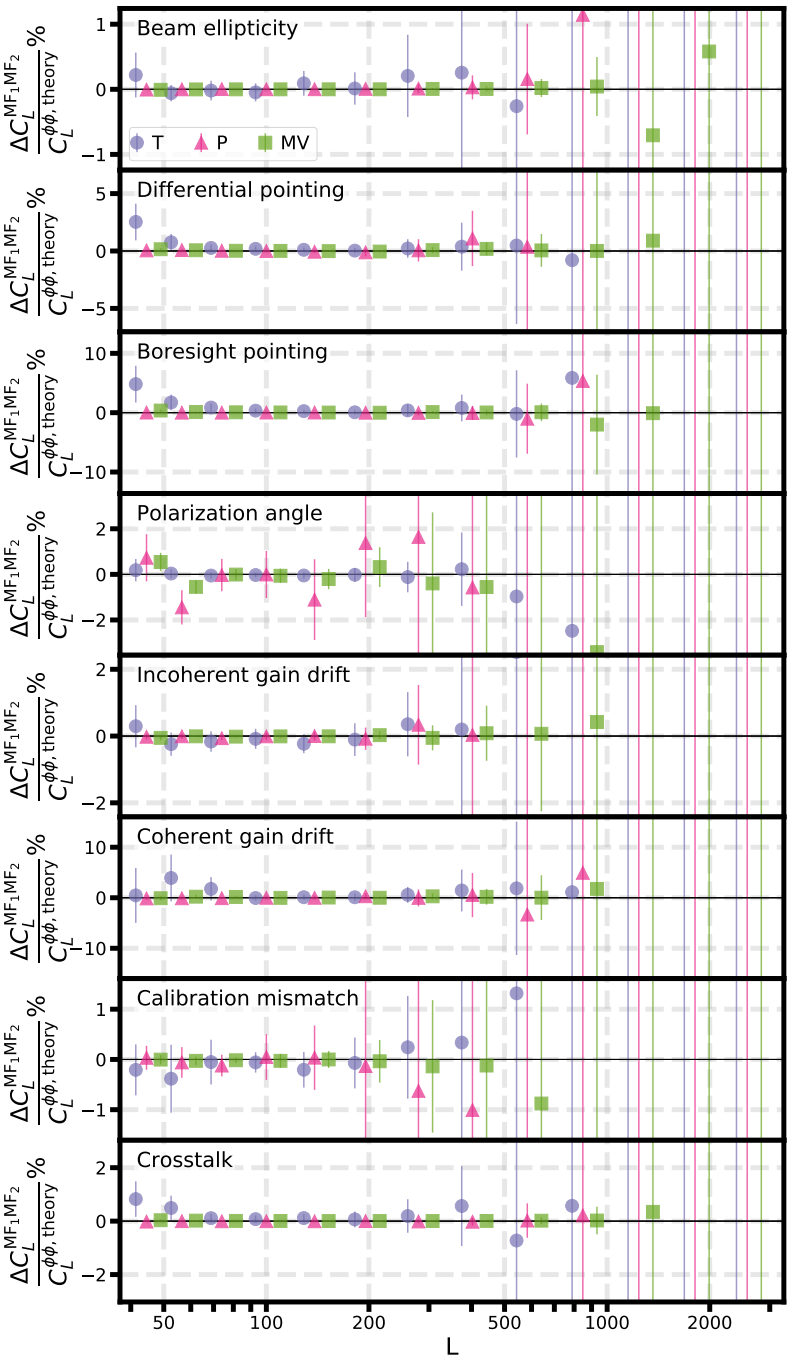

Figure 3.14: The fractional differences between $\Delta C_L^{\mathrm{MF_1MF_2}}$ and $C_L^{\phi\phi,\mathrm{theory}}$. $\Delta C_L^{\mathrm{MF_1MF_2}}$ is the difference between the MF cross-spectra calculated using simulations with and without systematics for T (purple circles), P (pink triangles), and MV (green squares) lensing reconstructions.

systematic-free ${}^{(\mathrm{RD})}N_{0,L}^{\phi\phi}$ amplitude. The ${}^{(\mathrm{RD})}N_{0,L}^{\phi\phi}$ amplitude is also affected by the biases of the other systematics, however their lensing spectrum biases remain large compared to the systematics-free spectrum. The largest ${}^{(\mathrm{RD})}N_{0,L}^{\phi\phi}$ amplitude deviation results from the polarization angle and coherent gain drift systematics. While the use of this debiasing term does help with decreasing the lensing spectrum bias, it does not necessarily mitigate it to negligible significance levels.

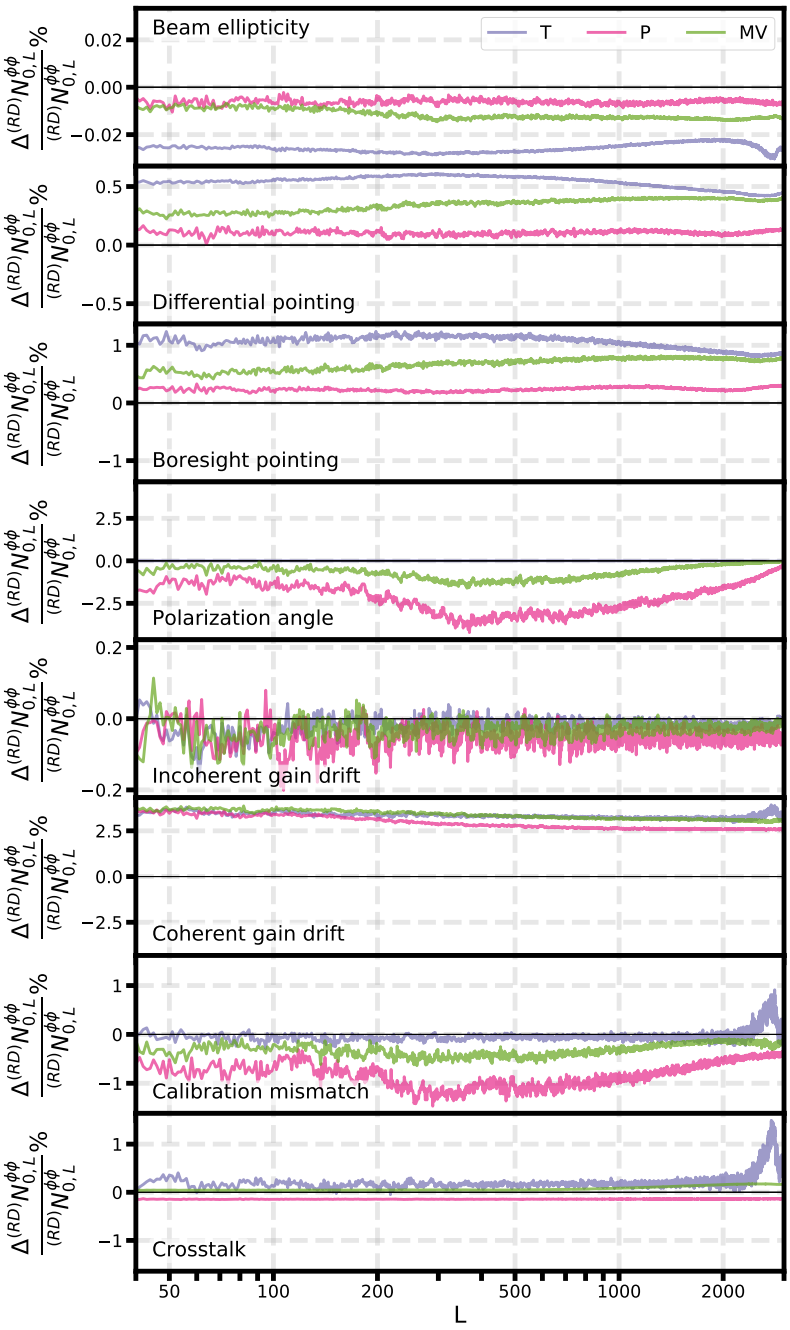

Figure 3.15: The fractional differences between ${}^{(\mathrm{RD})}N^{\phi\phi}_{0,L}$ with and without systematics for T (purple lines), P (pink), and MV (green lines) lensing reconstructions for a given CMB+noise realization "data" simulation.

As an alternative to full modelling of systematic effects in the MC simulations, some biases can be mitigated by using a different fiducial beam in the lensing reconstruction analysis. We have shown in Subsec. 3.4.1 that the main beam ellipticity, differential pointing and boresight pointing systematics biases appear as a change in the effective beam model. In practice, the beam model is often determined by dedicated observations of point sources [212, 222, 238]. These empirical measurements include the same observational systematics, so the effective beam model determined from them should already mitigate some of the beam-like effects to some extent.

To test how well an effective beam can mitigate the lensing systematics we, performed lensing reconstructions which included an effective beam. We corrected our baseline Gaussian beam, which has a width $\sigma_{\rm FWHM}$, by a correction beam with width $\sigma_{\rm corr}$. The value of $\sigma_{\rm corr}$ was obtained from fitting the C_ℓ^{TT} fractions with and without systematics to an effective circular Gaussian beam model. The total width of the effective beam, $\sigma_{\rm eff}$, is then given by

$$\sigma_{\rm eff}^{-2} \equiv \sigma_{\rm FWHM}^{-2} + \sigma_{\rm corr}^{-2}. \tag{3.43}$$

More generally, one could define an effective beam transfer function as a general function of ℓ, but using the simple Gaussian model already captures the main systematic effect.

Boresight pointing jitters are expected to be well captured by an effective beam. We find that the correction determined from the power spectrum gives an effective beam correction $\sigma_{\rm corr}$ that matches the input pointing distribution width very well (13 arcseconds, matched to about 0.4%). Applying this effective beam lowers the lensing bias detection levels to 0.06 (T), 0.001 (P), 0.07 (MV). The boresight pointing jitters are not correlated to the scan in the basic model we considered, and do not depend on detector-level properties, which makes this effect simple to mitigate. The main effect should be included automatically in beam measurements from point sources. In more realistic cases, pointing errors might be correlated to the motion of the telescope, or through systematic errors in the pointing solution that relate the recorded position of the telescope encoder to the true sky position. Such correlations could introduce larger biases in lensing reconstruction as they could mimic correlated shifts on the sky, however they are hard to model and quantify in advance as they are highly instrument-dependent. A similar mitigation strategy could, however, reduce the overall effect. An effective beam transfer function known to at least 10-20% precision should be sufficient to mitigate the boresight pointing bias effectively.

Differential pointing produced an effective-beam like effect, but also $T \rightarrow P$ leakage. This systematic is mainly due to distortions in the focal plane and in the telescope mirror, so the effect is coupled to the scanning strategy and overall cross-linking of different pixels. Employing an effective beam in this case can only partly mitigate the effect, since it would not correct $T \rightarrow P$ leakage. The beam correction is also likely to be less well captured by point-source beam measurements, since point source scans are usually different than the scanning strategy used for CMB observations. If the leakage corrections can be constrained or measured well enough from calibration observations, and they are relatively stable in time, it may be possible to propagate them through simulations to define an effective transfer function that would mitigate most of the effect. We found that by using the effective beam determined from the power spectra, the differential pointing bias detection significance levels decrease to 0.03 (T), 0.02 (P) and 0.01 (MV). These

residual detection levels are consistent with the biases expected from having only the leakage terms involving b_- of Eq. (3.11) that give rise to $T \leftrightarrow P$ leakage in the data simulations. Using an effective beam should therefore remove the majority of the differential pointing bias, as the $T \leftrightarrow P$ leakage biases are subdominant. The fitted correction width $\sigma_{\rm corr}$ deviates from the mean of the differential pointing distribution, 15 arcseconds, by about 12%.

The beam ellipticity bias mainly originates from the b_+ leakage terms; removing the b_+ terms results in biases which are $\sim$2 orders of magnitude smaller, so the majority of this bias is also corrected by an effective beam. Measurements of the beam transfer function from calibration observations should be sufficient to capture the majority of the ellipticity systematic and correct for it. However, there may be some deviations between the "true" and measured beam shapes due to the coupling to the scanning strategy.

To assess how accurately the effective beam needs to be known, we used a beam correction width reduced by a factor of 2 from the best value to correct for the differential pointing bias. This lead to a reduction of the bias detection levels by about a factor of 2 compared to using no effective beam. For boresight pointing, the effective beam is likely to be measured better than this, as calibration observations are expected to estimate the correct beam shape for this systematic quite well; however, our results suggest that even an approximate beam model may be sufficient to substantially reduce the lensing biases.

The most common method for mitigating polarization angle systematics is by fitting the resulting non-zero EB cross-spectrum to the analytical expression [215],

$$C_\ell^{\tilde{E}\tilde{B}} = \frac{1}{2}\sin\left(4\Delta\psi\right)\left[C_\ell^{EE} - C_\ell^{BB}\right], \tag{3.44}$$

where $\tilde{X}$ is a polarization field affected by the polarization angle systematic for a constant angle shift $\Delta\psi$. To test the effectiveness of this mitigation method, we fitted the resulting EB power spectrum, shown in Fig. 3.13, to the analytic formula of Eq. (3.44) using the theoretical E and B power spectra to obtain the effective angle $\Delta\psi$, and used it to rotate the input Q and U maps for the lensing analysis. Although this method approximates the systematic to be a global map-level effect, while the systematic is in practice injected at the per-detector level, it corrects for most of the effect and considerably mitigates both the lensing biases and the curl signal to undetectable levels. After mitigation, the lensing bias detection levels reduce to 0.04σ (P) and 0.03σ (MV). This mitigation does not affect the already-negligible bias detection levels for a temperature-only reconstruction significantly. We note that this mitigation strategy makes assumptions on the underlying cosmology, i.e. $C_\ell^{\tilde{E}\tilde{B}} = 0$ in absence of systematics. This suggests that it could also unwantedly remove any signals which are caused from other sources, such as cosmic

birefringence. As this systematic produces a lensing curl signal, which could potentially also be coupled with cosmic birefringence, it may be possible to include the curl signal as an additional diagnostic tool to break the degeneracy between systematic-induced and cosmologically-induced rotations.

Gain systematic effects can also be mitigated to some extent, following the common practice of most CMB ground-based experiments, by cross-correlating the resulting maps with external data sets such as the Planck maps [171, 247–249]. This calibration can help correct an overall mean gain error, however position-dependent gain variations may still remain after this absolute gain calibration.

In this work, we have we used QEs to assess the effect of instrumental systematics on the lensing reconstruction. Other reconstruction methods could have different sensitivities to these effects, and some may be able to mitigate systematic effects, at least partially. For example, one could in theory produce a bias-hardened reconstruction which is less sensitive to various systematic effects by construction [169]. Methods which avoid the need for reconstruction bias subtraction [250] may also be less sensitive to instrumental systematics, as they do not need to accurately model systematics that affect debiasing terms that are no longer needed. Performing a lensing reconstruction from split data may also prove to be useful against systematics biases, as different data points are affected differently by systematics (and uncorrelated instrument noise) such that their effect on the lensing contractions may average out [245]. Nonetheless, the lensing pipeline we used proved to perform well against these biases, as most of their effects could be corrected directly by ${}^{(\mathrm{RD})}N_0$ subtraction, by implementing an effective beam in the lensing analysis, or by rotating the polarization maps prior to the lensing analysis.

3.6 CONCLUSIONS AND FUTURE PROSPECTS

In this work, we explored how various instrumental systematics affect the lensing reconstruction power spectrum. We reconstructed the lensing potential from CMB simulations that include realistic levels of contamination due to different instrumental systematics expected for an SO-like instrument, and assessed the significance of the resulting biases. We showed that for the instrument specifications and scanning strategy we used, most of the systematics we considered will have a relatively small effect on lensing reconstruction for upcoming CMB experiments, with significance levels of up to 0.5σ, apart from the boresight pointing, polarization angle and coherent gain drift systematics, which produce biases with $> 0.5\sigma$ significance levels when left unmitigated. We also investigated whether these instrumental systematics produce a lensing curl

signal, and found that when not calibrating for polarization angle errors the signal can be detectable. All of the significance levels we have presented in this work might be somewhat different for a full observation run, especially for gain drifts and calibration mismatch where the biases average out with time. Systematics that appear in the maps' power spectra as an effective beam are also likely to be substantially mitigated once the beam is empirically calibrated.

Future CMB experiments, such as CMB-S4, which will produce CMB maps with even lower instrument noise, may be more sensitive to these systematics, as their lensing reconstruction noise level is expected to be even lower. A more accurate quantitative assessment of the impact of instrumental systematics on lensing reconstruction for a given experiment depends on the details of its scanning strategy, focal plane configuration and instrument properties. These can only be characterized in their full complexity during the observational campaign. As such, the absolute value of the systematics we explored may differ from the results presented in this work. Nonetheless, our results are a useful guide toward identifying the most relevant potential problems and planning the lensing analysis for upcoming ground-based CMB experiments.

Throughout this work we made various simplifications and assumptions, which should be investigated more carefully in the future. Modelling multi-frequency bolometers would allow for a more robust estimator, with some handle on frequency-dependent systematics and foregrounds. However, having more than one band potentially increases the range of possible systematics, and some small systematics could become relatively more important due to the process of foreground cleaning. We also neglected any foreground residuals in the post-cleaning CMB maps and any systematics that may couple to bright foreground emission. Another effect which may be crucial for upcoming ground-based CMB experiments is correlated noise. When observing the sky from the ground, the resulting time streams are contaminated by atmospheric emission. This could have a significant impact on the resulting CMB maps, which could then bias the lensing reconstruction. Residuals from various correlated noise cleaning methods could also negatively affect the lensing reconstruction. Additional filtering on the map level could improve the reconstruction accuracy from correlated-noise-contaminated maps [170], however a full optimization analysis for such methods has not yet been performed. Exploring systemically how filtering affects lensing biases specifically would require implementing a more sophisticated map-making method than the one we used here [251], and simulation tests would require realistic atmospheric noise simulations [124].

Apart from modelling different systematics, testing how the biases change for different scanning strategies could also be useful for planning optimal scans for future experiments. Many instrumental systematics effects are mitigated when the same area of the sky is scanned multiple

times from different angles during several observation runs. Since scanning more area of the sky is also beneficial to reduce cosmic variance, performing an optimization analysis to understand how this interplay affects systematics could be key for future CMB experiment planning.

Another important aspect of CMB lensing is the ability to delens CMB maps with high precision. Systematics may affect a delensing analysis somewhat differently, and some may even prove to be relatively more important for delensing rather than for the lensing power spectrum. Performing a delensing analysis using CMB maps which include systematics would be the next step toward a comprehensive investigation on the effects of systematics on lensing-related analyses.

So far, our results show a promising future for lensing-related CMB cosmology. We have demonstrated that most of the systematics we considered should be relatively negligible for an SO-like experiment, especially when using many more detectors compared to our analysis and observing more sky area and for longer times, or could be mitigated effectively. Within the limitations of our work, we conclude that the upcoming generation of instruments such as SO should be able to deliver the lensing science case they target.

CHAPTER 4

Improved lensing analysis estimates using the Planck NPIPE maps

MARK MIRMELSTEIN, JULIEN CARRON, ANTONY LEWIS

Abstract

The reconstruction of the gravitational lensing potential from cosmic microwave background radiation (CMB) observations is one of the main targets of past, current, and future CMB experiments. An accurate reconstruction of the lensing field is important for constraining inflationary physics via delensing, for learning more about the matter evolution in the Universe, and for providing insights on neutrino mass. The most accurate lensing measurements to date were produced by the Planck collaboration, who presented minimum-variance lensing estimates across a large multipole range.

The Planck collaboration has recently released updated CMB maps using an improved pipeline known as NPIPE, which, due to their lower noise levels, could provide more accurate lensing estimates. In this work, we reconstruct the lensing potential using these newly-available NPIPE maps using a similar method used by Planck in their 2018 lensing analysis. We introduce a new filtering step to this pipeline, which approximates the reconstruction noise as locally homogeneous to filter the lensing quadratic estimators. We compare the lensing estimates of the lensing reconstruction pipeline with and without this additional filtering step and use their respective likelihoods to estimate the lensing-related cosmological parameter.

We show that the anisotropy of the Planck pixel noise variance is large enough that applying the additional filtering step on the lensing quadratic estimators improves the lensing power spectrum uncertainty by an additional 7% at $L \lesssim 200$. We also show that using the new analysis method can improve the uncertainties of the estimated lensing-related cosmological parameters by up to $\sim 16\%$. This work is the first demonstration of the κ-filtering process on real CMB data, and the results we obtained could motivate the use of our analysis method in future lensing reconstruction analyses.

4.1 INTRODUCTION

In the last decade, one of the main experiments that provided new cosmological insights that helped to shape our knowledge on the Universe was Planck. Planck's full-sky observations enabled a deep view into the CMB anisotropies, which allowed cosmologists to reconstruct the lensing potential from CMB observations for a wide multipole range [123, 252].

Since the first Planck release, both the lensing reconstruction techniques and the map building capabilities have improved. The first iteration of the Planck lensing analysis used the temperature CMB map and homogeneous noise in the filters [123]. As more Planck measurements became available, the Planck maps themselves also improved by having less intrinsic noise. The improved polarization sensitivity specifically enabled the inclusion of the Planck polarization maps in the lensing pipeline to achieve a minimum-variance (MV) reconstruction [98], and the more recent lensing analysis of Planck also including the full map covariance in the filtering weights [100]. The collaboration's foreground-cleaning and map-making pipelines have also been enhanced over time [197, 253, 254]. The lensing reconstruction accuracy improved significantly through its iterations, with current results agreeing with the theoretical ΛCDM lensing spectrum by 40σ.

In this work, we continue to explore the possible lensing reconstruction improvements that can be made using the Planck data maps. We use a recent data release of the Planck temperature and polarization maps made using the processing pipeline NPIPE (NERSC PIPEline[1]) [255], to perform a joint temperature+polarization lensing reconstruction. These newly-available data benefit from having less overall noise, which by itself allows for a more precise lensing reconstruction. We use these new data as an opportunity to apply the latest Planck lensing pipeline, which uses optimal filters, and compare its results to a similar reconstruction pipeline which includes an additional κ-filtering step (see Chapter 2 for more details about this filter). Previous work showed that adding this to a lensing reconstruction pipeline improves the lensing uncertainties by up to $\sim$30 for a Simons Observatory-like experiment at $L \lesssim 1000$, however this new method has not yet been used on data. Here, we will concentrate on the differences made by including this additional step to show how the Planck lensing analysis benefits from it, both at the level of the lensing power spectrum, and at the cosmological parameter estimation level.

This chapter is structured as follows. In Sec. 4.2 we describe the NPIPE data maps which are used in the lensing reconstruction analyses. We briefly outline the two lensing reconstruction methods used in this work in Sec. 4.3 and compare the results of the two methods on the lensing power spectrum uncertainty and the parameter estimations from their respective likelihoods in

[1]The National Energy Research Scientific Computer Center (NERSC) is the high-performance computing facility which hosts the machines on which this processing pipeline was developed and run.

Sec. 4.4. Our findings are then summarised in Sec. 4.5. Throughout this work we consider a Gaussian lensing field and work with the Planck best-fit ΛCDM parameters when producing fiducial power spectra and CMB simulations.

4.2 THE NPIPE MAPS

In this work, we use one of the more recent Planck maps releases for lensing reconstruction. These maps were made using Planck's new processing pipeline NPIPE [255][2]. It produces calibrated CMB temperature and polarization maps which are combined from both the low- and high-frequency instruments of Planck. Some of the main improvements of this pipeline compared to the previous ones are:

1. Including additional measurements that were carried out during the instrument's repointing manoeuvres. These add up to having ∼8% more data in the final maps.
2. Applying a low-pass filter for the low-frequency instrument to reduce the amount of uncorrelated noise in the differenced signal.
3. Estimating the detectors' polarization parameters more accurately by integrating information from the flight data.

Overall, the pipeline yields maps with 10% less noise and reduced level of systematic effects at all angular scales compared to the third Planck data release.

For this work, the raw multi-frequency NPIPE maps were used to construct a foreground-cleaned map by applying a cleaning pipeline that resembles the 2018 SMICA (Spectral Matching Independent Component Analysis) method [68, 256–258]. The SMICA process produces CMB maps by linearly combining the frequency channels measurements in harmonic space with multipole-dependent weights for $\ell \lesssim 4000$. The weights are optimised so that the mismatch between modelled foreground templates and the auto- and cross-power spectra of the frequency maps is minimised. This process is done independently for the temperature and polarization maps. The resulting maps have an effective beam window function of 5 arcminutes. The weights using in the cleaning process are the 2018 SMICA weights rescaled by the new noise levels and effective transfer functions of each frequency channel of the NPIPE maps. The required rescaling was estimated from cross-correlating the NPIPE maps with CMB simulations

[2]The temperature and polarization NPIPE maps are available at https://lambda.gsfc.nasa.gov/product/planck/curr/planck_prod_irsa.cfm.

that have similar features to those of the SMICA-cleaned maps from the 2018 analysis. The resulting foreground-cleaned NPIPE maps, shown masked in Fig. 4.1, are the input data maps in our lensing reconstruction pipeline. The mask used in this analysis is comprised of the mask used in the latest Planck lensing analysis [100] and the latest released component separation mask [68].

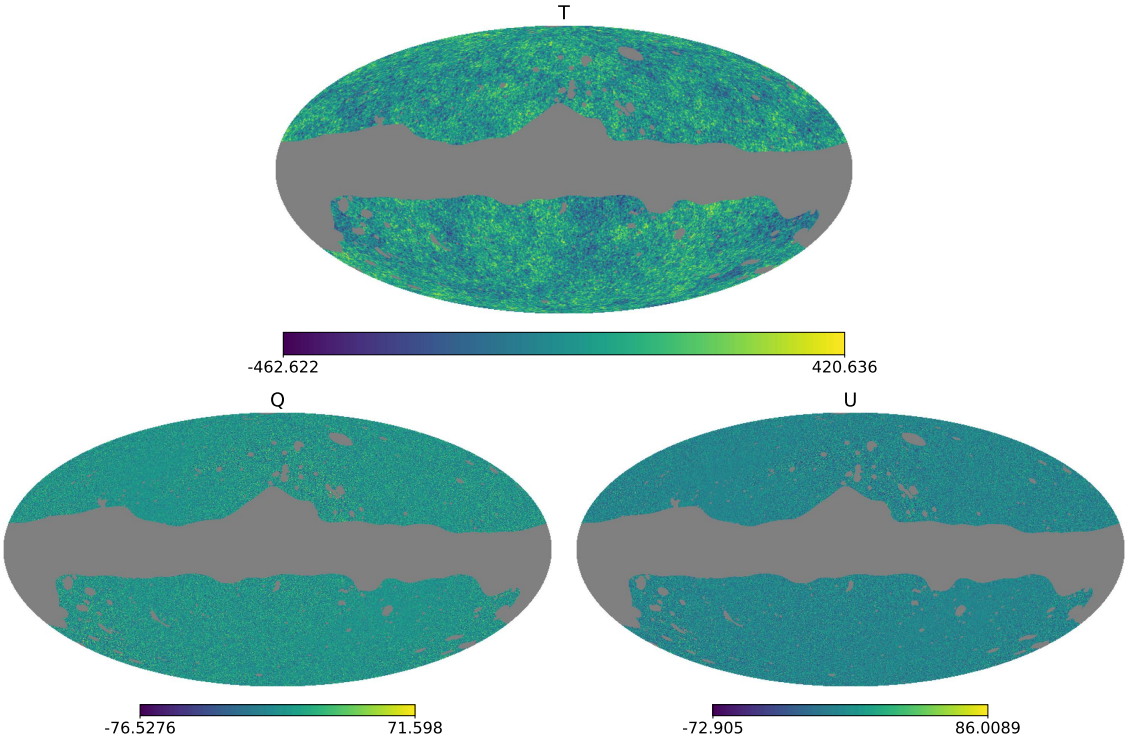

Figure 4.1: The masked foreground-cleaned temperature and polarization NPIPE maps we use in our lensing analyses. The mask is comprised of the mask used in the 2018 Planck lensing analysis [100] and the latest released component separation mask of Planck [68]. All of the curved-sky figures shown were made using the healpy [259] Python package.

4.3 LENSING ANALYSIS

In this work, we use two of the lensing methods that were described in Chapter 2, where we used a flat-sky version of the analysis presented here. The main difference between these two cases is the way in which the quadratic estimators (QEs) are calculated. We apply an optimal Wiener filter (WF) to the input maps $X^{\rm dat}$ (for $X \in \{T, Q, U\}$) using similar procedures as described in Chapter 2 (see also Appendix A.2),

$$\begin{pmatrix} T^{\rm WF} \\ E^{\rm WF} \\ B^{\rm WF} \end{pmatrix} \equiv \boldsymbol{C}_{\rm fid} \boldsymbol{\mathcal{T}}^{\top} \mathbf{Cov}^{-1} \begin{pmatrix} T^{\rm dat} \\ Q^{\rm dat} + iU^{\rm dat} \\ Q^{\rm dat} - iU^{\rm dat} \end{pmatrix}, \tag{4.1}$$

where $\boldsymbol{C}_{\rm fid}$ is a set of fiducial lensed CMB spectra, $\boldsymbol{\mathcal{T}}$ is the full transfer function from multipoles to pixel-space (which also depends on the maps' beam b), $\mathbf{Cov} \equiv \boldsymbol{\mathcal{T}}\boldsymbol{C}_{\rm fid}\boldsymbol{\mathcal{T}}^\top + \boldsymbol{N}$ is the pixel-space covariance, and $\boldsymbol{N}$ is the pixel-space noise. As before, we invert $\mathbf{Cov}$ using a multigrid-preconditioned conjugate-gradient search [148].

The filtered maps are then used to derive the spin-1 pixel-space unnormalized lensing displacement estimate,

$$ {}_1\hat{d}(\hat{\mathbf{n}}) = -\sum_{s=0,\pm2} {}_{-s}X^{\rm IVF}(\hat{\mathbf{n}}) \left[\eth_s X^{\rm WF}\right](\hat{\mathbf{n}}), \tag{4.2}$$

where $\eth_s$ are the spin-raising and lowering operators [260] such that

$$\begin{aligned}
\left[\eth_0 X^{\rm WF}\right](\hat{\mathbf{n}}) &\equiv \sum_{\ell m} \sqrt{\ell(\ell+1)}\, T^{\rm WF}_{\ell m}\, {}_1Y_{\ell m}(\hat{\mathbf{n}}),\\
\left[\eth_{-2} X^{\rm WF}\right](\hat{\mathbf{n}}) &\equiv -\sum_{\ell m} \sqrt{(\ell+1)(\ell-1)} \left[E^{\rm WF}_{\ell m} - iB^{\rm WF}_{\ell m}\right] {}_{-1}Y_{\ell m}(\hat{\mathbf{n}}),\\
\left[\eth_{+2} X^{\rm WF}\right](\hat{\mathbf{n}}) &\equiv -\sum_{\ell m} \sqrt{(\ell-2)(\ell+3)} \left[E^{\rm WF}_{\ell m} + iB^{\rm WF}_{\ell m}\right] {}_{+3}Y_{\ell m}(\hat{\mathbf{n}}),
\end{aligned} \tag{4.3}$$

and the inverse-variance-filtered (IVF) maps are defined as

$$\boldsymbol{X}^{\rm IVF}(\hat{\mathbf{n}}) \equiv \left[\boldsymbol{b}^\top \mathbf{Cov}^{-1} \boldsymbol{X}^{\rm dat}\right](\hat{\mathbf{n}}). \tag{4.4}$$

The deflection estimate is then decomposed into the gradient $\hat{g}^\phi_{LM}$ and curl $\hat{c}^\phi_{LM}$ QEs,

$$ {}_{\pm1}\hat{d}(\hat{\mathbf{n}}) \equiv \mp \sum_{LM} \left(\frac{\hat{g}^\phi_{LM} \pm i\hat{c}^\phi_{LM}}{\sqrt{L(L+1)}}\right) {}_{\pm1}Y_{LM}(\hat{\mathbf{n}}), \tag{4.5}$$

although here we only use the gradient term, as it contains the information on the lensing potential.

Once the QEs are obtained, we filter them using the methodology that was introduced in Chapter 2. The unmasked regions of the sky are partitioned into 64 patches based on their relative pixel noises. The number of patches was chosen such that the theoretical lensing power spectrum variance of Eq. (2.28), which includes the contribution of κ-filtering, is converged. The noise variance in each patch is approximated as homogeneous, which is the main requirement for this filtering process. This partitioning scheme is used to construct an effective response map, $\mathcal{R}^\kappa_{\rm eff}$, which is used to normalize the unnormalized and unfiltered QEs, and to obtain the effective lensing reconstruction noise level of each patch, $N^\kappa_{0,\rm eff}$, which is used in the filtering process. The effective noise values are calculated from averaging the values of $N^\kappa_{0,L}$ (the isotropic reconstruction noise $N_{0,L}$ for $\kappa_{LM} \equiv L(L+1)\phi_{LM}/2$) over the multipole range $8 \leq L \leq 100$. In this multipole range the reconstruction noise is relatively white. The values for the response

map $\mathcal{R}^{\kappa}_{\rm eff}$ are obtained in a similar way from the response

$$\mathcal{R}^{\phi\phi}_{L} = \frac{1}{2\,(2L+1)} \sum_{\ell_1} \sum_{\ell_2} f_{XZ}(\boldsymbol{\ell}_1, \boldsymbol{\ell}_2) F_{XZ}(\boldsymbol{\ell}_1, \boldsymbol{\ell}_2), \tag{4.6}$$

where $\mathcal{R}^{\kappa}_{L} = 4\mathcal{R}^{\phi\phi}_{L}/[L(L+1)]^2$, $\boldsymbol{\ell}_1 + \boldsymbol{\ell}_2 = \mathbf{L}$, and $f_{X,Y}$ and F_{XY} are given in Table 1.2. Fig. 4.2 shows the reconstruction noise map which is used to filter the QEs, where we set $N^{\kappa}_{0,\rm eff}(\mathbf{x})^{-1} = 0$ in masked areas. This filter is applied on the lensing convergence κ rather than the lensing potential ϕ, as the κ reconstruction noise is approximately white and local in real-space, such that it is uncorrelated between patches on large scales.

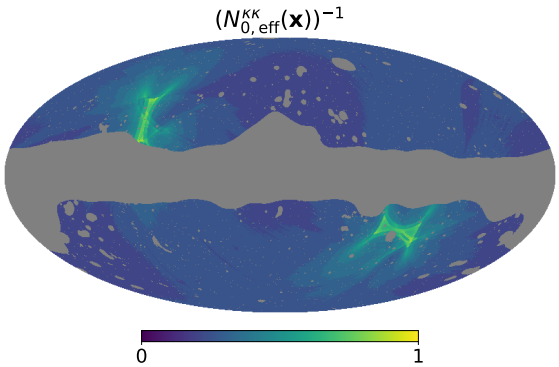

Figure 4.2: The normalized inverse approximate lensing reconstruction noise $\left(N^{\kappa\kappa}_{0,\rm eff}(\mathbf{x})\right)^{-1}$ for an MV lensing reconstruction using 64 patches. The approximate effective white reconstruction noise in each patch is defined as the average value of the isotropic $N^{\kappa\kappa}_{0,L}$ over the multipole range $8 \leq L \leq 100$.

We define the κ-filtered estimator as

$$\hat{\boldsymbol{\kappa}}^{\rm filt} \equiv \boldsymbol{C}^{\kappa\kappa}_{\rm fid} \left(\boldsymbol{C}^{\kappa\kappa}_{\rm fid} + \boldsymbol{N}^{\kappa}_{0,\rm eff}\right)^{-1} (\boldsymbol{\mathcal{R}}^{\kappa}_{\rm eff})^{-1}\, \hat{\boldsymbol{g}}^{\kappa}, \tag{4.7}$$

where $\boldsymbol{C}^{\kappa\kappa}_{\rm fid}$ is the theory κ power spectrum, and the QE map $\hat{\boldsymbol{g}}^{\kappa}$ is defined, in harmonic space, as

$$\hat{g}^{\kappa}_{LM} \equiv \left(\hat{g}^{\phi}_{LM} - \langle \hat{g}^{\phi}_{LM} \rangle_{\rm MC}\right) \times \frac{2}{L(L+1)}. \tag{4.8}$$

The inverse variance, $\left(C^{\kappa\kappa}_{\rm fid} + N^{\kappa}_{0,\rm eff}\right)^{-1}$, that is needed for this filtering step is calculated using the same conjugate gradient method used for the inverse-variance of the CMB maps. We produce two filtered QEs, where each one is unbiased using a different mean-field (MF) estimator $\langle \hat{g}^{\phi}_{LM} \rangle_{\rm MC}$.

We calculate the lensing power spectrum twice, once from the two unfiltered QEs, and once from the two filtered κ estimators. For the unfiltered QEs, this power spectrum is

$$C^{\hat{\phi}_{\rm MF_1}\hat{\phi}_{\rm MF_2}}_{L} \equiv \frac{1}{(2L+1) f_{\rm sky}} \sum_{M=-L}^{L} \hat{\phi}_{{\rm MF}_1, LM} \hat{\phi}^{*}_{{\rm MF}_1, LM}, \tag{4.9}$$

such that the unbiased power spectrum is obtained:

$$\hat{C}_L^{\phi\phi} \equiv \left(C_L^{\hat{\phi}_{\rm MF_1}\hat{\phi}_{\rm MF_2}} - {}^{\rm (RD)}N_{0,L}^{\phi\phi} - {}^{\rm (MC)}N_{1,L}^{\phi\phi} \right) \times f_{A,L}\mathcal{A}_{\rm MC}. \tag{4.10}$$

Similar relations hold for $\kappa^{\rm filt}$. The analytic correction,

$$f_{A,L} \equiv \sum_p f_p (w_L^p)^2, \tag{4.11}$$

is required to unbias the power spectrum. It is the effective map area fraction (see [178] and Chapter 2), which also corrects for the filtering weights,

$$w_L^p = \frac{C_{L,\rm fid}^{\kappa\kappa}}{C_{L,\rm fid}^{\kappa\kappa} + N_{0,\rm eff}^{\kappa,p}} \frac{\mathcal{R}_L^{\kappa,p}}{\mathcal{R}_{\rm eff}^{\kappa,p}}. \tag{4.12}$$

The final applied multiplicative MC correction, $\mathcal{A}_{\rm MC} \equiv \hat{C}_{L,\rm MC}^{\kappa\kappa}/C_L^{\kappa\kappa,\rm th}$, is obtained using the reconstructed lensing power spectra of 480 MC simulations by calculating the ratio between the resulting averaged power $\hat{C}_{L,\rm MC}^{\kappa\kappa}$ and the theoretical power $C_L^{\kappa\kappa,\rm th}$. This correction is expected to correct for mode-mixing effects, and for calibration of the QE responses [100]. We also use 480 MC simulations to calculate the two MF estimates and ${}^{\rm (RD)}N_{0,L}$ (given in Eq. (3.37)), and 95 simulations for calculating ${}^{\rm (MC)}N_{1,L}$ (given in Eq. (2.11)).

The final unbiased power spectra are then binned using

$$\hat{C}_{L_{\rm b}}^{\kappa\kappa} \equiv \left(\sum_{L=L_{\rm min}^{\rm b}}^{L_{\rm max}^{\rm b}} \mathcal{B}_{\rm b}^L \hat{C}_L^{\kappa\kappa} \right) \left(\frac{\sum_{L=L_{\rm min}^{\rm b}}^{L_{\rm max}^{\rm b}} \mathcal{B}_{\rm b}^L C_{L,\rm fid}^{\kappa\kappa}}{\sum_{L=L_{\rm min}^{\rm b}}^{L_{\rm max}^{\rm b}} \mathcal{B}_{\rm b}^L \left\langle \hat{C}_L^{\kappa\kappa} \right\rangle_{\rm MC}} \right). \tag{4.13}$$

where the convergence power is defined as

$$\hat{C}_L^{\kappa\kappa} \equiv \left[\frac{L(L+1)}{2} \right]^2 \hat{C}_L^{\phi\phi}. \tag{4.14}$$

We use the same binning weights of Planck,

$$\mathcal{B}_{L,\rm b} \equiv \frac{C_{L_{\rm b},\rm fid}^{\kappa\kappa} C_{L,\rm fid}^{\kappa\kappa} V_L^{-1}}{\sum_{L'=L_{\rm min}^{\rm b}}^{L_{\rm max}^{\rm b}} \left(C_{L',\rm fid}^{\kappa\kappa} \right)^2 V_{L'}^{-1}}, \tag{4.15}$$

where L_b are the binned multipoles,

$$L_\mathrm{b} \equiv \frac{\sum_{L=L^\mathrm{b}_\mathrm{min}}^{L^\mathrm{b}_\mathrm{max}} \mathcal{B}_{L,\mathrm{b}} L}{\sum_{L=L^\mathrm{b}_\mathrm{min}}^{L^\mathrm{b}_\mathrm{max}} \mathcal{B}_{L,\mathrm{b}}}, \tag{4.16}$$

and

$$V_L \equiv \frac{2\left(C_L^{\hat{\kappa}\hat{\kappa}} f_{A,L} \mathcal{A}_\mathrm{MC}\right)^2}{(2L+1)\, f_\mathrm{sky}} \tag{4.17}$$

is the reconstruction variance. The binning weights are defined such that the binned fiducial spectrum at a given bin L_b is equal to the fiducial spectrum at $L = L_\mathrm{b}$.

4.4 RESULTS

4.4.1 LENSING POWER SPECTRUM

We compare the reconstructed lensing power spectra obtained from the NPIPE maps with and without κ-filtering. Figure 4.3 shows both power spectra for an MV reconstruction using the NPIPE maps in the multipole range $8 \leq L \leq 400$. This conservative binning scheme concentrates on the multipoles where the signal-to-noise of the estimator is maximal [98, 100, 123]. The resulting band powers of the two power spectra do not differ significantly, although the MC correction $\mathcal{A}_\mathrm{MC}$, shown in the right panel of Fig. 4.4, do differ; the correction for the κ-filtered case is slightly smaller in magnitude.

The main benefit from including the additional filtering step is having lower band power uncertainties. The resulting uncertainties of both lensing reconstructions are given in Table. 4.1. The uncertainties are lower for $L \lesssim 200$ by up to 7%, and only increase slightly compared to the results of the original Planck analysis by up to 2.5% for $200 \lesssim L \lesssim 300$. It may be possible to further optimise the κ-filtering process to avoid the increased reconstruction uncertainties in the latter multipole range. For example, by producing several κ-filtered estimators, where each filtering is done using different noise levels, the combined estimator might be more optimal. Since the benefit of κ-filtering is already quite significant at low-L, we do not try to optimise it further in this work.

We also compare the uncertainty improvements with the theoretical prediction, which is shown in Fig. 4.4. This figure compares the variances of lensing reconstructions with and without this filtering step. The κ-filtering variances were calculated using the theoretical lensing power

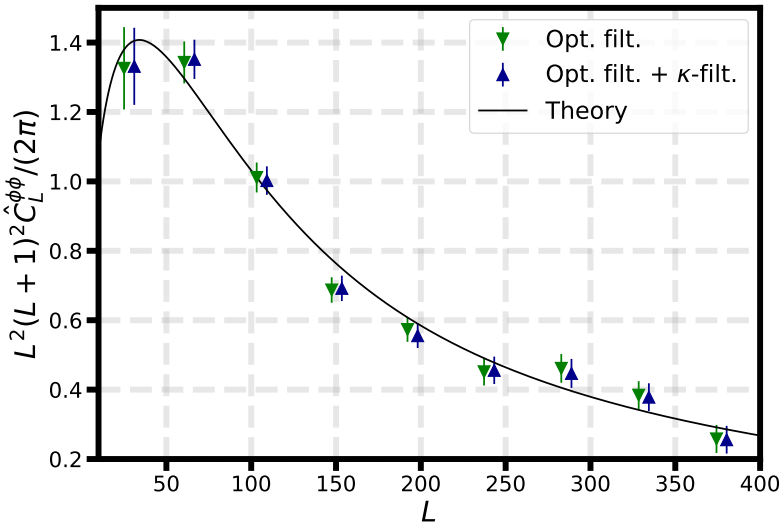

Figure 4.3: The reconstructed lensing power spectra with (blue) and without (green) the κ-filtering using the Planck NPIPE data maps. The multipole range shown is for $8 \leq L \leq 400$, which is around the peak of the lensing power spectrum where the reconstruction noise is minimal. The bins and errorbars are given in Table 4.1. The additional filtering step does not change the bin means considerably. The power spectrum uncertainties were obtained from the lensing power spectrum covariance, calculated using 480 MC simulations.

spectrum variance of Eq. (2.28). The variance improvement from analysing the NPIPE data (green curve) is in good agreement with the theoretical expectations for an MV reconstruction (dark purple curve). The theoretical improvement is also shown for temperature-only and polarization-only reconstructions. It is evident that the noise-dominated polarization-only lensing reconstruction could also benefit from this approximated filtering, slightly more than the MV case, although this reconstruction would already have larger variance due to the high noise level. The polarization-only analysis will be carried out in future work.

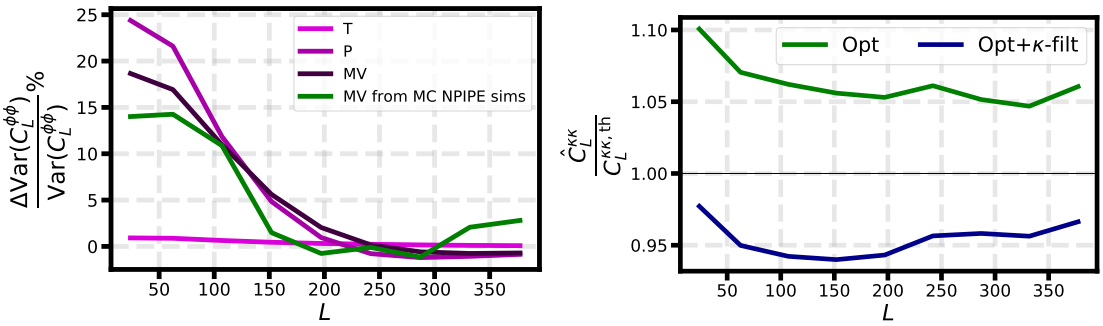

Figure 4.4: *Left*: Fractional improvement in the theoretical binned variance of $\hat{C}_L^{\phi\phi}$ when using an additional κ-filtering step for temperature-only (pink), polarization-only (purple) and MV (dark purple) reconstructions. The variances are obtained analytically from the theoretical lensing power spectrum variance of Eq. (2.28) using an analytic patch approximation with 64 patches, each with its own noise level, which is assumed to be homogeneous within a patch. The green curve is the comparison between the variances obtained from the reconstruction made in this work using the NPIPE data. It is in good agreement with the MV predictions.
Right: The required MC corrections for lensing reconstructions with (blue) and without (green) the κ-filtering step.

L range	$\sigma_{C_L^{\phi\phi}}$ Opt. filt.	Opt. filt. + κ-filt.
8 - 40	0.119	0.111
41 - 84	0.060	0.057
85 - 129	0.043	0.041
130 - 174	0.037	0.037
175 - 219	0.035	0.035
220 - 264	0.039	0.040
265 - 309	0.041	0.042
310 - 354	0.040	0.040
355 - 400	0.040	0.040

Table 4.1: Lensing reconstruction uncertainties for analyses with and without κ-filtering. The values are colour-coded from higher (darker green) to lower (lighter green) improvements. As expected from the theoretical variance predictions (shown in Fig. 4.4), most of the benefit from the κ-filtering procedure is for bins at $L \lesssim 200$, while a few bins around $200 \lesssim L \lesssim 300$ show a slightly better uncertainty without this procedure. The reconstruction values are shown in Fig. 4.3.

4.4.2 COSMOLOGICAL PARAMETER ESTIMATION

Apart from demonstrating the improvements on the lensing reconstruction uncertainty, we also show how the cosmological parameter estimation benefits from the increased large-scale lensing reconstruction accuracy. We calculate the likelihoods of the obtained power spectra and use them to estimate the cosmological parameters of the ΛCDM model using the Markov Chain Monte Carlo sampling method (see Appendix A.3 for details) with `Cobaya`[3] [261]. The resulting samples are then analysed using `GetDist`[4] [262].

We follow the Planck lensing analyses of Refs. [98, 100] to demonstrate the improvements from the additional filtering step by using lensing-only likelihoods, and also a joint constraint which includes information from baryonic acoustic oscillation (BAO) measurements. Adding BAO likelihoods tightens the constraints on most of the parameters relevant for lensing, especially H_0 due to its strong dependency on redshift. These tight constraints on H_0 helps to breaks the σ_8-Ω_m degeneracy such that these parameters could be estimated individually. The BAO likelihoods are adopted from the results of the 6dF Galaxy Survey [263], and the Baryon Oscillation Spectroscopic Survey (BOSS) [264, 265].

[3] Available at https://github.com/CobayaSampler/cobaya.
[4] Available at https://github.com/cmbant/getdist.

We calculate the likelihood of the lensing power spectrum $\mathcal{L}_\phi$ using the same binning scheme of Eq. 4.15,

$$-2\ln\left(\mathcal{L}_\phi\right) = \mathcal{B}_i^L \left(\hat{C}_L^{\phi\phi} - C_L^{\phi\phi,\mathrm{th}}\right) \left[\Sigma^{-1}\right]^{ij} \mathcal{B}_j^{L'} \left(\hat{C}_{L'}^{\phi\phi} - C_{L'}^{\phi\phi,\mathrm{th}}\right), \tag{4.18}$$

where i and j are bin indices, and Σ is the covariance matrix. To use this likelihood for sampling, both $C_L^{\phi\phi,\mathrm{th}}$ and $\hat{C}_L^{\phi\phi}$ need to be evaluated using different parameter values. Since reconstructing $\hat{C}_L^{\phi\phi}$ multiple times using fiducial power spectra that are produced from different parameter values is numerically very expensive, we can instead define $C_L^{\phi\phi,\mathrm{th}}$ to include an approximately-linear correction which would include any deviation that $\hat{C}_L^{\phi\phi}$ might have from different parameter values. As with the Planck lensing analyses [98, 100], the approximations we use are:

1. *Neglecting the dependency of ${}^{(RD)}N_{0,L}^{\phi\phi}$ and the MF estimates on the sampled parameters*: These debiasing terms are by construction insensitive to leading order potential discrepancies in the fiducial CMB power spectra, so we do not incorporate their dependency on the fiducial spectra in the analysis.

2. *Linearizing the dependency of the response functions and ${}^{(MC)}N_{1,L}^{\phi\phi}$ on the CMB power spectra*: This considerably simplifies the likelihood calculation. Such linear correction is a good approximation because the power spectra are already measured to percent-level accuracy by Planck.

3. *Assuming that the MC correction does not depend on the cosmology*: The MC correction is already very small (see left panel of Fig. 4.4), so correcting for its parameter dependency should be negligible for the overall analysis.

These assumptions allow us to define $C_L^{\phi\phi,\mathrm{th}}$ more easily by considering only the dependencies of the response $\mathcal{R}_L^{\phi\phi}$ and the debiasing term $N_{1,L}^{\phi\phi}$ on the sampled parameters. We therefore define it to be

$$C_L^{\phi\phi,\mathrm{th}} \equiv \left(\frac{\mathcal{R}_L^{\phi\phi}|_{\boldsymbol{\theta}}}{\mathcal{R}_L^{\phi\phi}|_{\mathrm{fid}}}\right)^2 C_L^{\phi\phi}|_{\boldsymbol{\theta}} + N_{1,L}^{\phi\phi}|_{\boldsymbol{\theta}} - N_{1,L}^{\phi\phi}|_{\mathrm{fid}}, \tag{4.19}$$

where $\boldsymbol{\theta}$ are the parameters we estimate and the subscript fid refers to terms which are evaluated using the fixed set of parameters (the Planck CMB best-fit estimates shown in Table 1.1). These parameters are also used to calculate the CMB power spectra which are used in the construction of the QEs. For small deviations from the fiducial model, we can Taylor-expand Eq. (4.19) around

the fiducial values to get

$$C_L^{\phi\phi,\mathrm{th}} \approx C_L^{\phi\phi}|_{\boldsymbol{\theta}} + \frac{d\ln\left[\left(\mathcal{R}_L^{\phi\phi}\right)^2\right]}{dC_{\ell'}^{j}}\left(C_{\ell'}^{j}|_{\boldsymbol{\theta}} - C_{\ell'}^{j}|_{\mathrm{fid}}\right) C_L^{\phi\phi}|_{\mathrm{fid}} + \mathcal{M}_{LL',1}\left(C_{L'}^{\phi\phi}|_{\boldsymbol{\theta}} - C_{L'}^{\phi\phi}|_{\mathrm{fid}}\right) + \frac{dN_{1,L}^{\phi\phi}}{dC_{\ell'}^{j}}\left(C_{\ell'}^{j}|_{\boldsymbol{\theta}} - C_{\ell'}^{j}|_{\mathrm{fid}}\right), \tag{4.20}$$

where the sums of index j are over all T, E, and B power spectra combinations, and $M_{LL',1}$ is the approximated linear dependency of the analytic $N_{1,L}^{\phi\phi}$ on the lensing potential for fixed CMB power spectra, which is pre-computed along with the other derivatives using the fiducial parameter values.

As with Planck, we adopt several weak priors for constraining the parameters using the lensing likelihoods. We fix the reionization optical depth to $\tau = 0.055$, as the dependency of the lensing deflections on reionization is very small and can be neglected. We put broad priors on the spectral index using $n_s = 0.96 \pm 0.02$ due to the weak dependency of the results on its value for a plausible range. We put tight priors on the baryon density using $\Omega_b h^2 = 0.0222 \pm 0.0005$ due to its very accurate measurement from Big Bang nucleosynthesis models combined with quasar absorption-line observations, which are independent of CMB measurements [266]. We also set a top-hat prior for the reduced Hubble constant at range $0.4 < h < 1$ to limit the extent of the parameter degeneracy in a way which does not affect the results over the region of interest when adding BAO constraints. Although these priors are biased towards results which are in agreement with ΛCDM, we apply them to see the differences in parameter estimates from the two lensing analyses better for comparison, which is the aim of this work.

We concentrate on comparing the estimator's uncertainties specifically for the cosmological parameters that are most relevant for CMB lensing. As CMB lensing directly depends on the matter in the Universe, the CMB lensing likelihood especially helps to constrain the matter-related parameters and their various couplings. The estimated parameter values for lensing-only and lensing+BAO likelihoods are shown in Table 4.2. Most of the parameters we estimated are slightly better constrained from the κ-filtering likelihoods. Specifically, the highest improvement in uncertainty is for both Ω_m and Ω_Λ, whose uncertainties are $\sim$15.6% better using the κ filter. Their identical uncertainty improvements, which also occurs in their lensing+BAO estimates, are due to the relation of the two parameters, namely that $\Omega_{m,0} + \Omega_{\Lambda,0} = 1$. The main parameter which is well-constrained from lensing alone, without the additional BAO likelihoods,

is $\sigma_8\Omega_m^{0.25}$ [267]. Its uncertainty, however, improves only marginally by $\sim$2.8% with and without the BAO likelihoods. Overall, the joint lensing+BAO analysis benefits slightly less from κ-filtering. For this analysis, $\Omega_c h^2$ sees the highest level of improvement in uncertainty of $\sim$8.2%, which is closely followed by $\Omega_m h^2$ with a $\sim$7.8% improvement. The Hubble constant estimates are shown only for the joint lensing+BAO analysis, which constrains it better. Its constraints with and without κ-filtering have an almost identical uncertainty, suggesting that the contribution from the additional filtering step to its accuracy is minimal compared to the added BAO likelihoods. Using the likelihoods with the κ-filtered QEs results in a reduced confidence level for two parameters, $\sigma_8/h^{0.5}$ by $\sim$2.3% for the lensing-only analysis, and $\Omega_b h^2$ by 0.2% for the lensing+BAO analysis, however both reductions are very small compared to the benefits of the other parameters.

	Lensing-only			Lensing+BAO		
Parameter	Opt . filt.	Opt. filt. + κ-filt	%	Opt. filt.	Opt. filt. + κ-filt	%
$\Omega_\mathrm{b}h^2$	0.022197 ± 0.000503	0.022215 ± 0.000500	0.6	0.022201 ± 0.000498	0.022204 ± 0.000499	-0.2
$\Omega_\mathrm{c}h^2$	$0.1244^{+0.0105}_{-0.0131}$	$0.1179^{+0.0100}_{-0.0118}$	7.6	$0.1290^{+0.0100}_{-0.0123}$	$0.12166^{+0.00968}_{-0.01080}$	8.2
H_0	—	—	—	$68.88^{+1.13}_{-1.29}$	68.30 ± 1.20	0.8
Ω_m	$0.3668^{+0.0601}_{-0.2190}$	$0.3322^{+0.0435}_{-0.1920}$	15.6	$0.3197^{+0.0155}_{-0.0175}$	0.3095 ± 0.0158	4.2
$\Omega_\mathrm{m}h^2$	$0.1473^{+0.0106}_{-0.0132}$	$0.1408^{+0.0101}_{-0.0118}$	8.0	$0.1519^{+0.0100}_{-0.0124}$	$0.14451^{+0.00975}_{-0.01090}$	7.8
Ω_Λ	$0.633^{+0.2190}_{-0.0601}$	$0.668^{+0.1920}_{-0.0435}$	15.6	$0.6802^{+0.0175}_{-0.0155}$	0.6905 ± 0.0158	4.2
σ_8	$0.818^{+0.1430}_{-0.0758}$	$0.820^{+0.1350}_{-0.0656}$	8.3	0.8277 ± 0.0171	0.8172 ± 0.0168	1.8
$\sigma_8/h^{0.5}$	0.9898 ± 0.0195	$0.9804^{+0.0212}_{-0.0187}$	-2.3	0.9974 ± 0.0180	0.9888 ± 0.0178	1.1
$\sigma_8\Omega_\mathrm{m}^{0.5}$	$0.4659^{+0.0462}_{-0.0748}$	$0.4454^{+0.0403}_{-0.0735}$	6.0	0.4680 ± 0.0178	0.4545 ± 0.0170	4.5
$\sigma_8\Omega_\mathrm{m}^{0.25}$	0.6128 ± 0.0181	0.6002 ± 0.0176	2.8	0.6223 ± 0.0172	0.6094 ± 0.0167	2.9

Table 4.2: The estimated parameters and their 68% confidence uncertainties using the optimal filtering and the optimal filtering+κ-filtering lensing-only and lensing+BAO likelihoods. Only the main lensing-related parameters of the ΛCDM model are presented. The colour-coded columns show the relative change in the uncertainties of the estimates between the two filtering analyses, which range from high (darker green) to low (lighter green) improvements from using the κ-filtering process. The red shading similarly indicates reduced uncertainties when including κ-filtering in the analysis. The lensing-only estimates for H_0 are not shown here, as this parameter is not well-constrained without redshift-dependent information. The Hubble parameter is defined as $h \equiv H_0/(100 \text{ km sec}^{-1} \text{ Mpc}^{-1})$, where H_0 is the Hubble constant today. The dimensions of the H_0 values in the table are km sec^{-1} Mpc^{-1}.

We also show how the mutual dependencies of the main cosmological parameters change for each likelihood. These dependencies, from the lensing+BAO likelihoods, are shown in Fig. 4.5 for H_0, Ω_m and σ_8. The estimations from both reconstructions mostly overlap. They have almost the same distributions, but with a different mean, as expected from Table 4.2. The additional filtering step slightly shifts the confidence contours closer to the Planck 2018 analysis (pre-NPIPE) means, which are indicated by the grey lines. The NPIPE-specific shifts that push the contours away

from the mean for the baseline analysis (without κ-filtering) compared to the pre-NPIPE results is currently not understood and will be explored in future work.

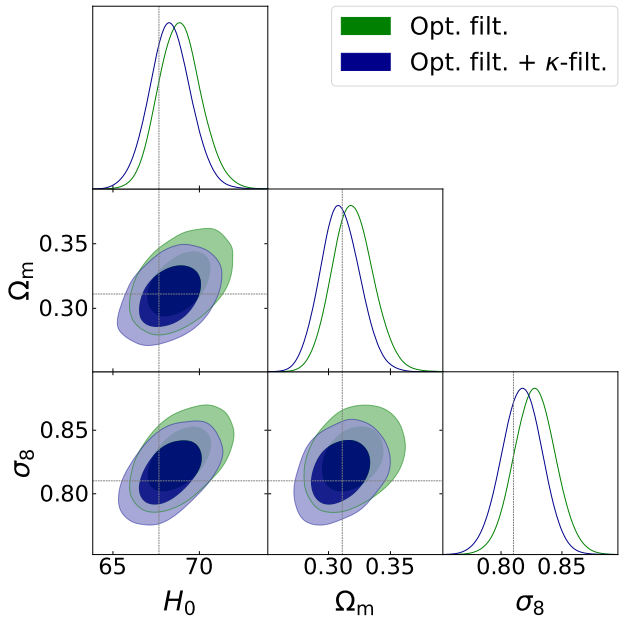

Figure 4.5: The 68% confidence contours for the Hubble constant H_0 (in km sec^{-1} Mpc^{-1}), the matter density parameter Ω_m and σ_8 using lensing+BAO likelihoods with (blue) and without (green) κ-filtering. The estimations using the κ-filtering likelihoods are slightly more constrained and are closer to the cosmological parameters obtained from CMB alone. The grey lines indicate the mean of the parameters from Planck's most recent parameter estimation from the CMB likelihoods [37].

4.5 CONCLUSIONS AND FUTURE WORK

Measuring the lensing potential with high precision from CMB measurements is one of the main goals of current and future CMB experiments. In this work, we demonstrated a proof-of-concept for how more precise lensing estimates can be achieved by filtering the QEs as a part of the lensing reconstruction analysis. We demonstrated this using a recent release of the Planck CMB maps, and found that the new lensing analysis step decreases the uncertainty of the lensing power spectrum by up to $\sim$7% between $8 \leq L \leq 200$ for Planck's NPIPE maps. This improvement in uncertainty is in good agreement with the predicted variance levels. We then used the reconstructed lensing band powers to estimate the main cosmological parameters of the ΛCDM model which are relevant for CMB lensing. The improved band power uncertainties propagate onto the parameter uncertainties, which results in uncertainty improvements of up to $\sim$16% from the lensing-only analysis, and up to $\sim$8% from the lensing+BAO likelihoods. The parameter estimations of future experiments such as the Simons Observatory and CMB-S4 might benefit even more from filtering the QEs in the lensing analysis, as following the analysis of Chapter 2 their expected lensing variance improvement is much higher than the Planck variance.

Since the benefit from κ-filtering depends on the amount of noise inhomogeneity and the noise level of the CMB experiment, adding it to the lensing analyses of other experiments may not result in large uncertainty improvements. The theoretical variance can be used as a first step to estimate how beneficial κ-filtering would be for an experiment. Apart from implementing the κ filter as we do in this work in future analyses, it may also be possible to further optimise it to achieve somewhat better improvements. One possible way to optimise this filtering step is by changing the range of multipoles over which the effective reconstruction noise of each patch is estimated. Different patches may benefit more from higher or lower noise in the filter, and optimising the noise chosen for each patch may also prevent the slight worsening of the variance we showed across multipoles for which the patch approximation breaks down. It may also be possible to optimise the filter weights for individual multipole ranges; by filtering the same map with different effective noise values, it may be possible to construct a lensing power spectrum from combining filtered estimates, each with an improved variance over a different multipole range. This way, more multipoles would benefit from the filtering process and the variance may be consistently better compared to the power spectrum estimates from unfiltered QEs. Although we have not tried to optimise this method here, we expect further improvements would be less significant in comparison to the overall benefits which we demonstrated. We leave the optimisation of the κ-filter to future work.

CHAPTER 5

A method for detecting the CMB Rayleigh scattering signal

MARK MIRMELSTEIN, ANTONY LEWIS, JULIEN PELOTON

Abstract

During and shortly after recombination, Rayleigh scattering of the cosmic microwave background radiation (CMB) produced additional CMB anisotropies. Detecting these Rayleigh scattering signals might be within reach of several upcoming CMB experiments. Such a detection could allow better constraints on early universe physics and cosmological parameters. In this work, we construct a method for detecting the Rayleigh signal from individual frequency bands of CMB observations. The method involves cleaning the individual frequency CMB maps and obtaining noise-reduced power spectra of both the primary and Rayleigh-induced anisotropies to isolate the Rayleigh signal. The main limiting factor to detect the Rayleigh scattering signal using our method is the residual foregrounds in the cleaned maps. We demonstrate this pipeline using the multi-frequency Planck CMB maps, and provide a forecast for the detection of this signal for a future CMB experiment that resembles the capabilities of the upcoming Simons Observatory (SO). We show that an SO-like experiment could detect the Rayleigh signal with a significance level of up to $\sim 5.8\sigma$ when neglecting potential foreground residuals. Although detecting this signal is unlikely with Planck, future experiments, such as liteBIRD and the proposed PRISM, COrE and PICO, are expected to be sensitive enough for its detection. The method we present could be used as a guideline for these collaborations to construct their Rayleigh scattering detection pipeline.

5.1 INTRODUCTION

About 380,000 years after the Big Bang, at a redshift $z \approx 1100$, the temperature in the Universe was sufficiently cold to enable electrons and protons to form neutral hydrogen atoms. This process halted the continuous scattering of the photons from the free electrons, which enabled the radiation, known as the cosmic microwave background (CMB) radiation, to travel almost freely across the Universe. At that stage, most of the baryonic matter was in the form of neutral hydrogen, which could also interact with the CMB photons in a process known as Rayleigh scattering [268]. This frequency-dependent scattering of photons off of atoms is present in our everyday lives; it is a contributing factor to the reason we see the sky as blue, and why dusty windows are not as see-through as clean ones are [269]. The same scattering also affected the newly-unbound photons in the early Universe. They 'exited' the surface of last scattering as an almost perfect black body polarized radiation with some amount of anisotropies. Because some of these photons will have scattered off of the newly-formed hydrogen atoms, the observed anisotropies of the CMB are expected to have slightly lower power on small scales. Due to the strong frequency-dependency of this effect, higher CMB frequencies are more likely to experience Rayleigh scattering. Most of these scattering events occurred during a short time period during and after recombination, while the expanding Universe had relatively high hydrogen density.

The effects of Rayleigh scattering on the CMB photons were first thought to be large enough to erase the primordial information in the observed CMB [270]. It was soon after shown that these effects are actually much smaller [271]. Since then, several works in the literature have characterised the effect of the Rayleigh scattering on CMB photons in great detail [272–274]. Other works have presented forecasts on the detection ability of the Rayleigh scattering for future CMB experiments without considering the impact of foregrounds, and how it may be used to improve cosmological parameters constraints [275–277].

Measuring this effect could have several implications for cosmology. Since we know this effect should be present in the CMB anisotropies, it is important to model it accurately and consistently for constraining cosmological parameters, cleaning foregrounds from and performing component separation using CMB maps, and include it in any analyses which require a more accurate description of the CMB anisotropies. As Rayleigh scattering occurred at a very early stage in the evolution of the Universe, its detection might also provide new insights about the early Universe and potentially help to constrain the expansion rate and ionization history around recombination.

In this work, we develop an analysis pipeline aimed at the detection of the effect of Rayleigh

scattering from CMB measurements at individual frequencies. We demonstrate the capabilities of this pipeline using the multi-frequency Planck CMB maps. This is mainly motivated by the work in Ref. [273], which suggests that it might be possible to detect the Rayleigh signal using Planck's 353 GHz channel. As several upcoming CMB experiments are expected to be much more sensitive to this signal compared to Planck, the method we show here can be adopted to construct a pipeline for its detection from future multi-frequency CMB observations.

This chapter is structured as follows. In Sec. 5.2 we describe the physics of Rayleigh scattering, and how it affects the CMB anisotropies and their power spectra. In Sec. 5.3 we present our method for extracting the Rayleigh signal from CMB observations, and show the results of applying it on the Planck CMB measurements. Lastly, we carry out an updated forecast for the detection likelihood of the Rayleigh signal from the Planck maps, and forecast this likelihood for an experiment similar to the upcoming Simons Observatory (SO) in Sec. 5.4. Our conclusions and future prospects are discussed in Sec. 5.5. Throughout, we assume a Gaussian unlensed CMB for CMB simulations, approximate the lensed CMB as Gaussian for the purpose of likelihood analyses, and consider a fiducial ΛCDM model with parameter values similar to those estimated by Planck [31] for generating CMB statistics.

5.2 RAYLEIGH SCATTERING AND THE CMB

The surface of last scattering is defined to have occurred at a specific time in which the CMB photons underwent their last scattering off of free electrons. It occurred because the density of the unbound electrons drops dramatically following recombination. Between then and now, however, the CMB photons could have still experienced various scattering processes. The main scattering they underwent following recombination was during reionization, when free electrons fill the Universe once more. Both recombination and reionization scattering effects are known as Thomson scattering, which is the scattering of radiation off of charged particles. The cross-section of this scattering process only depends on the mass of the scattering particle, and not on the frequency of the radiation. Following recombination, most of the baryonic matter in the Universe was in the form of neutral hydrogen atoms, and these too could scatter the CMB photons. This scattering, of radiation off of neutral atoms, is known as the Rayleigh scattering. Although this effect is the dominant photon scattering process in the newly-neutral Universe, the majority of the scattering events are very close to recombination. This is mainly due to the expansion of the Universe, which decreases the density of neutral hydrogen, the main scattering atom, as $(1+z)^3$, which sharply decreases the scattering probability. Moreover, the CMB

frequencies decrease as $(1+z)^{-1}$ in the expanding Universe, which decreases this frequency-dependent scattering probability even further.

Unlike Thomson scattering, Rayleigh scattering not only depends on the mass of the scattering particle, but also on the photon's frequency. The Rayleigh scattering cross-section is usually expressed as [274]

$$\sigma_R(\nu) = \sigma_T \left[\sum_{j=2}^{\infty} f_{j1} \frac{\nu^2}{\nu_{j1}^2 - \nu^2} \right]^2 , \tag{5.1}$$

where σ_T is the Thomson scattering cross-section, ν is the scattered photon's frequency, and ν_{j1} and f_{j1} are the Lyman series frequencies and oscillator strengths of electrons going from state j to the ground state 1, respectively. Because the photon frequencies at recombination are much smaller than the Lyman series frequencies[1], Eq. (5.1) can be approximated as a series expansion for $\nu_{j1}/\nu \ll 1$. The Rayleigh cross-section then becomes [273, 279]

$$\sigma_R(\nu) \approx \left(\frac{\nu}{\nu_{\rm eff}}\right)^4 \left[1 + A_2 \left(\frac{\nu}{\nu_{\rm eff}}\right)^2 + A_4 \left(\frac{\nu}{\nu_{\rm eff}}\right)^4 + \dots\right] \sigma_T, \tag{5.2}$$

where $\nu_{\rm eff} = \sqrt{8/9}\, c R_\infty \approx 3.1 \times 10^6$ GHz, R_∞ is the Rydberg constant[2], c is the speed of light, and A_{2k} are the expansion factors given in Ref. [279][3].

To express how Rayleigh scattering affects the CMB anisotropies we measure today, we need to add the contribution of this effect to the evolution of the CMB anisotropies from recombination until today. Previous works have shown that the effective contribution of this effect can be expressed as Taylor-expansion terms similar to those of Eq. (5.2). Given a harmonic decomposition of the, e.g., temperature anisotropies of the CMB at frequency ν_i,

$$\frac{\Delta T^{\rm obs}_{\nu_i}(\mathbf{x})}{T_{0,\nu_i}} = \sum_{\ell=1}^{\infty} \sum_{m=-\ell}^{\ell} T_{\ell m,\nu_i} Y_{\ell m}(\mathbf{x}), \tag{5.3}$$

where T_{0,ν_i} is the mean CMB temperature today, and $Y_{\ell m}$ are the spherical harmonics functions, the effective harmonic space expansion terms can be written for a CMB field $X \in \{T, E, B\}$ as

$$X_{\ell m,\nu_i} \approx X_{\ell m} + \sum_{k=2}^{\infty} \left(\frac{\nu_i}{\nu_0}\right)^{2k} \Delta X_{2k,\ell m,\nu_i} \tag{5.4}$$

[1] At recombination, the CMB temperature is $T^{\rm re}_{\rm CMB} \approx 0.25$ eV, which provides a peak black-body frequency of $\nu_{\rm CMB,re} \approx 1.7 \times 10^5$ GHz. The lowest Lyman series frequency is the Lyman-α frequency, $\nu_{21} \approx 2.5 \times 10^6$ GHz [278] from state 2 to 1.

[2] The Rydberg constant, $R_\infty = \dfrac{m_e e^4}{8\varepsilon_0^2 h^3 c} \approx 10,973,731.6\ \mathrm{m}^{-1}$, expresses the maximal value of the wavenumber (the inverse wavelength) of a photon that can be emitted from an atom with an infinite nuclear mass, where m_e is the electron mass, e is the elementary charge, ε_0 is the permittivity in vacuum, h is the Planck constant, and c is the speed of light in vacuum [280].

[3] Their coefficients c_k are related to A_{2k} via $A_{2k} = c_k\, (c_0)^{-(1+k/2)}$.

where ν_0 is some reference frequency, $X_{\ell m}$ is the frequency-independent primary CMB anisotropy, and $\Delta X_{2k,\ell m,\nu_i}$ are the Rayleigh scattering contributions at frequency ν_i for the frequency scaling with a power $2k$. Using this expansion, we can estimate the effect of Rayleigh scattering on the CMB power spectra for any two maps X_{ν_i} and Y_{ν_j},

$$\begin{aligned} C_\ell^{X_{\nu_i}Y_{\nu_j}} =& \frac{1}{2\ell+1}\sum_{m=-\ell}^{\ell} X_{\ell m,\nu_i} Y^*_{\ell m,\nu_j} \\ \approx& C_\ell^{XY} + \left(\frac{1}{\nu_0}\right)^4 \left[\nu_j^4 C_\ell^{X\Delta Y_{4,\nu_j}} + \nu_i^4 C_\ell^{\Delta X_{4,\nu_i} Y}\right] \\ &+ \left(\frac{1}{\nu_0}\right)^6 \left[\nu_j^6 C_\ell^{X\Delta Y_{6,\nu_j}} + \nu_i^6 C_\ell^{\Delta X_{6,\nu_i} Y}\right] \\ &+ \left(\frac{\nu_i\nu_j}{\nu_0^2}\right)^4 C_\ell^{\Delta X_{4,\nu_i}\Delta Y_{4,\nu_j}} + \dots . \end{aligned} \tag{5.5}$$

While Rayleigh scattering affects both temperature and polarization CMB anisotropies, detection levels for the Rayleigh signal using the TE power spectrum alone are expected to be about 4 times lower compared to detection levels using the TT power spectrum. The detection levels decrease even further when using only the EE power spectrum [273]. The effects of foreground were not included in these previous detection estimates. Adding foregrounds in detection analyses could somewhat change the detection levels, as polarization maps are usually less contaminated by foregrounds. Nonetheless, we will concentrate on using the CMB temperature maps alone for detecting the Raleigh signal (such that $X = Y = T$ above), although our methodology could be easily expanded to include polarization measurements as well.

The different terms in Eq. (5.5) are split into three types:

1. *Primary×Primary*: The first term, C_ℓ^{XX}, is the isolated CMB primary anisotropies, which do not depend on Rayleigh scattering. To distinguish it, we shall later refer to it as C_ℓ^{PP}.

2. *Primary×Rayleigh*: The second and third (and all other higher-order contributions of the same type) are cross-spectra between the primary X and Rayleigh ΔX contributions, $C_\ell^{X\Delta X}$. We will concentrate on their detection, as these are expected to be the dominant contributions from Rayleigh scattering to the full power spectrum. It will be later referred to as C_ℓ^{PR}.

3. *Rayleigh×Rayleigh*: Lastly, we have the terms which depend solely on Rayleigh scattering, $C_\ell^{\Delta X\Delta X}$. These are much more negligible, and we therefore do not try to detect them directly. They will be referred to as C_ℓ^{RR}.

All of these contributions to the temperature power spectrum are shown in Fig. 5.1 for Planck's

highest frequencies. The largest Rayleigh contributions come from the cross spectra of the primary temperature signal with the Rayleigh contribution, especially for 545 and 857 GHz. In the Planck analyses, these band powers were not cleaned for measuring the primary anisotropies. Instead, they were used as templates for removing foregrounds from the lower-frequency maps.

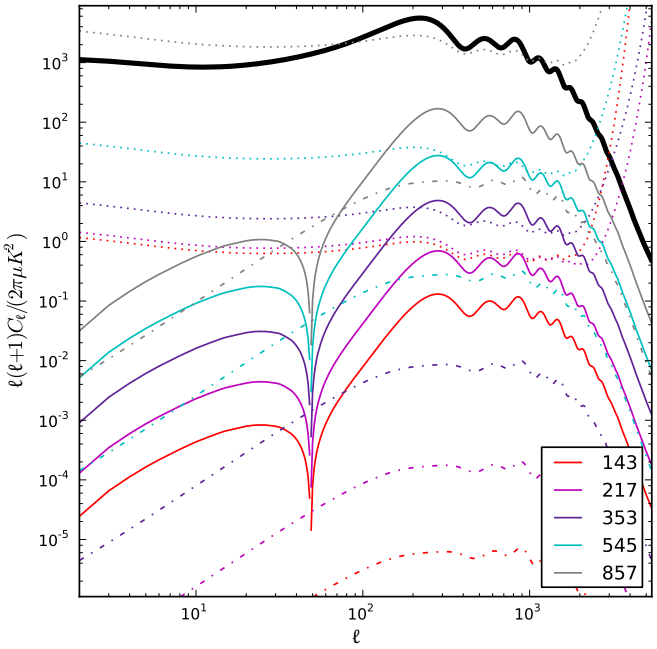

Figure 5.1: Comparison between the primary temperature anisotropies power spectrum C_ℓ^{PP} (black line), the primary×Rayleigh cross-power spectra C_ℓ^{PR} (solid lines) and the Rayleigh auto-power spectra C_ℓ^{RR} (dash-dot lines) for the high Planck frequencies 143-857 GHz. The dotted lines show a rough estimate of the foreground-free noise levels for each frequency. The values of the cross-power spectrum at $\ell \lesssim 50$ are negative. Source: Lewis [273].

Throughout this chapter, we will demonstrate our method for measuring the Rayleigh scattering signal from CMB maps using Planck's single-frequency maps[4]. Due to the dependency of Rayleigh scattering on the radiation frequency, it is necessary to use high-frequency CMB observations for such endeavour. We use the Planck maps mainly because they are the most versatile and suitable set of measurements for the task at hand. Future experiments, such as the Lite (Light) satellite for the study of B-mode polarization and Inflation from cosmic background Radiation Detection (liteBIRD) [136] and the proposed Cosmic Origins Explorer (COrE) [281], Polarized Radiation Imaging and Spectroscopy Mission (PRISM) [282], and Probe of Inflation and Cosmic Origins (PICO) [283], are expected to outperform Planck and measure the sky using a larger variety of (high) frequencies, which would make them much more ideal for detecting the Rayleigh signal. The detection method we develop here could be used by such experiments for this purpose.

[4]All of the Planck data used in this work is available at http://pla.esac.esa.int/pla.

5.3 METHODOLOGY

In this section, we show the method devised for detecting the Rayleigh scattering signature in the CMB temperature power spectrum. The full methodology pipeline is summarised in Fig. 5.2. As mentioned in the previous section, because this effect is already very small compared to the primary anisotropies power, our aim is to detect its cross-correlation with the primary anisotropies, C_ℓ^{PR}, rather than its auto-correlation C_ℓ^{RR}. We are also aiming at detecting it from a single frequency map. Although this signal is most dominant at the 545 and 857 GHz Planck bands, the maps at these high frequencies have the largest amount of foreground contamination, which mainly comes from the thermal dust emissions in our galaxy (see reviews on the various CMB foregrounds in Refs. [284, 285]). We therefore concentrate on the 353 GHz map to calculate C_ℓ^{PR}. The Rayleigh signal of this frequency is estimated to have the highest detection likelihood as well, given the Planck instrumental noises [273]. For the "R" part of the correlation, we need to use a foreground-cleaned 353 GHz temperature map, while for the "P" part we need a map which will be dominated by the primary CMB signal. Because the primary CMB anisotropies also exist in the "R" map, we also need to calculate C_ℓ^{PP} and use it to subtract the primary contribution from the full power spectrum C_ℓ^{TT}. Since the Rayleigh signal is negligible at lower frequencies, we can calculate C_ℓ^{PP} and C_ℓ^{PR} using low-frequency maps.

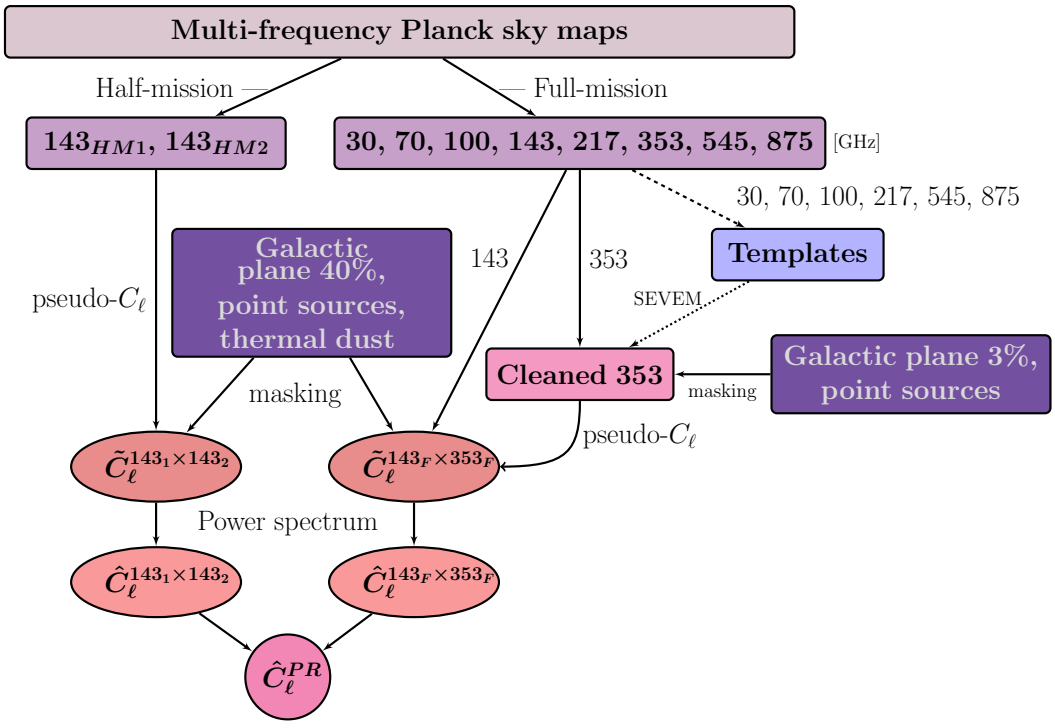

Figure 5.2: Summary of the methodology for isolating the Rayleigh scattering signal using the full- and half-mission multi-frequency Planck CMB maps. The half-mission maps of the 143 GHz measurements are used as "Rayleigh-free" CMB measurements to obtain a low-noise $\hat{C}_\ell^{PP}$ power spectrum to subtract the primary CMB signal from the "Rayleigh-rich" $\hat{C}_\ell^{143\times353}$ power spectrum.

To understand how C_ℓ^{PR} can be isolated from the full temperature power spectrum, let us consider a general temperature measurement at a given pixel p. We can write down such measurement at frequency ν as

$$T_\nu^{\rm raw}(p) = (1+g_\nu)\mathcal{B}_\nu(p)\left[P(p) + R_\nu(p) + f_\nu(p)\right] + n_\nu(p), \tag{5.6}$$

where P is the primary CMB temperature anisotropy, R_ν is the Rayleigh contribution to the CMB anisotropy signal, f_ν is the total contribution of all foregrounds (e.g., thermal dust, point sources, synchrotron radiation), and n_ν is the instrumental noise. Here, we also included two instrumental effects: a gain deviation g_ν and a beam $\mathcal{B}_\nu$. In this simplification, we neglect any possible effects of other instrumental systematics, such as crosstalk, which could also affect the temperature measurements. In this section, we neglect any possible gain deviations. The related gain uncertainties will be reintroduced in Sec. 5.4 for our likelihood analyses. Throughout, we neglect any uncertainties in the beams.

The angular power spectrum of two temperature maps at frequencies ν_i and ν_j can then be written as

$$\begin{aligned} C_\ell^{T_{\nu_i}T_{\nu_j}} =& \frac{1}{2\ell+1}\sum_{m=-\ell}^{\ell} T_{\ell m,\nu_i} T^*_{\ell m,\nu_j} \\ =& C_\ell^{PP} + C_\ell^{PR_{\nu_i}} + C_\ell^{PR_{\nu_j}} + C_\ell^{R_{\nu_i}R_{\nu_j}} + C_\ell^{f_{\nu_i}f_{\nu_j}} + \mathcal{N}_\ell^{\nu_i\nu_j}, \end{aligned} \tag{5.7}$$

where $C_\ell^{f_{\nu_i}f_{\nu_j}}$ is a contribution from foregrounds to the measured power spectrum, $\mathcal{N}_\ell^{\nu_i\nu_j}$ is the instrumental noise power spectrum, and we neglect any correlations between the CMB photons, the foregrounds, and the instrumental noise. To good approximation, we can neglect any correlations between instrumental noises at different frequencies, such that $\mathcal{N}_\ell^{\nu_i\nu_j} = 0$ for $i \neq j$. This noise term also vanishes if the two correlated maps are of the same frequency but were obtained from different observation time splits. If both $\nu_i, \nu_j \lesssim 200$ GHz, all terms which depend on the Rayleigh signal are negligible compared to the other terms, such that they can be neglected. Lastly, the contribution from foregrounds can be less significant when two different frequencies are correlated, especially when correlating two foreground-cleaned maps.

We can then use two low-frequency half-mission (HM) maps for calculating C_ℓ^{PP}, and two full-mission (FM) maps at high and low frequencies that will produce the Rayleigh signal term C_ℓ^{PR}. Using the correlations of Planck temperature maps in 143 GHz and 353 GHz, we can then

get

$$C_\ell^{T_{143}^{\rm FM}T_{353}^{\rm FM}} - C_\ell^{T_{143}^{\rm HM_1}T_{143}^{\rm HM_2}} \approx C_\ell^{PP} + C_\ell^{PR_{353}} + C_\ell^{f_{143_{\rm FM}}f_{353_{\rm FM}}} - \left(C_\ell^{PP} + C_\ell^{f_{143_{\rm HM_1}}f_{143_{\rm HM_2}}}\right)$$
$$= C_\ell^{PR_{353}} + C_\ell^{f_{143_{\rm FM}}f_{353_{\rm FM}}} - C_\ell^{f_{143_{\rm HM_1}}f_{143_{\rm HM_2}}}. \tag{5.8}$$

Instead of using the full- and half-missions at 143 GHz, we can also use even lower frequencies for which the Rayleigh contribution is even smaller in order to fully subtract the primary anisotropy contribution. The main reason for using the 143 GHz maps specifically is that at this frequency the sky maps are already relatively clean of foregrounds, such that we can expect $C_\ell^{f_{143_{\rm HM_1}}f_{143_{\rm HM_2}}}$ to be low. When correlating the 353 GHz map with the full-mission 143 GHz map, we are effectively left with one Rayleigh-dependent power spectrum, $C_\ell^{PR_{353}}$. By using the same "Rayleigh-free" frequency for estimating the two temperature power spectra, the surviving foreground power spectrum terms would be somewhat correlated, such that their combined contribution could be decreased due to their opposite signs. Instead of correlating a "Rayleigh-free" map with a "Rayleigh-rich" map, we could also use another high frequency map to have additional Rayleigh terms to improve detection possibilities. Since higher frequency maps are more contaminated by foregrounds, such correlation may result in larger foreground residuals, even if both maps are first cleaned from foregrounds. Eq. (5.8) shows that what limits the detection of $C_\ell^{PR_{353}}$ is the foreground correlations. The ability to clean individual frequency maps from foregrounds is therefore very important for this analysis.

The contributions of Rayleigh scattering to the CMB temperature power spectrum relative to the primary temperature power spectrum for different frequency combinations without any foreground contamination are shown in Fig. 5.3, using

$$\frac{\Delta\mathcal{D}_\ell}{\mathcal{D}_\ell} \equiv \frac{\mathcal{D}_\ell^{PP} - \mathcal{D}_\ell^{T_{\nu_i}T_{\nu_j}}}{\mathcal{D}_\ell^{PP}}, \tag{5.9}$$

where

$$\mathcal{D}_\ell \equiv \frac{\ell(\ell+1)}{2\pi}C_\ell. \tag{5.10}$$

These fractional differences are shown both from theoretical power spectra (dark green lines) and from maps of Primary+Rayleigh CMB simulations (without instrumental noise or foregrounds). The power spectra which include the effect of Rayleigh scattering on the CMB anisotropies were

generated using the Rayleigh branch of the Boltzmann code CAMB[5] [113]. Expectedly, the largest contributions come from the auto- and cross-correlations with the 545 GHz map. While the Rayleigh contributions would be even higher for correlations with the 875 GHz map, we do not show them here as this map is exclusively used in the foreground cleaning process. Since the Rayleigh signal from the 143×353 correlation is very small compared to the primary signal, subtracting the primary contribution is essential for its detection. Below we describe the way in which the individual frequency mas can be cleaned before estimating their correlations.

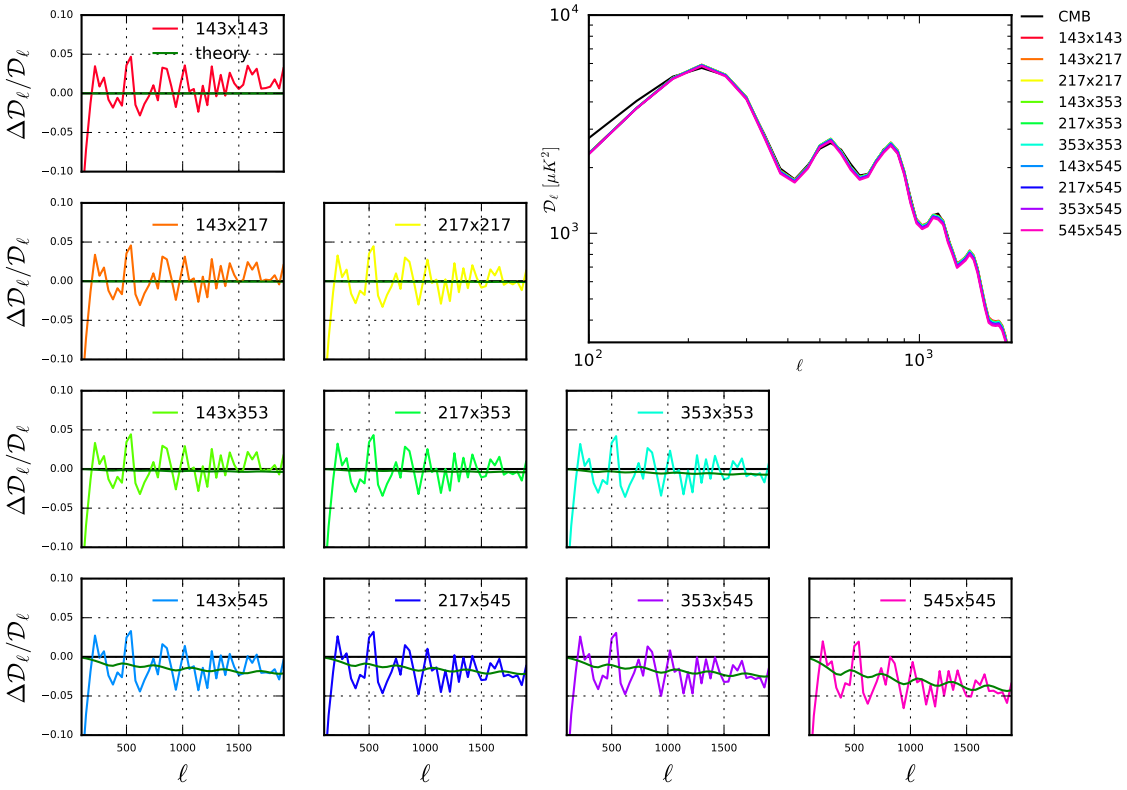

Figure 5.3: The primary and Rayleigh scattering contributions to the total CMB temperature power spectrum for pairs of high frequency Planck channels. The top right panel shows C_ℓ^{PP} (black line) and the full TT power spectrum of each frequency combination (coloured lines). The other panels show the fractional difference of Eq. 5.9. The dark green lines were calculated from theoretical power spectra, while the other lines were obtained from primary+Rayleigh simulations (with no instrumental noise or foregrounds) using Eq. (5.8).

5.3.1 CLEANING THE CMB MAPS

While there are many methods for cleaning CMB maps, most of them produce one cleaned map which is composed of the CMB anisotropies from all frequency maps. One of the main cleaning methods used by the Planck collaboration, for example, is the SMICA (Spectral Matching

[5]More information on CAMB can be found at http://camb.info/readme.html. The Rayleigh branch used in this work is available at https://github.com/cmbant/CAMB/tree/rayleigh.

Independent Component Analysis) method [68, 256–258]. It was used to produce the CMB maps shown in Fig. 1.2, have an effective smoothing similar to that of the 143 GHz channel. Since we are interested in extracting Rayleigh information of a specific frequency, we need to use a method which cleans the individual frequency maps. For this, we use one of the other cleaning methods that were used by Planck, the SEVEM (Spectral Estimation Via Expectation Maximization) method [258, 286–288][6]. The main purpose of this method is to produce clean CMB maps of each frequency using cleaning templates made by combining maps of other frequencies. As the CMB anisotropies are not frequency-dependent, differencing two CMB maps of different frequencies results in a CMB-free map. These maps can then be used as templates in the cleaning process. While the templates can be constructed from external maps (i.e., from other experiments), using internal maps might be best to avoid potential inconsistencies. One of the main advantages of SEVEM is that no assumptions need to be made on the foregrounds or noise levels in the maps for the cleaning process. Such assumptions could bias the cleaning process which could increase overall uncertainties when using the cleaned maps.

For our methodology, we construct the cleaning template in a similar way. The templates are constructed by differencing two maps of frequencies ν_a and ν_b to obtain foreground-dominated maps. The cleaning process can be improved by smoothing the two maps so that they have a common resolution prior to subtraction. For this, each map can be convolved with the beam of the other map, which could minimise the CMB residues in the template. A template for cleaning map of frequency ν_j using maps of frequencies ν_a and ν_b is then given by

$$\mathcal{T}_{\nu_i,j}(\mathbf{x}) \equiv \left(\mathcal{B}_{\nu_b} T^{\rm raw}_{\nu_a}\right)(\mathbf{x}) - \left(\mathcal{B}_{\nu_a} T^{\rm raw}_{\nu_b}\right)(\mathbf{x}). \tag{5.11}$$

The frequencies used for the templates are different than those used to calculate C_ℓ^{PR} to avoid unwanted correlations. As mentioned before, the higher frequency maps are usually used in the templates due to their higher level of foregrounds. These maps can, however, add more Rayleigh-depending terms in the resulting power spectra. Such contributions could be added to the theoretical predictions for the expected Rayleigh signal.

Several of the templates that can be used to clean the Planck maps in our analysis are shown in Fig. 5.4. Since we are interested specifically in the 353 GHz and 143 GHz maps, the templates are constructed using all other frequency maps.

[6] More details are also available at https://wiki.cosmos.esa.int/planckpla/index.php/CMB_and_astrophysical_component_maps#SEVEM_2.

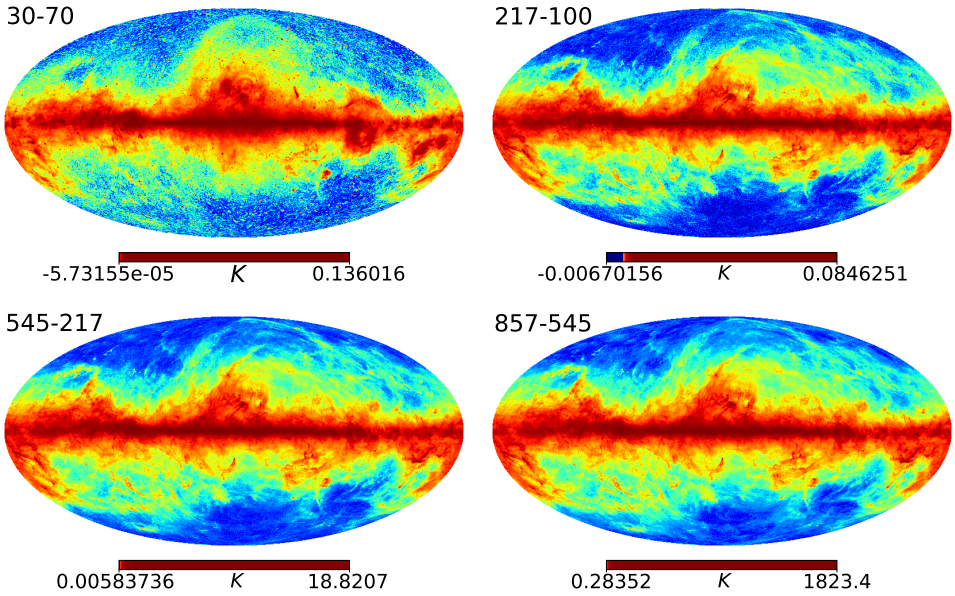

Figure 5.4: Example templates from subtracting Planck maps of different frequencies, as described in Eq. (5.11). By construction, the templates do not have any primary CMB anisotropies, and are dominated by foregrounds. Although the spatial features are relatively similar in all maps, the foreground contamination levels are very different.

A resulting cleaned map of frequency ν_i can be written as

$$T^{\rm clean}_{\nu_i}(\mathbf{x}) = T^{\rm raw}_{\nu_i}(\mathbf{x}) - \sum_{j=1}^{n_t} \alpha_{\nu_i,j} \mathcal{T}_{\nu_i,j}(\mathbf{x}) \tag{5.12}$$

where $T^{\rm raw}_{\nu_i}(\mathbf{x})$ is the raw map of the same frequency, $\mathcal{T}_{\nu_i,j}(\mathbf{x})$ is the $j^{\rm th}$ cleaning template for cleaning a map at frequency ν_i, n_t is the number of templates. The $\alpha_{\nu_i,j}$ are template weights, which are estimated by minimising the variance of the cleaned masked map,

$$\chi^2 = \sum_p \left[\left(T^{\rm raw}_{\nu_i}(p) - \sum_{j=1}^{n_t} \alpha_j \mathcal{T}_{\nu_i,j}(p) \right) \times {\rm Mask}(p) \right]^2 \tag{5.13}$$

$$\frac{\partial \chi^2}{\partial \alpha_l} = 0 \;\Rightarrow\; \sum_{k \neq l} \alpha_k \sum_p \mathcal{T}_{\nu_i,l}(p) \mathcal{T}_{\nu_i,k}(p) = \sum_p \mathcal{T}_{\nu_i,l}(p) T^{\rm raw}_{\nu_i}(p) \tag{5.14}$$

where the sum is over pixels p of the map and template, and the applied mask acts as an effective inverse variance. The sum over p in Eq. (5.14) is over the unmasked pixels. To estimate these coefficients for Planck, the mask used is Planck's confidence mask, which masks around $\sim$3% of the sky, in combination with Planck's point sources mask.

The Planck collaboration published SEVEM-cleaned 100, 143 and 217 GHz maps. Here we repeat their cleaning procedure as a proof-of-concept and continue to clean the 353 and 545 GHz maps for demonstrating the capabilities of this cleaning method and for attempting to extract the Rayleigh signal from them. All of the cleaned maps are shown in Fig. 5.5. The lower frequency

maps are in good agreement with the Planck cleaned maps; their masked power spectra are similar by more than 95% across all multipole range. While some of the areas in the 353 GHz map do possess CMB anisotropy features, both high frequency maps are still contaminated by foregrounds more than the other maps.

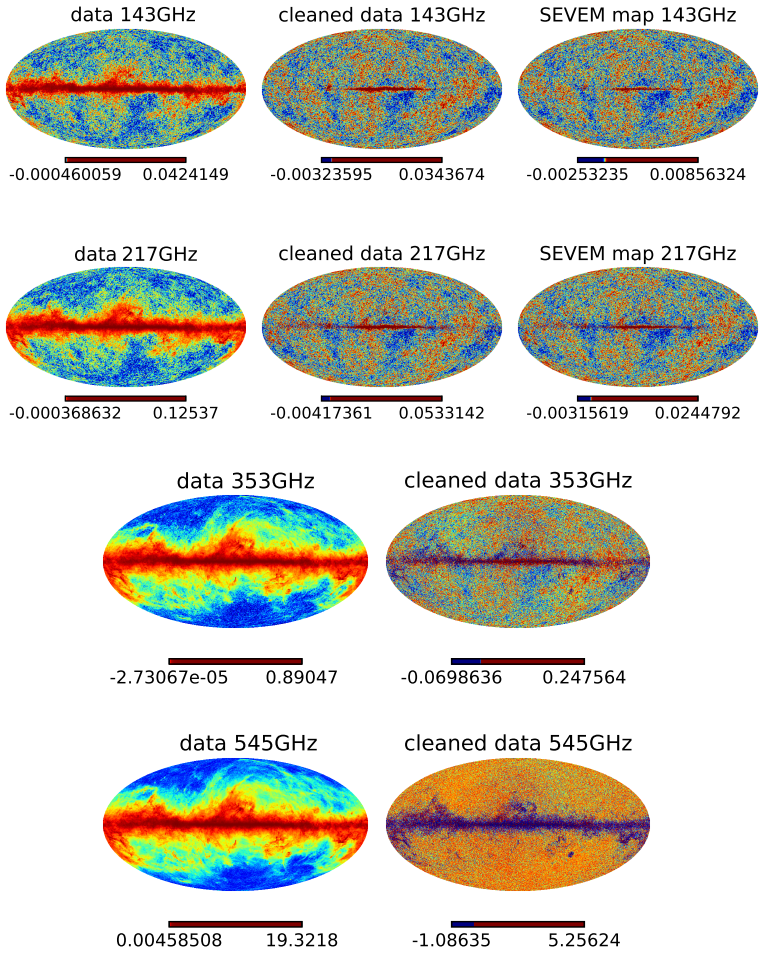

Figure 5.5: Comparison between the raw (left-most figure in each row) and cleaned Planck temperature maps of different frequencies. The first two rows are for the 143 and 217 GHz frequencies, which Planck provided SEVEM-cleaned maps for. These clean Planck maps are the right-most figure in these rows, shown for comparison with the results of our similar cleaning implementation (the middle figure in these rows). The higher 353 and 545 GHz frequencies were not cleaned individually by Planck. The colorbars are in Kelvin. For 143 and 217 GHz the maximal amplitudes of our cleaned maps are not exactly as those of the Planck SEVEM maps. This might be due to the point sources inpainting procedure Planck performed in their analysis. Instead of inpainting, we mask these regions when calculating the power spectra. The resulting power spectra of the cleaned maps are consistent with those of the SEVEM maps.

The success of this cleaning procedure depends on several choices: Which frequency combinations to use for making the templates, which template combinations to use to clean each frequency map, how much of the map area should be masked for the minimisation process, and which template smoothing level would produce the best cleaning results. These choices would be different for each experiment, but they can easily be made by performing the cleaning procedure using different choice combinations, as the cleaning process is very fast and not numerically-expensive.

5.3.2 POWER SPECTRUM ESTIMATES

The cleaned frequency maps are used to estimate the power spectra of Eq. (5.8) to obtain $C_\ell^{PR_{353}}$. We use the $1^{\rm st}$ and $2^{\rm nd}$ half-mission maps at 143 GHz to calculate our "Rayleigh-free" power spectrum, which will be subtracted from the cross-power of the 143 GHz and 353 GHz maps. The power spectra are calculated from the masked maps. The masked applied in this stage covers a larger area compared to the mask used to estimate the α coefficients in the cleaning process. This is done so that areas dominated by foregrounds could help in the cleaning process, whereas masking more areas to estimate the power spectra helps in reducing residual foregrounds. As before, the mask used is a combination of several masks. Here, we combine the point source mask with the galactic plane mask that masks 40% of the sky. We also include a custom-made mask using the Planck full focal plane (FFP) foreground simulations[7] [289], which include pixel-space information from the measured thermal dust emissions. Specifically, we identified foreground-dominated areas (pixels with exceptionally-high intensity) in the FFP8 143 GHz foreground map and nullify their coordinates in the combined mask prior to apodization.

To avoid contaminating the power spectra with power leakage due to sharp transitions at the boundary of the masks, they need to be apodized before they are applied to the maps. Apodization smooths the spectral features of the mask and helps to produce a more accurate power spectrum [178]. The total apodized mask we applied on the cleaned Planck maps is show in Fig. 5.6. The total mask was apodized using an apodization scale of 30 arcmin.

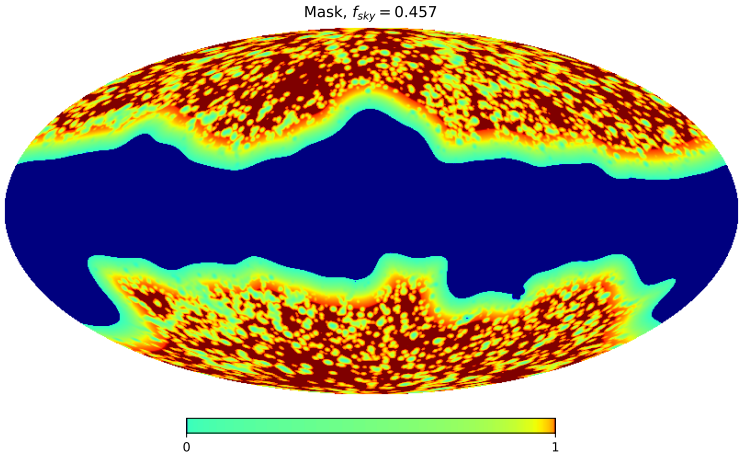

Figure 5.6: Our composite mask used to evaluate $\hat{C}_\ell^{T_{143}^{\rm HM_1} T_{143}^{\rm HM_2}}$ and $\hat{C}_\ell^{T_{143}^{\rm FM} T_{353}^{\rm FM}}$ using the Planck data maps. The mask combines the Planck galactic plane mask, which masks 40% of the sky, the 100 and 217 GHz Planck point source masks, and an additional custom-made mask that masks areas with exceptionally-high intensity in the Planck FFP8 foreground map at 143 GHz. The mask is apodized with apodization length of 30 arcminutes to avoid power spectrum distortions.

[7] More information about the simulations can be found at https://wiki.cosmos.esa.int/planckpla2015/index.php/Simulation_data.

The power spectra for each combination of masked and cleaned maps is obtained for each frequency using the pseudo-C_ℓ method [89, 90, 236, 237, 290]. This method is used to recover the power spectrum of maps that are partially masked, as then the number of modes m in each multipole ℓ of the map is different compared to the full-sky modes. For this method, we first estimate the pseudo-power spectrum of the masked maps using the same averaging of Eq. (5.7),

$$\tilde{C}_\ell^{T_{\nu_i}T_{\nu_j}} = \frac{1}{2\ell+1}\sum_{m=-\ell}^{\ell} \check{T}_{\ell m,\nu_i}\check{T}^*_{\ell m,\nu_j}, \tag{5.15}$$

where $\check{T}_{\ell m}$ are the harmonic coefficients of the masked temperature map $\check{T}(\hat{\mathbf{n}}) \equiv M(\hat{\mathbf{n}})T(\hat{\mathbf{n}})$. While this is not the full temperature angular power spectrum, its ensemble average is related to the true power spectrum estimate $\hat{C}_\ell$ via [89, 90]

$$\left\langle \tilde{C}_\ell^{T_{\nu_i}T_{\nu_j}} \right\rangle = \sum_{\ell'} \mathcal{M}_{\ell\ell'}\mathcal{B}^2_{\ell,\nu_i\times\nu_j}\mathcal{P}^2_\ell \left\langle \hat{C}_{\ell'}^{T_{\nu_i}T_{\nu_j}} \right\rangle, \tag{5.16}$$

where is the mixing matrix [291], $\mathcal{B}_{\ell,\nu_i\times\nu_j}$ is the cross- or auto-correlated beam window function of the $i^{\rm th}$ and $j^{\rm th}$ frequencies[8], and $\mathcal{P}_\ell$ is the pixel transfer function that describes the smoothing effect induced by the finite pixel size[9]. The mixing matrix,

$$\mathcal{M}_{\ell_1\ell_2} = \frac{2\ell_2+1}{4\pi}\sum_{\ell_3}(2\ell_3+1)\,\mathcal{W}_{\ell_3}\begin{pmatrix}\ell_1 & \ell_2 & \ell_3\\ 0 & 0 & 0\end{pmatrix}^2 \tag{5.17}$$

relates the number of missing modes to the full-sky modes using the Wigner-3j symbols [292] and the power spectrum of the mask,

$$\mathcal{W}_\ell = \frac{1}{2\ell+1}\sum_{m=-\ell}^{\ell}|M_{\ell m}|^2, \tag{5.18}$$

where

$$M_{\ell m} = \int d\Omega_{\hat{\mathbf{n}}} M(\hat{\mathbf{n}})Y^*_{\ell m}(\hat{\mathbf{n}}) \approx \Omega_{\rm pix}\sum_p M(p)Y^*_{\ell m}(p), \tag{5.19}$$

is the harmonic decomposition of the mask $M(\hat{\mathbf{n}})$ and $\Omega_{\rm pix}$ is the angular pixel area[10].

To obtain the full power spectrum estimator from the pseudo-power spectrum, we therefore

[8]The beam window functions for Planck can be found at https://irsa.ipac.caltech.edu/data/Planck/release_2/ancillary-data/.
[9]This function is given by HEALPix and depends on the resolution of the map [176].
[10]A map with $N_{\rm pix}$ pixels has an angular pixel area $\Omega_{\rm pix} = 4\pi/N_{\rm pix}$.

need to invert the mixing matrix and calculate

$$\hat{C}_\ell^{T_{\nu_i}T_{\nu_j}} = \sum_{\ell'} \frac{\mathcal{M}^{-1}_{\ell\ell'}\tilde{C}_{\ell'}^{T_{\nu_i}T_{\nu_j}}}{\mathcal{B}^2_{\ell,\nu_i\times\nu_j}\mathcal{P}^2_\ell}. \tag{5.20}$$

Using this method to obtain $\hat{C}_\ell^{T^{\rm HM1}_{143}T^{\rm HM2}_{143}}$ and $\hat{C}_\ell^{T^{\rm FM}_{143}T^{\rm FM}_{353}}$ from the Planck maps, our attempt at extracting the $C_\ell^{P_R 353}$ component of Eq. (5.8) is shown in Fig. 5.7. The two power spectra prior to subtraction are dominated by the primary CMB anisotropy and foregrounds. They both recover the first $\sim$4 peaks of the temperature power spectrum, however foreground residuals dominate on scales higher than $\ell \approx 1500$. The multipole range of the recovered peaks is also the multipole range where $C_\ell^{PR_{353}}$, shown in the dark green line, is maximal. We show the (binned) subtraction of the two power spectra when they are constructed from the raw maps (red points) and cleaned maps (purple points). While the cleaning process brings the resulting power closer to the expected signal around $\ell \approx 250$, the foreground residuals in maps are not sufficiently low to recover the Rayleigh signal. We nonetheless expect that a similar method could be used successfully by future CMB experiments with the guidelines discussed in our work if foregrounds can be removed sufficiently well.

5.4 DETECTION LIKELIHOODS AND FORECASTS

We conclude this work by performing a likelihood analysis similar to that of Ref. [273] to assess the detection levels of the Rayleigh signal using CMB observations at different frequencies. Here we add to the analysis possible gain variations by marginalizing over realistic gain deviation values, and also consider the effective instrumental noises which could contaminate the clean maps due to the cleaning process. We perform the likelihood analysis for both Planck and the upcoming Simons Observatory (SO) experiment [131], where the noise in the SO estimates does not include the contribution from cleaning the maps, which was not attempted in this work. Although SO will observe the sky in less and lower frequencies compared to Planck, the SO measurements will have significantly lower noise levels and a higher resolution, which is our motivation for performing this forecast analysis.

We use the Fisher matrix (see Appendix A.1 for more details) to estimate the detection likelihoods of the Rayleigh signal. The Fisher matrix components for each multipole ℓ can be written as

$$F_{ij,\ell} = \frac{2\ell+1}{2} f_{\rm sky} {\rm Tr}\left(\boldsymbol{C}_\ell^{-1}\frac{\partial \boldsymbol{C}_\ell}{\partial\theta_i}\boldsymbol{C}_\ell^{-1}\frac{\partial \boldsymbol{C}_\ell}{\partial\theta_j}\right), \tag{5.21}$$

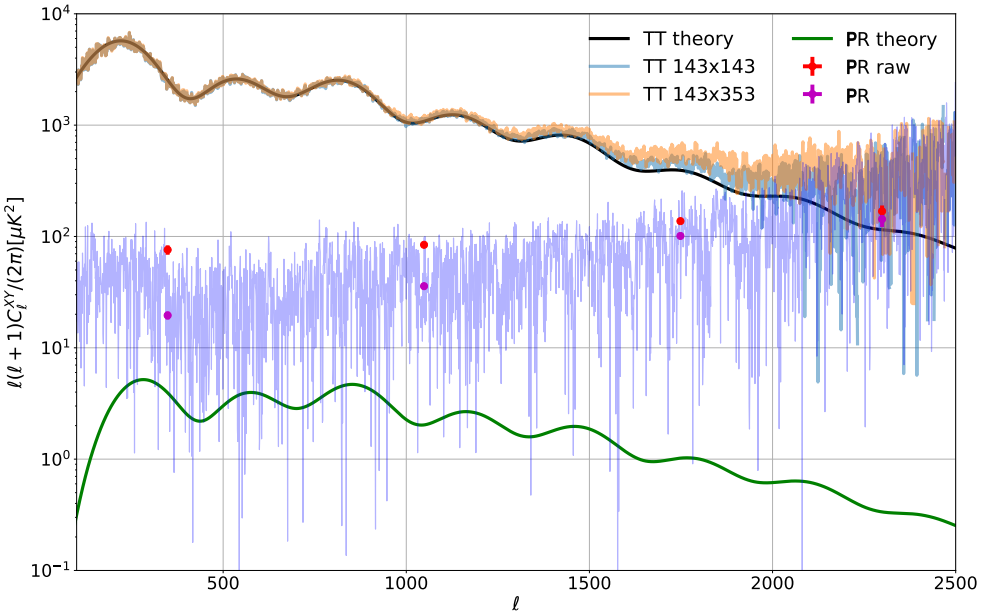

Figure 5.7: The final products of our pipeline to recover the temperature×Rayleigh cross-spectrum $C_\ell^{PR_{353}}$ (the theory spectrum shown in green). The efforts to recover this power spectrum used $\hat{C}_\ell^{T_{143}^{\rm HM1}T_{143}^{\rm HM2}}$ (blue line) that was subtracted from $\hat{C}_\ell^{T_{143}^{\rm FM}T_{353}^{\rm FM}}$ (orange line). The black line is the theory C_ℓ^{PP}. All of the maps used in the power spectrum estimates were cleaned. The binned result of the subtraction described in Eq. 5.8 is shown given power spectra that were constructing with the raw (red points) and cleaned (purple points; purple line is the unbinned result) temperature maps. Although using the cleaned maps improved the attempts of recovering the Rayleigh signal, especially at $\ell \lesssim 1500$, the result from subtracting the two power spectra of the maps is still significantly contaminated by foregrounds. The closest data point (around $\ell \lesssim 500$) is more than a factor of 2 higher than the theoretical signal.

where $f_{\rm sky}$ is the observed sky fraction of the experiment, and $\boldsymbol{C}_\ell \equiv \langle \boldsymbol{T}_{\ell m}\boldsymbol{T}_{\ell m}^*\rangle$ is a matrix of the CMB covariances. In our analysis, the parameter of interest is the amplitude of the Rayleigh scattering-related terms in the covariances, $\theta_1 \equiv R$. We also consider the calibration uncertainty of the experiment as a second parameter, $\theta_2 \equiv g_\nu$, for marginalization. The covariance matrix of frequency ν and the primary signal is then

$$\begin{aligned}\boldsymbol{C}_\ell &= \begin{pmatrix} (1+g_\nu)^2\left[C_\ell^{PP}+2RC_\ell^{PR_\nu}+R^2C_\ell^{R_\nu R_\nu}\right]+\mathcal{N}_{\ell,\nu} & (1+g_\nu)(1+g_0)\left[C_\ell^{PP}+RC_\ell^{PR_\nu}\right] \\ (1+g_\nu)(1+g_0)\left[C_\ell^{PP}+RC_\ell^{PR_\nu}\right] & (1+g_0)^2C_\ell^{PP}+\mathcal{N}_{\ell,0}\end{pmatrix} \\ &\approx \begin{pmatrix} (1+g_\nu)^2\left[C_\ell^{PP}+2RC_\ell^{PR_\nu}\right]+\mathcal{N}_{\ell,\nu} & (1+g_\nu)\left[C_\ell^{PP}+RC_\ell^{PR_\nu}\right] \\ (1+g_\nu)\left[C_\ell^{PP}+RC_\ell^{PR_\nu}\right] & C_\ell^{PP}+\mathcal{N}_{\ell,0}\end{pmatrix},\end{aligned} \tag{5.22}$$

where $\mathcal{N}_{\ell,0}$ is the noise of the reference black body (pure primary CMB anisotropies without the

contribution of Rayleigh scattering) which is taken to be uncorrelated between frequencies, and the black body gain calibration is assumed to be well known such that $g_0 = 0$. We also neglect the contribution of $C_\ell^{R_\nu R_\nu}$ to simplify the computation, as it is much smaller compared to both $C_\ell^{PR_\nu}$ and C_ℓ^{PP}. The derivative of the covariance matrix with respect to R is then

$$\frac{\partial \boldsymbol{C}_\ell}{\partial R} \approx \begin{pmatrix} 2(1+g_\nu)^2 C_\ell^{PR_\nu} & (1+g_\nu) C_\ell^{PR_\nu} \\ (1+g_\nu) C_\ell^{PR_\nu} & 0 \end{pmatrix}, \tag{5.23}$$

and with respect to g_ν

$$\frac{\partial \boldsymbol{C}_\ell}{\partial g_\nu} = \begin{pmatrix} 2(1+g_\nu)\left[C_\ell^{PP} + 2RC_\ell^{PR_\nu}\right] & C_\ell^{PP} + RC_\ell^{PR_\nu} \\ C_\ell^{PP} + RC_\ell^{PR_\nu} & 0 \end{pmatrix}. \tag{5.24}$$

The process of cleaning the maps from foregrounds also adds additional noise to the cleaned map, as the templates themselves have noise. We estimate the effective noise levels in the cleaned maps by multiplying the white noise levels of each map with the respective α coefficients of the cleaning process and the respective beams (see Eq. (5.11)). These effective noise levels of the cleaned maps, which are shown in Fig. 5.8, are used as the noise estimates in our Planck forecast. Although this noise addition can be substantial in the likelihood analysis, we expect it to not affect the accuracy of our detection method, as these noise terms do not affect the cross-spectra estimates.

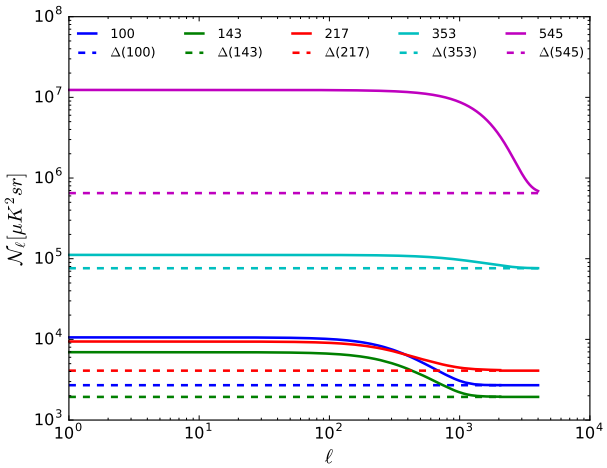

Figure 5.8: Noise levels in the cleaned maps (solid lines) compared to the instrumental white noise (dashed lines) of the multi-frequency Planck maps [293]. The cleaned 545 GHz has the highest amount of noise contamination from the templates, while the cleaned 353 GHz, which is our main map in the analysis, has the minimal noise addition. The effective noise at small scales converges to the instrument white noise due to the effective beams of the template maps. This convergence happens at smaller angular scales for the lower frequencies.

Apart from considering the effective noise levels in the analysis, we also introduce a gain uncertainty by marginalizing over the gain deviations using the gain variance $\sigma^2_{g_\nu}$. The marginalized expression of the Rayleigh×Rayleigh component of the Fisher matrix is then given

by

$$F^{\rm marg}_{RR,\nu} = \left\{ \left[\sum_\ell \begin{pmatrix} F_{00,\ell} & F_{01,\ell} \\ F_{10,\ell} & F_{11,\ell} + \frac{1}{\sigma^2_{g_\nu}} \end{pmatrix} \right]^{-1} \Bigg|_{RR} \right\}^{-1}, \tag{5.25}$$

which included the additional information on the calibration uncertainty σ_{g_ν}. The values for σ_{g_ν} for Planck were taken from [293], and we set the mean gain deviation to be zero. The instrument specifications for SO were chosen prior to any official SO publication, however they are consistent with values which have been published for the SO large aperture telescope after the work in this chapter was carried out [131]. The SO gain uncertainties are taken as 0.5% for all frequencies.

The resulting likelihood estimates for both experiments are known in Fig. 5.9. For Planck, the previously forecasted detection level for the 353 GHz measurements, $\sim 3.2\sigma$, goes down to $\sim 2.9\sigma$ (shown in the legends of the figure) without including foreground contribution. This suggests that optimising the cleaning method may still not be sufficient for a 3σ detection of the Rayleigh signal. Although the SO frequencies are lower compared to the Planck frequencies, the expected SO noise levels are substantially lower compared to Planck. Without considering the effects of foreground residuals, the Rayleigh signal is forecasted for an SO-like experiment to be detectable by 5.8σ and 4.1σ using the 220 GHz and 270 GHz channels, respectively. Because foregrounds are the limiting factor of this detection, a more robust forecast is required to provide more realistic detection levels. Nonetheless, these promising results encourage the efforts for constructing an SO-specific Rayleigh detection pipeline along the lines of the methodology described in this work.

5.5 CONCLUSIONS AND FUTURE PROSPECTS

Rayleigh scattering affected the CMB during and shortly after recombination, and the resulting changes in the CMB anisotropies can be modelled very accurately both analytically and numerically. Detecting this signal could help to better constrain early universe physics due to its dependency on the baryon density in the early Universe, and its consistent modelling could improve foreground modelling for cleaning the CMB and for component separation analyses.

The aim of this work was to provide a guide for constructing pipelines for detecting the Rayleigh signal using multi-frequency CMB observations. We demonstrated our methodology by applying it on the available high-frequency Planck data maps. Although the Rayleigh signal was not detected in the Planck maps using our pipeline, we forecast that it may be detectable using high frequency measurements of the upcoming Simons Observatory experiment by up to $\sim 5.8\sigma$.

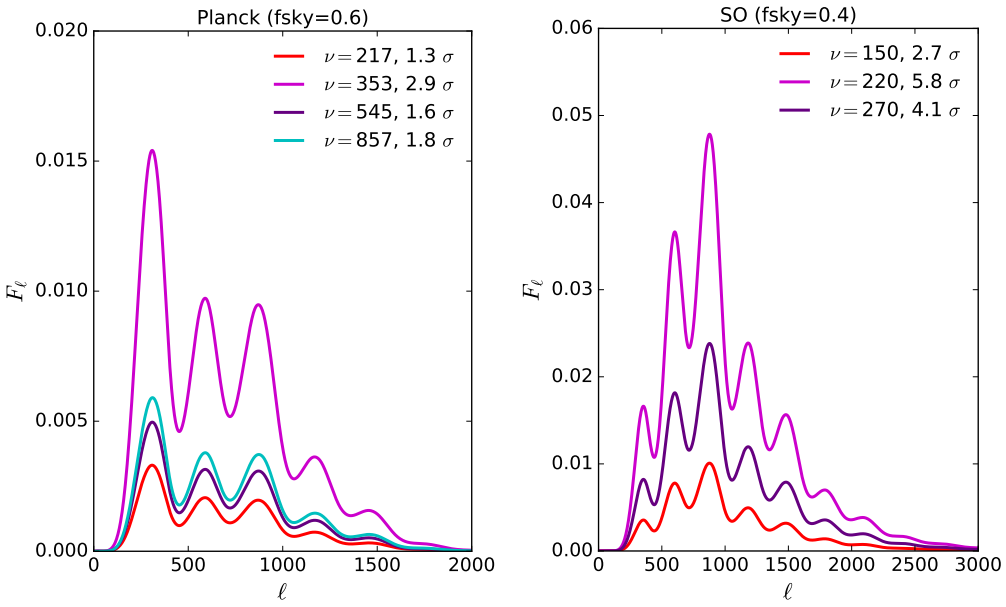

Figure 5.9: Fisher analysis results for detecting the effect of Rayleigh scattering on the CMB for a Planck-like experiment with cleaned multi-frequency maps (left) and for a Simons Observatory-like experiment using approximated experiment sensitivities (right). The instrument specifications used for SO were internal collaboration values prior to any official SO publications, but are consistent with current published values for the SO large aperture telescope [131]. The gain uncertainty of both experiments were marginalized. The gain uncertainty values for Planck were adopted from Ref. [293], while for SO we assume 0.5% uncertainty for all frequencies. The legends show the statistical significance ($N\sigma$) of the detection for each frequency.

The method presented here is fairly simple and not computationally expensive, such that any future CMB experiment that observes at high-enough frequencies could easily implement it without the need for specific instrumentation requirements. Despite its simplicity, it can be improved and tailored for each CMB experiment to optimise detection feasibility. It is expected that future CMB experiments such as LiteBIRD, and the proposed PICO mission, would be able to detect this signal using a similar pipeline. LiteBIRD is expected to perform full-sky observations for 3 years in 15 frequencies between 34-488 GHz, while PICO intends to observe for 5 years in 21 frequencies between 21-799 GHz. These specifications make the two experiments very ideal for detecting the Rayleigh signal with high significance level.

The detection method presented in this work could be further extended and possibly even optimised. The main limitation for detecting the Rayleigh signal is residual foregrounds, and therefore applying better cleaning methods could significantly improve detection likelihoods for future experiments. Other methods which could be used to clean individual CMB frequency maps, such as the Delta-Map method [294], might produce better results compared to the `SEVEM` method shown here. Moreover, it may also be possible to construct a Wiener filter (see Appendix A.2 for more details) to optimise the detection of the Rayleigh signal. Our likelihood

forecast can also be further improved by including the impact of foregrounds in our covariance matrices. While our method aims at detecting the Rayleigh signal using individual frequency maps, it might be possible to detect an effective Rayleigh signal by using a SMICA-like method to clean the CMB maps, which is designed to optimise the Rayleigh signal instead of the primary CMB anisotropies. One could also perform a full joint-likelihood analysis of the primary anisotropies and Rayleigh signals which includes models of residual foregrounds for an improved forecast. We leave these further explorations to future work.

CHAPTER 6

Conclusions

This thesis explored various aspects of CMB data analysis which are relevant for current and future high-sensitivity CMB experiments. The CMB has been one of the most powerful tools in cosmology over the last few decades, as its measurements have been used to put extremely tight constraints on the standard cosmological model. As our abilities to observe the CMB with higher precision advance, it is key to improve our analysis methods to use the full potential of the measurements. The results shown in this thesis are a small yet essential part in this endeavour.

We have examined in detail several CMB analysis methods, mainly around the topic of CMB lensing. Chapter 2 demonstrated the effectiveness of different ways the CMB maps could be filtered to establish an optimal filtering method. We showed that exploiting the full covariance matrix of the data in the filter is essential to obtain the most accurate lensing reconstruction using the quadratic estimator method. We also developed another filtering step, using a similar filtering process, to filter the quadratic estimators. Using simulations, we showed that our new filtering step can improve the accuracy of lensing estimation even further, especially when including polarization measurements in the lensing reconstruction analysis. This was performed specifically for the upcoming Simons Observatory (SO) and CMB-S4 experiments that are expected to provide very high resolution and low-noise CMB measurements. The results of this work could be used as a guideline for establishing an optimal quadratic-estimator-based lensing pipeline for these and other future CMB experiments.

Continuing with explorations around the accuracy of the lensing analysis, Chapter 3 examined how different instrumental systematics could affect the lensing reconstruction accuracy. Using the optimal methods of Chapter 2 in the lensing pipeline, we showed how significant the different systematics biases are on the lensing potential power spectrum for an SO-like experiment, and

how it may be possible to mitigate their effects for analyses of future ground-based CMB experiments. Our results concluded that current mitigation strategies which are used to tackle the effects of the most problematic systematics could reduce the impact of systematics on the lensing reconstruction analysis. Apart from providing this forecast, we have shown how the systematics biases manifest at different levels of the lensing analysis, which could be useful for understanding biases in future lensing analyses and guide their construction to be less vulnerable to instrumental systematic effects. The methodology and results of this chapter could also be used during the planning stages of a CMB experiment to help understand instrumental requirements for obtaining optimal science products in general.

The last lensing-related work is presented in Chapter 4, where we applied our new lensing analysis to real data for the first time. Prompted by the new Planck release, NPIPE, we set out to analyse the new maps using the 2018 Planck lensing pipeline and assess the possible improvements from using of our κ-filtering method. Our results showed that the new method does indeed improve the lensing reconstruction uncertainties, and that the improvement is consistent with our theoretical predictions given the noise covariance. While in the previous chapters our results concentrated on the reconstruction uncertainty, in this chapter we went a step further and used the reconstruction results to estimate some of the cosmological parameters using their likelihoods. We showed that even when the reconstruction uncertainty is only improved by up to $\sim 7\%$ at a limited multipole range $L \lesssim 200$, the improvements in uncertainties of some of the parameter estimates can be up to $\sim 16\%$. This is yet another motivation for applying our method in future lensing analyses, especially those that we forecasted in Chapter 2 to have a much greater benefit from it. The work done in this chapter is only a part of current on-going work around the NPIPE maps. We have yet to explore, using these maps, the ability of our method to improve a polarization-only reconstruction as our calculations predict. The comparisons we demonstrated here can be made more thorough by applying our method on the previous Planck release as well. These comparisons will be included in a future publication.

Although most of our work around lensing reconstruction involved the use of quadratic estimators, developing even more capable lensing reconstruction techniques will be crucial in the next few years. There is yet much work to be done to continue to improve our methods and ability to extract lensing information from CMB measurements, and our work is a small part of this on-going and exciting quest.

Lastly, we deviated from the main theme of lensing reconstruction to look into the detection of

yet another CMB effect, albeit a much smaller one in comparison — the Rayleigh scattering of the CMB. In Chapter 5 we presented a possible pipeline for detecting the Rayleigh signal using multi-frequency CMB measurements, and as with Chapter 4, used Planck data to test its capabilities. The work on this project was mainly motivated by the promising forecasts done in the literature for detecting the Rayleigh signal, which showed that, without the consideration of foregrounds, it could be detected using Planck data with a significance level slightly higher than 3σ. Although we were not able to detect the Rayleigh signal using our pipeline, we provide the guidelines necessary for such detection from future CMB experiments, which would be much more ideal for the task compared to Planck. More work can also be done to improve and develop our pipeline further. Such work would require a proper testing environment using foreground simulations, as foregrounds are the most limiting factors of this detection. Looking more closely into the correlation of foregrounds at both high and low frequencies, and developing better methods for cleaning individual frequency maps, would be key to the successful detection of the Rayleigh signal.

Our results portray a very optimistic and promising future for CMB science. Equipped with our new insights, we now continue the endless journey of gaining a better understanding on the perplexing universe we live in.

APPENDIX A

Statistical tools and data analysis methods in CMB cosmology

A.1 THE FISHER MATRIX

The Fisher matrix formalism provides a simple way to forecast how experiments could constrain parameters of given a model [295–298]. It relies on the assumption that the likelihood of the model is Gaussian. Given a vector of random Gaussian variables $\boldsymbol{\theta}$, The element in the Fisher information matrix $\boldsymbol{F}$ which corresponds to the $i^{\rm th}$ and $j^{\rm th}$ variables is defined as

$$F_{ij} \equiv -\left\langle \frac{\partial^2 \ln\left(\mathcal{L}\right)}{\partial\theta_i \partial\theta_j}\bigg|_{\boldsymbol{\theta}=\bar{\boldsymbol{\theta}}} \right\rangle \tag{A.1}$$

where $\mathcal{L} \equiv \mathcal{L}\left(\boldsymbol{d}, m(\boldsymbol{\theta})\right)$ is the likelihood for model m with parameters $\boldsymbol{\theta}$ given measurements $\boldsymbol{d}$, and $\bar{\boldsymbol{\theta}}$ is a vector with fiducial parameters that maximize the likelihood. The most common use for the Fisher matrix in CMB cosmology is to estimate the cosmological parameters given CMB power spectra.

Using the Gaussian distribution with zero mean, we can write down the Gaussian likelihood for a model m with n parameters $\boldsymbol{\theta}$ as

$$\mathcal{L}\left(\boldsymbol{d}, m(\boldsymbol{\theta})\right) = \frac{1}{\sqrt{(2\pi)^n \left|\boldsymbol{\mathcal{C}}\right|}} e^{-\frac{1}{2} d_i \mathcal{C}_{ij}^{-1} d_j}, \tag{A.2}$$

where $\langle d_i \rangle_d = 0$,

$$\langle d_i d_j \rangle_d = \mathcal{C}_{ij} \tag{A.3}$$

is the covariance matrix of the measurements $\boldsymbol{d}$, and double indices are summed on. The best-fit

parameters of the model m are those that maximise the likelihood,

$$\left.\frac{\partial \mathcal{L}}{\partial \boldsymbol{\theta}}\right|_{\boldsymbol{\theta}=\bar{\boldsymbol{\theta}}} = 0. \tag{A.4}$$

For a Gaussian likelihood, it is more convenient to use the natural logarithm of the likelihood to calculate derivatives. Differentiating the log of the Gaussian likelihood with respect to parameter θ_i gives

$$\begin{aligned}\frac{\partial \ln(\mathcal{L})}{\partial \theta_i} =& \frac{1}{2}\frac{\partial}{\partial \theta_i}\left[\ln|\boldsymbol{\mathcal{C}}| + \boldsymbol{d}^\top \boldsymbol{\mathcal{C}}^{-1}\boldsymbol{d}\right] \\ =& \frac{1}{2}\left[\boldsymbol{d}^\top \boldsymbol{\mathcal{C}}^{-1}\frac{\partial \boldsymbol{\mathcal{C}}}{\partial \theta_i}\boldsymbol{\mathcal{C}}^{-1}\boldsymbol{d} - \mathrm{Tr}\left(\boldsymbol{\mathcal{C}}^{-1}\frac{\partial \boldsymbol{\mathcal{C}}}{\partial \theta_i}\right)\right],\end{aligned} \tag{A.5}$$

where we used the identity $\ln|A| = \mathrm{Tr}(\ln A)$. The second derivative, with respect to parameter θ_j, is then

$$\begin{aligned}\frac{\partial^2 \ln(\mathcal{L})}{\partial\theta_j\partial\theta_i} &= -\frac{1}{2}\left[\boldsymbol{d}^\top \frac{\partial}{\partial\theta_j}\left(\boldsymbol{\mathcal{C}}^{-1}\frac{\partial \boldsymbol{\mathcal{C}}}{\partial\theta_i}\boldsymbol{\mathcal{C}}^{-1}\right)\boldsymbol{d} - \mathrm{Tr}\left(\frac{\partial}{\partial\theta_j}\left(\boldsymbol{\mathcal{C}}^{-1}\frac{\partial \boldsymbol{\mathcal{C}}}{\partial\theta_i}\right)\right)\right], \\ &= -\frac{1}{2}\left[\boldsymbol{d}^\top \boldsymbol{\mathcal{C}}^{-1}\frac{\partial \boldsymbol{\mathcal{C}}^{-1}}{\partial\theta_j}\boldsymbol{\mathcal{C}}^{-1}\frac{\partial \boldsymbol{\mathcal{C}}}{\partial\theta_i}\boldsymbol{\mathcal{C}}^{-1}\boldsymbol{d} - \boldsymbol{d}^\top \boldsymbol{\mathcal{C}}^{-1}\frac{\partial^2 \boldsymbol{\mathcal{C}}}{\partial\theta_j\partial\theta_i}\boldsymbol{\mathcal{C}}^{-1}\boldsymbol{d} + \boldsymbol{d}^\top \boldsymbol{\mathcal{C}}^{-1}\frac{\partial \boldsymbol{\mathcal{C}}}{\partial\theta_i}\boldsymbol{\mathcal{C}}^{-1}\frac{\partial \boldsymbol{\mathcal{C}}^{-1}}{\partial\theta_j}\boldsymbol{\mathcal{C}}^{-1}\boldsymbol{d}\right. \\ &\quad \left. -\mathrm{Tr}\left(\boldsymbol{\mathcal{C}}^{-1}\frac{\partial \boldsymbol{\mathcal{C}}^{-1}}{\partial\theta_j}\boldsymbol{\mathcal{C}}^{-1}\frac{\partial \boldsymbol{\mathcal{C}}}{\partial\theta_i}\right) + \mathrm{Tr}\left(\boldsymbol{\mathcal{C}}^{-1}\frac{\partial^2 \boldsymbol{\mathcal{C}}}{\partial\theta_j\partial\theta_i}\right)\right].\end{aligned} \tag{A.6}$$

To calculate the Fisher matrix elements of Eq. (A.1), we need to take the ensemble average of Eq. (A.6) over realisations of d. Using the definition of the covariance matrix in Eq. (A.3), the three terms which are averaged on become

$$\begin{aligned}\left\langle \boldsymbol{d}^\top \boldsymbol{\mathcal{C}}^{-1}\frac{\partial \boldsymbol{\mathcal{C}}^{-1}}{\partial\theta_j}\boldsymbol{\mathcal{C}}^{-1}\frac{\partial \boldsymbol{\mathcal{C}}}{\partial\theta_i}\boldsymbol{\mathcal{C}}^{-1}\boldsymbol{d}\right\rangle &= \left\langle d_m^\top \mathcal{C}^{-1}_{mn}\frac{\partial \mathcal{C}^{-1}_{np}}{\partial\theta_j}\mathcal{C}^{-1}_{pq}\frac{\partial \mathcal{C}_{qr}}{\partial\theta_i}\mathcal{C}^{-1}_{rs}d_s\right\rangle = \mathcal{C}^{-1}_{mn}\frac{\partial \mathcal{C}^{-1}_{np}}{\partial\theta_j}\mathcal{C}^{-1}_{pq}\frac{\partial \mathcal{C}_{qr}}{\partial\theta_i}\mathcal{C}^{-1}_{rs}\mathcal{C}_{sm} \\ &= \mathrm{Tr}\left(\boldsymbol{\mathcal{C}}^{-1}\frac{\partial \boldsymbol{\mathcal{C}}^{-1}}{\partial\theta_j}\boldsymbol{\mathcal{C}}^{-1}\frac{\partial \boldsymbol{\mathcal{C}}}{\partial\theta_i}\right), \\ \left\langle \boldsymbol{d}^\top \boldsymbol{\mathcal{C}}^{-1}\frac{\partial^2 \boldsymbol{\mathcal{C}}}{\partial\theta_j\partial\theta_i}\boldsymbol{\mathcal{C}}^{-1}\boldsymbol{d}\right\rangle &= \left\langle d_m^\top \mathcal{C}^{-1}_{mn}\frac{\partial^2 \mathcal{C}_{np}}{\partial\theta_j\partial\theta_i}\mathcal{C}^{-1}_{pq}d_q\right\rangle = \mathcal{C}^{-1}_{mn}\frac{\partial^2 \mathcal{C}_{np}}{\partial\theta_j\partial\theta_i}\mathcal{C}^{-1}_{pq}\mathcal{C}_{qm} \\ &= \mathrm{Tr}\left(\boldsymbol{\mathcal{C}}^{-1}\frac{\partial^2 \boldsymbol{\mathcal{C}}}{\partial\theta_j\partial\theta_i}\right), \\ \left\langle \boldsymbol{d}^\top \boldsymbol{\mathcal{C}}^{-1}\frac{\partial \boldsymbol{\mathcal{C}}}{\partial\theta_i}\boldsymbol{\mathcal{C}}^{-1}\frac{\partial \boldsymbol{\mathcal{C}}^{-1}}{\partial\theta_j}\boldsymbol{\mathcal{C}}^{-1}\boldsymbol{d}\right\rangle &= \left\langle d_m^\top \mathcal{C}^{-1}_{mn}\frac{\partial \mathcal{C}_{np}}{\partial\theta_i}\mathcal{C}^{-1}_{pq}\frac{\partial \mathcal{C}^{-1}_{qr}}{\partial\theta_j}\mathcal{C}^{-1}_{rs}d_s\right\rangle = \mathcal{C}^{-1}_{mn}\frac{\partial \mathcal{C}_{np}}{\partial\theta_i}\mathcal{C}^{-1}_{pq}\frac{\partial \mathcal{C}^{-1}_{qr}}{\partial\theta_j}\mathcal{C}^{-1}_{rs}\mathcal{C}_{sm} \\ &= \mathrm{Tr}\left(\boldsymbol{\mathcal{C}}^{-1}\frac{\partial \boldsymbol{\mathcal{C}}}{\partial\theta_i}\boldsymbol{\mathcal{C}}^{-1}\frac{\partial \boldsymbol{\mathcal{C}}^{-1}}{\partial\theta_j}\right) = \mathrm{Tr}\left(\boldsymbol{\mathcal{C}}^{-1}\frac{\partial \boldsymbol{\mathcal{C}}}{\partial\theta_j}\boldsymbol{\mathcal{C}}^{-1}\frac{\partial \boldsymbol{\mathcal{C}}^{-1}}{\partial\theta_i}\right),\end{aligned} \tag{A.7}$$

where we used $\mathcal{C}^{-1}_{ij}\mathcal{C}_{jk} = \mathbb{1}_{ik}$ and $\mathrm{Tr}(\boldsymbol{ABC}) = A_{ij}B_{jk}C_{ki} = \mathrm{Tr}(\boldsymbol{CAB}) = \mathrm{Tr}(\boldsymbol{BCA})$. The

elements of the Fisher matrix are then simply

$$F_{ij} = \frac{1}{2}\mathrm{Tr}\left(\boldsymbol{\mathcal{C}}^{-1}\frac{\partial\boldsymbol{\mathcal{C}}}{\partial\theta_i}\boldsymbol{\mathcal{C}}^{-1}\frac{\partial\boldsymbol{\mathcal{C}}}{\partial\theta_j}\right). \tag{A.8}$$

A similar derivation can be used for estimating the uncertainties of the best-fit parameters found by maximising the likelihood. Such calculations are usually done iteratively using root finding algorithms. These usually start with a best guess for the parameters, $\boldsymbol{\theta}_0$, and progress toward $\bar{\boldsymbol{\theta}}$ with steps $\delta\boldsymbol{\theta}$. The log likelihood derivative can be approximated as

$$\left.\frac{\partial\ln(\mathcal{L})}{\partial\theta_i}\right|_{\boldsymbol{\theta}=\bar{\boldsymbol{\theta}}} \approx \left.\frac{\partial\ln(\mathcal{L})}{\partial\theta_i}\right|_{\boldsymbol{\theta}=\boldsymbol{\theta}_0} + \delta\theta_j\left.\frac{\partial^2\ln(\mathcal{L})}{\partial\theta_i\partial\theta_j}\right|_{\boldsymbol{\theta}=\boldsymbol{\theta}_0} = 0 \tag{A.9}$$

to get

$$\delta\theta_j \approx \left[\left.\frac{\partial^2\ln(\mathcal{L})}{\partial\theta_i\partial\theta_j}\right|_{\boldsymbol{\theta}=\boldsymbol{\theta}_0}\right]^{-1}\left.\frac{\partial\ln(\mathcal{L})}{\partial\theta_i}\right|_{\boldsymbol{\theta}=\boldsymbol{\theta}_0} \approx \left.\left[F_{ij}^{-1}\frac{\partial\ln(\mathcal{L})}{\partial\theta_i}\right]\right|_{\boldsymbol{\theta}=\boldsymbol{\theta}_0}, \tag{A.10}$$

where $\delta\theta_j \equiv \bar{\theta}_j - \theta_{j,0}$ are the steps for iteratively finding the best-fit parameters $\bar{\boldsymbol{\theta}}$. The variance of the estimated parameters can then be estimated as $\sigma_{ij}^2 \equiv \langle\delta\theta_i\delta\theta_j\rangle$,

$$\begin{aligned}\langle\delta\theta_i\delta\theta_j\rangle &\approx \frac{1}{4}F_{im}^{-1}F_{jn}^{-1}\left\langle\left[\boldsymbol{d}^\top\boldsymbol{\mathcal{C}}^{-1}\frac{\partial\boldsymbol{\mathcal{C}}}{\partial\theta_m}\boldsymbol{\mathcal{C}}^{-1}\boldsymbol{d} - \mathrm{Tr}\left(\boldsymbol{\mathcal{C}}^{-1}\frac{\partial\boldsymbol{\mathcal{C}}}{\partial\theta_m}\right)\right]\left[\boldsymbol{d}^\top\boldsymbol{\mathcal{C}}^{-1}\frac{\partial\boldsymbol{\mathcal{C}}}{\partial\theta_n}\boldsymbol{\mathcal{C}}^{-1}\boldsymbol{d} - \mathrm{Tr}\left(\boldsymbol{\mathcal{C}}^{-1}\frac{\partial\boldsymbol{\mathcal{C}}}{\partial\theta_n}\right)\right]\right\rangle \\ &= \frac{1}{4}F_{im}^{-1}F_{jn}^{-1}\left[\langle d_k d_l d_p d_q\rangle\,\mathcal{C}_{kr}^{-1}\frac{\partial\mathcal{C}_{rs}}{\partial\theta_m}\mathcal{C}_{sl}^{-1}\mathcal{C}_{pv}^{-1}\frac{\partial\mathcal{C}_{vw}}{\partial\theta_n}\mathcal{C}_{wq}^{-1} - \langle d_k d_l\rangle\,\mathcal{C}_{kr}^{-1}\frac{\partial\mathcal{C}_{rs}}{\partial\theta_m}\mathcal{C}_{sl}^{-1}\mathrm{Tr}\left(\boldsymbol{\mathcal{C}}^{-1}\frac{\partial\boldsymbol{\mathcal{C}}}{\partial\theta_n}\right)\right. \\ &\quad \left. - \langle d_k d_l\rangle\,\mathcal{C}_{kr}^{-1}\frac{\partial\mathcal{C}_{rs}}{\partial\theta_n}\mathcal{C}_{sl}^{-1}\mathrm{Tr}\left(\boldsymbol{\mathcal{C}}^{-1}\frac{\partial\boldsymbol{\mathcal{C}}}{\partial\theta_m}\right) + \mathrm{Tr}\left(\boldsymbol{\mathcal{C}}^{-1}\frac{\partial\boldsymbol{\mathcal{C}}}{\partial\theta_m}\right)\mathrm{Tr}\left(\boldsymbol{\mathcal{C}}^{-1}\frac{\partial\boldsymbol{\mathcal{C}}}{\partial\theta_n}\right)\right].\end{aligned} \tag{A.11}$$

The first term in this equation can be expanded using Wick's theorem [147] and the covariance definition,

$$\begin{aligned}\langle d_k d_l d_p d_q\rangle &= \langle d_k d_l\rangle\langle d_p d_q\rangle + \langle d_k d_p\rangle\langle d_l d_q\rangle + \langle d_k d_q\rangle\langle d_l d_p\rangle \\ &= \mathcal{C}_{kl}\mathcal{C}_{pq} + \mathcal{C}_{kp}\mathcal{C}_{lq} + \mathcal{C}_{kq}\mathcal{C}_{lp}\,,\end{aligned} \tag{A.12}$$

to get

$$\begin{aligned}\langle d_k d_l d_p d_q\rangle\,\mathcal{C}_{kr}^{-1}\frac{\partial\mathcal{C}_{rs}}{\partial\theta_m}\mathcal{C}_{sl}^{-1}\mathcal{C}_{pv}^{-1}\frac{\partial\mathcal{C}_{vw}}{\partial\theta_n}\mathcal{C}_{wq}^{-1} &= \mathcal{C}_{kl}\mathcal{C}_{pq}\mathcal{C}_{kr}^{-1}\frac{\partial\mathcal{C}_{rs}}{\partial\theta_m}\mathcal{C}_{sl}^{-1}\mathcal{C}_{pv}^{-1}\frac{\partial\mathcal{C}_{vw}}{\partial\theta_n}\mathcal{C}_{wq}^{-1} \\ &\quad + \mathcal{C}_{kp}\mathcal{C}_{lq}\mathcal{C}_{kr}^{-1}\frac{\partial\mathcal{C}_{rs}}{\partial\theta_m}\mathcal{C}_{sl}^{-1}\mathcal{C}_{pv}^{-1}\frac{\partial\mathcal{C}_{vw}}{\partial\theta_n}\mathcal{C}_{wq}^{-1} + \mathcal{C}_{kq}\mathcal{C}_{lp}\mathcal{C}_{kr}^{-1}\frac{\partial\mathcal{C}_{rs}}{\partial\theta_m}\mathcal{C}_{sl}^{-1}\mathcal{C}_{pv}^{-1}\frac{\partial\mathcal{C}_{vw}}{\partial\theta_n}\mathcal{C}_{wq}^{-1} \\ &= \frac{\partial\mathcal{C}_{ls}}{\partial\theta_m}\mathcal{C}_{sl}^{-1}\frac{\partial\mathcal{C}_{qw}}{\partial\theta_n}\mathcal{C}_{wq}^{-1} + \frac{\partial\mathcal{C}_{pq}}{\partial\theta_m}\mathcal{C}_{pv}^{-1}\frac{\partial\mathcal{C}_{vw}}{\partial\theta_n}\mathcal{C}_{wq}^{-1} + \frac{\partial\mathcal{C}_{qp}}{\partial\theta_m}\mathcal{C}_{pv}^{-1}\frac{\partial\mathcal{C}_{vw}}{\partial\theta_n}\mathcal{C}_{wq}^{-1} \\ &= \mathrm{Tr}\left(\boldsymbol{\mathcal{C}}^{-1}\frac{\partial\boldsymbol{\mathcal{C}}}{\partial\theta_m}\right)\mathrm{Tr}\left(\boldsymbol{\mathcal{C}}^{-1}\frac{\partial\boldsymbol{\mathcal{C}}}{\partial\theta_n}\right) + 2F_{mn} + 2F_{mn}.\end{aligned} \tag{A.13}$$

Similarly, the next two terms simplify to the same expression of the last term (with different signs), and we are left with

$$\begin{aligned}\sigma_{ij}^2 = \frac{1}{4}F_{im}^{-1}F_{jn}^{-1}\Bigg[&\mathrm{Tr}\left(\boldsymbol{\mathcal{C}}^{-1}\frac{\partial\boldsymbol{\mathcal{C}}}{\partial\theta_m}\right)\mathrm{Tr}\left(\boldsymbol{\mathcal{C}}^{-1}\frac{\partial\boldsymbol{\mathcal{C}}}{\partial\theta_n}\right) + 2F_{mn} + 2F_{mn} - \mathrm{Tr}\left(\boldsymbol{\mathcal{C}}^{-1}\frac{\partial\boldsymbol{\mathcal{C}}}{\partial\theta_m}\right)\mathrm{Tr}\left(\boldsymbol{\mathcal{C}}^{-1}\frac{\partial\boldsymbol{\mathcal{C}}}{\partial\theta_n}\right)\\ &- \mathrm{Tr}\left(\boldsymbol{\mathcal{C}}^{-1}\frac{\partial\boldsymbol{\mathcal{C}}}{\partial\theta_m}\right)\mathrm{Tr}\left(\boldsymbol{\mathcal{C}}^{-1}\frac{\partial\boldsymbol{\mathcal{C}}}{\partial\theta_n}\right) + \mathrm{Tr}\left(\boldsymbol{\mathcal{C}}^{-1}\frac{\partial\boldsymbol{\mathcal{C}}}{\partial\theta_m}\right)\mathrm{Tr}\left(\boldsymbol{\mathcal{C}}^{-1}\frac{\partial\boldsymbol{\mathcal{C}}}{\partial\theta_n}\right)\Bigg]\\ =&F_{im}^{-1}F_{jn}^{-1}F_{mn}\\ =&F_{ij}^{-1}.\end{aligned} \tag{A.14}$$

The Fisher matrix is therefore a useful tool for estimating the error on the model's parameters. The marginalized error of a parameter θ_i in the model can be estimated using

$$\sigma_i \equiv \sigma(\theta_i) = \sqrt{(\boldsymbol{F}^{-1})_{ii}}. \tag{A.15}$$

The Fisher matrix can be used to express the uncertainty of the CMB power spectra. For an experiments which measures the CMB anisotropy $a_{\ell m}$, the measurements can be described $d_{\ell m} = b_\ell a_{\ell m} + n_{\ell m}$ with effective beam b_ℓ and noise $n_{\ell m}$. The covariance matrix is then $\mathcal{C}_{\ell m,\ell' m'} = \langle a_{\ell m} a^*_{\ell' m'}\rangle = \delta_{\ell\ell'}\delta_{mm'}\left[b_\ell^2 C_\ell + N_\ell\right]$, where N_ℓ is the noise variance. The resulting Fisher matrix elements for the parameters C_ℓ are given by

$$\begin{aligned}F_{\ell\ell'} =&\frac{1}{2}\mathrm{Tr}\left(\boldsymbol{\mathcal{C}}^{-1}\frac{\partial\boldsymbol{\mathcal{C}}}{\partial C_\ell}\boldsymbol{\mathcal{C}}^{-1}\frac{\partial\boldsymbol{\mathcal{C}}}{\partial C_{\ell'}}\right)\\ =&\frac{1}{2}\mathcal{C}^{-1}_{\ell_1 m_1,\ell_2 m_2}\frac{\partial\mathcal{C}_{\ell_2 m_2,\ell_3 m_3}}{\partial C_\ell}\mathcal{C}^{-1}_{\ell_3 m_3,\ell_4 m_4}\frac{\partial\mathcal{C}_{\ell_4 m_4,\ell_1 m_1}}{\partial C_{\ell'}}\\ =&\frac{1}{2}\frac{\delta_{\ell_1\ell_2}\delta_{m_1 m_2}}{b_\ell^2 C_\ell + N_\ell}\delta_{\ell_2\ell_3}\delta_{m_2 m_3}b^2_{\ell_2}\delta_{\ell_2\ell}\frac{\delta_{\ell_3\ell_4}\delta_{m_3 m_4}}{b^2_{\ell'}C_{\ell'} + N_{\ell'}}\delta_{\ell_3\ell_4}\delta_{m_3 m_4}b^2_{\ell_4}\delta_{\ell_4\ell'}\\ =&\frac{\delta_{\ell\ell'}\delta_{m_1 m_1}}{2}\left[\frac{b_\ell^2}{b_\ell^2 C_\ell + N_\ell}\right]^2\\ =&\frac{\delta_{\ell\ell'}(2\ell+1)}{2}\left[\frac{1}{C_\ell + b_\ell^{-2}N_\ell}\right]^2,\end{aligned} \tag{A.16}$$

where the number of modes m for multipole ℓ on the full sky is given by $\delta_{m_1 m_1} = 2\ell + 1$. The power spectrum variance, assuming uncorrelated noise, is then

$$\mathrm{Var}\left(C_\ell\right) = F^{-1}_{\ell\ell} = \frac{2}{2+1}\left[C_\ell + b_\ell^{-2}N_\ell\right]^2. \tag{A.17}$$

A similar calculation can also be done to evaluate how the CMB covariance depends on other

parameters of a theory. Then, the more general expression for the Fisher matrix becomes

$$F_{ij,\ell} = \frac{2\ell+1}{2} f_{\rm sky} \mathrm{Tr}\left(\boldsymbol{C}_\ell^{-1} \frac{\partial \boldsymbol{C}_\ell}{\partial \theta_i} \boldsymbol{C}_\ell^{-1} \frac{\partial \boldsymbol{C}_\ell}{\partial \theta_j} \right), \tag{A.18}$$

where we also consider partial sky observations with fractional sky area $f_{\rm sky}$. This expression of the Fisher matrix is used in Chapter 5 to produce forecasts on the Rayleigh scattering amplitude.

A.2 WIENER FILTER

Maps produced by CMB experiments usually contain some level of instrument noise, which should be reduced before using them in cosmological analyses. One way to do this is by implementing a Wiener filter [299] on the maps. Wiener filter is a generic name for any filter which uses an assumed signal and noise power to produce an estimate of the desired signal from a signal-plus-noise input by minimizing the mean square error between the assumed and desired processes. It was first introduced in 1949 in the context of time-domain signal analysis.

Given a data vector $\boldsymbol{d}$ of length $N_{\rm pix}$ which measures a signal $\boldsymbol{s}$ with noise $\boldsymbol{n}$,

$$\boldsymbol{d} = \boldsymbol{s} + \boldsymbol{n}, \tag{A.19}$$

the Wiener filter is defined as the transfer function $\mathcal{F}_{\rm WF}$ for which the estimator for $\boldsymbol{s}$ is given by

$$\hat{\boldsymbol{s}} = \mathcal{F}_{\rm WF} \boldsymbol{d}. \tag{A.20}$$

We can find $\mathcal{F}_{\rm WF}$ by maximizing the likelihood of $\boldsymbol{s}$ given the data using Bayes' theorem [300–302],

$$P(\boldsymbol{s}|\boldsymbol{d}) = \frac{P(\boldsymbol{s})P(\boldsymbol{d}|\boldsymbol{s})}{P(\boldsymbol{d})}. \tag{A.21}$$

If we assume that the signal and noise are Gaussian, which is a good assumption for CMB signal and noise, this likelihood becomes [303]

$$P(\boldsymbol{s}|\boldsymbol{d}) = \frac{1}{\sqrt{(2\pi)^{N_{\rm pix}}\,|\boldsymbol{S}|}} e^{-\frac{1}{2}\boldsymbol{s}^\dagger \boldsymbol{S}^{-1} \boldsymbol{s}} \frac{1}{\sqrt{(2\pi)^{N_{\rm pix}}\,|\boldsymbol{N}|}} e^{-\frac{1}{2}(\boldsymbol{d}-\boldsymbol{s})^\dagger \boldsymbol{N}^{-1}(\boldsymbol{d}-\boldsymbol{s})} \frac{1}{P(\boldsymbol{d})}, \tag{A.22}$$

where

$$\boldsymbol{S}(\ell) = \begin{pmatrix} C_\ell^{TT} & C_\ell^{TE} & 0 \\ C_\ell^{TE} & C_\ell^{EE} & 0 \\ 0 & 0 & C_\ell^{BB} \end{pmatrix}, \tag{A.23}$$

is the signal covariance with $C_\ell^{TB} = C_\ell^{EB} = 0$, and $\boldsymbol{N}$ is the noise covariance, which can either be approximated as diagonal with an effective noise level, or be the full noise covariance of the experiment, which is usually not diagonal. The probability of the data $P(\boldsymbol{d})$ is arbitrary, and does not affect the maximization analysis, so below it is set to unity.

As is often the case with Gaussian likelihoods, we can use the natural logarithm of the likelihood,

$$\mathcal{L} \equiv \ln P(\boldsymbol{s}|\boldsymbol{d}) = -\frac{1}{2}\ln\left((2\pi)^{2N_{\rm pix}}\,|\boldsymbol{S}|\,|\boldsymbol{N}|\right) - \frac{1}{2}\boldsymbol{s}^\dagger\boldsymbol{S}^{-1}\boldsymbol{s} - \frac{1}{2}\left(\boldsymbol{d}-\boldsymbol{s}\right)^\dagger\boldsymbol{N}^{-1}\left(\boldsymbol{d}-\boldsymbol{s}\right), \quad \text{(A.24)}$$

and differentiate it with respect to $\boldsymbol{s}$ to find the estimate of $\boldsymbol{s}$ which maximizes the likelihood,

$$\left.\frac{\partial\mathcal{L}(\boldsymbol{s},\boldsymbol{d})}{\partial\boldsymbol{s}}\right|_{\boldsymbol{s}=\hat{\boldsymbol{s}}} = 0. \quad \text{(A.25)}$$

We then get

$$\left[-\boldsymbol{S}^{-1}\boldsymbol{s} - \boldsymbol{N}^{-1}\left(\boldsymbol{d}-\boldsymbol{s}\right)\right]_{\boldsymbol{s}=\hat{\boldsymbol{s}}} = 0, \quad \text{(A.26)}$$

such that isolating $\boldsymbol{s}$ leads to the estimate

$$\hat{\boldsymbol{s}} = \boldsymbol{S}\left(\boldsymbol{S}+\boldsymbol{N}\right)^{-1}\boldsymbol{d}. \quad \text{(A.27)}$$

The estimator of Eq. (A.20) is therefore optimal when

$$\mathcal{F}_{\rm WF} \equiv \boldsymbol{S}\left(\boldsymbol{S}+\boldsymbol{N}\right)^{-1}. \quad \text{(A.28)}$$

This is the Wiener filter. It is related to the inverse-variance filter (IVF) via $\mathcal{F}_{\rm WF} = \boldsymbol{S}\mathcal{F}_{\rm IVF}$. The first use of the Wiener filtering in CMB cosmology was as an optimal filter on the COBE CMB maps [304]. In CMB lensing, due to the nature of the quadratic estimators of the lensing potential, this filter is used to obtain the maximum-likelihood lensing estimators that are described in Chapter 1 and used throughout Chapters 2-4.

The $\left(\boldsymbol{S}+\boldsymbol{N}\right)^{-1}$ component of the filter weights each mode of the CMB map by the inverse of its total variance, such that modes which have large noise variance contribute less for estimating the filtered signal. Different modes in the map have different noise levels mainly due to the inhomogeneities introduced through scanning patterns. The noise in a pixel of a CMB map is directly related to the inverse of the time spent observing this pixel. As such, areas of the sky which are observed for less time will have higher noise levels, so their overall contribution to the

estimated signal should be reduced to increase the estimator's accuracy.

To use this filter in practice, the $\boldsymbol{S}+\boldsymbol{N}$ matrix must be inverted. The inverse of this matrix can be estimated using the Conjugate gradient method [148, 159, 305]. This method can be used to efficiently solve equations of the form

$$\boldsymbol{A}\mathbf{x}=\mathbf{b}, \tag{A.29}$$

where $\boldsymbol{A}$ and $\mathbf{b}$ are a known matrix and vector, respectively, and $\mathbf{x}$ is the desired quantity. In the case of the IVF, for example, $\boldsymbol{A}=\boldsymbol{S}+\boldsymbol{N}$, $\mathbf{x}=\hat{\boldsymbol{s}}$ and $\mathbf{b}=\boldsymbol{d}$. Since we know $\boldsymbol{S}$, finding $\mathbf{x}$ for the IVF and multiplying the result by $\boldsymbol{S}$ gives the WF estimator.

To solve this equation for $\mathbf{x}$, we can define a function

$$f(\mathbf{x})=\frac{1}{2}\mathbf{x}^{\top}\boldsymbol{A}\mathbf{x}-\mathbf{b}^{\top}\mathbf{x}+\mathbf{c}, \tag{A.30}$$

and find $\mathbf{x}$ which minimizes it, i.e. the solution for a rearranged version of Eq. (A.29),

$$\boldsymbol{\nabla} f=\boldsymbol{A}\mathbf{x}-\mathbf{b}=0. \tag{A.31}$$

The minimization is performed iteratively by searching for directions $\mathbf{p}_k$ in each iteration k such that in each iteration $f(\mathbf{x}_k+\alpha_k\mathbf{p}_k)$ is minimised. The next iteration step in the search is given by $\mathbf{x}_{k+1}=\mathbf{x}_k+\alpha_k\mathbf{p}_k$. For initial values $\mathbf{x}_0=\mathbf{r}_0=\mathbf{p}_0$, the direction for each iteration is set using the relations

$$\begin{aligned}\alpha_k =&\frac{\mathbf{p}_k^{\top}\mathbf{r}_k}{\mathbf{p}_k^{\top}\boldsymbol{A}\mathbf{p}_k},\\ \mathbf{r}_k =&\mathbf{b}-\boldsymbol{A}\mathbf{x}_k,\\ \mathbf{p}_k =&\mathbf{r}_k-\sum_{i<k}\frac{\mathbf{p}_i^{\top}\boldsymbol{A}\mathbf{r}_k}{\mathbf{p}_i^{\top}\boldsymbol{A}\mathbf{p}_i}\mathbf{p}_i.\end{aligned} \tag{A.32}$$

The way in which α_k and $\mathbf{p}_k$ are calculated for each iteration optimizes the search by having more search points closer to the minimum. The main traits of this method is that the residuals $\mathbf{r}_k$ satisfy $\mathbf{r}_i^{\top}\mathbf{r}_j=0$, and the directions $\mathbf{p}_k$ satisfy the relation $\mathbf{p}_i^{\top}\boldsymbol{A}\mathbf{p}_j=0$. These allow for fast convergence. The stopping criteria of the iterations is determined by the wanted accuracy of the residuals $\mathbf{r}$.

A.3 MARKOV CHAIN MONTE CARLO

In Chapter 4 we estimate cosmological parameters using lensing and BAO likelihoods. The way in which cosmological parameters are usually estimated from likelihoods is via the Markov Chain Monte Carlo (MCMC) sampling method [147, 159]. MCMC is one of the most useful tools for estimating parameters in cosmology. Given a cosmological model, such as ΛCDM, with parameters $\boldsymbol{\theta}$, the parameter values can be estimated from cosmological observations $\boldsymbol{d}$ by asking, "how likely is a value of a specific parameter given the data?". This approach to parameter estimation is especially convenient especially when there is a large number of parameters to estimate.

The method uses Bayes' theorem [300–302],

$$P\left(\boldsymbol{\theta}|\boldsymbol{d}\right) = \frac{P\left(\boldsymbol{d}|\boldsymbol{\theta}\right) P\left(\boldsymbol{\theta}\right)}{P\left(\boldsymbol{d}\right)}, \tag{A.33}$$

where $P(\boldsymbol{\theta}|\boldsymbol{d})$ is the posterior probability for $\boldsymbol{\theta}$, whose quantity answers the above question, $P(\boldsymbol{d}|\boldsymbol{\theta})$ is the probability of observing the data $\boldsymbol{d}$ given the values of $\boldsymbol{\theta}$, $P(\boldsymbol{\theta})$ is the prior probability distribution, which summarises our knowledge about the parameters regardless of the data, and $P(\boldsymbol{d})$ acts as the normalization factor for the posterior probability. This normalization can be defined as the marginal likelihood,

$$P(\boldsymbol{d}) \equiv \int d\boldsymbol{\theta} P\left(\boldsymbol{d}|\boldsymbol{\theta}\right) P\left(\boldsymbol{\theta}\right). \tag{A.34}$$

To calculate the posterior probability for a given parameter θ_i, we need to integrate, or *marginalize*, over all other parameters $\theta_{j\neq i}$,

$$P(\theta_i|\boldsymbol{d}) \propto \int d\theta_1 ... d\theta_{j\neq i} P\left(\boldsymbol{\theta}|\boldsymbol{d}\right). \tag{A.35}$$

Given a set of priors and a likelihood function from measurements, we can evaluate this integral using Bayes' theorem in Eq. (A.33) using a sampling algorithm. A sampling algorithm is required when the integrals cannot be solved analytically, as is the case with the standard cosmological model. The most popular sampling method for this purpose is the MCMC method.

Given a starting value for each parameter, the MCMC method implements the Markov process to relate each step to the previous step. The way in which consecutive steps are related is through an acceptance criterion. One of the more commonly-used criteria, which is also implemented in the parameter estimation analysis of Chapter 4, is the Metropolis-Hastings (MH) acceptance criterion [306, 307]. The full sampling algorithm operates according to the following steps:

1. The initial parameter values $\boldsymbol{\theta}_0$ are used to calculate the likelihood $P(\boldsymbol{d}|\boldsymbol{\theta}_0)$ and the prior $P(\boldsymbol{\theta}_0)$ to obtain the initial value of the posterior $P(\boldsymbol{\theta}_0|\boldsymbol{d})$.

2. The next parameter values $\boldsymbol{\theta}_1 = \boldsymbol{\theta}_0 + \delta\boldsymbol{\theta}$ are set using random Gaussian numbers $\delta\boldsymbol{\theta}$. Priors on the parameters can be used to restrict the values of $\delta\theta$ for faster convergence.

3. The new posterior is calculated as in Step 1, using $\boldsymbol{\theta}_1$.

4. The ratio of the posteriors of the two steps is then calculated, $P(\boldsymbol{\theta}_1|\boldsymbol{d})/P(\boldsymbol{\theta}_0|\boldsymbol{d})$.

5. If the obtained ratio is larger than a uniformly-generated random number between 0 and 1, the new values $\boldsymbol{\theta}_1$ are used as the new initial guess, and the process starts again from Step 1. If the ratio is equal or smaller to the generated number, the initial values continue to be $\boldsymbol{\theta}_0$ for the next iteration.

Step 5 is specific for the MH acceptance criterion. Because the probability of acceptance depends on the value of the posteriors, this criterion helps the algorithm to avoid local minima and to sample the parameter space more efficiently.

A common way of using MCMC is by running several sampling chains at the same time until convergence is reached. This convergence is usually defined by specifying a stopping value for the Gelman-Rubin convergence function [308],

$$R \equiv \frac{(N-1)\,W + \left(1 + \frac{1}{M}\right) B}{NW}, \tag{A.36}$$

where M is the number of chains, each with N samples,

$$B^i \equiv \frac{N}{M-1} \sum_{k=1}^{M} \left(\bar{\theta}_k^i - \bar{\theta}^i\right)^2 \tag{A.37}$$

is the variance between chains for parameter i, and

$$W^i \equiv \frac{1}{M\,(N-1)} \sum_{k=1}^{M} \sum_{j=1}^{N} \left(\bar{\theta}_{k,j}^i - \bar{\theta}_k^i\right)^2 \tag{A.38}$$

is the combined variance of parameter i from all chains. Using this halting condition assures the parameter uncertainties are sufficiently converged. A halting condition which is based on the convergence of the variances rather than the mean of the parameters can also be useful, especially when comparing parameter estimation accuracies as we do in Chapter 4, however such convergence function was not developed for this work.

APPENDIX B

Optimal filtering performance

Optimal filtering of the CMB maps (Eq. (2.6)) must be performed iteratively to have a tractable numerical cost. This appendix discusses the performance of our solver and convergence criteria, for both temperature and polarization.

We use the same algorithms used for the Planck lensing 2015 [98] and 2018 [100] analyses, using the flat-sky implementation in the LENSIT package. The inversion is performed using a simple conjugate-gradient descent, which can be coupled to a multi-grid preconditioner [148] to try and improve the convergence properties of the iterative search. When solving for $\mathbf{x}$ in the linear equation $\mathbf{x} = \mathbf{A^{-1}b}$, we determine convergence by monitoring the ratio ϵ_n^2 of the squared norm of the residual vector at iteration n, $\mathbf{Ax_n} - \mathbf{b}$, to that of the initial residual $\mathbf{b}$ (we always start with $\mathbf{x_0} = \mathbf{0}$). We then ensure that this ratio has dropped below a specific tolerance level ϵ.

Fig. B.1 shows the dependence of the lensing reconstruction on the choice of tolerance level, in units of the statistical error bars, when using the simplest possible diagonal isotropic preconditioner. The figure shows the difference to the result for $\epsilon = 10^{-6}$ (the smallest tolerance we consider) in units of the expected statistical error bars $\sigma_L[N_0]$ induced by the reconstruction noise, but excluding the lensing map cosmic variance. For this we use the approximation

$$\sigma_L^2[N_{0,L}] \equiv \frac{2\left({}^{(\mathrm{MC})}N_{0,L}\right)^2}{f_{A,L} n_L \Delta L}. \tag{B.1}$$

These noise-only error bars are the most relevant for applications where the lensing map rather than its spectrum must be reconstructed accurately (such as for delensing). Fig. B.1 shows the power spectrum difference at the iteration for which $\epsilon \simeq 10^{-2}$ (blue), 10^{-3} (orange), 10^{-4} (green), 10^{-5} (red), and for T, P and MV analyses (from top to bottom). Polarization filtering is a lot better behaved than temperature. This is striking, both from the figure and in the number of iterations required to reach these tolerance levels: about 80 steps are necessary to reach $\epsilon = 10^{-4}$ for

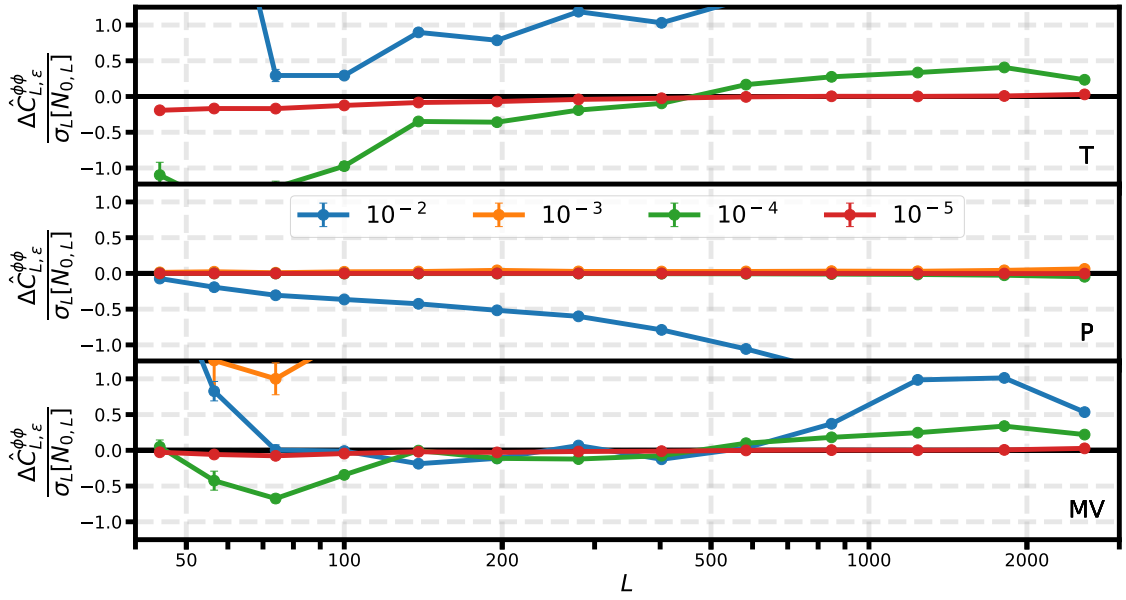

Figure B.1: Lensing power spectra differences built from partially conjugate-gradient-converged inverse-variance filtered CMB maps, in units of the reconstruction noise statistical error. The points shown are for the T (top panel), P (middle panel) or MV (bottom panel) lensing spectrum estimates, for convergence levels $\epsilon = 10^{-2}$ (blue), 10^{-3} (orange), 10^{-4} (green), 10^{-5} (red), where ϵ monitors the decrease of the residual vector norm. Convergence for P is always substantially faster than for T or MV. The points with $\epsilon = 10^{-3}$ are off the scale for T and most of MV, but close to the zero for P. Our baseline T and MV analyses use $\epsilon = 10^{-5}$, where the bias is at most $0.2\sigma[N_0]$ in T, and $\epsilon = 10^{-4}$ for P analysis. For T and MV the convergence is not monotonic; small changes in the high-ℓ temperature maps in the iterative search have a large impact on the lensing power iterations.

temperature or MV filtering, but 50 for polarization. For $\epsilon = 10^{-5}$ this becomes 430 and 100, and for $\epsilon = 10^{-6}$ this worsens to 2480 and 125, respectively.

Our T and MV baseline results used a tolerance of 10^{-5} and our P results used 10^{-4}, which is enough to ensure convergence on all relevant scales to below $0.2\sigma[N_{0,L}]$. To test for broadband correlations we have evaluated biases in the overall reconstructed lensing spectrum amplitude in the following way. Using an approximation to the spectrum variance $\sigma^2_L[C^{\phi\phi} + N_0]$ (defined as in Eq. (B.1), but including the lens cosmic variance), we test for a non-zero lensing amplitude in the residual

$$\hat{C}^{\phi\phi}_{L,\epsilon} - \hat{C}^{\phi\phi}_{L,\epsilon=10^{-6}} \equiv A_\epsilon C^{\phi\phi,\mathrm{fid}}_L \tag{B.2}$$

using the inverse-variance weighting amplitude estimator

$$\hat{A}_\epsilon = \sigma^2_A \sum_{L=40}^{3000} \frac{C^{\phi\phi,\mathrm{fid}}_L \left(\hat{C}^{\phi\phi}_{L,\epsilon} - \hat{C}^{\phi\phi}_{L,\epsilon=10^{-6}}\right)}{\sigma^2_L[C^{\phi\phi,\mathrm{fid}}_L + N_{0,L}]}, \tag{B.3}$$

with normalization

$$\frac{1}{\sigma^2_A} = \sum_{L=40}^{3000} \frac{\left(C^{\phi\phi,\mathrm{fid}}_L\right)^2}{\sigma^2_L[C^{\phi\phi,\mathrm{fid}}_L + N_{0,L}]}. \tag{B.4}$$

σ^2_A is also the Fisher variance $\mathrm{Var}\left(\hat{A}_\epsilon\right)$ of the lensing amplitude estimator. For $\epsilon = 10^{-5}$, in

temperature case we find a maximal bias of $0.06\sigma_A$. For the cases of polarization and MV, the bias is much smaller still. It takes only about 5 minutes on a standard laptop to filter the maps in temperature or polarization, and 15 for joint filtering, hence the entire process remains very practical. We use the same filtering method to filter the reconstructed κ map. In this case, the convergence is much faster, $\lesssim 1$ minute for $\epsilon = 10^{-7}$, mostly because the noise is much larger compared to the lensing signal.

Our optimal CMB filtering step remains fast and easily fast enough for use in many simulations. However, we used the flat-sky approximation throughout, where harmonic transforms are fast Fourier transforms, which will not be adequate for future surveys covering a significant fraction of the sky. On the curved sky the filtering step will be more time consuming given the much more expensive cost of the high-resolution spherical harmonic transforms, and further numerical optimization of the filter will potentially be of significant benefit. For our flat sky analysis we investigated several multigrid preconditioners but found no clear-cut improvements in execution time. However, this conclusion may well change on the curved sky where the numerical cost is distributed differently. Given the very configuration-specific timing performance of the inversion, it seems likely that a good solution is probably best found on a case-by-case basis. For these reasons we do not perform further performance comparisons here and leave a systematic study of the conjugate-gradient inversion performance for future work. The convergence criteria could also be refined to more closely match the actual requirements in terms of numerical precision of the filtered maps.

Bibliography

[1] Albert Einstein. 'Die Feldgleichungen der Gravitation'. In: *Sitzungsberichte der Königlich Preußischen Akademie der Wissenschaften (Berlin* (Jan. 1915), pp. 844–847 (cit. on p. 2).

[2] A. Friedmann. 'Über die Krümmung des Raumes'. In: *Zeitschrift für Physik* 10 (Jan. 1922), pp. 377–386. DOI: 10.1007/BF01332580 (cit. on p. 2).

[3] A. Friedmann. 'Über die Möglichkeit einer Welt mit konstanter negativer Krümmung des Raumes'. In: *Zeitschrift für Physik* 21.1 (Dec. 1924), pp. 326–332. DOI: 10.1007/BF01328280 (cit. on p. 2).

[4] G. Lemaître. 'Expansion of the universe, A homogeneous universe of constant mass and increasing radius accounting for the radial velocity of extra-galactic nebulae'. In: *MNRAS* 91 (Mar. 1931), pp. 483–490. DOI: 10.1093/mnras/91.5.483 (cit. on p. 2).

[5] Georges Lemaître. 'L'Univers en expansion'. In: *Annales de la Société Scientifique de Bruxelles* 53 (Jan. 1933), p. 51 (cit. on p. 2).

[6] H. P. Robertson. 'Kinematics and World-Structure'. In: *ApJ* 82 (Nov. 1935), p. 284. DOI: 10.1086/143681 (cit. on p. 2).

[7] H. P. Robertson. 'Kinematics and World-Structure II.' In: *ApJ* 83 (Apr. 1936), p. 187. DOI: 10.1086/143716 (cit. on p. 2).

[8] H. P. Robertson. 'Kinematics and World-Structure III.' In: *ApJ* 83 (May 1936), p. 257. DOI: 10.1086/143726 (cit. on p. 2).

[9] A. G. Walker. 'On Milne's Theory of World-Structure*'. In: *Proceedings of the London Mathematical Society* s2-42.1 (1937), pp. 90–127. DOI: https://doi.org/10.1112/plms/s2-42.1.90. eprint: https://londmathsoc.onlinelibrary.wiley.com/doi/pdf/10.1112/plms/s2-42.1.90 (cit. on p. 2).

[10] Edmund J. Copeland, M. Sami and Shinji Tsujikawa. 'Dynamics of dark energy'. In: *Int. J. Mod. Phys. D* 15 (2006), pp. 1753–1936. DOI: 10.1142/S021827180600942X. arXiv: hep-th/0603057 (cit. on p. 3).

[11] Julien Lesgourgues and Sergio Pastor. 'Massive neutrinos and cosmology'. In: *Phys. Rept.* 429 (2006), pp. 307–379. DOI: 10.1016/j.physrep.2006.04.001. arXiv: astro-ph/0603494 (cit. on pp. 4, 8).

[12] Anne M. Green. 'Dark Matter in Astrophysics/Cosmology'. In: Sept. 2021. arXiv: 2109.05854 [hep-ph] (cit. on p. 4).

[13] Stephane Colombi, Scott Dodelson and Lawrence M. Widrow. 'Large scale structure tests of warm dark matter'. In: *Astrophys. J.* 458 (1996), p. 1. DOI: 10.1086/176788. arXiv: astro-ph/9505029 (cit. on p. 5).

[14] B. Ryden. *Introduction to cosmology*. Cambridge University Press, 1970. ISBN: 978-1-107-15483-4, 978-1-316-88984-8, 978-1-316-65108-7. DOI: 10.1017/9781316651087 (cit. on pp. 5, 8).

[15] R. Brout, F. Englert and E. Gunzig. 'The Creation of the Universe as a Quantum Phenomenon'. In: *Annals Phys.* 115 (1978), p. 78. DOI: 10.1016/0003-4916(78)90176-8 (cit. on p. 5).

[16] Alexei A. Starobinsky. 'A New Type of Isotropic Cosmological Models Without Singularity'. In: *Phys. Lett. B* 91 (1980). Ed. by I. M. Khalatnikov and V. P. Mineev, pp. 99–102. DOI: 10.1016/0370-2693(80)90670-X (cit. on p. 5).

[17] D. Kazanas. 'Dynamics of the universe and spontaneous symmetry breaking'. In: *ApJ* 241 (Oct. 1980), pp. L59–L63. DOI: 10.1086/183361 (cit. on p. 5).

[18] K. Sato. 'First-order phase transition of a vacuum and the expansion of the Universe'. In: *MNRAS* 195 (May 1981), pp. 467–479. DOI: 10.1093/mnras/195.3.467 (cit. on p. 5).

[19] Alan H. Guth. 'The Inflationary Universe: A Possible Solution to the Horizon and Flatness Problems'. In: *Phys. Rev. D* 23 (1981). Ed. by Li-Zhi Fang and R. Ruffini, pp. 347–356. DOI: 10.1103/PhysRevD.23.347 (cit. on p. 5).

[20] Andrei D. Linde. 'A New Inflationary Universe Scenario: A Possible Solution of the Horizon, Flatness, Homogeneity, Isotropy and Primordial Monopole Problems'. In: *Phys. Lett. B* 108 (1982). Ed. by Li-Zhi Fang and R. Ruffini, pp. 389–393. DOI: 10.1016/0370-2693(82)91219-9 (cit. on p. 5).

[21] Andrei D. Linde. 'Chaotic Inflation'. In: *Phys. Lett. B* 129 (1983), pp. 177–181. DOI: 10.1016/0370-2693(83)90837-7 (cit. on p. 5).

[22] Andreas Albrecht and Paul J. Steinhardt. 'Cosmology for Grand Unified Theories with Radiatively Induced Symmetry Breaking'. In: *Phys. Rev. Lett.* 48 (1982). Ed. by Li-Zhi Fang and R. Ruffini, pp. 1220–1223. DOI: 10.1103/PhysRevLett.48.1220 (cit. on p. 5).

[23] Brian D. Fields, Paolo Molaro and Subir Sarkar. 'Big-Bang Nucleosynthesis'. In: *Chin. Phys. C* 38 (2014), pp. 339–344. arXiv: 1412.1408 [astro-ph.CO] (cit. on p. 6).

[24] R. A. Sunyaev and Ya. B. Zeldovich. 'Small-Scale Fluctuations of Relic Radiation'. In: *Ap&SS* 7.1 (Apr. 1970), pp. 3–19. DOI: 10.1007/BF00653471 (cit. on pp. 7, 19, 20).

[25] P. J. E. Peebles and J. T. Yu. 'Primeval Adiabatic Perturbation in an Expanding Universe'. In: *ApJ* 162 (Dec. 1970), p. 815. DOI: 10.1086/150713 (cit. on pp. 7, 19).

[26] Daniel J. Eisenstein et al. 'Detection of the baryon acoustic peak in the large-scale correlation function of SDSS luminous red galaxies'. In: *Astrophys.J.* 633 (2005), pp. 560–574. DOI: 10.1086/466512. arXiv: astro-ph/0501171 [astro-ph] (cit. on p. 7).

[27] Robert H. Becker et al. 'Evidence for Reionization at z 6: Detection of a Gunn-Peterson Trough in a z=6.28 Quasar'. In: *Astron. J.* 122 (2001), p. 2850. eprint: astro-ph/0108097 (cit. on p. 7).

[28] A. Kogut et al. 'Wilkinson Microwave Anisotropy Probe (WMAP) first year observations: TE polarization'. In: *Astrophys. J. Suppl.* 148 (2003), p. 161. DOI: 10.1086/377219. arXiv: astro-ph/0302213 (cit. on pp. 7, 22).

[29] John H. Wise. 'Cosmic reionisation'. In: *Contemp. Phys.* 60.2 (2019), pp. 145–163. DOI: 10.1080/00107514.2019.1631548. arXiv: 1907.06653 [astro-ph.CO] (cit. on p. 8).

[30] Edward L. Wright. 'A Cosmology Calculator for the World Wide Web'. In: *Publ. Astron. Soc. Pac.* 118 (2006), pp. 1711–1715. DOI: 10.1086/510102. arXiv: astro-ph/0609593 (cit. on p. 8).

[31] Planck Collaboration XIII. 'Planck 2015 results. XIII. Cosmological parameters'. In: *A&A* 594 (2016), A13. DOI: 10.1051/0004-6361/201525830. arXiv: 1502.01589 [astro-ph.CO] (cit. on pp. 8, 44, 71, 133).

[32] Lloyd Knox and Marius Millea. 'Hubble constant hunter's guide'. In: *Phys. Rev. D* 101.4 (2020), p. 043533. DOI: 10.1103/PhysRevD.101.043533. arXiv: 1908.03663 [astro-ph.CO] (cit. on p. 9).

[33] Weikang Lin, Katherine J. Mack and Liqiang Hou. 'Investigating the Hubble Constant Tension – Two Numbers in the Standard Cosmological Model'. In: *Astrophys. J. Lett.* 904.2 (2020), p. L22. DOI: 10.3847/2041-8213/abc894. arXiv: 1910.02978 [astro-ph.CO] (cit. on p. 9).

[34] G. Efstathiou. 'A Lockdown Perspective on the Hubble Tension (with comments from the SH0ES team)'. In: (July 2020). arXiv: 2007.10716 [astro-ph.CO] (cit. on p. 9).

[35] Eleonora Di Valentino et al. 'In the realm of the Hubble tension—a review of solutions'. In: *Class. Quant. Grav.* 38.15 (2021), p. 153001. DOI: 10.1088/1361-6382/ac086d. arXiv: 2103.01183 [astro-ph.CO] (cit. on p. 9).

[36] Paul Shah, Pablo Lemos and Ofer Lahav. 'A buyer's guide to the Hubble Constant'. In: (Sept. 2021). arXiv: 2109.01161 [astro-ph.CO] (cit. on p. 9).

[37] N. Aghanim et al. 'Planck 2018 results. VI. Cosmological parameters'. In: *Astron. Astrophys.* 641 (2020), A6. DOI: 10.1051/0004-6361/201833910. arXiv: 1807.06209 [astro-ph.CO] (cit. on pp. 9, 19, 20, 129).

[38] Chung-Pei Ma and Edmund Bertschinger. 'Cosmological perturbation theory in the synchronous versus conformal Newtonian gauge'. In: (Jan. 1994). arXiv: astro-ph/9401007 (cit. on pp. 9, 14, 27).

[39] Max Tegmark et al. 'The 3-D power spectrum of galaxies from the SDSS'. In: *Astrophys. J.* 606 (2004), pp. 702–740. DOI: 10.1086/382125. arXiv: astro-ph/0310725 (cit. on p. 10).

[40] N. Aghanim et al. 'Planck 2018 results. I. Overview and the cosmological legacy of Planck'. In: *Astron. Astrophys.* 641 (2020), A1. DOI: 10.1051/0004-6361/201833880. arXiv: 1807.06205 [astro-ph.CO] (cit. on pp. 10, 11, 21, 70).

[41] Solène Chabanier, Marius Millea and Nathalie Palanque-Delabrouille. 'Matter power spectrum: from Lyα forest to CMB scales'. In: *Mon. Not. Roy. Astron. Soc.* 489.2 (2019), pp. 2247–2253. DOI: 10.1093/mnras/stz2310. arXiv: 1905.08103 [astro-ph.CO] (cit. on pp. 10, 11).

[42] Max Tegmark and Matias Zaldarriaga. 'Separating the early universe from the late universe: Cosmological parameter estimation beyond the black box'. In: *Phys. Rev. D* 66 (2002), p. 103508. DOI: 10.1103/PhysRevD.66.103508. arXiv: astro-ph/0207047 (cit. on pp. 10, 12).

[43] N. Kaiser. 'On the spatial correlations of Abell clusters.' In: *ApJ* 284 (Sept. 1984), pp. L9–L12. DOI: 10.1086/184341 (cit. on p. 11).

[44] J. M. Bardeen, J. R. Bond, N. Kaiser and A. S. Szalay. 'The statistics of peaks of Gaussian random fields'. In: *ApJ* 304 (May 1986), pp. 15–61. DOI: 10.1086/164143 (cit. on p. 11).

[45] H. J. Mo and S. D. M. White. 'An analytic model for the spatial clustering of dark matter haloes'. In: *MNRAS* 282.2 (Sept. 1996), pp. 347–361. DOI: 10.1093/mnras/282.2.347. arXiv: astro-ph/9512127 [astro-ph] (cit. on p. 11).

[46] R. G. Mann, J. A. Peacock and A. F. Heavens. 'Eulerian bias and the galaxy density field'. In: *MNRAS* 293.3 (Jan. 1998), pp. 209–221. DOI: 10.1046/j.1365-8711.1998.01053.x. arXiv: astro-ph/9708031 [astro-ph] (cit. on p. 11).

[47] Max Tegmark and P. J. E. Peebles. 'The Time Evolution of Bias'. In: *ApJ* 500.2 (June 1998), pp. L79–L82. DOI: 10.1086/311426. arXiv: astro-ph/9804067 [astro-ph] (cit. on p. 11).

[48] Beth A. Reid et al. 'Cosmological constraints from the clustering of the Sloan Digital Sky Survey DR7 luminous red galaxies'. In: *MNRAS* 404.1 (May 2010), pp. 60–85. DOI: 10.1111/j.1365-2966.2010.16276.x. arXiv: 0907.1659 [astro-ph.CO] (cit. on p. 11).

[49] Michael Rauch. 'The lyman alpha forest in the spectra of quasistellar objects'. In: *Ann. Rev. Astron. Astrophys.* 36 (1998), pp. 267–316. DOI: 10.1146/annurev.astro.36.1.267. arXiv: astro-ph/9806286 (cit. on p. 11).

[50] Matteo Viel, Martin G. Haehnelt and Volker Springel. 'Inferring the dark matter power spectrum from the Lyman- alpha forest in high-resolution QSO absorption spectra'. In: *MNRAS* 354 (2004), p. 684. eprint: astro-ph/0404600 (cit. on p. 11).

[51] M. A. Troxel et al. 'Dark Energy Survey Year 1 Results: Cosmological Constraints from Cosmic Shear'. In: *ArXiv e-prints* (2017). arXiv: 1708.01538 [astro-ph.CO] (cit. on p. 11).

[52] J. A. Peacock and S. J. Dodds. 'Nonlinear evolution of cosmological power spectra'. In: *Mon. Not. Roy. Astron. Soc.* 280 (1996), p. L19. DOI: 10.1093/mnras/280.3.L19. arXiv: astro-ph/9603031 (cit. on p. 12).

[53] M. Davis and P. J. E. Peebles. 'A survey of galaxy redshifts. V. The two-point position and velocity correlations.' In: *ApJ* 267 (Apr. 1983), pp. 465–482. DOI: 10.1086/160884 (cit. on p. 12).

[54] S. D. M. White, G. Efstathiou and C. S. Frenk. 'The amplitude of mass fluctuations in the universe'. In: *MNRAS* 262.4 (June 1993), pp. 1023–1028. DOI: 10.1093/mnras/262.4.1023 (cit. on p. 12).

[55] Max Tegmark et al. 'Cosmological parameters from SDSS and WMAP'. In: *Phys. Rev. D* 69 (2004), p. 103501. DOI: 10.1103/PhysRevD.69.103501. arXiv: astro-ph/0310723 (cit. on p. 12).

[56] Wayne Hu, Naoshi Sugiyama and Joseph Silk. 'The Physics of microwave background anisotropies'. In: *Nature* 386 (1997), pp. 37–43. DOI: 10.1038/386037a0. arXiv: astro-ph/9604166 (cit. on p. 13).

[57] Joseph Silk. 'Cosmic Black-Body Radiation and Galaxy Formation'. In: *ApJ* 151 (Feb. 1968), p. 459. DOI: 10.1086/149449 (cit. on p. 13).

[58] K. T. Story et al. 'A Measurement of the Cosmic Microwave Background Damping Tail from the 2500-Square-Degree SPT-SZ Survey'. In: *ApJ* 779.1, 86 (Dec. 2013), p. 86. DOI: 10.1088/0004-637X/779/1/86. arXiv: 1210.7231 [astro-ph.CO] (cit. on p. 13).

[59] R. K. Sachs and A. M. Wolfe. 'Perturbations of a Cosmological Model and Angular Variations of the Microwave Background'. In: *ApJ* 147 (Jan. 1967), p. 73. DOI: 10.1086/148982 (cit. on pp. 13, 19).

[60] Martin J. White and Wayne Hu. 'The Sachs-Wolfe effect'. In: *Astron. Astrophys.* 321 (1997), pp. 8–9. arXiv: astro-ph/9609105 (cit. on p. 13).

[61] Atsushi J. Nishizawa. 'The integrated Sachs–Wolfe effect and the Rees–Sciama effect'. In: *PTEP* 2014 (2014), 06B110. DOI: 10.1093/ptep/ptu062. arXiv: 1404.5102 [astro-ph.CO] (cit. on p. 13).

[62] Michael R. Nolta et al. 'First year Wilkinson Microwave Anisotropy Probe (WMAP) observations: Dark energy induced correlation with radio sources'. In: *Astrophys. J.* 608 (2004), pp. 10–15. DOI: 10.1086/386536. arXiv: astro-ph/0305097 (cit. on p. 14).

[63] Chung-Pei Ma and Edmund Bertschinger. 'Cosmological perturbation theory in the synchronous and conformal Newtonian gauges'. In: *Astrophys. J.* 455 (1995), pp. 7–25. DOI: 10.1086/176550. arXiv: astro-ph/9506072 (cit. on p. 14).

[64] D.J. Fixsen. 'The Temperature of the Cosmic Microwave Background'. In: *ApJ* 707 (2009), pp. 916–920. DOI: 10.1088/0004-637X/707/2/916. arXiv: 0911.1955 [astro-ph.CO] (cit. on p. 15).

[65] Subrahmanyan Chandrasekhar. *Radiative transfer*. 1960 (cit. on p. 15).

[66] E. Bavarsad, M. Haghighat, Z. Rezaei, R. Mohammadi, I. Motie and M. Zarei. 'Generation of circular polarization of the CMB'. In: *Phys. Rev. D* 81 (2010), p. 084035. DOI: 10.1103/PhysRevD.81.084035. arXiv: 0912.2993 [hep-th] (cit. on p. 16).

[67] Keisuke Inomata and Marc Kamionkowski. 'Circular polarization of the cosmic microwave background from vector and tensor perturbations'. In: *Phys. Rev. D* 99.4 (2019), p. 043501. DOI: 10.1103/PhysRevD.99.043501. arXiv: 1811.04957 [astro-ph.CO] (cit. on p. 16).

[68] Y. Akrami et al. 'Planck 2018 results. IV. Diffuse component separation'. In: *Astron. Astrophys.* 641 (2020), A4. DOI: 10.1051/0004-6361/201833881. arXiv: 1807.06208 [astro-ph.CO] (cit. on pp. 16, 118, 119, 141).

[69] Uros Seljak. 'Measuring polarization in cosmic microwave background'. In: *Astrophys. J.* 482 (1997), p. 6. DOI: 10.1086/304123. arXiv: astro-ph/9608131 (cit. on p. 16).

[70] Matias Zaldarriaga and Uros Seljak. 'An all sky analysis of polarization in the microwave background'. In: *Phys. Rev. D* 55 (1997), pp. 1830–1840. DOI: 10.1103/PhysRevD.55.1830. arXiv: astro-ph/9609170 (cit. on pp. 16, 85).

[71] Marc Kamionkowski, Arthur Kosowsky and Albert Stebbins. 'Statistics of cosmic microwave background polarization'. In: *Phys. Rev. D* 55 (1997), pp. 7368–7388. DOI: 10.1103/PhysRevD.55.7368. arXiv: astro-ph/9611125 (cit. on p. 16).

[72] Matias Zaldarriaga. 'Nature of the E B decomposition of CMB polarization'. In: *Phys. Rev. D* 64 (2001), p. 103001. DOI: 10.1103/PhysRevD.64.103001. arXiv: astro-ph/0106174 (cit. on p. 16).

[73] M. C. Guzzetti, N. Bartolo, M. Liguori and S. Matarrese. 'Gravitational waves from inflation'. In: *Riv. Nuovo Cim.* 39.9 (2016), pp. 399–495. DOI: 10.1393/ncr/i2016-10127-1. arXiv: 1605.01615 [astro-ph.CO] (cit. on p. 17).

[74] Uros Seljak and Matias Zaldarriaga. 'Signature of gravity waves in polarization of the microwave background'. In: *PRDLett.* 78 (1997), pp. 2054–2057. eprint: astro-ph/9609169 (cit. on p. 17).

[75] Scott Dodelson, William H. Kinney and Edward W. Kolb. 'Cosmic microwave background measurements can discriminate among inflation models'. In: *Phys. Rev. D* 56 (1997), pp. 3207–3215. DOI: 10.1103/PhysRevD.56.3207. arXiv: astro-ph/9702166 (cit. on p. 17).

[76] Marc Kamionkowski, Arthur Kosowsky and Albert Stebbins. 'A Probe of primordial gravity waves and vorticity'. In: *Phys. Rev. Lett.* 78 (1997), pp. 2058–2061. DOI: 10.1103/PhysRevLett.78.2058. arXiv: astro-ph/9609132 (cit. on pp. 17, 85).

[77] P. A. R. Ade et al. 'Planck 2013 results. XXII. Constraints on inflation'. In: *Astron. Astrophys.* 571 (2014), A22. DOI: 10.1051/0004-6361/201321569. arXiv: 1303.5082 [astro-ph.CO] (cit. on pp. 17, 21).

[78] M. Betoule, E. Pierpaoli, J. Delabrouille, M. Le Jeune and J. F. Cardoso. 'Measuring the tensor to scalar ratio from CMB B-modes in the presence of foregrounds'. In: *A&A* 503.3 (Sept. 2009), pp. 691–706. DOI: 10.1051/0004-6361/200911624. arXiv: 0901.1056 [astro-ph.CO] (cit. on p. 17).

[79] Benjamin Racine et al. 'Measurements of Degree-Scale B-mode Polarization with the BICEP/*Keck* Experiments at South Pole'. In: *53rd Rencontres de Moriond on Cosmology*. 2018, pp. 113–120. arXiv: 1807.02199 [astro-ph.CO] (cit. on p. 17).

[80] Kendrick M. Smith, Duncan Hanson, Marilena LoVerde, Christopher M. Hirata and Oliver Zahn. 'Delensing CMB Polarization with External Datasets'. In: *JCAP* 1206 (2012), p. 014. DOI: 10.1088/1475-7516/2012/06/014. arXiv: 1010.0048 [astro-ph.CO] (cit. on p. 17).

[81] Gabrielle Simard, Duncan Hanson and Gil Holder. 'Prospects for Delensing the Cosmic Microwave Background for Studying Inflation'. In: *ApJ* 807.2 (2015), p. 166. DOI: 10.1088/0004-637X/807/2/166. arXiv: 1410.0691 [astro-ph.CO] (cit. on p. 17).

[82] Neelima Sehgal, Mathew S. Madhavacheril, Blake Sherwin and Alexander van Engelen. 'Internal Delensing of Cosmic Microwave Background Acoustic Peaks'. In: *PRD* 95.10 (2017), p. 103512. DOI: 10.1103/PhysRevD.95.103512. arXiv: 1612.03898 [astro-ph.CO] (cit. on p. 17).

[83] Julien Carron, Antony Lewis and Anthony Challinor. 'Internal delensing of Planck CMB temperature and polarization'. In: *JCAP* 1705.05 (2017), p. 035. DOI: 10.1088/1475-7516/2017/05/035. arXiv: 1701.01712 [astro-ph.CO] (cit. on p. 17).

[84] A. Manzotti et al. 'CMB Polarization B-mode Delensing with SPTpol and Herschel'. In: *ApJ* 846.1 (2017), p. 45. DOI: 10.3847/1538-4357/aa82bb. arXiv: 1701.04396 [astro-ph.CO] (cit. on p. 17).

[85] Daniel Green, Joel Meyers and Alexander van Engelen. 'CMB Delensing Beyond the B Modes'. In: *JCAP* 1712.12 (2017), p. 005. DOI: 10.1088/1475-7516/2017/12/005. arXiv: 1609.08143 [astro-ph.CO] (cit. on p. 17).

[86] Domenico Marinucci. 'Testing for Non-Gaussianity on Cosmic Microwave Background Radiation: A Review'. In: *Statist. Sci.* 19 (2004), p. 294. DOI: 10.1214/088342304000000783 (cit. on p. 18).

[87] Mona Frommert, Ruth Durrer and Jérôme Michaud. 'The Kolmogorov-Smirnov test for the CMB'. In: *JCAP* 2012.1, 009 (Jan. 2012), p. 009. DOI: 10.1088/1475-7516/2012/01/009. arXiv: 1108.5354 [astro-ph.CO] (cit. on p. 18).

[88] J. R. Bond and G. Efstathiou. 'The statistics of cosmic background radiation fluctuations'. In: *MNRAS* 226 (June 1987), pp. 655–687. DOI: 10.1093/mnras/226.3.655 (cit. on pp. 18, 19).

[89] Benjamin D. Wandelt, Eric Hivon and Krzysztof M. Gorski. 'The pseudo-c_l method: cosmic microwave background anisotropy power spectrum statistics for high precision cosmology'. In: *Phys. Rev.* D64 (2001), p. 083003. DOI:

10.1103/PhysRevD.64.083003. arXiv: astro-ph/0008111 [astro-ph] (cit. on pp. 19, 145).

[90] G. Efstathiou. 'Myths and truths concerning estimation of power spectra'. In: *Mon. Not. Roy. Astron. Soc.* 349 (2004), p. 603. DOI: 10.1111/j.1365-2966.2004.07530.x. arXiv: astro-ph/0307515 (cit. on pp. 19, 145).

[91] Michael L. Brown, P. G. Castro and A. N. Taylor. 'CMB temperature and polarisation pseudo-C(l) estimators and covariances'. In: *Mon. Not. Roy. Astron. Soc.* 360 (2005), pp. 1262–1280. DOI: 10.1111/j.1365-2966.2005.09111.x. arXiv: astro-ph/0410394 (cit. on p. 19).

[92] Kendrick M. Smith. 'Pseudo-C_ℓ estimators which do not mix E and B modes'. In: *Phys. Rev.* D74 (2006), p. 083002. DOI: 10.1103/PhysRevD.74.083002. arXiv: astro-ph/0511629 [astro-ph] (cit. on pp. 19, 51, 97).

[93] Antony Lewis, Anthony Challinor and Neil Turok. 'Analysis of CMB polarization on an incomplete sky'. In: *PRD* 65 (2002), p. 023505. DOI: 10.1103/PhysRevD.65.023505. arXiv: astro-ph/0106536 [astro-ph] (cit. on p. 19).

[94] Emory F. Bunn. 'Detectability of microwave background polarization'. In: *Phys. Rev. D* 65 (2002), p. 043003. DOI: 10.1103/PhysRevD.65.043003. arXiv: astro-ph/0108209 (cit. on p. 19).

[95] Emory F. Bunn, Matias Zaldarriaga, Max Tegmark and Angelica de Oliveira-Costa. 'E/B decomposition of finite pixelized CMB maps'. In: *Phys. Rev. D* 67 (2003), p. 023501. DOI: 10.1103/PhysRevD.67.023501. arXiv: astro-ph/0207338 (cit. on p. 19).

[96] Kendrick M. Smith and Matias Zaldarriaga. 'A general solution to the E-B mixing problem'. In: *Phys. Rev. D* 76 (2007), p. 043001. DOI: 10.1103/PhysRevD.76.043001. arXiv: astro-ph/0610059 (cit. on p. 19).

[97] Kendrick M. Smith. 'Pure pseudo-C_l estimators for CMB B-modes'. In: *New Astron. Rev.* 50 (2006), pp. 1025–1029. DOI: 10.1016/j.newar.2006.09.015. arXiv: astro-ph/0608662 (cit. on p. 19).

[98] Planck Collaboration XV. 'Planck 2015 results. XV. Gravitational lensing'. In: *A&A* 594 (2016), A15. DOI: 10.1051/0004-6361/201525941. arXiv: 1502.01591 [astro-ph.CO] (cit. on pp. 19, 23, 33, 50, 54, 60, 95, 96, 117, 123, 125, 126, 164).

[99] P. A. R. Ade et al. 'Planck intermediate results. XLI. A map of lensing-induced B-modes'. In: *A&A* 596 (Dec. 2016), A102. DOI: 10.1051/0004-6361/201527932. arXiv: 1512.02882 [astro-ph.CO] (cit. on pp. 19, 20).

[100] N. Aghanim et al. 'Planck 2018 results. VIII. Gravitational lensing'. In: *Astron. Astrophys.* 641 (2020), A8. DOI: 10.1051/0004-6361/201833886. arXiv: 1807.06210 [astro-ph.CO] (cit. on pp. 19, 23, 33, 43, 44, 46, 50, 57–59, 95, 117, 119, 122, 123, 125, 126, 164).

[101] J. R. Bond and G. Efstathiou. 'Cosmic background radiation anisotropies in universes dominated by nonbaryonic dark matter'. In: *ApJ* 285 (Oct. 1984), pp. L45–L48. DOI: 10.1086/184362 (cit. on p. 19).

[102] Jon A. Holtzman. 'Microwave Background Anisotropies and Large-Scale Structure in Universes with Cold Dark Matter, Baryons, Radiation, and Massive and Massless Neutrinos'. In: *Ap. J. Suppl.* 71 (Sept. 1989), p. 1. DOI: 10.1086/191362 (cit. on p. 19).

[103] E. Komatsu et al. 'First year Wilkinson Microwave Anisotropy Probe (WMAP) observations: tests of gaussianity'. In: *Astrophys. J. Suppl.* 148 (2003), pp. 119–134. DOI: 10.1086/377220. arXiv: astro-ph/0302223 (cit. on p. 19).

[104] J. R. Fergusson, M. Liguori and E. P. S. Shellard. 'The CMB bispectrum'. In: *JCAP* 2012.12, 032 (Dec. 2012), p. 032. DOI: 10.1088/1475-7516/2012/12/032. arXiv: 1006.1642 [astro-ph.CO] (cit. on p. 19).

[105] P. A. R. Ade et al. 'Planck 2013 results. XXIII. Isotropy and statistics of the CMB'. In: *Astron. Astrophys.* 571 (2014), A23. DOI: 10.1051/0004-6361/201321534. arXiv: 1303.5083 [astro-ph.CO] (cit. on p. 19).

[106] Matias Zaldarriaga. 'Polarization of the microwave background in reionized models'. In: *Phys. Rev. D* 55 (1997), pp. 1822–1829. DOI: 10.1103/PhysRevD.55.1822. arXiv: astro-ph/9608050 (cit. on p. 20).

[107] M. Kaplinghat, M. Chu, Z. Haiman, G. Holder, L. Knox and C. Skordis. 'Probing the reionization history of the universe using the cosmic microwave background polarization'. In: *Astrophys. J.* 583 (2003), pp. 24–32. DOI: 10.1086/344927. arXiv: astro-ph/0207591 (cit. on p. 20).

[108] Olivier Dore et al. 'The Signature of Patchy Reionization in the Polarization Anisotropy of the CMB'. In: *Phys. Rev. D* 76 (2007), p. 043002. DOI: 10.1103/PhysRevD.76.043002. arXiv: astro-ph/0701784 (cit. on p. 20).

[109] Ya. B. Zeldovich and R. A. Sunyaev. 'The Interaction of Matter and Radiation in a Hot-Model Universe'. In: *Ap&SS* 4.3 (July 1969), pp. 301–316. DOI: 10.1007/BF00661821 (cit. on p. 20).

[110] P. A. R. Ade et al. 'Planck 2013 results. XX. Cosmology from Sunyaev–Zeldovich cluster counts'. In: *Astron. Astrophys.* 571 (2014), A20. DOI: 10.1051/0004-6361/201321521. arXiv: 1303.5080 [astro-ph.CO] (cit. on p. 21).

[111] P. A. R. Ade et al. 'Planck 2015 results. XXIV. Cosmology from Sunyaev-Zeldovich cluster counts'. In: *Astron. Astrophys.* 594 (2016), A24. DOI: 10.1051/0004-6361/201525833. arXiv: 1502.01597 [astro-ph.CO] (cit. on p. 21).

[112] N. Aghanim et al. 'Planck 2013 results. XXVII. Doppler boosting of the CMB: Eppur si muove'. In: *Astron. Astrophys.* 571 (2014), A27. DOI: 10.1051/0004-6361/201321556. arXiv: 1303.5087 [astro-ph.CO] (cit. on p. 21).

[113] Antony Lewis, Anthony Challinor and Anthony Lasenby. 'Efficient computation of CMB anisotropies in closed FRW models'. In: *ApJ* 538 (2000), pp. 473–476. DOI: 10.1086/309179. arXiv: astro-ph/9911177 [astro-ph] (cit. on pp. 22, 56, 95, 140).

[114] A. A. Penzias and R. W. Wilson. 'A Measurement of Excess Antenna Temperature at 4080 Mc/s.' In: *ApJ* 142 (July 1965), pp. 419–421. DOI: 10.1086/148307 (cit. on p. 22).

[115] Andrew McKellar. 'Molecular Lines from the Lowest States of Diatomic Molecules Composed of Atoms Probably Present in Interstellar Space'. In: *Publications of the Dominion Astrophysical Observatory Victoria* 7 (Jan. 1941), p. 251 (cit. on p. 22).

[116] Ralph A. Alpher and Robert Herman. 'Evolution of the Universe'. In: *Nature* 162.4124 (Nov. 1948), pp. 774–775. DOI: 10.1038/162774b0 (cit. on p. 22).

[117] N. W. Boggess et al. 'The COBE Mission: Its Design and Performance Two Years after Launch'. In: *ApJ* 397 (Oct. 1992), p. 420. DOI: 10.1086/171797 (cit. on p. 22).

[118] C. L. Bennett et al. 'Four-Year COBE DMR Cosmic Microwave Background Observations: Maps and Basic Results'. In: *ApJ* 464 (June 1996), p. L1. DOI: 10.1086/310075. arXiv: astro-ph/9601067 [astro-ph] (cit. on p. 22).

[119] D. J. Fixsen, E. S. Cheng, J. M. Gales, J. C. Mather, R. A. Shafer and E. L. Wright. 'The Cosmic Microwave Background Spectrum from the Full COBE FIRAS Data Set'. In: *ApJ* 473 (Dec. 1996), p. 576. DOI: 10.1086/178173. arXiv: astro-ph/9605054 [astro-ph] (cit. on p. 22).

[120] C. L. Bennett et al. 'The Microwave Anisotropy Probe (MAP) mission'. In: *Astrophys. J.* 583 (2003), pp. 1–23. DOI: 10.1086/345346. arXiv: astro-ph/0301158 (cit. on p. 22).

[121] Planck. 'Planck: The scientific programme'. In: *ESA publication* (2006). eprint: astro-ph/0604069 (cit. on p. 23).

[122] J. M. Lamarre et al. 'Planck pre-launch status: The HFI instrument, from specification to actual performance'. In: *A&A* 520, A9 (Sept. 2010), A9. DOI: 10.1051/0004-6361/200912975 (cit. on p. 23).

[123] P. A. R. Ade et al. 'Planck 2013 results. XVII. Gravitational lensing by large-scale structure'. In: *Astron. Astrophys.* 571 (2014), A17. DOI: 10.1051/0004-6361/201321543. arXiv: 1303.5077 [astro-ph.CO] (cit. on pp. 23, 33, 50, 95, 117, 123).

[124] J. Errard et al. 'Modeling atmospheric emission for CMB ground-based observations'. In: *Astrophys. J.* 809 (2015), p. 63. DOI: 10.1088/0004-637X/809/1/63. arXiv: 1501.07911 [astro-ph.IM] (cit. on pp. 23, 114).

[125] Arthur Kosowsky. 'The Atacama Cosmology Telescope'. In: *New Astron. Rev.* 47 (2003), pp. 939–943. DOI: 10.1016/j.newar.2003.09.003. arXiv: astro-ph/0402234 (cit. on p. 23).

[126] The Polarbear Collaboration et al. 'The new generation CMB B-mode polarization experiment: POLARBEAR'. In: *arXiv e-prints*, arXiv:1011.0763 (Nov. 2010), arXiv:1011.0763. arXiv: 1011.0763 [astro-ph.IM] (cit. on p. 23).

[127] Thomas Essinger-Hileman et al. 'CLASS: the cosmology large angular scale surveyor'. In: *Millimeter, Submillimeter, and Far-Infrared Detectors and Instrumentation for Astronomy VII*. Ed. by Wayne S. Holland and Jonas Zmuidzinas. Vol. 9153. Society of Photo-Optical Instrumentation Engineers (SPIE) Conference Series. July 2014,

p. 91531I. DOI: 10.1117/12.2056701. arXiv: 1408.4788 [astro-ph.IM] (cit. on p. 23).

[128] John E. Ruhl et al. 'The South Pole Telescope'. In: *Proc. SPIE Int. Soc. Opt. Eng.* 5498 (2004), p. 11. DOI: 10.1117/12.552473. arXiv: astro-ph/0411122 (cit. on p. 23).

[129] B. G. Keating et al. 'BICEP: a large angular scale CMB polarimeter'. In: *Polarimetry in Astronomy. Proceedings of the SPIE, Volume 4843*. Ed. by S. Fineschi. Feb. 2003, pp. 284–295 (cit. on p. 23).

[130] C. D. Sheehy et al. 'The Keck Array: a pulse tube cooled CMB polarimeter'. In: *arXiv e-prints*, arXiv:1104.5516 (Apr. 2011), arXiv:1104.5516. arXiv: 1104.5516 [astro-ph.IM] (cit. on p. 23).

[131] Peter Ade et al. 'The Simons Observatory: Science goals and forecasts'. In: *JCAP* 02 (2019), p. 056. DOI: 10.1088/1475-7516/2019/02/056. arXiv: 1808.07445 [astro-ph.CO] (cit. on pp. 24, 43, 62, 70, 75, 76, 146, 149, 150).

[132] Adrian Lee et al. 'The Simons Observatory'. In: *Bulletin of the American Astronomical Society*. Vol. 51. Sept. 2019, p. 147. arXiv: 1907.08284 [astro-ph.IM] (cit. on p. 24).

[133] Kevork N. Abazajian et al. 'CMB-S4 Science Book, First Edition'. In: (2016). arXiv: 1610.02743 [astro-ph.CO] (cit. on pp. 24, 43, 62, 70).

[134] Maximilian H. Abitbol et al. 'CMB-S4 Technology Book, First Edition'. In: *arXiv e-prints*, arXiv:1706.02464 (June 2017), arXiv:1706.02464. arXiv: 1706.02464 [astro-ph.IM] (cit. on p. 24).

[135] Kevork Abazajian et al. 'CMB-S4 Decadal Survey APC White Paper'. In: *Bull. Am. Astron. Soc.* 51.7 (2019), p. 209. DOI: 10.2172/1556957. arXiv: 1908.01062 [astro-ph.IM] (cit. on pp. 24, 62).

[136] M. Hazumi et al. 'LiteBIRD: JAXA's new strategic L-class mission for all-sky surveys of cosmic microwave background polarization'. In: *Proc. SPIE Int. Soc. Opt. Eng.* 11443 (2020), 114432F. DOI: 10.1117/12.2563050. arXiv: 2101.12449 [astro-ph.IM] (cit. on pp. 24, 136).

[137] H. G. Khachatryan, A. L. Kashin, E. Poghosyan and G. Yegoryan. 'On the detection of point sources in Planck LFI 70 GHz CMB maps based on cleaned K-map'. In: *Mod. Phys. Lett. A* 30.14 (2015), p. 1550083. DOI: 10.1142/S0217732315500832. arXiv: 1503.00346 [astro-ph.GA] (cit. on p. 25).

[138] E. L. Wright et al. 'The Wilkinson Microwave Anisotropy Probe (WMAP) Source Catalog'. In: *Astrophys. J. Suppl.* 180 (2009), pp. 283–295. DOI: 10.1088/0067-0049/180/2/283. arXiv: 0803.0577 [astro-ph] (cit. on p. 25).

[139] E. E. Rigby et al. 'Herschel-ATLAS: first data release of the Science Demonstration Phase source catalogues'. In: *MNRAS* 415.3 (Aug. 2011), pp. 2336–2348. DOI: 10.1111/j.1365-2966.2011.18864.x. arXiv: 1010.5787 [astro-ph.IM] (cit. on p. 25).

[140] P. A. R. Ade et al. 'Planck 2015 results. XXVI. The Second Planck Catalogue of Compact Sources'. In: *Astron. Astrophys.* 594 (2016), A26. DOI: 10.1051/0004-6361/201526914. arXiv: 1507.02058 [astro-ph.CO] (cit. on p. 25).

[141] Bernard F. Schutz. *A First Course in General Relativity*. Cambridge, UK: Cambridge Univ. Pr., 1985 (cit. on p. 26).

[142] Antony Lewis and Anthony Challinor. 'Weak gravitational lensing of the CMB'. In: *Phys. Rept.* 429 (2006), pp. 1–65. DOI: 10.1016/j.physrep.2006.03.002. arXiv: astro-ph/0601594 [astro-ph] (cit. on pp. 27, 28, 43, 45, 70).

[143] Wayne Hu. 'Weak lensing of the CMB: A harmonic approach'. In: *PRD* 62 (2000), p. 043007. DOI: 10.1103/PhysRevD.62.043007. arXiv: astro-ph/0001303 [astro-ph] (cit. on p. 30).

[144] Michael H. Kesden, Asantha Cooray and Marc Kamionkowski. 'Lensing reconstruction with CMB temperature and polarization'. In: *Phys. Rev. D* 67 (2003), p. 123507. DOI: 10.1103/PhysRevD.67.123507. arXiv: astro-ph/0302536 (cit. on pp. 30, 38, 39, 54, 96).

[145] Wayne Hu and Takemi Okamoto. 'Mass reconstruction with cmb polarization'. In: *ApJ* 574 (2002), pp. 566–574. DOI: 10.1086/341110. arXiv: astro-ph/0111606 [astro-ph] (cit. on pp. 30, 56).

[146] Antony Lewis, Anthony Challinor and Duncan Hanson. 'The shape of the CMB lensing bispectrum'. In: *JCAP* 1103 (2011), p. 018. DOI: 10.1088/1475-7516/2011/03/018. arXiv: 1101.2234 [astro-ph.CO] (cit. on pp. 31, 45, 56).

[147] Florent Leclercq, Alice Pisani and Benjamin D. Wandelt. 'Cosmology: from theory to data, from data to theory'. In: *Proc. Int. Sch. Phys. Fermi* 186 (2014). Ed. by A. Cooray, E. Komatsu, A. Melchiorri and L. Lamagna, pp. 189–233. DOI: 10.3254/978-1-61499-476-3-189. arXiv: 1403.1260 [astro-ph.CO] (cit. on pp. 32, 157, 162).

[148] Kendrick M. Smith, Oliver Zahn and Olivier Dore. 'Detection of Gravitational Lensing in the Cosmic Microwave Background'. In: *PRD* 76 (2007), p. 043510. DOI: 10.1103/PhysRevD.76.043510. arXiv: 0705.3980 [astro-ph] (cit. on pp. 32, 50, 95, 120, 161, 164).

[149] Christopher M. Hirata, Shirley Ho, Nikhil Padmanabhan, Uros Seljak and Neta A. Bahcall. 'Correlation of CMB with large-scale structure: II. Weak lensing'. In: *PRD* 78 (2008), p. 043520. DOI: 10.1103/PhysRevD.78.043520. arXiv: 0801.0644 [astro-ph] (cit. on p. 32).

[150] Sudeep Das et al. 'Detection of the Power Spectrum of Cosmic Microwave Background Lensing by the Atacama Cosmology Telescope'. In: *Phys. Rev. Lett.* 107 (2011), p. 021301. DOI: 10.1103/PhysRevLett.107.021301. arXiv: 1103.2124 [astro-ph.CO] (cit. on p. 32).

[151] A. van Engelen et al. 'A measurement of gravitational lensing of the microwave background using South Pole Telescope data'. In: *Astrophys. J.* 756 (2012), p. 142. DOI: 10.1088/0004-637X/756/2/142. arXiv: 1202.0546 [astro-ph.CO] (cit. on p. 32).

[152] P. A. R. Ade et al. 'Measurement of the Cosmic Microwave Background Polarization Lensing Power Spectrum with the POLARBEAR experiment'. In: *Phys. Rev. Lett.* 113 (2014), p. 021301. DOI: 10.1103/PhysRevLett.113.021301. arXiv: 1312.6646 [astro-ph.CO] (cit. on p. 32).

[153] K. T. Story et al. 'A Measurement of the Cosmic Microwave Background Gravitational Lensing Potential from 100 Square Degrees of SPTpol Data'. In: *Astrophys. J.* 810.1 (2015), p. 50. DOI: 10.1088/0004-637X/810/1/50. arXiv: 1412.4760 [astro-ph.CO] (cit. on pp. 32, 43, 50, 54, 95, 96).

[154] P. A. R. Ade et al. 'BICEP2 / Keck Array VIII: Measurement of gravitational lensing from large-scale B-mode polarization'. In: *Astrophys. J.* 833.2 (2016), p. 228. DOI: 10.3847/1538-4357/833/2/228. arXiv: 1606.01968 [astro-ph.CO] (cit. on pp. 33, 51).

[155] Ethan Anderes, Benjamin Wandelt and Guilhem Lavaux. 'Bayesian inference of CMB gravitational lensing'. In: *ApJ* 808.2 (2015), p. 152. DOI: 10.1088/0004-637X/808/2/152. arXiv: 1412.4079 [astro-ph.CO] (cit. on p. 34).

[156] M. Millea et al. 'Optimal CMB Lensing Reconstruction and Parameter Estimation with SPTpol Data'. In: (Dec. 2020). arXiv: 2012.01709 [astro-ph.CO] (cit. on p. 34).

[157] Robert G. Parr. *Density-functional theory of atoms and molecules*. eng. Oxford University Press ; 1989 - 1989 (cit. on p. 34).

[158] Duncan Hanson, Anthony Challinor and Antony Lewis. 'Weak lensing of the CMB'. In: *Gen. Rel. Grav.* 42 (2010), pp. 2197–2218. DOI: 10.1007/s10714-010-1036-y. arXiv: 0911.0612 [astro-ph.CO] (cit. on pp. 35–37, 43, 45, 95).

[159] W.H. Press, S.A. Teukolsky, W.T. Vetterling and B.P. Flannery. *Numerical Recipes: The Art of Scientific Computing*. 3rd ed. Cambridge University Press, 2007. ISBN: 9780521880688 (cit. on pp. 35, 161, 162).

[160] Julien Carron and Antony Lewis. 'Maximum a posteriori CMB lensing reconstruction'. In: *PRD* 96.6 (2017), p. 063510. DOI: 10.1103/PhysRevD.96.063510. arXiv: 1704.08230 [astro-ph.CO] (cit. on pp. 36, 43, 68).

[161] Christopher M. Hirata and Uros Seljak. 'Reconstruction of lensing from the cosmic microwave background polarization'. In: *PRD* 68 (2003), p. 083002. DOI: 10.1103/PhysRevD.68.083002. arXiv: astro-ph/0306354 [astro-ph] (cit. on pp. 36, 43, 44, 52, 68, 104).

[162] Christopher M. Hirata and Uros Seljak. 'Analyzing weak lensing of the cosmic microwave background using the likelihood function'. In: *PRD* 67 (2003), p. 043001. DOI: 10.1103/PhysRevD.67.043001. arXiv: astro-ph/0209489 [astro-ph] (cit. on pp. 37, 43, 45).

[163] Matthias Bartelmann and Peter Schneider. 'Weak gravitational lensing'. In: *Phys. Rept.* 340 (2001), pp. 291–472. DOI: 10.1016/S0370-1573(00)00082-X. arXiv: astro-ph/9912508 (cit. on p. 37).

[164] Giulio Fabbian, Antony Lewis and Dominic Beck. 'CMB lensing reconstruction biases in cross-correlation with large-scale structure probes'. In: *JCAP* 10 (2019), p. 057. DOI: 10.1088/1475-7516/2019/10/057. arXiv: 1906.08760 [astro-ph.CO] (cit. on pp. 37, 56).

[165] Ellie Kitanidis and Martin White. 'Cross-Correlation of Planck CMB Lensing with DESI-Like LRGs'. In: *Mon. Not. Roy. Astron. Soc.* 501.4 (2021), pp. 6181–6198. DOI: 10.1093/mnras/staa3927. arXiv: 2010.04698 [astro-ph.CO] (cit. on p. 37).

[166] Duncan Hanson, Anthony Challinor, George Efstathiou and Pawel Bielewicz. 'CMB temperature lensing power reconstruction'. In: *PRD* 83.4, 043005 (Feb. 2011), p. 043005. DOI: 10.1103/PhysRevD.83.043005. arXiv: 1008.4403 [astro-ph.CO] (cit. on pp. 38, 96).

[167] Ethan Anderes. 'Decomposing CMB lensing power with simulation'. In: *PRD* 88 (Oct. 2013), p. 083517. DOI: 10.1103/PhysRevD.88.083517. arXiv: 1301.2576 [astro-ph.IM] (cit. on p. 38).

[168] Julien Peloton, Marcel Schmittfull, Antony Lewis, Julien Carron and Oliver Zahn. 'Full covariance of CMB and lensing reconstruction power spectra'. In: *PRD* 95.4 (2017), p. 043508. DOI: 10.1103/PhysRevD.95.043508. arXiv: 1611.01446 [astro-ph.CO] (cit. on p. 39).

[169] Toshiya Namikawa, Duncan Hanson and Ryuichi Takahashi. 'Bias-hardened CMB lensing'. In: *MNRAS* 431.1 (May 2013), pp. 609–620. DOI: 10.1093/mnras/stt195. arXiv: 1209.0091 [astro-ph.CO] (cit. on pp. 39, 113).

[170] Blake D. Sherwin et al. 'Two-season Atacama Cosmology Telescope polarimeter lensing power spectrum'. In: *PRD* 95.12 (2017), p. 123529. DOI: 10.1103/PhysRevD.95.123529. arXiv: 1611.09753 [astro-ph.CO] (cit. on pp. 43, 51, 114).

[171] P. A. R. Ade et al. 'A Measurement of the Cosmic Microwave Background B-Mode Polarization Power Spectrum at Sub-Degree Scales from 2 years of POLARBEAR Data'. In: *Astrophys. J.* 848.2 (2017), p. 121. DOI: 10.3847/1538-4357/aa8e9f. arXiv: 1705.02907 [astro-ph.CO] (cit. on pp. 43, 70, 71, 80, 113).

[172] Takemi Okamoto and Wayne Hu. 'CMB lensing reconstruction on the full sky'. In: *PRD* 67 (2003), p. 083002. DOI: 10.1103/PhysRevD.67.083002. arXiv: astro-ph/0301031 [astro-ph] (cit. on pp. 43, 45).

[173] Duncan Hanson, Anthony Challinor, George Efstathiou and Pawel Bielewicz. 'CMB temperature lensing power reconstruction'. In: *PRD* 83 (2011), p. 043005. arXiv: 1008.4403 [astro-ph.CO] (cit. on pp. 45, 54, 60).

[174] Marcel M. Schmittfull, Anthony Challinor, Duncan Hanson and Antony Lewis. 'On the joint analysis of CMB temperature and lensing-reconstruction power spectra'. In: *PRD* 88 (2013), p. 063012. DOI: 10.1103/PhysRevD.88.063012. arXiv: 1308.0286 [astro-ph.CO] (cit. on p. 46).

[175] Jason R. Stevens et al. 'Designs for next generation CMB survey strategies from Chile'. In: *Proc. SPIE Int. Soc. Opt. Eng.* 10708 (2018), p. 1070841. DOI: 10.1117/12.2313898. arXiv: 1808.05131 [astro-ph.IM] (cit. on pp. 48, 73).

[176] K. M. Gorski et al. 'HEALPix - A Framework for high resolution discretization, and fast analysis of data distributed on the sphere'. In: *Astrophys. J.* 622 (2005), pp. 759–771. DOI: 10.1086/427976. arXiv: astro-ph/0409513 (cit. on pp. 48, 80, 145).

[177] J. D. Hunter. 'Matplotlib: A 2D Graphics Environment'. In: *Computing in Science & Engineering* 9.3 (2007), pp. 90–95. DOI: 10.1109/MCSE.2007.55 (cit. on p. 49).

[178] Aurelien Benoit-Levy, Typhaine Dechelette, Karim Benabed, Jean-Francois Cardoso, Duncan Hanson et al. 'Full-sky CMB lensing reconstruction in presence of sky-cuts'. In: *A&A* 555 (July 2013), A37. DOI: 10.1051/0004-6361/201321048. arXiv: 1301.4145 [astro-ph.CO] (cit. on pp. 50, 57, 122, 144).

[179] Ruth Pearson, Blake Sherwin and Antony Lewis. 'CMB lensing reconstruction using cut sky polarization maps and pure-B modes'. In: *Phys. Rev.* D90.2 (2014), p. 023539. DOI: 10.1103/PhysRevD.90.023539. arXiv: 1403.3911 [astro-ph.CO] (cit. on p. 51).

[180] S. Plaszczynski, A. Lavabre, L. Perotto and J-L Starck. 'A hybrid approach to CMB lensing reconstruction on all-sky intensity maps'. In: *Astron. Astrophys.* 544 (2012), A27. DOI: 10.1051/0004-6361/201218899. arXiv: 1201.5779 [astro-ph.CO] (cit. on p. 58).

[181] Toshiya Namikawa and Ryo Nagata. 'Lensing reconstruction from a patchwork of polarization maps'. In: *JCAP* 1409 (2014), p. 009. DOI: 10.1088/1475-7516/2014/09/009. arXiv: 1405.6568 [astro-ph.CO] (cit. on p. 58).

[182] Moritz Münchmeyer and Kendrick M. Smith. 'Fast Wiener filtering of CMB maps with Neural Networks'. In: (2019). arXiv: 1905.05846 [astro-ph.CO] (cit. on p. 65).

[183] Wayne Hu, Matthew M. Hedman and Matias Zaldarriaga. 'Benchmark parameters for CMB polarization experiments'. In: *Phys. Rev. D* 67 (2003), p. 043004. DOI: 10.1103/PhysRevD.67.043004. arXiv: astro-ph/0210096 (cit. on p. 70).

[184] N. J. Miller, M. Shimon and B. G. Keating. 'CMB Beam Systematics: Impact on Lensing Parameter Estimation'. In: *Phys. Rev.* D79 (2009), p. 063008. DOI: 10.1103/PhysRevD.79.063008. arXiv: 0806.3096 [astro-ph] (cit. on pp. 70, 77, 82).

[185] Meng Su, Amit P.S. Yadav and Matias Zaldarriaga. 'Impact of Instrumental Systematic Contamination on the Lensing Mass Reconstruction using the CMB Polarization'. In: *Phys. Rev. D* 79 (2009), p. 123002. DOI: 10.1103/PhysRevD.79.123002. arXiv: 0901.0285 [astro-ph.CO] (cit. on pp. 70, 82).

[186] L. Pagano, J.-M. Delouis, S. Mottet, J.-L. Puget and L. Vibert. 'Reionization optical depth determination from Planck HFI data with ten percent accuracy'. In: *Astron. Astrophys.* 635 (2020), A99. DOI: 10.1051/0004-6361/201936630. arXiv: 1908.09856 [astro-ph.CO] (cit. on p. 70).

[187] Kevin T. Crowley et al. 'Studies of systematic uncertainties for Simons Observatory: detector array effects'. In: *Proc. SPIE Int. Soc. Opt. Eng.* 10708 (2018), 107083Z. DOI: 10.1117/12.2313414. arXiv: 1808.10491 [astro-ph.IM] (cit. on pp. 70, 71, 80, 90–92).

[188] M. A. O. Aguilar Faúndez et al. 'Measurement of the Cosmic Microwave Background Polarization Lensing Power Spectrum from Two Years of POLARBEAR Data'. In: *Astrophys. J.* 893 (2020), p. 85. DOI: 10.3847/1538-4357/ab7e29. arXiv: 1911.10980 [astro-ph.CO] (cit. on p. 70).

[189] Giulio Fabbian and Julien Peloton. 'Simulating instrumental systematics of Cosmic Microwave Background experiments with s4cmb'. In: *J. Open Source Softw.* 6.60 (2021), p. 3022. DOI: 10.21105/joss.03022. arXiv: 2104.11816 [astro-ph.IM] (cit. on p. 71).

[190] Patricio A. Gallardo et al. 'Studies of Systematic Uncertainties for Simons Observatory: Optical Effects and Sensitivity Considerations'. In: *Proc. SPIE Int. Soc. Opt. Eng.* 10708 (2018). Ed. by George Z. Angeli and Philippe Dierickx, 107083Y. DOI: 10.1117/12.2312971. arXiv: 1808.05152 [astro-ph.IM] (cit. on pp. 71, 80).

[191] Maria Salatino et al. 'Studies of systematic uncertainties for Simons Observatory: polarization modulator related effects'. In: *Millimeter, Submillimeter, and Far-Infrared Detectors and Instrumentation for Astronomy IX*. Ed. by Jonas Zmuidzinas and Jian-Rong Gao. Vol. 10708. Society of Photo-Optical Instrumentation Engineers (SPIE) Conference Series. July 2018, p. 1070848. DOI: 10.1117/12.2312993. arXiv: 1808.07442 [astro-ph.IM] (cit. on p. 71).

[192] P.A.R. Ade et al. 'A Measurement of the Cosmic Microwave Background B-Mode Polarization Power Spectrum at Sub-Degree Scales with POLARBEAR'. In: *Astrophys. J.* 794.2 (2014), p. 171. DOI: 10.1088/0004-637X/794/2/171. arXiv: 1403.2369 [astro-ph.CO] (cit. on pp. 71, 82, 85, 89).

[193] Max Tegmark. 'CMB mapping experiments: A designer's guide'. In: *Phys. Rev. D* 56 (8 1997), pp. 4514–4529. DOI: 10.1103/PhysRevD.56.4514 (cit. on p. 72).

[194] Radek Stompor et al. 'Making maps of the cosmic microwave background: The MAXIMA example'. In: *Phys. Rev.* D65 (2001), p. 022003. DOI: 10.1103/PhysRevD.65.022003. arXiv: astro-ph/0106451 [astro-ph] (cit. on p. 72).

[195] William C. Jones et al. 'Instrumental and Analytic Methods for Bolometric Polarimetry'. In: *Astron. Astrophys.* 470 (2007), p. 771. DOI: 10.1051/0004-6361:20065911. arXiv: astro-ph/0606606 (cit. on p. 72).

[196] Davide Poletti et al. 'Making maps of Cosmic Microwave Background polarization for B-mode studies: the POLARBEAR example'. In: *Astron. Astrophys.* 600 (2017), A60. DOI: 10.1051/0004-6361/201629467. arXiv: 1608.01624 [astro-ph.IM] (cit. on p. 72).

[197] R. Adam et al. 'Planck 2015 results. VIII. High Frequency Instrument data processing: Calibration and maps'. In: *Astron. Astrophys.* 594 (2016), A8. DOI: 10.1051/0004-6361/201525820. arXiv: 1502.01587 [astro-ph.CO] (cit. on pp. 72, 117).

[198] Christopher G. R. Wallis, A. Bonaldi, Michael L. Brown and Richard A. Battye. 'A new map-making algorithm for CMB polarization experiments'. In: *Mon. Not. Roy. Astron. Soc.* 453.2 (2015), pp. 2058–2069. DOI: 10.1093/mnras/stv1689. arXiv: 1503.03285 [astro-ph.CO] (cit. on p. 72).

[199] J.-M. Delouis, L. Pagano, S. Mottet, J.-L. Puget and L. Vibert. 'SRoll2: an improved mapmaking approach to reduce large-scale systematic effects in the Planck High Frequency Instrument legacy maps'. In: *Astron. Astrophys.* 629 (2019), A38. DOI: 10.1051/0004-6361/201834882. arXiv: 1901.11386 [astro-ph.CO] (cit. on p. 72).

[200] Kevork Abazajian et al. 'CMB-S4: Forecasting Constraints on Primordial Gravitational Waves'. In: (Aug. 2020). arXiv: 2008.12619 [astro-ph.CO] (cit. on p. 73).

[201] Daniel B. Thomas, Nialh McCallum and Michael L. Brown. 'Controlling systematics in ground-based CMB surveys with partial boresight rotation'. In: *Mon. Not. Roy. Astron. Soc.* 491.2 (2020), pp. 1960–1969. DOI: 10.1093/mnras/stz2607. arXiv: 1905.12647 [astro-ph.CO] (cit. on pp. 73, 106).

[202] Jon E. Gudmundsson et al. 'The Simons Observatory: modeling optical systematics in the Large Aperture Telescope'. In: *Appl. Opt.* 60.4 (2021), pp. 823–837. DOI: 10.1364/AO.411533. arXiv: 2009.10138 [astro-ph.IM] (cit. on pp. 74, 80).

[203] Charles A. Hill et al. 'BoloCalc: a sensitivity calculator for the design of Simons Observatory'. In: *Proc. SPIE Int. Soc. Opt. Eng.* 10708 (2018). Ed. by George Z. Angeli and Philippe Dierickx, p. 1070842. DOI: 10.1117/12.2313916. arXiv: 1806.04316 [astro-ph.IM] (cit. on p. 75).

[204] Sean A. Bryan et al. 'Modeling and characterization of the SPIDER half-wave plate'. In: ed. by Andrew D. Holland. Vol. 7741. 2010, 77412B. DOI: 10.1117/12.857837. arXiv: 1006.3874 [astro-ph.IM] (cit. on p. 76).

[205] A. Kusaka et al. 'Modulation of cosmic microwave background polarization with a warm rapidly rotating half-wave plate on the Atacama B-Mode Search instrument'. In: *Rev. Sci. Instrum.* 85 (2014), p. 024501. DOI: 10.1063/1.4862058. arXiv: 1310.3711 [astro-ph.IM] (cit. on p. 76).

[206] G. D'Alessandro et al. 'Systematic effects induced by half-wave plate precession into measurements of the cosmic microwave background polarization'. In: *Astron. Astrophys.* 627 (2019), A160. DOI: 10.1051/0004-6361/201834495. arXiv: 1906.07010 [astro-ph.IM] (cit. on p. 76).

[207] Christopher G. R. Wallis, Michael L. Brown, Richard A. Battye, Giampaolo Pisano and Luca Lamagna. 'Removing beam asymmetry bias in precision CMB temperature and polarization experiments'. In: *Mon. Not. Roy. Astron. Soc.* 442.3 (2014), pp. 1963–1979.

DOI: 10.1093/mnras/stu856. arXiv: 1401.2075 [astro-ph.CO] (cit. on p. 77).

[208] Eric Hivon, Sylvain Mottet and Nicolas Ponthieu. 'QuickPol: Fast calculation of effective beam matrices for CMB polarization'. In: *Astron. Astrophys.* 598 (2017), A25. DOI: 10.1051/0004-6361/201629626. arXiv: 1608.08833 [astro-ph.CO] (cit. on p. 77).

[209] S. Mitra et al. 'Fast Pixel Space Convolution for CMB Surveys with Asymmetric Beams and Complex Scan Strategies: FEBeCoP'. In: *Astrophys. J. Suppl.* 193 (2011), p. 5. DOI: 10.1088/0067-0049/193/1/5. arXiv: 1005.1929 [astro-ph.CO] (cit. on p. 77).

[210] P.A.R. Ade et al. 'BICEP2 III: Instrumental Systematics'. In: *Astrophys. J.* 814.2 (2015), p. 110. DOI: 10.1088/0004-637X/814/2/110. arXiv: 1502.00608 [astro-ph.IM] (cit. on p. 77).

[211] BICEP2 Collaboration, Keck Array Collaboration, P. A. R. Ade et al. 'BICEP2/Keck Array XI: Beam Characterization and Temperature-to-Polarization Leakage in the BK15 Data Set'. In: *ApJ* 884.2, 114 (Oct. 2019), p. 114. DOI: 10.3847/1538-4357/ab391d. arXiv: 1904.01640 [astro-ph.IM] (cit. on p. 80).

[212] Matthew Hasselfield et al. 'The Atacama Cosmology Telescope: Beam Measurements and the Microwave Brightness Temperatures of Uranus and Saturn'. In: *Astrophys. J. Suppl.* 209 (2013), p. 17. DOI: 10.1088/0067-0049/209/1/17. arXiv: 1303.4714 [astro-ph.IM] (cit. on pp. 80, 110).

[213] Charles R. Harris, K. Jarrod Millman, St'efan J. van der Walt, Ralf Gommers, Pauli Virtanen, David Cournapeau et al. 'Array programming with NumPy'. In: *Nature* 585.7825 (Sept. 2020), pp. 357–362. DOI: 10.1038/s41586-020-2649-2 (cit. on p. 81).

[214] Pauli Virtanen, Ralf Gommers, Travis E. Oliphant, Matt Haberland, Tyler Reddy, David Cournapeau et al. 'SciPy 1.0: Fundamental Algorithms for Scientific Computing in Python'. In: *Nature Methods* 17 (2020), pp. 261–272. DOI: 10.1038/s41592-019-0686-2 (cit. on p. 81).

[215] Brian G. Keating, Meir Shimon and Amit P. S. Yadav. 'Self-calibration of Cosmic Microwave Background Polarization Experiments'. In: *ApJ* 762.2, L23 (Jan. 2013),

p. L23. DOI: 10.1088/2041-8205/762/2/L23. arXiv: 1211.5734 [astro-ph.CO] (cit. on pp. 85, 86, 99, 112).

[216] Maximilian H. Abitbol et al. 'The Simons Observatory: gain, bandpass and polarization-angle calibration requirements for B-mode searches'. In: *JCAP* 05 (2021), p. 032. DOI: 10.1088/1475-7516/2021/05/032. arXiv: 2011.02449 [astro-ph.CO] (cit. on p. 85).

[217] Marc Kamionkowski, Arthur Kosowsky and Albert Stebbins. 'Statistics of cosmic microwave background polarization'. In: *Phys. Rev. D* 55 (12 1997), pp. 7368–7388. DOI: 10.1103/PhysRevD.55.7368 (cit. on p. 85).

[218] Nathan F. Lepora. 'Cosmological birefringence and the microwave background'. In: (Dec. 1998). arXiv: gr-qc/9812077 (cit. on p. 85).

[219] Arthur Lue, Li-Min Wang and Marc Kamionkowski. 'Cosmological signature of new parity violating interactions'. In: *Phys. Rev. Lett.* 83 (1999), pp. 1506–1509. DOI: 10.1103/PhysRevLett.83.1506. arXiv: astro-ph/9812088 (cit. on p. 85).

[220] A. Ferté and J. Grain. 'Detecting chiral gravity with the pure pseudospectrum reconstruction of the cosmic microwave background polarized anisotropies'. In: *Phys. Rev. D* 89.10 (2014), p. 103516. DOI: 10.1103/PhysRevD.89.103516. arXiv: 1404.6660 [astro-ph.CO] (cit. on p. 85).

[221] Luca Pagano et al. 'CMB Polarization Systematics, Cosmological Birefringence and the Gravitational Waves Background'. In: *Phys. Rev. D* 80 (2009), p. 043522. DOI: 10.1103/PhysRevD.80.043522. arXiv: 0905.1651 [astro-ph.CO] (cit. on p. 85).

[222] P.A.R. Ade et al. 'A Measurement of the Cosmic Microwave Background B-Mode Polarization Power Spectrum at Sub-Degree Scales with POLARBEAR'. In: *Astrophys. J.* 794.2 (2014), p. 171. DOI: 10.1088/0004-637X/794/2/171. arXiv: 1403.2369 [astro-ph.CO] (cit. on pp. 86, 107, 110).

[223] BICEP2 Collaboration, P. A. R. Ade et al. 'Detection of B-Mode Polarization at Degree Angular Scales by BICEP2'. In: *PRL* 112.24, 241101 (June 2014), p. 241101. DOI: 10.1103/PhysRevLett.112.241101. arXiv: 1403.3985 [astro-ph.CO] (cit. on p. 86).

[224] R.J. Thornton et al. 'The Atacama Cosmology Telescope: The polarization-sensitive ACTPol instrument'. In: *Astrophys. J. Suppl.* 227.2 (2016), p. 21. DOI:

10.3847/1538-4365/227/2/21. arXiv: 1605.06569 [astro-ph.IM] (cit. on p. 86).

[225] F. Bianchini, W. L. K. Wu, P. A. R. Ade, A. J. Anderson, J. E. Austermann, J. S. Avva et al. 'Searching for anisotropic cosmic birefringence with polarization data from SPTpol'. In: *PRD* 102.8, 083504 (Oct. 2020), p. 083504. DOI: 10.1103/PhysRevD.102.083504. arXiv: 2006.08061 [astro-ph.CO] (cit. on p. 86).

[226] S. Adachi et al. 'A Measurement of the Degree Scale CMB B-mode Angular Power Spectrum with POLARBEAR'. In: *Astrophys. J.* 897.1 (2020), p. 55. DOI: 10.3847/1538-4357/ab8f24. arXiv: 1910.02608 [astro-ph.CO] (cit. on p. 87).

[227] J.T. Sayre et al. 'Measurements of B-mode Polarization of the Cosmic Microwave Background from 500 Square Degrees of SPTpol Data'. In: *Phys. Rev. D* 101.12 (2020), p. 122003. DOI: 10.1103/PhysRevD.101.122003. arXiv: 1910.05748 [astro-ph.CO] (cit. on p. 89).

[228] M.A. Dobbs et al. 'Frequency Multiplexed SQUID Readout of Large Bolometer Arrays for Cosmic Microwave Background Measurements'. In: *Rev. Sci. Instrum.* 83 (2012), p. 073113. DOI: 10.1063/1.4737629. arXiv: 1112.4215 [astro-ph.IM] (cit. on pp. 90, 91).

[229] B. Dober et al. 'A microwave SQUID multiplexer optimized for bolometric applications'. In: *Appl. Phys. Lett.* 118.6 (2021), p. 062601. DOI: 10.1063/5.0033416. arXiv: 2010.07998 [astro-ph.IM] (cit. on pp. 90, 91).

[230] K. Hattori et al. 'Development of readout electronics for POLARBEAR-2 Cosmic Microwave Background experiment'. In: *J. Low Temp. Phys.* 184.1-2 (2016). Ed. by Philippe Camus, Alexandre Juillard and Alessandro Monfardini, pp. 512–518. DOI: 10.1007/s10909-015-1448-x. arXiv: 1512.07663 [astro-ph.IM] (cit. on p. 90).

[231] A.N. Bender et al. 'On-Sky Performance of the SPT-3G Frequency-Domain Multiplexed Readout'. In: *J. Low Temp. Phys.* 199.1-2 (2019), pp. 182–191. DOI: 10.1007/s10909-019-02280-w. arXiv: 1907.10947 [astro-ph.IM] (cit. on p. 90).

[232] J. A. B. Mates et al. 'Crosstalk in microwave SQUID multiplexers'. In: *Applied Physics Letters* 115.20 (2019), p. 202601. DOI: 10.1063/1.5116573. eprint: https://doi.org/10.1063/1.5116573 (cit. on p. 91).

[233] R. Adam et al. 'Planck 2015 results VII. High Frequency Instrument data processing: Time-ordered information and beams'. In: *Astron. Astrophys.* 594 (2016), A7. DOI: 10.1051/0004-6361/201525844. arXiv: 1502.01586 [astro-ph.IM] (cit. on p. 94).

[234] N. Aghanim et al. 'Planck intermediate results. XLVI. Reduction of large-scale systematic effects in HFI polarization maps and estimation of the reionization optical depth'. In: *Astron. Astrophys.* 596 (2016), A107. DOI: 10.1051/0004-6361/201628890. arXiv: 1605.02985 [astro-ph.CO] (cit. on p. 94).

[235] K. Arnold et al. 'The bolometric focal plane array of the Polarbear CMB experiment'. In: vol. 8452. 2012, p. 84521D. DOI: 10.1117/12.927057. arXiv: 1210.7877 [astro-ph.IM] (cit. on p. 94).

[236] E. Hivon et al. 'MASTER of the CMB Anisotropy Power Spectrum: A Fast Method for Statistical Analysis of Large and Complex CMB Data Sets'. In: *ApJ* 567 (Mar. 2002), pp. 2–17. DOI: 10.1086/338126. arXiv: astro-ph/0105302 (cit. on pp. 97, 145).

[237] David Alonso, Javier Sanchez, Anže Slosar and LSST Dark Energy Science Collaboration. 'A unified pseudo-C_ℓ framework'. In: *MNRAS* 484.3 (Apr. 2019), pp. 4127–4151. DOI: 10.1093/mnras/stz093. arXiv: 1809.09603 [astro-ph.CO] (cit. on pp. 97, 145).

[238] J.W. Henning et al. 'Measurements of the Temperature and E-Mode Polarization of the CMB from 500 Square Degrees of SPTpol Data'. In: *Astrophys. J.* 852.2 (2018), p. 97. DOI: 10.3847/1538-4357/aa9ff4. arXiv: 1707.09353 [astro-ph.CO] (cit. on pp. 104, 110).

[239] Asantha Cooray and Wayne Hu. 'Second order corrections to weak lensing by large scale structure'. In: *ApJ* 574 (2002), p. 19. DOI: 10.1086/340892. arXiv: astro-ph/0202411 [astro-ph] (cit. on p. 104).

[240] Geraint Pratten and Antony Lewis. 'Impact of post-Born lensing on the CMB'. In: *JCAP* 1608.08 (2016), p. 047. DOI: 10.1088/1475-7516/2016/08/047. arXiv: 1605.05662 [astro-ph.CO] (cit. on p. 104).

[241] Giulio Fabbian, Matteo Calabrese and Carmelita Carbone. 'CMB weak-lensing beyond the Born approximation: a numerical approach'. In: *JCAP* 02 (2018), p. 050. DOI: 10.1088/1475-7516/2018/02/050. arXiv: 1702.03317 [astro-ph.CO] (cit. on p. 104).

[242] Toshiya Namikawa, Daisuke Yamauchi and Atsushi Taruya. 'Full-sky lensing reconstruction of gradient and curl modes from CMB maps'. In: *JCAP* 1201 (2012), p. 007. DOI: 10.1088/1475-7516/2012/01/007. arXiv: 1110.1718 [astro-ph.CO] (cit. on p. 104).

[243] Nialh McCallum, Daniel B. Thomas, Michael L. Brown and Nicolas Tessore. 'Spin characterization of systematics in CMB surveys – a comprehensive formalism'. In: *Mon. Not. Roy. Astron. Soc.* 501.1 (2021), pp. 802–832. DOI: 10.1093/mnras/staa3609. arXiv: 2008.00011 [astro-ph.CO] (cit. on pp. 106, 107).

[244] Christopher Sheehy. 'Deprojecting beam systematics for next-generation CMB B-mode searches'. In: (Nov. 2019). arXiv: 1911.03547 [astro-ph.IM] (cit. on p. 107).

[245] Mathew S. Madhavacheril, Kendrick M. Smith, Blake D. Sherwin and Sigurd Naess. 'CMB lensing power spectrum estimation without instrument noise bias'. In: *Journal of Cosmology and Astroparticle Physics* 2021.05 (2021), p. 028. DOI: 10.1088/1475-7516/2021/05/028. arXiv: 2011.02475 [astro-ph.CO] (cit. on pp. 107, 113).

[246] Duncan Hanson, Antony Lewis and Anthony Challinor. 'Asymmetric Beams and CMB Statistical Anisotropy'. In: *PRD* 81 (2010), p. 103003. arXiv: 1003.0198 [astro-ph.CO] (cit. on p. 108).

[247] Amir Hajian, Viviana Acquaviva, Peter A. R. Ade, Paula Aguirre, Mandana Amiri, John William Appel et al. 'The Atacama Cosmology Telescope: Calibration with the Wilkinson Microwave Anisotropy Probe Using Cross-correlations'. In: *ApJ* 740.2, 86 (Oct. 2011), p. 86. DOI: 10.1088/0004-637X/740/2/86. arXiv: 1009.0777 [astro-ph.CO] (cit. on p. 113).

[248] Thibaut Louis et al. 'The Atacama Cosmology Telescope: Cross Correlation with Planck maps'. In: *JCAP* 07 (2014), p. 016. DOI: 10.1088/1475-7516/2014/07/016. arXiv: 1403.0608 [astro-ph.CO] (cit. on p. 113).

[249] Steve K. Choi et al. 'The Atacama Cosmology Telescope: a measurement of the Cosmic Microwave Background power spectra at 98 and 150 GHz'. In: *JCAP* 12 (2020), p. 045.

DOI: 10.1088/1475-7516/2020/12/045. arXiv: 2007.07289 [astro-ph.CO] (cit. on p. 113).

[250] Blake D. Sherwin and Sudeep Das. 'CMB Lensing - Power Without Bias'. In: (Nov. 2010). arXiv: 1011.4510 [astro-ph.CO] (cit. on p. 113).

[251] Giancarlo de Gasperis, Alessandro Buzzelli, Paolo Cabella, Paolo de Bernardis and Nicola Vittorio. 'Optimal cosmic microwave background map-making in the presence of cross-correlated noise'. In: *Astron. Astrophys.* 593 (2016), A15. DOI: 10.1051/0004-6361/201628143. arXiv: 1601.04464 [astro-ph.CO] (cit. on p. 114).

[252] L. Perotto, J. Bobin, S. Plaszczynski, J. L. Starck and A. Lavabre. 'Reconstruction of the cosmic microwave background lensing for Planck'. In: *A&A* 519, A4 (Sept. 2010), A4. DOI: 10.1051/0004-6361/200912001 (cit. on p. 117).

[253] P. A. R. Ade et al. 'Planck 2013 results. VIII. HFI photometric calibration and mapmaking'. In: *Astron. Astrophys.* 571 (2014), A8. DOI: 10.1051/0004-6361/201321538. arXiv: 1303.5069 [astro-ph.CO] (cit. on p. 117).

[254] N. Aghanim et al. 'Planck 2018 results. III. High Frequency Instrument data processing and frequency maps'. In: *Astron. Astrophys.* 641 (2020), A3. DOI: 10.1051/0004-6361/201832909. arXiv: 1807.06207 [astro-ph.CO] (cit. on p. 117).

[255] Y. Akrami et al. '*Planck* intermediate results. LVII. Joint Planck LFI and HFI data processing'. In: *Astron. Astrophys.* 643 (2020), A42. DOI: 10.1051/0004-6361/202038073. arXiv: 2007.04997 [astro-ph.CO] (cit. on pp. 117, 118).

[256] Jacques Delabrouille, J. F. Cardoso and G. Patanchon. 'Multi-detector multi-component spectral matching and applications for CMB data analysis'. In: *Mon. Not. Roy. Astron. Soc.* 346 (2003), p. 1089. DOI: 10.1111/j.1365-2966.2003.07069.x. arXiv: astro-ph/0211504 (cit. on pp. 118, 141).

[257] Jean-Francois Cardoso, Maude Martin, Jacques Delabrouille, Marc Betoule and Guillaume Patanchon. 'Component separation with flexible models. Application to the separation of astrophysical emissions'. In: (Mar. 2008). arXiv: 0803.1814 [astro-ph] (cit. on pp. 118, 141).

[258] P. A. R. Ade et al. 'Planck 2013 results. XII. Diffuse component separation'. In: *Astron. Astrophys.* 571 (2014), A12. DOI: 10.1051/0004-6361/201321580. arXiv: 1303.5072 [astro-ph.CO] (cit. on pp. 118, 141).

[259] Andrea Zonca et al. 'healpy: equal area pixelization and spherical harmonics transforms for data on the sphere in Python'. In: *Journal of Open Source Software* 4.35 (2019), p. 1298. DOI: 10.21105/joss.01298 (cit. on p. 119).

[260] J. N. Goldberg, A. J. Macfarlane, E. T. Newman, F. Rohrlich and E. C. G. Sudarshan. 'Spin-s Spherical Harmonics and ð'. In: *Journal of Mathematical Physics* 8.11 (1967), pp. 2155–2161. DOI: 10.1063/1.1705135. eprint: https://doi.org/10.1063/1.1705135 (cit. on p. 120).

[261] Jesus Torrado and Antony Lewis. 'Cobaya: Code for Bayesian Analysis of hierarchical physical models'. In: *JCAP* 05 (2021), p. 057. DOI: 10.1088/1475-7516/2021/05/057. arXiv: 2005.05290 [astro-ph.IM] (cit. on p. 125).

[262] Antony Lewis. 'GetDist: a Python package for analysing Monte Carlo samples'. In: (2019). arXiv: 1910.13970 [astro-ph.IM] (cit. on p. 125).

[263] Florian Beutler et al. 'The 6dF Galaxy Survey: baryon acoustic oscillations and the local Hubble constant'. In: *MNRAS* 416.4 (Oct. 2011), pp. 3017–3032. DOI: 10.1111/j.1365-2966.2011.19250.x. arXiv: 1106.3366 [astro-ph.CO] (cit. on p. 125).

[264] Ashley J. Ross, Lado Samushia, Cullan Howlett, Will J. Percival, Angela Burden and Marc Manera. 'The clustering of the SDSS DR7 main Galaxy sample – I. A 4 per cent distance measure at $z = 0.15$'. In: *MNRAS* 449.1 (2015), pp. 835–847. DOI: 10.1093/mnras/stv154. arXiv: 1409.3242 [astro-ph.CO] (cit. on p. 125).

[265] Shadab Alam et al. 'The clustering of galaxies in the completed SDSS-III Baryon Oscillation Spectroscopic Survey: cosmological analysis of the DR12 galaxy sample'. In: *Mon. Not. Roy. Astron. Soc.* 470.3 (2017), pp. 2617–2652. DOI: 10.1093/mnras/stx721. arXiv: 1607.03155 [astro-ph.CO] (cit. on p. 125).

[266] M. Pettini and R. Cooke. 'A new, precise measurement of the primordial abundance of deuterium'. In: *MNRAS* 425 (Oct. 2012), pp. 2477–2486. DOI: 10.1111/j.1365-2966.2012.21665.x. arXiv: 1205.3785 (cit. on p. 127).

[267] Z. Pan, L. Knox and M. White. 'Dependence of the Cosmic Microwave Background Lensing Power Spectrum on the Matter Density'. In: *Mon. Not. Roy. Astron. Soc.* 445.3 (2014), pp. 2941–2945. DOI: 10.1093/mnras/stu1971. arXiv: 1406.5459 [astro-ph.CO] (cit. on p. 128).

[268] Lord Rayleigh F.R.S. 'X. On the electromagnetic theory of light'. In: *The London, Edinburgh, and Dublin Philosophical Magazine and Journal of Science* 12.73 (1881), pp. 81–101. DOI: 10.1080/14786448108627074. eprint: https://doi.org/10.1080/14786448108627074 (cit. on p. 132).

[269] K.R. Lang. *Essential Astrophysics*. Undergraduate Lecture Notes in Physics. Springer Berlin Heidelberg, 2013. ISBN: 9783642359637 (cit. on p. 132).

[270] D. La. 'The existence of a limiting wavelength for small-scale temperature fluctuations'. In: *ApJ* 341 (June 1989), pp. 575–578. DOI: 10.1086/167517 (cit. on p. 132).

[271] Fumio Takahara and Shin Sasaki. 'Effect of Rayleigh Scattering on Cosmic Microwave Background Anisotropies'. In: *Progress of Theoretical Physics* 86.5 (Nov. 1991), pp. 1021–1030. ISSN: 0033-068X. DOI: 10.1143/ptp/86.5.1021. eprint: https://academic.oup.com/ptp/article-pdf/86/5/1021/5430029/86-5-1021.pdf (cit. on p. 132).

[272] Qing-Juan Yu, David N. Spergel and Jeremiah P. Ostriker. 'Rayleigh scattering and microwave background fluctuations'. In: *Astrophys. J.* 558 (2001), pp. 23–28. DOI: 10.1086/322482. arXiv: astro-ph/0103149 (cit. on p. 132).

[273] Antony Lewis. 'Rayleigh scattering: blue sky thinking for future CMB observations'. In: *JCAP* 1308 (2013), p. 053. DOI: 10.1088/1475-7516/2013/08/053. arXiv: 1307.8148 [astro-ph.CO] (cit. on pp. 132–137, 146).

[274] Elham Alipour, Kris Sigurdson and Christopher M. Hirata. 'Effects of Rayleigh scattering on the CMB and cosmic structure'. In: *Phys. Rev.* D91.8 (2015), p. 083520. DOI: 10.1103/PhysRevD.91.083520. arXiv: 1410.6484 [astro-ph.CO] (cit. on pp. 132, 134).

[275] Elham Alipour Khayer. 'The Cosmic Neutrino Background and Effects of Rayleigh Scattering on the CMB and Cosmic Structure'. PhD thesis. British Columbia U., 2015. DOI: 10.14288/1.0216007 (cit. on p. 132).

[276] Benjamin Beringue, P. Daniel Meerburg, Joel Meyers and Nicholas Battaglia. 'Cosmology with Rayleigh Scattering of the Cosmic Microwave Background'. In: *JCAP*

01 (2021), p. 060. DOI: 10.1088/1475-7516/2021/01/060. arXiv: 2008.11688 [astro-ph.CO] (cit. on p. 132).

[277] William R. Coulton, Benjamin Beringue and P. Daniel Meerburg. 'Primordial information content of Rayleigh anisotropies'. In: *Phys. Rev. D* 103.4 (2021), p. 043501. DOI: 10.1103/PhysRevD.103.043501. arXiv: 2010.10481 [astro-ph.CO] (cit. on p. 132).

[278] Alexander Kramida and Yuri Ralchenko. *NIST Atomic Spectra Database, NIST Standard Reference Database 78*. en. 1999. DOI: 10.18434/T4W30F (cit. on p. 134).

[279] Hee-Won Lee. 'Exact low-energy expansion of the Rayleigh scattering cross-section by atomic hydrogen'. In: *Monthly Notices of the Royal Astronomical Society* 358.4 (Apr. 2005), pp. 1472–1476. ISSN: 0035-8711. DOI: 10.1111/j.1365-2966.2005.08859.x. eprint: https://academic.oup.com/mnras/article-pdf/358/4/1472/18660986/358-4-1472.pdf (cit. on p. 134).

[280] Peter J. Mohr, Barry N. Taylor and David B. Newell. 'CODATA Recommended Values of the Fundamental Physical Constants: 2006'. http://physics.nist.gov/cuu/Constants/codata.pdf. 2006 (cit. on p. 134).

[281] F.R. Bouchet et al. 'COrE (Cosmic Origins Explorer) A White Paper'. In: (2011). arXiv: 1102.2181 [astro-ph.CO] (cit. on p. 136).

[282] Philippe Andre et al. 'PRISM (Polarized Radiation Imaging and Spectroscopy Mission): A White Paper on the Ultimate Polarimetric Spectro-Imaging of the Microwave and Far-Infrared Sky'. In: *ArXiv e-prints* (2013). arXiv: 1306.2259 [astro-ph.CO] (cit. on p. 136).

[283] Shaul Hanany et al. 'PICO: Probe of Inflation and Cosmic Origins'. In: (Mar. 2019). arXiv: 1902.10541 [astro-ph.IM] (cit. on p. 136).

[284] Kiyotomo Ichiki. 'CMB foreground: A concise review'. In: *Progress of Theoretical and Experimental Physics* 2014.6, 06B109 (June 2014), 06B109. DOI: 10.1093/ptep/ptu065 (cit. on p. 137).

[285] Clive Dickinson. 'CMB foregrounds - A brief review'. In: *51st Rencontres de Moriond on Cosmology*. June 2016, pp. 53–62. arXiv: 1606.03606 [astro-ph.CO] (cit. on p. 137).

[286] E. Martinez-Gonzalez, J. M. Diego, P. Vielva and J. Silk. 'CMB power spectrum estimation and map reconstruction with the expectation - Maximization algorithm'. In: *Mon. Not. Roy. Astron. Soc.* 345 (2003), p. 1101. DOI: 10.1046/j.1365-2966.2003.06885.x. arXiv: astro-ph/0302094 (cit. on p. 141).

[287] S. M. Leach et al. 'Component separation methods for the Planck mission'. In: *Astron. Astrophys.* 491 (2008), pp. 597–615. DOI: 10.1051/0004-6361:200810116. arXiv: 0805.0269 [astro-ph] (cit. on p. 141).

[288] R. Fernández-Cobos, P. Vielva, R. B. Barreiro and E. Martínez-González. 'Multiresolution internal template cleaning: an application to the Wilkinson Microwave Anisotropy Probe 7-yr polarization data'. In: *MNRAS* 420.3 (Mar. 2012), pp. 2162–2169. DOI: 10.1111/j.1365-2966.2011.20182.x. arXiv: 1106.2016 [astro-ph.CO] (cit. on p. 141).

[289] P. A. R. Ade et al. 'Planck 2015 results. XII. Full Focal Plane simulations'. In: *Astron. Astrophys.* 594 (2016), A12. DOI: 10.1051/0004-6361/201527103. arXiv: 1509.06348 [astro-ph.CO] (cit. on p. 144).

[290] G. Hinshaw et al. 'First Year Wilkinson Microwave Anisotropy Probe (WMAP) Observations: Angular Power Spectrum'. In: *Ap. J. Suppl.* 148 (2003), p. 135. eprint: astro-ph/0302217 (cit. on p. 145).

[291] M. G. Hauser and P. J. E. Peebles. 'Statistical Analysis of Catalogs of Extragalactic Objects. II. the Abell Catalog of Rich Clusters'. In: *ApJ* 185 (Nov. 1973), pp. 757–786. DOI: 10.1086/152453 (cit. on p. 145).

[292] Albert. Messiah. *Quantum mechanics. Volume 2*. eng. Oxford: North-Holland, 1986 - 1961. ISBN: 9780720400458 (cit. on p. 145).

[293] R. Adam et al. 'Planck 2015 results. I. Overview of products and scientific results'. In: *Astron. Astrophys.* 594 (2016), A1. DOI: 10.1051/0004-6361/201527101. arXiv: 1502.01582 [astro-ph.CO] (cit. on pp. 148–150).

[294] Kiyotomo Ichiki, Hiroaki Kanai, Nobuhiko Katayama and Eiichiro Komatsu. 'Delta-map method of removing CMB foregrounds with spatially varying spectra'. In: *PTEP* 2019.3 (2019), 033E01. DOI: 10.1093/ptep/ptz009. arXiv: 1811.03886 [astro-ph.CO] (cit. on p. 150).

[295] Ruth Durrer. *The Cosmic Microwave Background*. Cambridge: Cambridge University Press, 2008. ISBN: 978-0-511-81720-5. DOI: 10.1017/CBO9780511817205 (cit. on p. 155).

[296] Andreas Albrecht et al. 'Findings of the Joint Dark Energy Mission Figure of Merit Science Working Group'. In: *arXiv e-prints*, arXiv:0901.0721 (Jan. 2009), arXiv:0901.0721. arXiv: 0901.0721 [astro-ph.IM] (cit. on p. 155).

[297] Dan Coe. 'Fisher Matrices and Confidence Ellipses: A Quick-Start Guide and Software'. In: *arXiv e-prints*, arXiv:0906.4123 (June 2009), arXiv:0906.4123. arXiv: 0906.4123 [astro-ph.IM] (cit. on p. 155).

[298] W. L. K. Wu et al. 'A Guide to Designing Future Ground-based Cosmic Microwave Background Experiments'. In: *Astrophys. J.* 788 (2014), p. 138. DOI: 10.1088/0004-637X/788/2/138. arXiv: 1402.4108 [astro-ph.CO] (cit. on p. 155).

[299] Norbert Wiener. *Extrapolation and Smoothing of Stationary Time Series*. NY: Wiley, 1949 (cit. on p. 159).

[300] George B. Rybicki and William H. Press. 'Interpolation, Realization, and Reconstruction of Noisy, Irregularly Sampled Data'. In: *ApJ* 398 (Oct. 1992), p. 169. DOI: 10.1086/171845 (cit. on pp. 159, 162).

[301] *Bayesian Methods in Cosmology*. Cambridge University Press, 2009. DOI: 10.1017/CBO9780511802461 (cit. on pp. 159, 162).

[302] Roberto Trotta. 'Bayesian Methods in Cosmology'. In: Jan. 2017. arXiv: 1701.01467 [astro-ph.CO] (cit. on pp. 159, 162).

[303] Scott Dodelson. *Modern Cosmology*. Amsterdam: Academic Press, 2003. ISBN: 978-0-12-219141-1 (cit. on p. 159).

[304] Emory F. Bunn, Karl B. Fisher, Yehuda Hoffman, Ofer Lahav, Joseph Silk and Saleem Zaroubi. 'Wiener filtering of the COBE Differential Microwave Radiometer data'. In: *Astrophys. J. Lett.* 432 (1994), p. L75. DOI: 10.1086/187515. arXiv: astro-ph/9404007 (cit. on p. 160).

[305] J. Shewchuk. 'An Introduction to the Conjugate Gradient Method Without the Agonizing Pain'. In: 1994 (cit. on p. 161).

[306] Nicholas Metropolis, Arianna W. Rosenbluth, Marshall N. Rosenbluth, Augusta H. Teller and Edward Teller. 'Equation of State Calculations by Fast Computing Machines'. In: *The Journal of Chemical Physics* 21.6 (1953), pp. 1087–1092. DOI: 10.1063/1.1699114. eprint: https://doi.org/10.1063/1.1699114 (cit. on p. 162).

[307] W. K. Hastings. 'Monte Carlo sampling methods using Markov chains and their applications'. In: *Biometrika* 57.1 (Apr. 1970), pp. 97–109. ISSN: 0006-3444. DOI: 10.1093/biomet/57.1.97. eprint: https://academic.oup.com/biomet/article-pdf/57/1/97/23940249/57-1-97.pdf (cit. on p. 162).

[308] Andrew Gelman and Donald B. Rubin. 'Inference from Iterative Simulation Using Multiple Sequences'. In: *Statistical Science* 7.4 (1992), pp. 457 –472. DOI: 10.1214/ss/1177011136 (cit. on p. 163).